Nuclear Related Responses to Osmotic Challenge in Chondrocytes

Jerome Irianto

Submitted in part fulfilment of the requirements for the degree of

Doctor of Philosophy

School of Engineering and Materials Science

Queen Mary, University of London

Mile End Road

London, E1 4NS

2013

ABSTRACT

The application of prolonged mechanical loading to cartilage alters the osmolality of the extracellular environment, with osmotic challenge known to alter the gene expression and the metabolic activity of chondrocytes. However, the mechanisms by which osmolality controls chondrocyte activity remain unclear. Previous study on various cell types, including chondrocytes, showed that hyper-osmotic challenge induces the condensation of chromatin, with highly condensed chromatin often associated with gene poor regions of DNA and gene silencing. The present study investigated the effect of osmotic challenge on chromatin organisation, genome wide gene-expression and the cellular and nuclear deformability of chondrocytes. In order to observe a broad effect of osmotic challenge on the nuclei, the chondrocytes were subjected to a range of hypo- and hyper-osmotic challenge and imaged by confocal microscopy. Chromatin condensation was quantified by the Sobel edge algorithm in MATLAB. Hyper-osmotic challenge on chondrocytes induced an increase in chromatin condensation. Interestingly, the most marked condensation occurred within the osmolality range of articular cartilage *in vivo*. The effect of osmotic challenge varied between the monolayer cultured and agarose seeded chondrocytes, which may be due to the differences in cytoskeleton organisation between the two culture conditions. Additionally, chromatin condensation induced by hyper-osmotic challenge was shown to be reversible. Marked differences were observed in the deformability of the cell and nucleus in chondrocytes post osmotic challenge, compared to the 300 mOsm/kg conditions typically used for *in vitro* isolated chondrocyte studies. From the microarray study, the application of 500 mOsm/kg for both 1 and 5 hours altered the gene expression, including the expression of histone related genes, with a higher number of genes affected by the 5 hours hyper-osmotic challenge. The findings of this study suggest that osmotically-induced alterations in nuclei morphology and chromatin structure may provide a direct biophysical mechanism that controls chondrocytes activity.

ACKNOWLEDGEMENTS

I dedicate this thesis to my beloved parents.

First of all, I wish to express my most sincere gratitude and appreciation to my supervisors, Prof. David A. Lee and Prof. Martin M. Knight, for their patience, guidance and encouragement throughout the development of this project. I truly feel that they are great supervisors.

Thanks to all my friends in the Cell and Tissue Engineering Lab. Rui P. Martins, for his guidance and many insightful discussions throughout the project. Angus Wann, Hannah Heywood, Eijiro Maeda and Girish Pattappa, for their guidance and support. Erica di Federico, for the countless discussions. Clare Thompson, Ke Bai, Mo Waked, Chavaunne Thorpe and Stephen Thorpe, for making the lab a fun environment.

Also essential to this project, "Big" Mike Collins, Dougie Thomson, Chris Mole, Shafir Iqbal, Tony Willis, Dennis Ife, Catherine Jones, Jonathon Hills and Chris Straw, thank you for all the support that they gave into this project.

I would like to thank all my friends in the office (from ENG 374 in the early days till G24 in the later days). Chetan, Mayo, Pili and Zack for being my senior, guiding me through the project. Hassan for being my motivating 'rival'. Milan, Stephan and Shen Ren for accepting me into the 'cozy' office G24.

I would like to thank my girlfriend, Lydia Bumrungkarn, for being very understanding, supporting and patient with me throughout the writing-up period. Especially for the lovely home-cooked late dinners when I need to work late.

Lastly, and most important, I would like to thank my parents, sister and brother in-law for their reminders and immense support to keep me in track along the up and the down of this project.

I would to say thank you to all of you again, with the absent of any of you, I will not be able to complete this project.

"Success is the ability to go from one failure to another with no loss of enthusiasm"
-Sir Winston Churchill

TABLE OF CONTENTS

LIST OF FIGURES

Chapter 1

Chapter 2

Chapter 3

Chapter 4

Chapter 5

Chapter 6

Appendix

LIST OF TABLES

Chapter 1

Chapter 2

Chapter 5

Appendix

ABBREVIATIONS

2D	Two dimensions
3D	Three dimensions
ATMIN	ATM interactor
BLM	Bloom syndrome homolog
BMP	Bone morphogenetic protein
BP	Biological process
C230052I12RIK	RIKEN cDNA C230052I12 gene
CASP9	Caspase 9
CC	Cellular component
CCND1	Cyclin D1
CDKN1A	Cyclin-dependent kinase inhibitor 1A
CDNA	Complementary deoxyribonucleic acid
CLSM	Confocal laser scanning microscope
CLSPN	Claspin homolog
CRNA	Complementary ribonucleic acid
DABCO	1,4-Diazabicyclo[2.2.2]octane
DMEM	Dulbecco's modified Eagle's medium
DNA	Deoxyribonucleic acid
DNASE I	Deoxyribonuclease I
EBSS	Earle's balanced salt solution
ECM	Extracellular matrix
EEF1E1	Eukaryotic translation elongation factor 1 epsilon 1
FACIT	Fibril-associated collagens with interrupted triple helices
F-ACTIN	Filamentous actin
FCD	Fixed charge density
FCS	Foetal calf serum
FGF	Fibroblast growth factor
GADD45A	Growth arrest and DNA-damage-inducible 45 alpha
GAG	Glycosaminoglycan
GFP-PDNA	Green fluorescence protein plasmid deoxyribonucleic acid

GO	Gene ontology
GTF2H1	General transcription factor II H, polypeptide 1
GTF2H2	General transcription factor II H, polypeptide 2
GTF2H3	General transcription factor IIH, polypeptide 3
H2AFX	H2A histone family, member X
H2B	Histone 2B
HAS	Hyaluronan synthase
HEPES	4-(2-hydroxyethyl)-1-piperazineethanesulfonic acid
HIST1H1C	Histone cluster 1, h1c
HIST1H2AB	Histone cluster 1, h2ab
HIST1H2AC	Histone cluster 1, h2ac
HIST1H2AD	Histone cluster 1, h2ad
HIST1H2AF	Histone cluster 1, h2af
HIST1H2AG	Histone cluster 1, h2ag
HIST1H2AH	Histone cluster 1, h2ah
HIST1H2AK	Histone cluster 1, h2ak
HIST1H2BC	Histone cluster 1, h2bc
HIST1H2BF	Histone cluster 1, h2bf
HIST1H2BH	Histone cluster 1, h2bh
HIST1H2BJ	Histone cluster 1, h2bj
HIST1H2BK	Histone cluster 1, h2bk
HIST1H2BM	Histone cluster 1, h2bm
HIST1H2BN	Histone cluster 1, h2bn
HIST1H3A	Histone cluster 1, h3a
HIST1H4F	Histone cluster 1, h4f
HIST1H4H	Histone cluster 1, h4h
HIST1H4I	Histone cluster 1, h4i
HIST1H4J	Histone cluster 1, h4j
HIST2H2AN	Histone cluster 2, h2an
HIST2H2AO	Histone cluster 2, h2ao
HMOX1	Heme oxygenase
HSPA1A	Heat shock protein 1A

HUS1	Hus1 homolog
IGF-1	Insulin-like growth factor 1
IL-1	Interleukin 1
ILMN ID	Illumina ID
IMS	Industrial methylated spirit
ING4	Inhibitor of growth family, member 4
KEGG	Kyoto Encyclopaedia of Genes and Genomes
LIF	Leukaemia inhibitory factor
MAPK	Mitogen-activated protein kinase
MF	Molecular function
MMP	Matrix mettaloprotease
MRNA	Messenger ribonucleic acid
MSH6	Muts homolog 6
MUS81	MUS81 endonuclease homolog
NA	Numerical aperture
NASP	Nuclear autoantigenic sperm protein
NSBP1	Nucleosome binding protein 1
NSMCE2	Non-SMC element 2 homolog
NUPR1	Nuclear protein 1
OA	Osteoarthritis
OMIM	Online Mendelian Inheritance in Man
PARP2	Poly (ADP-ribose) polymerase family, member 2
PCNA	Proliferating cell nuclear antigen
PHLDA3	Pleckstrin homology-like domain, family A, member 3
PML	Promyelocytic leukemia
PML	Promyelocytic leukemia
PMT	Photomultiplier tube
POLD1	Polymerase (DNA directed), delta 1, catalytic subunit
POLL	Polymerase (DNA directed), lambda
PRMT6	Protein arginine N-methyltransferase 6
PTTG1	Pituitary tumor-transforming 1
RAD1	RAD1 homolog

RAD17	RAD17 homolog
RAD50	RAD50 homolog
RBX1	Ring-box 1
RDNA	Ribosomal deoxyribonucleic acid
RNF8	Ring finger protein 8
ROI	Region of interest
RPAIN	RPA interacting protein
RRNA	Ribosomal ribonucleic acid
RVD	Regulatory volume decrease
RVI	Regulatory volume increase
SGK1	Serum/glucocorticoid regulated kinase 1
SIRT1	Sirtuin 1
SMUG1	Single-strand selective monofunctional uracil DNA glycosylase
TEM	Transmission electron microscopy
TGF-B	Transforming growth factor β
TIPIN	Timeless interacting protein
TLK1	Tousled-like kinase 1
TNF-A	Tumour necrosis factor α
TOPORS	Topoisomerase I binding, arginine/serine-rich
TRIAP1	TP53 regulated inhibitor of apoptosis 1
XPA	Xeroderma pigmentosum, complementation group A
XPC	Xeroderma pigmentosum, complementation group C
XRCC2	X-ray repair complementing defective repair in Chinese hamster cells 2
ZMAT3	Zinc finger matrin type 3

Chapter 1 Articular Cartilage

1.1 Introduction

Articular cartilage is a highly specialised connective tissue found within diarthrodial joints (Figure 1.1) that provide a key biomechanical function necessary for the smooth articulation of the joint. It comprises a single cell type, the chondrocyte and a notably specialised extracellular matrix (ECM). Cartilaginous tissues are characterised by their ECM organisation, which is closely linked to their biomechanical function, with alterations in biochemical composition and the molecular organisation of the matrix distinguishing the biomechanical properties of the tissue.

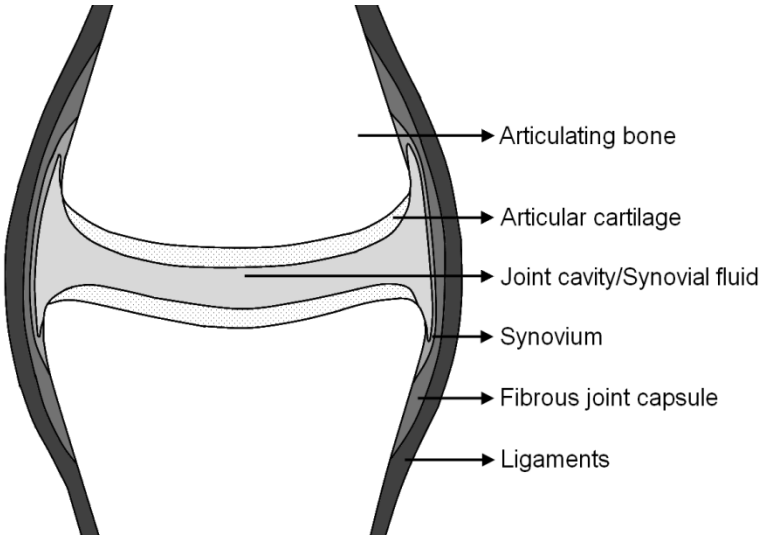

Figure 1.1 Schematic of a diarthrodial joint.

Articular cartilage is the most common and the most studied hyaline cartilage (Mow *et al.* 1992; Mankin *et al.* 2000). Hyaline comes from a Greek word 'hyalos', meaning glass or transparent. Thus on appearance, hyaline cartilage is glassy smooth, glistening, and bluish-white in younger and healthy tissue, although it tends to lose this appearance in degenerated or older tissue. Articular cartilage covers the articulating surfaces within all diarthrodial joints. Within freely moveable joints such as knee or hip, articular cartilage can withstand immense loading and additionally provide a smooth lubricating bearing material with minimal wear (Greenwald and O'Connor 1971; Bader and Lee 2000). It is well established that the application of mechanical loading to the cartilage during normal activity results in a cellular response that is necessary to maintain the function state of the tissue. This process is known as mechanotransduction.

Cartilage tissue is susceptible to damage and degeneration associated with trauma and pathological conditions such as osteoarthritis (OA), which may result in pain and loss of function within load-bearing joints. The onset and progression of degenerative conditions of cartilage may result from a variety of mechanical, biochemical, and humoral factors that manifest in an acute and traumatic form or in a chronic fashion. Degenerative conditions alter the biochemical properties of the cartilage tissue, ultimately reducing its performance as the load bearing material (Howell *et al.* 1992). Articular cartilage has a poor intrinsic capacity for repair or regeneration. One of the reasons is the avascular nature of articular cartilage, where progenitor cells cannot access partial thickness defects and the resulting repairs by the cells adjacent to the wound or the synovial cells are very limited. Additionally, in full thickness defects, repairs by the progenitor cells that reside in the bone marrow space of subchondral bone result in the formation of fibrocartilaginous tissue, which is a poor substitute for the original articular cartilage tissue (see Redman *et al.* 2005). There is currently great interest in the development of cellular-based therapies, such as autologous chondrocyte implantation to overcome these clinical problems (Watanabe *et al.* 1998; Brittberg 2003). However, these approaches will ultimately involve the implanted cells being subject to mechanical loading within the restored tissue and understanding the process by which chondrocytes detect and respond to load is key to the restoration of a functional engineered tissue that demonstrates a normal adaptive response.

The osmolality of articular cartilage tissue depends on the concentration of the negatively charged proteoglycan in the ECM. Proteoglycan concentration increases along the depth of the tissue and upon the extrusion of fluid out of the tissue during the application of mechanical loading, which increase the osmolality. Pathological degradation of the ECM lowers proteoglycan concentration, which consequently reduce the tissue's osmolality. It is well established that the application of osmotic stress in both cartilage tissue and isolated chondrocytes alters matrix synthesis. Osmotic stress also alters nuclear morphology and chromatin structure, which may provide a direct biophysical mechanism for controlling cellular metabolism. The work presented in this thesis aims to investigate the effect of osmotic challenge on the nucleus of chondrocytes, both in terms of morphological changes and genome function.

1.2 Extracellular Matrix

Articular cartilage may be regarded as a multi-phasic material with water and electrolytes composing the fluid phase and a solid phase comprising collagen, proteoglycans, other proteins and chondrocytes. Water is the most abundant component of articular cartilage, occupying 60 to 85% of the cartilage, followed by type II collagen at 15 to 22% and aggrecan at 4 to 7%. The rest of articular cartilage ECM (less than 5%) is characterised by a wide variety of other matrix components, such a various minor collagens (types I, V, VI, IX and XI), link proteins, hyaluronan, smaller proteoglycans (decorin, biglycan, fibromodulin, perlecan), fibronectin, and thrombospondins (Maroudas *et al.* 1980; Poole *et al.* 2001; Eyre 2002).

1.2.1 Interstitial Fluid

Alteration in the water content significantly affects the mechanical, fluid transport and swelling properties of articular cartilage. The water content depends broadly on two factors. The first is the concentration of negatively charged proteoglycan and other ions in the interstitial fluid. The main ions dissolved in the interstitial fluid are sodium, chloride, potassium and calcium. Most of the fluid and ions within the articular cartilage can diffuse freely with the bathing solution around the tissue. Extrusion of the interstitial fluid may also be triggered by the application of compression or pressure gradients across the tissue. When interstitial fluid flows through the pores in the collagen-proteoglycan solid matrix, it creates significant frictional drag forces on the walls of the pores, constricting the fluid flow. This phenomenon results in strain-dependent permeability, such that the flow of fluid is progressively restricted with prolonged compression (Armstrong and Mow 1982; Holmes *et al.* 1985; Mow *et al.* 1989; Torzilli *et al.* 1990; Lai *et al.* 1991).

Secondly, the water content also depends on the organisation of the collagen network, which surrounds the proteoglycans and counteracts the swelling pressure. In healthy cartilage, roughly 30% of the water within the articular cartilage dwells within the intrafibrillar space of collagen, which determines the diameter of the collagen fibres. The water level within the intrafibrillar compartment remains relatively constant in normal tissues and with age, additionally, it appears to be unavailable for transport during the application of mechanical loading (Maroudas 1976; Maroudas and Schneiderman 1987; Maroudas *et al.* 1991; Wachtel *et al.* 1995).

1.2.2 Collagen

The two main functions of the collagen in articular cartilage are to provide tensile strength and stiffness for the tissue and to accommodate the swelling pressure exerted by the embedded proteoglycans. Based on their structure and biological functions, collagens can be divided into a number of subclasses. Collagen type I, II, V, and XI falls into fibril-forming collagens class, while collagen type VI is a beaded filament-forming collagen and collagen type IX belongs to fibril-associated collagens with interrupted triple helices (FACIT) group.

Structure

Collagens are made of three polypeptide α-chains, which form a tight right-handed collagen triple helix. Different collagen types are named according to the genetic type and the combination of the α-chains making up the collagen, where a collagen may be made of identical or different α-chains. For example, the main collagen in articular cartilage type II is made of three identical α1(II) chains, while type IX collagen is made of three distinct α-chains α1(IX) α2(IX) α3(IX) and type I collagen is made of two identical and a distinct α-chains $\alpha1(I)_2\alpha2(I)$ (Hulmes 2008).

An α-chain, made of repeating $(Gly\text{-}X\text{-}Y)_n$ triplets, forms a natural left-handed helix, where X is usually proline and Y is usually hydroxyproline (Figure 1.2). The repetition number of Gly-X-Y varies in different collagen types. In case of fibril-forming collagen it is often found that the repetition goes over 1000-amino-acid length, where the repeats are generally broken off by other non-collagenous domains in the nonfibrillar collagens. The sequential alteration of glycine, proline, and hydroxyproline are responsible for the tightly packed and rigid triple helix structure, which is the foundation of collagen's tensile strength. At the end of each α-chain, there is a short sequence of about 25 amino acid residues (telopeptides) that do not have a triple helix structure (Kempson *et al.* 1973; Akizuki *et al.* 1986; Prockop and Kivirikko 1995; see Bader and Lee 2000).

The triple right-handed helix structure of the α-chains is called a tropocollagen molecule, and can further polymerise extracellularly in a staggered lateral manner to form collagen fibril. The tropocollagen molecules are packed side by side and staggered along the axis with a periodicity of 680Å (1.0 D), which is called the D-period (Hulmes *et al.* 1981). The

fibrils are stabilised by covalent intermolecular cross-links, enforcing the main function of collagen to provide the tensile stiffness for the tissue. These fibrils are usually heterogeneous, i.e. consisting more than one type of collagen. In the case of articular cartilage, where type II collagen is the major collagen component, type XI collagen can be found within the fibril structure cross-linked covalently to type II that commonly occurs in smaller fibrils. Meanwhile, type IX can be found on the surface of the fibril, which can bind covalently to the other type IX collagen molecules, thus helping to form and stabilise the three-dimensional collagen fibril meshwork within the tissue (Mendler *et al.* 1989; Schmidt *et al.* 1990; Wu *et al.* 1992; Blaschke *et al.* 2000).

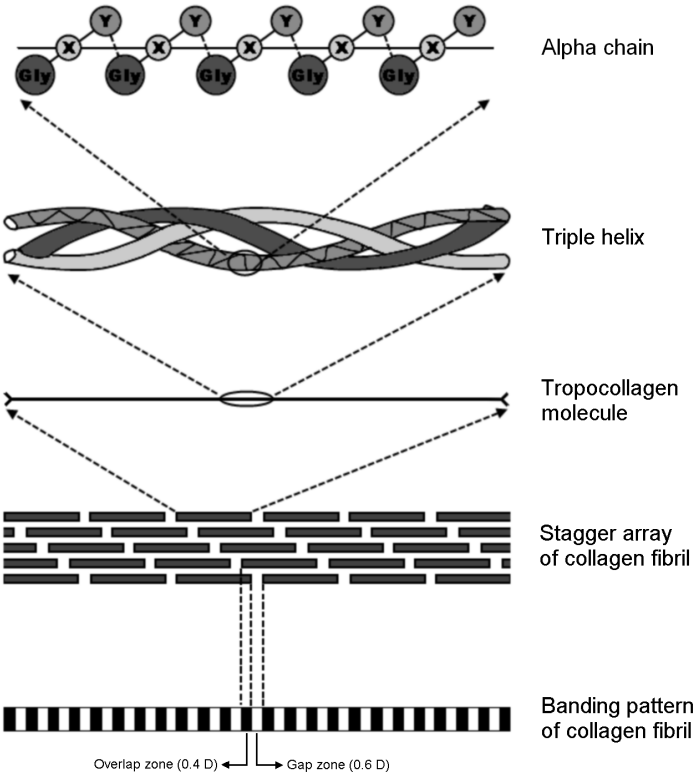

Figure 1.2 Schematic drawing of collagen fibril structure.

The diameter of a collagen fibril varies from 10 to 300 nm, depending on the collagen types and its location within the tissue. For example, in articular cartilage, the type II tropocollagen forms small diameter fibrils (10 to 250 nm) around the pericellular region,

while in the territorial and inter-territorial matrix it forms larger diameter fibrils (300 nm) (Mow *et al.* 2005).

Synthesis

Synthesis of collagen starts with the transcription of the collagen genes in the nucleus, which involves a series of tissue specific and developmentally regulated alternative splicings (Ryan and Sandell 1990; Sandell *et al.* 1991). In the case of fibril-forming collagens, the messenger ribonucleic acid (mRNA) produced is then translated and transferred to the endoplasmic reticulum as prepro-α-chains. Within the reticulum, the signal peptides of these chains are cleaved, thereby producing procollagen chains, which will undergo a series of post-translational modifications such as the hydroxylation of proline into hydroxyproline and glycosylation. Still inside the reticulum, the α-chains are assembled from the COOH terminus towards the NH_2 terminus, into a triple-helix structure and secreted from the chondrocyte. In the extracellular space, the tropocollagen is produced by cleaving the registration peptides of the triple-helix molecule secreted. Finally, the tropocollagen molecules come together, self aggregate and connect with intermolecular crosslinks to form collagen fibrils (Bader and Lee 2000).

1.2.3 Proteoglycan

The main function of the proteoglycans in cartilage is to provide compressive stiffness for the tissue. Proteoglycans can be described as large complex molecules composed of a core protein to which at least one glycosaminoglycan (GAG) chain is covalently attached (Bader and Lee 2000). There is an enormous diversity in proteoglycan as a class of molecules. This is because there are many types of GAG and in addition to the huge number of possible combination between the core proteins and GAGs.

In articular cartilage, 80 to 90% of the proteoglycan is composed of aggrecan and its presence is considered as a marker for chondrogenesis. Aggrecan is a member of the large aggregating proteoglycan family, due to its ability to create larger aggregates. This aggregation of aggrecan by attaching to hyaluronan and link protein creates a macromolecular aggregate, which can be immobilised by the collagen network. The nature of these large aggregates is responsible for the ability of cartilage to withstand compressive

loading (Hardingham 1979; Muir 1983). Besides aggrecan, other proteoglycans also present in the articular cartilage are biglycan, decorin, fibromodulin, lumican, and perlecan.

Structure

GAGs are unbranched polysaccharides composed by repeating disaccharides of alternating uronic acid and acetylated amino sugar. Chondroitin sulphate is made of repeating disaccharide glucuronic acid and N-acetyl-galactosamine with a sulphate group attached to each disaccharide. While keratan sulphate is made of galactose and N-acetyl-glucosamine also with a sulphate group attached to each disaccharide.

GAG chains in proteoglycan play a major role in their physicochemical properties. GAGs are one of the most anionic molecules in the body, due to the highly negatively charged sulphate and carboxyl groups attached to them, which makes GAGs charged in solution and *in situ*, providing a fixed charge density (FCD). The total FCD in cartilage was measured to be 0.05 to 0.3 mEq/g wet weight of the tissue (Maroudas 1968).

The fixed negative charge of GAG attracts counterions, such as Na^+, increasing the osmotic pressure, which in turn promotes hydration of the tissue. Secondly, GAGs tend to repel each other due to their negative charges. These two observable phenomena responsible for the swelling pressure of cartilage tissues, measured to be approximately 0.25 MPa. The swelling pressure contributes to the compressive stiffness of the ECM within cartilage, which is around 0.5 to 1 MPa. Besides this, FCD is also responsible in controlling the transport of electrolytes and electrokinetic properties of cartilage (Lai *et al.* 1991; Athanasiou *et al.* 1995).

Aggrecan is composed of chondroitin sulphate chains, keratan sulphate chains, and a core protein (Figure 1.3). The core protein contributes to 10% of the aggrecan and the rest comprises of the GAG chains. There are around 30 keratan sulphate chains and 100 chondroitin sulphate chains attached to a core protein. The structure of chondroitin sulphate changes depends on the depth of articular cartilage and the chain length decreases with age. The molecular mass of a core protein is around 210-250 kDa. In term of its structure, a core protein has three globular domains, G1 at NH_2 terminus, G2, and G3 at COOH terminus. Between G1 and G2, there is an interglobular domain. Between G2 and G3, there are keratan sulphate and chondroitin sulphate attachment domains. G1 is the part of core protein that attaches to hyaluronan. This attachment is stabilised by a link protein, which

binds to both hyaluronan and G1 non-covalently, thereby creating an aggrecan-hyaluronan-link protein complex. This binding interaction cannot be dissociated under physiological conditions, unless proteases are present. The size of aggrecan aggregates can reach 300 to 400 million Da, although this reduces with age and in disease states (Hardingham 1979; Heinegard and Oldberg 1989; Hardingham and Fosang 1992; Bayliss *et al.* 1999).

The GAG chains for biglycan and decorin are chondroitin sulphate and dermatan sulphate. Biglycan has two GAG chains and decorin has one GAG chain. Within adult articular cartilage, biglycan can be found in the pericellular matrix and is associated with positive regulation of bone formation; whereas decorin is in the inter-territorial matrix, and is associated with the assembly regularity and the tensile strength of various collagen fibrils. However, decorin deficiency does not seem to affect collagen type II which is the major collagen in articular cartilage (Scott 1996; Xu *et al.* 1998).

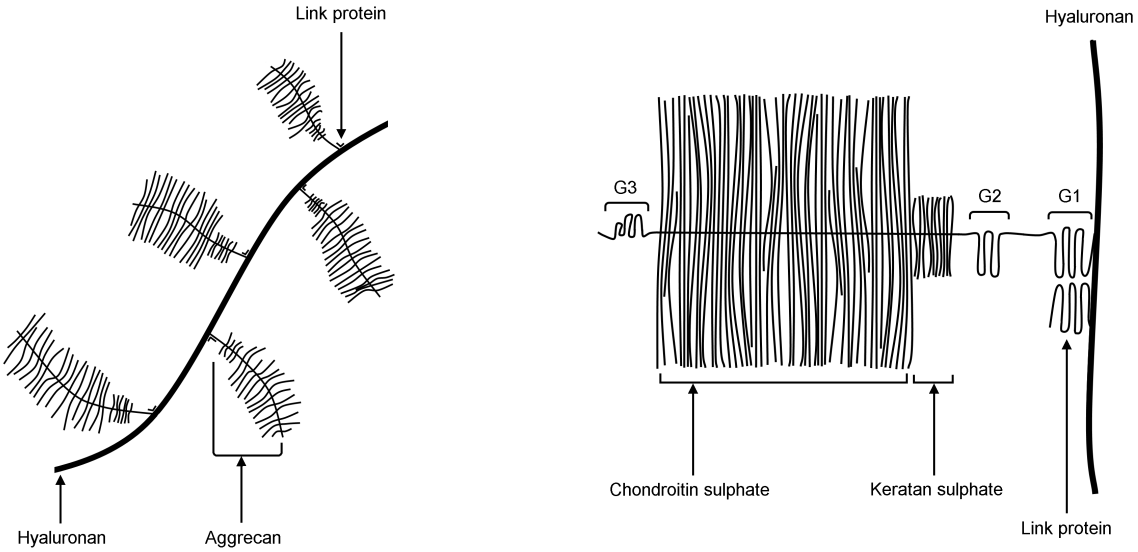

Figure 1.3 Schematic presentation of aggrecan aggregate (left) and aggrecan (right) (Adapted from Bader et al. 2000).

When pure proteoglycan is diluted in aqueous solution, it occupies five to ten times larger domain than the space available in the interfibrillar space of cartilage tissue. Thus, proteoglycan *in situ* is folded into a compacted state to fit within the collagen matrix. This phenomenon is responsible for its immobilisation inside the matrix and also contribute to the flow-dependent viscoelastic properties of cartilage during compressive loading by means of steric exclusion and frictional drag (Muir 1983; Gu *et al.* 1993).

Synthesis

In cartilage, chondrocytes are responsible for the synthesis, modification, assembly, and organisation of proteoglycan molecules. For aggrecan, the core protein is synthesised in the endoplasmic reticulum, which is followed with the addition of N-linked oligosaccharide, the initiation of GAG chains assembly. The product is then transported into the Golgi apparatus, where the elongation and complex post-translational modification of GAG takes place. Still in the Golgi apparatus, serine residues are linked to the long GAG chains and sulphotransferase enzyme then sulphates the GAG chains. Finally, the aggrecan are secreted out of the cell (Mankin *et al.* 2000).

Link protein is often synthesised together with aggrecan and at a similar rate, even though they are coded by different genes and regulated independently. Hyaluronan is synthesised by hyaluronan synthase (HAS), which is located on the plasma membrane and is directly secreted into the pericellular matrix. The assembly of aggrecan-hyaluronan-link protein aggregate takes place in the ECM. Hyaluronan that is not attached by the aggrecan, may interact with CD44, a hyaluronan receptor on the chondrocyte. In synovial fluid, hyaluronan also being produced by synoviocytes to act as a lubricant (Prehm 1983; Ratcliffe *et al.* 1987; Knudson *et al.* 1996).

1.2.4 Other Proteins

In cartilage tissue, growth factors, cytokines and hormones affect chondrocytes in various aspects, including the regulation of matrix synthesis and degradation, proliferation rate and differentiation (Allen *et al.* 2012). Some cytokines control both anabolic and catabolic processes, thus acting as a regulator. The anabolic controlling cytokines includes insulin-like growth factor I (IGF-1), transforming growth factor β (TGF-β), bone morphogenetic protein (BMP) and fibroblast growth factor (FGF). While the ones controlling catabolic activities include interleukin 1 (IL-1), IL-17, IL-18, tumour necrosis factor α (TNF-α) and leukaemia inhibitory factor (LIF). IL-6 is an example of a cytokine which controls both catabolic and anabolic activities. Abnormal synthesis and activity of growth factors and cytokines often lead to the destruction of the tissue. Both IGF-1 and TGF-β promotes chondrocytes proliferation, differentiation, matrix production and inhibit matrix degradation (Trippel 1995; Gouttenoire *et al.* 2010). In contrast, IL-1 inhibits proteoglycan and collagen synthesis, and it mediates proteoglycan and collagen degradation by

promoting the production of destructive proteases (see Dijkgraaf *et al.* 1995; McInnes and Schett 2007).

Degradative enzymes

Matrix mettaloproteinases (MMPs) are major enzymes responsible for controlling cartilage matrix degradation, which are active at neutral pH and up-regulated by IL-1 and TNF-α. There are around 20 proteases in MMPs family, which can degrade various ECM proteins such as collagen, proteoglycan, fibronectin, fibrinogen and thrombospondin. MMPs activity depends on their activation rate by other proteases, such as plasmin and urokinase plasminogen activator, along with the ratio of the MMPs and their inhibitors (Benaud *et al.* 1998).

Depending on the substrate affected, MMPs can be divided into collagenases, gelatinases, stromelysins and membrane-type MMPs. Collagenases such as MMP 1, 8, and 13, cleaves helical collagens, making them vulnerable for further cleavage by other MMPs, including gelatinases and stromelysins. The cleavage site for collagens is situated approximately three quarter of the collagen helix from the NH_2 terminus. MMP 13 is most efficient in cleaving type II collagen, the main collagen in articular cartilage. During the degradation of aggrecan, the cleavage sites situated between G1 and G2 of the core protein are cleaved by MMPs and aggrecanase, separating the GAG-containing region from the hyaluronan. These GAG-containing fragments then readily pass through the ECM into the synovial fluid (Reboul *et al.* 1996; Shlopov *et al.* 1997; Caterson *et al.* 2000).

1.2.5 Depth Dependent Organisation

The composition and structure of articular cartilage varies through its thickness. This variation involves alterations in chondrocyte morphology, proteoglycan densities, water content, collagen fibrils orientation and diameter (Figure 1.4).

In the superficial zone of human articular cartilage, which accounts for 10 to 20% of the cartilage tissue, the water content (75-80%) and collagen content (~85% dry weight) are at their highest. The collagen fibrils in this layer are fine (30 nm diameter) and densely arranged parallel to the articulating surface. This gives the superficial layer the highest tensile strength. Meanwhile, the aggrecan content is the lowest compared to the middle and deep layer. Additionally, during normal daily function, the superficial zone experiences the

highest tensile and compressive stresses. In the middle layer, which occupies 40 to 60% of the tissue, the aggrecan content is higher and the collagen content is lower than the superficial layer. However, the collagen fibrils have a greater diameter, are less dense and are randomly orientated. Finally, in the deep zone, which accounts for approximately at 30% of the tissue depth, aggrecan content is at the highest and the collagen content is similar to the middle zone. However, the collagen fibrils in this layer are intertwined to form large fibre bundles perpendicular to the surface and act as an anchorage crossing the 'tidemark' into the calcified cartilage and subchondral bone. The water content decreases with depth of the articular cartilage tissue (Stockwell 1967; Muir *et al.* 1970; Redler *et al.* 1975; Maroudas *et al.* 1980; Poole *et al.* 2001).

The size, shape, orientation and synthetic activities of the chondrocytes also vary through the depth of the articular cartilage. The cell density drops through the depth and with age. In the superficial zone, the cells are flattened in morphology and oriented parallel to the surface, while they synthesise more collagen and less proteoglycan. The chondrocytes in the middle zone are more rounded and have higher synthetic activities. The proteoglycan synthesis rate is higher and the collagen fibrils produced have a higher diameter size. Finally, in addition to the increase in synthetic activity, the chondrocytes in the deep layer are arranged in columns perpendicular to the surface, following the arrangement of the collagen fibrils around them (Bader and Lee 2000; Poole *et al.* 2001).

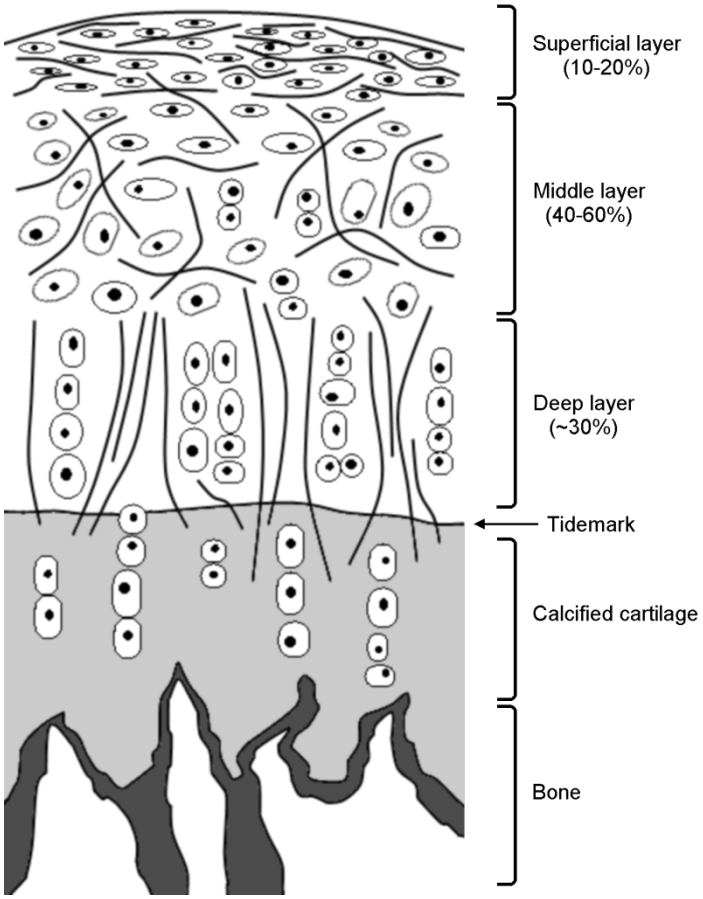

Figure 1.4 Schematic representing the layered structure of cartilage collagen network and chondrocytes morphology, showing three distinct regions.

1.3 Chondrocytes

The chondrocyte is the only cell type in adult articular cartilage, and is a highly specialised and terminally differentiated cell. The proliferation rate of mature chondrocytes in healthy articular cartilage is very limited. Meanwhile, upon injury of the tissue, an increase in both cell death and proliferation was observed (Tew *et al.* 2001). Large proportion of the tissue is occupied by ECM (>80%) and the cell density varies between species, body weight and joint sizes. For femoral condyle, the cell density varies from 14,100 cells/mm^3 for human to 334,000 cells/mm^3 for mouse, which suggests that the chondrocytes occupy around 1% to 17% of the tissue, respectively (Stockwell 1971).

In vivo, chondrocytes are generally surrounded by a pericellular matrix, which is around 2 μm thick and rich in type VI collagen. The chondrocyte and pericellular matrix forms a structural and functional unit called the chondron (Figure 1.5). Encapsulating the individual

chondron is the territorial matrix, which has thicker collagens forming radial bundles within the matrix. The matrix filling the spaces between the chondrocytes is termed the inter-territorial matrix (Poole *et al.* 1987).

Chondrocyte metabolic activities involve anabolic processes which includes synthesis, assembly, and organisation of the ECM, and catabolic activity, involved in the degradation and loss of ECM. Chondrocytes are responsible for the regulation of these anabolic and catabolic activities and keeping them in balance, thus maintaining the ECM integrity and the cartilage tissue's biological functions. This regulation process depends on changes in the environment surrounding the cells, involving soluble mediators, such as cytokines, growth factors, hormones, proteases and pharmaceutical agents; also the mechanical environment, such as stress, strain, osmotic pressure, flow velocities, hydraulic pressure, electric currents and potentials; and other physicochemical events. During pathological conditions such as osteoarthritis, this homeostasis is disturbed, leading to the degradation of the ECM, which involves the loss of aggrecan and collagen into the synovial fluid.

The interaction between the chondrocytes and ECM is facilitated by cell surface receptors such as integrins, annexin V and CD44. These receptors translate the mechanical and biochemical changes in the ECM around the cells, involving, for example ECM deformation due to mechanical loading and the composition changes caused by the degradation of the matrix which may induce an increase in cell proliferation (Rothwell and Bentley 1973) and matrix production (Chrisman 1969; Repo and Mitchell 1971).

CD44 is a hyaluronan receptor which is reported to be responsible for the inhibition of proteoglycan synthesis as it binds to hyaluronan (Knudson and Knudson 1993). Annexin V or anchorin CII is a type II collagen receptor, which binds to the telopeptides and the C-propeptide region of the collagen, anchoring the cells to the collagen fibrils. This receptor is also believed to act as a mechano-receptor on the chondrocyte cell surface (Turnay *et al.* 1995).

Integrins are heterodimeric receptors for adhesive proteins, composed by a α and a β subunit and they mediate a wide range of functions. Extracellularly, integrins bind to collagen, fibronectin, thrombospondin, vitronectin and laminin. $\alpha_1\beta_1$ and $\alpha_{10}\beta_1$ integrins mediate chondrocyte attachment to type II collagen, while the $\alpha_5\beta_1$ integrin is the primary fibronectin receptor. Intracellularly, integrins interact with components associated with

various signalling pathways and the cytoskeleton, affecting the transduction of alterations in integrin binding in response to the changes in ECM. The synthesis of integrins is regulated by growth factors and cytokines that regulate cartilage functions (e.g. IGF-1 and TGF-β), the development stage of the tissue, and the cell zonal location (Loeser 2000; Hynes 2002).

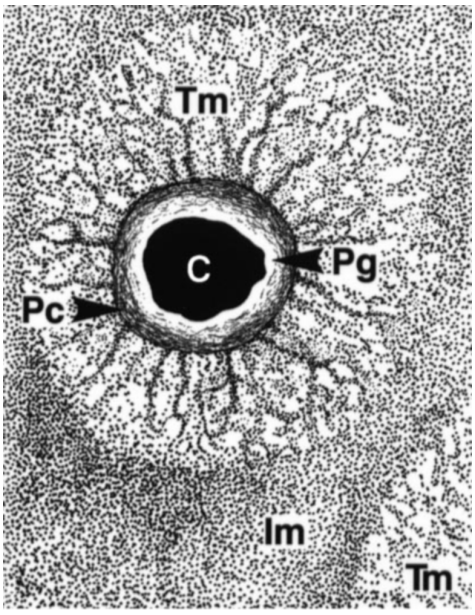

Figure 1.5 Diagrammatic representation of the microenvironment of a chondrocyte, showing the chondrocyte (C), pericellular glycocalyx (Pg), pericellular capsule (Pc), territorial matrix (Tm), and interterritorial matrix (Im) (Poole 1997).

1.3.1 Cytoskeleton

Like other eukaryotic cells, chondrocytes possess various organelles that are critical for a range of key cellular functions. The essential organelles for the production of cartilage matrix include the mitochondria, lysosomes, the Golgi apparatus, the endoplasmic reticulum and the nucleus. Additionally, chondrocytes possess a complex cytoskeletal network which is essential in mechanotransduction.

The cytoskeleton acts to maintain the morphology of the cell by means of a complex filamentous structure within the cytoplasm (Trickey *et al.* 2004). In chondrocytes, the cytoskeleton comprises a three dimensional network, which is composed of three major elements: microfilaments, microtubules and intermediate filaments.

The microfilaments are the thinnest among the cytoskeletal components, with a diameter of around 8 nm. The microfilament building block is a single monomer, actin that polymerises

to create a tightly packed simple helix known as filamentous actin (F-actin). This process is induced by increasing the concentration of K^+ and Mg^{2+}. The ends of the filament behave in a chemically distinct manner due to the oriented alignment of the monomers, providing a polar behaviour, which is essential to its functionality. For example, each end has a distinct critical concentration which triggers the polymerisation or depolymerisation of the filament. In most cells, actin microfilaments form a tangled cross-linked mesh. Microfilaments are most abundant at the periphery of cells, just beneath the plasma membrane, particularly in areas where the cell shape is rapidly changing. As such microfilaments are closely involved in maintenance of cell shape and motility (Neuhaus *et al.* 1983; Brown and Benya 1988; Grazi *et al.* 1992; Benjamin *et al.* 1994; Insall and Machesky 2001).

Microtubules have a diameter of around 25 nm, and comprise filaments of polymerised dimers formed from α and β tubulin sub-units. Each microtubule is created by 13 filaments encircling the hollow core, thereby bestowing them with a greater rigidity than actin microfilaments. Within a cell, the microtubules spread from a point near the nucleus and only occasionally extend to the edge of the cell. Microtubules play a role in the distribution of organelles and vesicles, cell division and the organisation of other cytoskeletal elements. For example, the centriole, which is composed by nine fused microtubule triplets forming a small cylinder, plays a major role during the redistribution of nuclear contents in the cell division process. Additionally, in chondrocytes, microtubules are essential in the biosynthesis and secretion of collagen and the proteoglycans (Benjamin *et al.* 1994; Insall and Machesky 2001).

Intermediate filaments have diameters of approximately 10 nm. Unlike microfilaments and microtubules, there are distinct types of intermediate filament involving different monomeric components. Each intermediate filament is made of a tetramer constructed by two anti-parallel dimers, which in turn is made of two intertwined monomers. Intermediate filaments are often long, forming a meshwork spanning along the whole width of the cell. Intermediate filaments play a role in maintaining the integrity of the cell against mechanical loading, especially tension and shear loading. Additionally, they are also involved in transport and signalling functions. Nuclear lamina, keratin and vimentin are examples of different intermediate filament types. In chondrocyte, the up-regulation of intermediate

filaments is often associated with the degeneration of cartilage (Benjamin *et al.* 1994; Langelier *et al.* 2000; Insall and Machesky 2001; Shieh and Athanasiou 2002).

Tension on integrins, which are connected to the cytoskeleton, has been shown to induce a deformation of the nucleus and redistribution of the nucleoli, suggesting a connection between the cytoskeleton and the nucleus (Maniotis *et al.* 1997). The nuclear membrane connected to the cytoskeleton via the LINC complex, involving SUN and KASH proteins (Crisp *et al.* 2006). However, the precise nature of the connections between the cytoskeleton and the chromatin remains an open question. One of the most popular models involves the existence of a cytoskeleton like structure inside the nucleus, called karyoskeleton, connecting the cytoskeleton bound nuclear lamina to the chromatin mass inside the nucleus. Support for this model is provided by the presence of a nuclear matrix (Berezney and Coffey 1974), involving polymeric actin (Clark and Merriam 1977; McDonald *et al.* 2006) and intermediate filament structures (Capco *et al.* 1982; Fey *et al.* 1984) within the nucleus. Alternatively, another model suggests that the attachment of chromosomes between the nuclear lamina and the relatively large immobile structures within the nucleus (e.g. splicing factor compartments) (Gieni and Hendzel 2008).

1.3.2 Nuclear Structure

The nucleus is a double membrane bound organelle, which contains genetic information that is stored in form of deoxyribonucleic acid (DNA). Many essential functions take place in the nucleus, such as the initial steps of gene expression including the generation of mRNA or transcription, DNA replication, repair, and recombination, as well as the production of ribosomal RNA (rRNA) (Prasanth and Spector 2005).

The double membrane separating the nucleus from the cytoplasm is called nuclear envelope. The outer envelope is continuous with the endoplasmic reticulum. Meanwhile, the inner envelope is attached to a layer of filament network called nuclear lamina and chromatin via various membrane proteins such as the lamin B receptor. The nuclear lamina mainly comprises the protein lamin, which is a member of the intermediate filament protein family. Lamins play a role in nuclear envelope assembly, DNA replication, transcription, apoptosis and provide anchorage sites for the chromatin. The depletion of lamins is shown to inhibit nuclear membrane and pore synthesis. Nuclear pores connect the cytoplasm and the nucleus and permit the free diffusion of small molecules and ions, as well as facilitate

receptor mediated transport of RNAs and various proteins (Aebi *et al.* 1986; Newport and Forbes 1987; Gruenbaum *et al.* 2005; Prasanth and Spector 2005; Dechat *et al.* 2008).

The DNA in the eukaryotic cell nucleus is grouped into a set of chromosomes. Each chromosome contains an extremely long linear DNA molecule associated with proteins that fold and pack the DNA into a more compact structure called chromatin. Based on their condensation level during interphase, chromatin can be classified into heterochromatin and euchromatin. Euchromatin consists of decondensed genetically active chromatin, which is often located toward the nuclear interior. Meanwhile, heterochromatin is composed of condensed genetically inactive chromatin, which is often located at the nuclear periphery, around the nucleolus and throughout the nucleoplasm as patches (Prasanth and Spector 2005; Alberts 2008).

The distribution of chromatin throughout the nucleus is not random. Instead, each chromosome occupies a specific domain referred as chromosome territory (Figure 1.6). The spaces between chromosome territories is called interchromatin compartment. The positioning of the chromatin within the nucleus affects its gene activity, gene rich chromosomes tend to be positioned in the internal nuclear region, whilst gene poor chromosomes are often positioned toward the periphery. These arrangements are relatively stable during interphase and may be rearranged extensively during cell division. Gene complexity and chromosome size are postulated to play a part in their positioning. Furthermore, rather than an absolute point, chromosomes seem to occupy specific domains within the nucleus, which may allow a degree of movement and interchromosomal interactions via the repositioning of gene loci. During interphase, the mobility of gene loci and chromosomes is limited to local diffusion within a volume of around 1 μm^3. The constrained mobility may be associated with the ratio between DNA concentration and nuclear volume, and the presence of heterochromatin as anchoring sites or the tethering of chromosomes by protein complexes to various structures in the nucleus such as the nuclear lamina, nuclear pores and nucleolus (Lamond and Earnshaw 1998; Walter *et al.* 2003; Foster and Bridger 2005; Murmann *et al.* 2005; Prasanth and Spector 2005; Lanctot *et al.* 2007).

Within the nucleus itself, there are some distinct non-membrane bounded substructures that contain a set of specific proteins (Figure 1.6). These domains include the nucleolus, nuclear speckles, promyelocytic leukemia (PML) bodies, Cajal bodies and various other small

bodies such as nuclear stress bodies, cleavage bodies, paraspeckles and Gemini of Cajal bodies.

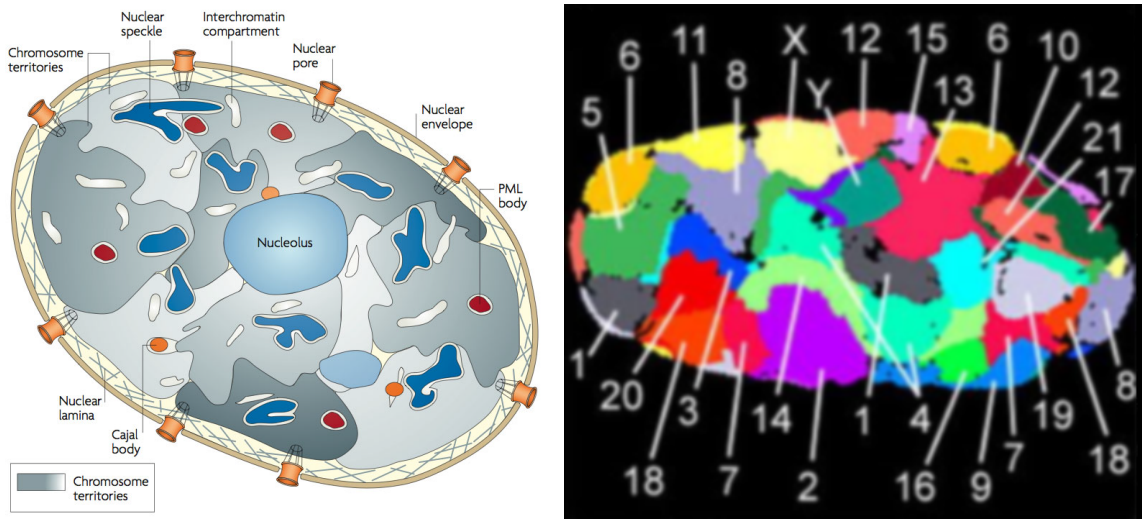

Figure 1.6 A schematic drawing of the mammalian cell nucleus (left) (Lanctot *et al.* 2007) and the nucleus of a human fibroblast showing the chromosome territories via fluorescence *in situ* hybridisation (FISH) (right) (Bolzer *et al.* 2005).

The main function of nucleolus is to synthesise rRNA and assemble ribosomal subunits. The structure of nucleolus can be separated into three distinctive components: the fibrillar centres, which are surrounded by the dense fibrillar components and the granular component. The fibrillar centres contain the ribosomal DNA (rDNA), which is transcribed by RNA polymerase I into pre-rRNA. Subsequently, the pre-rRNA is transferred into the dense fibrillar components to undergo post-transcriptional modification, and then transferred to the granular component and assembled into the ribosomal subunits (Lamond and Earnshaw 1998; Scheer and Hock 1999; Prasanth and Spector 2005; Shaw 2005).

The nuclear speckles act as storage, assembly and modification compartments that can supply splicing factors to active transcription sites within the nucleus. They are enriched with pre-mRNA splicing factors, as well as some kinases and phosphatases. PML bodies are small spherical structures, with a variety of functions including transcriptional regulation, nuclear storage centre, growth control and apoptosis. Cajal bodies are small spherical domains, which play a role in the maturation of nuclear ribonucleoprotein complexes. Both the PML and Cajal bodies in the nucleus are in defined locations relative to specific genes. Typically there are around 20 to 50 nuclear speckles, 10 to 30 PML

bodies and 2 to 8 Cajal bodies within a nucleus (Misteli *et al.* 1997; Lamond and Earnshaw 1998; Borden 2002; Ogg and Lamond 2002; Prasanth and Spector 2005).

1.4 The Effect of Mechanical Loading

As the bearing surface of synovial joints, articular cartilage is exposed to various loading regimes during the joint normal activity. Compared to the non-loaded bearing surface, , cartilage tissue was found to be mechanically stronger with higher proteoglycan concentration and chondrocytes are larger in load bearing surfaces (Bjelle 1975; Roberts *et al.* 1986; Slowman and Brandt 1986; Eggli *et al.* 1988), suggesting the role of loading nature in cartilage structure and chondrocytes metabolic activity.

A number of *in vivo* studies have been done to examine the effects of altering the normal pattern of joint loading, which were achieved by using animal models of joint instability, immobilisation, overuse and impact loading. For example, immobilisation of the joint in canines (Palmoski *et al.* 1979; Jurvelin *et al.* 1986; Behrens *et al.* 1989; Haapala *et al.* 2000), rabbit (Saamanen *et al.* 1987) and sheep (Caterson and Lowther 1978) lead to the reduction of tissue thickness, proteoglycan and collagen content and synthesis, and the softening of the tissue. Destabilisation of the joint by transection of the anterior cruciate ligament (Brandt *et al.* 1991; Ratcliffe *et al.* 1992; Muller *et al.* 1994; Setton *et al.* 1995) or meniscectomy (Floman *et al.* 1980; Shapiro and Glimcher 1980; Hoch *et al.* 1983), which cause alterations in contact areas and stresses (Kurosawa *et al.* 1980; Kaab *et al.* 2000), induced degenerative changes in cartilage tissue, similar to those in OA. Delivering an impact load to the joint has been shown to cause both immediate and progressive damage to the articular cartilage and the underlying subchondral bone (Radin *et al.* 1973; Donohue *et al.* 1983; Thompson *et al.* 1991; Vener *et al.* 1992; Oegema *et al.* 1993). Furthermore, strenuous exercise has been shown to reduce cartilage thickness and proteoglycan content in load bearing regions (Kiviranta *et al.* 1992; Arokoski *et al.* 1993). In contrast, moderate exercise was shown to increase cartilage thickness (Helminen *et al.* 2000), proteoglycan (Otterness *et al.* 1998) and collagen content (Saamanen *et al.* 1987), and was also shown to induce the recovery of immobilised joints (Videman *et al.* 1976; Tammi *et al.* 1983; Saamanen *et al.* 1990).

In vivo studies on human articular cartilage is far more limited compared to the animal studies, nevertheless, joint instability (Hinterwimmer *et al.* 2004) and immobilisation (Vanwanseele *et al.* 2002; Vanwanseele *et al.* 2003) were shown to induce cartilage atrophy and progressive thinning of cartilage. These *in vivo* studies have provided strong evidence that structure, composition, mechanical properties and metabolic activity of articular cartilage were significantly affected by joint loading.

Based on its structure, cartilage is a viscoelastic material, with a non-linear permeability, consisting of three principal phases: a charged solid phase, which is comprised of the negatively charged proteoglycan embedded in the collagen fibrillar mesh network, a fluid phase, which is the interstitial water, and an ion phase, which is the dissolved ionic species (Na^+, K^+, Ca^{2+}, Cl^-, etc) that are required to neutralise the negatively charged proteoglycan (Maroudas 1979; Lai *et al.* 1991; Gu *et al.* 1998).

The application of mechanical loading to cartilage tissue alters the extracellular matrix environment in a complex and multifaceted manner (Figure 1.7). Upon compressive loading, depending on the magnitude of the load, the tissue deforms to a certain extent, which then leads to the increase of hydrostatic pressure in the ECM within milliseconds (Weightman and Kempson 1979). The increase of hydrostatic pressure is primarily due to the entrapment of water within the solid matrix of the tissue because of its lower permeability (Maroudas 1968; Mansour and Mow 1976). This hydrostatic pressure disturbs the physicochemical equilibrium between the swelling pressure of proteoglycan and the tensile stresses generated within the collagen fibre network, resulting in a net pressure differential. If the load is maintained for a duration of time, this pressure differential induces the exudation and redistribution of the fluid within the tissue, i.e. fluid loss and fluid flow. In addition to 'creep' matrix deformation (Maroudas 1979), the loss of fluid also increases proteoglycan concentration and hence the swelling pressure. Fluid loss continues until a new state of equilibrium is achieved or until the load is released. Upon the removal of the load, the cartilage recovers to a limited extent, which then regains its original thickness gradually as water is re-imbibed into the cartilage matrix and the original equilibrium position is reached. Cyclic loading produces similar behaviour, however, the degree of the recovery within each cycle will depend on the loading pattern. All these changes provide potential signalling mechanisms during loading, which affect the functioning of the resident chondrocytes to induce the adaptive remodelling of cartilage

depending on the level of loading (Helminen *et al.* 1987; Ueki *et al.* 2008; Torzilli *et al.* 2010; Thomas *et al.* 2011). With this in mind, considerable *in vitro* studies has been directed toward understanding the transduction processes by which these physical signals are translated to biochemical signals by the chondrocytes. The use of *in vitro* systems, involving either cartilage explants or isolated chondrocyte cultures, allow for control of physical and biochemical environment, so that changes in metabolic activity can be correlated with the physical phenomena of interest.

1.4.1 Load-induced Cell Deformation

In vitro studies on cartilage explants showed that mechanical loading alters metabolic activity of the tissue (Parkkinen *et al.* 1992; Steinmeyer *et al.* 1999; Loening *et al.* 2000; Kurz *et al.* 2001), confirming the findings from the *in vivo* studies. One mechanism by which mammalian cells may perceive alterations in their physical environment is through cellular deformation. Chondrocytes deformation or changes in cell shape along the loading axis have been reported in intact articular cartilage explants subjected to physiological levels of applied stress and strain (Guilak 1995; Guilak *et al.* 1995). Guilak *et al.* showed that the application of 15% compressive strain of the tissue resulted in significant decreases in cell volume of 22%, 16% and 17% in the surface, middle and deep zones, respectively (1995). However, as mentioned above, mechanical loading on cartilage explants leads to various potential signals for the chondrocytes, such as hydrostatic pressure, fluid flow and increase in proteoglycan concentration.

In order to assess the importance of cell deformation in mechanotransduction, a number of studies have utilised isolated cell models that involve chondrocytes encapsulation in 3D hydrogel matrices, such as agarose, alginate and type I collagen (Buschmann *et al.* 1995; Ragan *et al.* 2000; Hunter *et al.* 2002). These experimental models enable cell deformation to be varied independently from other potential mechanotransduction signals. Encapsulating chondrocytes into agarose constructs allows the cells to adopt a spherical morphology and thus maintain phenotypic stability, as shown by the production of matrix containing aggrecan and type II collagen (Benya and Shaffer 1982; Buschmann *et al.* 1992). Furthermore, it was also shown that the application of physiological compressive strain on agarose seeded chondrocytes induced both cellular and nuclear deformation along the loading axis (Knight *et al.* 1998; Lee *et al.* 2000).

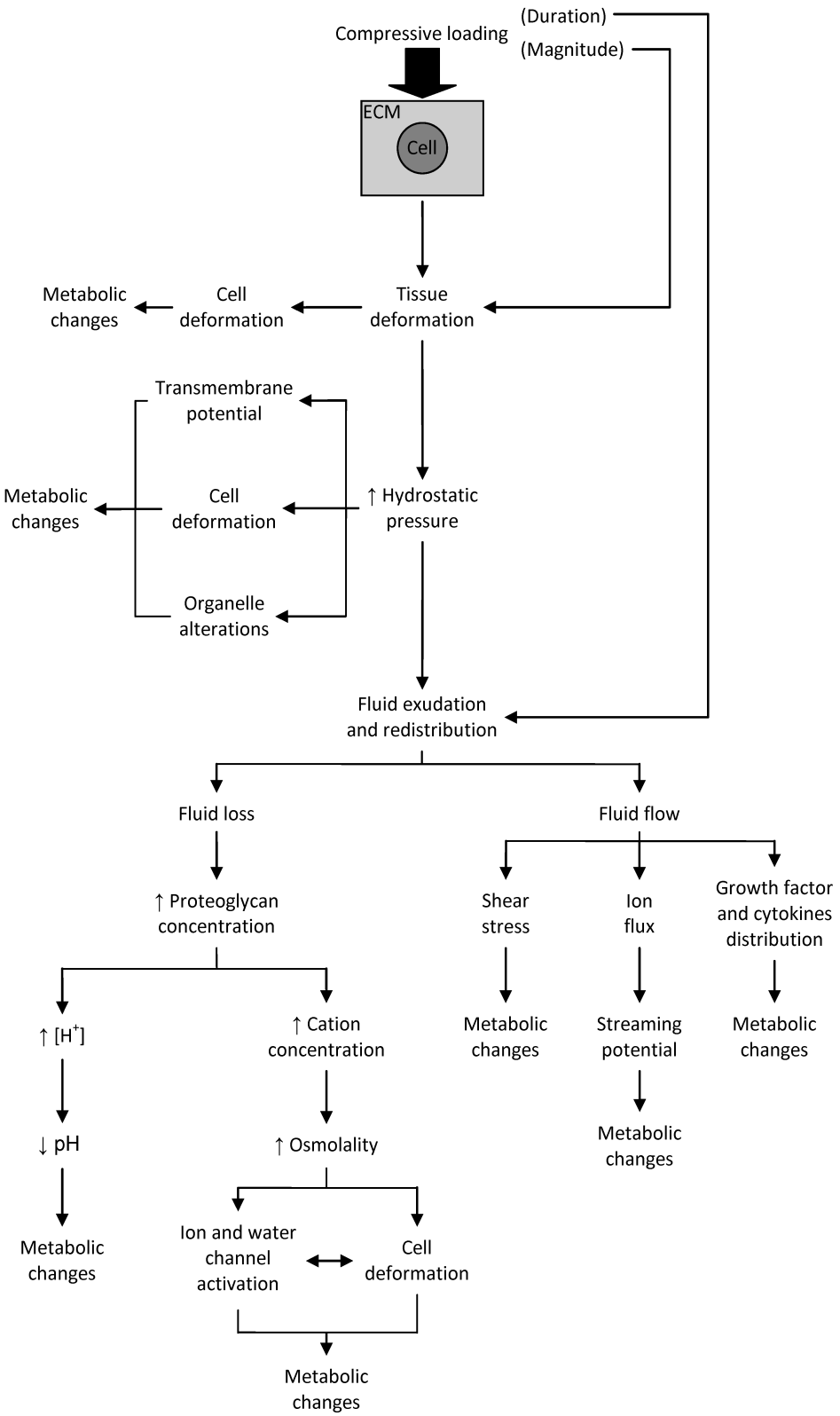

Figure 1.7 Schematic diagram showing the consequential effects of compressive loading on articular cartilage tissue, as possible mechanisms of chondrocyte mechanotransduction (see text for citations).

Static compressive strain on freshly isolated bovine articular chondrocytes in 3% agarose was shown to reduce proteoglycan synthesis, whilst dynamic compressive strain was found to increase matrix synthesis (Lee and Bader 1997; Mauck *et al.* 2000), suggesting the role of cell deformation in sensing the changes induced by mechanical loading. However, the mechanism by which cell deformation might produce a change in metabolic activity still need to be elucidated. Some studies showed the induction of signalling cascades (Chowdhury *et al.* 2008) upon dynamic mechanical loading, with the increase of intracellular Ca^{2+} signalling (Roberts *et al.* 2001; Pingguan-Murphy *et al.* 2006). These further support the hypothesis that cell deformation has a role in chondrocyte mechanotransduction.

1.4.2 Hydrostatic Pressure

The hydrostatic pressure within articular cartilage is around 0.2 MPa at rest, rising to around 4 to 5 MPa during walking, and may attain up to 20 MPa during some activities, such as jumping or standing up from a chair (Hodge *et al.* 1986; Mow *et al.* 2005). It was shown previously that the application of physiological hydrostatic pressure on cartilage explants did not cause appreciable deformation of the ECM (Bachrach *et al.* 1998). This makes it possible to investigate the effect of hydrostatic pressure in isolation to the other factors associated with mechanical loading, such as fluid flow. The application of hydrostatic pressure on cartilage explants has been shown to alter matrix synthesis (Hall *et al.* 1991; Parkkinen *et al.* 1993), suggesting the role of hydrostatic pressure as a signal for mechanotransduction in cartilage.

The nature of response appears to be highly dependent on the magnitude, duration and frequency of the hydrostatic pressure. Physiological level of hydrostatic pressure, 5 to 15 MPa, was shown to stimulate synthesis, whilst pressures above or below this range either inhibited synthesis or had minimal effect (Hall *et al.* 1991; Lammi *et al.* 1994; Elder and Athanasiou 2008). Cyclic 5 MPa pressure with a 0.5 Hz frequency increases the synthesis rate, while lower frequencies did not alter matrix synthesis (Parkkinen *et al.* 1993). Additionally, the application of pressure between 5 to 50 MPa, on cartilage explants and isolated chondrocytes, was shown to induce changes in cellular morphology (Takahashi *et al.* 1998; Fioravanti *et al.* 2003), cytoskeletal elements (Parkkinen *et al.* 1995; Fioravanti *et al.* 2005), Golgi apparatus (Parkkinen *et al.* 1993), transmembrane potential (Wright *et al.*

1992) and membrane transport (Browning *et al.* 1999; Hall 1999; Mizuno 2005), suggesting the possible mechanisms for hydrostatic pressure mechanotransduction in chondrocytes. Furthermore, the application of cyclic 5 MPa (1 Hz, 4 hours/day) hydrostatic pressure for 7 days on human bone marrow stromal cells was shown to increase collagen and GAG production, suggesting a pressure-induced chondrogenic differentiation (Angele *et al.* 2003).

1.4.3 Fluid flow

The average distance between the GAG chains in cartilage tissue is around 3-4 nm (Maroudas 1979). This small distance makes the proteoglycan complexes act as a selective permeability barrier within the cartilage tissue, thus larger solutes like immunoglobulin and albumin are excluded from cartilage. Additionally, it also slows down the diffusion rate, where a change of concentration in the serum may take hours to affect changes in the deep zone of articular cartilage. Finally, it also lowers the concentration of cytokines and growth factors within the tissue compared to the concentration in the serum. For example, the concentration of IGF-1 in the matrix is only 10-30% of that in the serum (Urban 1994).

Physiological mechanical loading has been shown to produce interstitial fluid flow with velocities ranging from 1 to 10 μm/s (Guilak and Hung 2005). Load-induced fluid flow may affects chondrocytes in several ways. For example, fluid flow alters the rate by which cytokines and growth factors reached the chondrocytes by solute movements, that in turn alters chondrocytes metabolism (O'Hara *et al.* 1990). Additionally, fluid flow also induces shear stresses on the surrounding matrix and cells, where the application of stretch or shear stresses on cells may lead to the activation of MAPK pathways, phospholipase C and membrane channels and an increase of calcium ion concentration, which then lead to alterations in the expression of matrix related genes (Fitzgerald *et al.* 2008; Wang *et al.* 2011). Furthermore, fluid flow also induces the flux of ions (dissolved within the interstitial fluid) relative to the fixed negatively charged proteoglycan, which give rise to an electrical potential, i.e. the streaming potential. Application of electrical fields on cartilage explants (Macginitie *et al.* 1994) and isolated chondrocytes (Lee *et al.* 1982) was shown to stimulate aggrecan synthesis. However, the effect is most significant at high frequencies above 100 Hz, which is not within the physiological range.

1.4.4 pH

Unlike the acute response of hydrostatic pressure or 'instantaneous' tissue deformation, fluid loss due to mechanical loading occur gradually for a period of time, where the amount and the rate depends on the magnitude of the load (Freeman and Maroudas 1975). Hence, it is important to note that changes due to loss of fluid in the cartilage also occur gradually along the load application.

Anaerobic glycolysis is the predominant source of energy in chondrocytes (Marcus 1973). As cartilage is avascular, the lactic acid produced needs to be transported through the matrix to be removed to the synovial fluid or serum. This gives rise to a pH gradient along the depth of the cartilage (Diamant *et al.* 1968; Holm *et al.* 1981). As the negatively charged proteoglycan attracts $[H^+]$, the pH of cartilage must always be lower than the external solution, which can be calculated with the formula given by Freeman and Maroudas (1975). For example, the middle zone of femoral head cartilage with a typical fixed charge density of 180 mEq/kg should have a pH that 0.3 lower than the synovial fluid. Proteoglycan concentration increases due to the load-induced fluid loss, hence, the $[H^+]$ concentration also rises, which in turn drops the extracellular pH. Altering the extracellular pH of agarose seeded bovine articular chondrocytes, in isolation of other load-induced responses, was shown to induce changes in GAG synthesis (Wu *et al.* 2007), which suggests that pH is one of the mechanotransduction signals for chondrocytes.

1.4.5 Osmolality

The variation of FCD due to the increase of proteoglycan concentration along the depth of articular cartilage increases the ECM osmolality from the surface to the deep layers of the tissue in the unloaded state (Table 1.1). The escalation of proteoglycan concentration, due to the load-induced fluid loss, also increases the cation concentration and hence the extracellular osmolality. A previous study by Oswald *et al.* showed that the application of static loading increases the osmolality in both layers to a similar level, load induced an increase in osmolality of approximately 80 mOsm/kg in the surface zone and by 20 mOsm/kg in the deep zone (Oswald *et al.* 2008). Furthermore, chondrocytes experienced a lower osmotic environment of approximately 280 mOsm/kg following pathological degradation of the ECM (Bush and Hall 2003). The alteration of osmolality, in isolation from the application of mechanical load, has been shown to alter the matrix synthesis in

both *in situ* and isolated chondrocytes, despite differences in cell attachment and morphology (Urban *et al.* 1993), suggesting the role of osmolality changes in mechanotransduction. The effect of osmolality alterations on chondrocytes is described further in the next section.

Table 1.1 The FCD, ions concentration, and osmolality in culture medium, synovial fluid, surface, and deep zone of articular cartilage in normal joints (Yielding *et al.* 1954; Gersh and Catchpole 1960; Maroudas 1979; Baumgarten *et al.* 1985; Urban 1994).

	Culture medium	**Synovial fluid**	**Surface**	**Deep**
Fixed charge density (mEq/L H_2O)	0	20	100-120	180-230
$[Na^+]$ mM	140	134-138	210-230	260-320
$[K^+]$ mM	5	4-5	7	9-11
$[Ca^{2+}]$ mM	2	4	4-6	8-15
$[Cl^-]$ mM	140	130	100-110	70-90
Osmolality (mOsm/kg)	280-310	347-461	350-360	380-440

1.5 The Effect of Osmotic Stress

As described in the previous section, load-induced fluid loss is a gradual process, thus changes that caused by the loss of fluid, including osmolality alterations, also occur gradually along the application of load. Likewise, the decrease of osmolality due to pathological conditions is likely to occur gradually with the degradation of the matrix. Conversely, in most studies, osmotic challenge was applied at a rapid rate, such as the replacement of the media, putting the findings' physiological relevance in question. Nevertheless, these sudden osmotic challenge studies are required to characterise the effect of osmotic alterations on chondrocytes.

1.5.1 Alteration in Metabolic Activity

Upon compressive loading, extrusion of fluid from the cartilage tissue increases the osmolality of ECM surrounding the chondrocytes. Alteration of osmolality in cartilage tissue has been shown to affect protein synthesis (Jones *et al.* 1982; Bayliss *et al.* 1986; Schneiderman *et al.* 1986; Urban and Bayliss 1989; Ohshima *et al.* 1995). Similarly, osmotic challenge directly on isolated chondrocytes has been shown to affect metabolic activities, including alterations in protein synthesis (Urban *et al.* 1993; Borghetti *et al.* 1995; Hopewell and Urban 2003) and gene expression (Hung *et al.* 2003; Tew *et al.* 2009; Tew *et al.* 2011).

Urban *et al.* (1993) showed that the incorporation rates of ^{3}H-proline and ^{35}S-sulphate, which represent the synthesis of collagen and GAGs respectively, were highest at 350-400 mOsm/kg in both isolated and *in situ* chondrocytes. A previous study by Hung *et al*. (2003) showed that the application of hyper-osmotic challenge (580 mOsm/kg) on monolayer cultured chondrocytes for 5 hours reduces aggrecan gene expression, while hypo-osmotic challenge (180 mOsm/kg) induced an opposite effect. In this study, Hung *et al*. also compared aggrecan gene expression of osmotically challenged chondrocytes seeded in alginate beads and agarose. Upon hypo-osmotic challenge, aggrecan gene expression in the agarose seeded chondrocytes also increased; however, the expression level decreased for the alginate seeded specimens. Upon hyper-osmotic challenge, aggrecan gene expression decreased in both agarose and alginate seeded samples. These findings agree with the study by Hopewell and Urban (2003) involving chondrocytes seeded in alginate beads and cultured in 500 mOsm/kg medium, which revealed that ^{35}S-sulphate incorporation was

reduced initially (4 hours), but increased after 24 hours of culture, suggesting the time-dependent response of chondrocytes toward hyper-osmotic conditions.

1.5.2 Alteration at the Cellular Level

The application of hyper-osmotic stress to chondrocytes leads to a decrease of cell volume due to the loss of intracellular fluid, while hypo-osmotic challenge increases the cell volume (Bush and Hall 2001). Subsequently, the change in cell volume is followed by the regulation of intracellular osmolytes (Waldegger *et al.* 1998), involving various ion channels, such as TRPV4 (Phan *et al.* 2009), which leads to regulatory volume decrease (RVD) post cell swelling by hypo-osmotic stress (Bush and Hall 2001). A limited regulatory volume increase (RVI) post cell shrinking by hyper-osmotic challenge is also evident (Kerrigan *et al.* 2006). Hypo-osmotic challenge leads to a significant reduction in the cellular elastic moduli and viscosity (Guilak *et al.* 2002). In addition, Ca^{2+} dependent dissociation and remodelling of F-actin cytoskeleton, mediated by gelsolin (an actin regulator protein), was also observed when chondrocytes were exposed to hypo-osmotic challenge (Erickson *et al.* 2003; Pritchard and Guilak 2004). Additionally, both hyper- and hypo-osmotic challenge induce the shortening of chondrocytes primary cilia (Rich and Clark 2012), which is known to play an important role in signal transduction. Furthermore, the pattern of osmotic challenge also plays a role in the change of cell volume. Dynamic osmotic challenge alters the cell volume only when the frequency is lower than 0.0125 Hz, which is much lower than the frequency of normal walking (1 Hz) (Chao *et al.* 2005).

1.5.3 Alteration at the Nuclear Level

Osmotic challenge has been shown to alter nuclear morphology in chondrocytes (Oswald *et al.* 2006). This phenomenon persists even after the cytoskeleton organization is disrupted, which suggests that mechanical translation of cell deformation during osmotic challenge via the cytoskeleton is not the principal factor that alters the nuclear morphology (Oswald *et al.* 2006). It was later shown that the volume of isolated nuclei was reduced only when the osmolality was increased by the addition of macromolecules and preserved when the osmolality was raised by increasing the ion concentration (Finan *et al.* 2009). This suggests that the osmotic effect on the nucleus is due to the larger molecules not being able to diffuse through the nuclear pores owing to their size. Additionally, previous studies on HeLa and other cell types, including chondrocytes, revealed that hyper-osmotic stress

induces chromatin condensation (Albiez *et al.* 2006; Finan *et al.* 2011), which was shown to recover after 24 hours of hyper-osmotic exposure (Mavrogonatou and Kletsas 2012), whilst hypo-osmotic stress induces the de-condensation of the chromatin structure (Delpire *et al.* 1985). Gene expression is influenced by chromatin organisation, with gene silencing generally associated with highly condensed heterochromatin at the nuclear periphery (Brown *et al.* 1997; Croft *et al.* 1999). This process is demonstrated during developmental silencing observed with lamin-associated chromatin, where the silenced genes are translocated to the lamina as higher order chromatin (Kosak *et al.* 2002; Reddy *et al.* 2008). Accordingly osmotically-induced alterations in higher-order chromatin structure may provide a mechanism for the reported effects of osmotic challenge on chondrocyte gene expression. As the osmotic environment varies within cartilage tissue, both with depth and during loading this phenomenon could provide a novel mechanotransduction mechanism necessary for normal load-induced homeostasis in the tissue that may be perturbed in degenerative pathologies.

1.6 Aim and Objectives

In articular cartilage, osmotic variation exists through the depth of the tissue. This is due to the increase of proteoglycan concentration from the surface to the deep zone, increasing the osmolality from 350 to 450 mOsm/kg respectively. Furthermore, chondrocytes are exposed to a higher osmotic environment during the application of mechanical loading and a lower osmotic environment during the pathological degradation of the ECM. It is well established that the application of osmotic stress in both cartilage tissue and isolated chondrocytes alters matrix synthesis and cellular and nuclear morphology. However, it remains unclear how osmotic-induced changes in cell morphology are involved in triggering the downstream metabolic response. Osmotic stress also alters nuclear morphology and chromatin structure, which may provide a direct biophysical mechanism for controlling cellular metabolism. With this in mind, the aim of this study is to contribute towards an understanding of the osmotically-induced responses of chondrocytes, by testing the hypothesis that osmotic challenge induces changes in nuclear and chromatin structure of chondrocytes. This will be accomplished by realising the following objectives:

- Investigating the effect of a range of osmolality on the chromatin condensation level of chondrocyte nuclei.
- Assessing the effect of osmotic challenge on chondrocytes nuclear morphology and chromatin structure that cultured in 2D and 3D systems.
- Assessing the reversibility and the time respond of the changes induced by the osmotic challenge.
- Assessing the deformability of chondrocytes and their nuclei upon compressive load, when exposed to different osmotic conditions.
- Assessing the changes in chondrocytes post hyper-osmotic challenge by a genome-wide expression analysis.

Chapter 2 General Methods and Characterisation

2.1 Introduction

This chapter describes procedures frequently employed throughout the experimental work of this thesis and their characterisation. Procedures specific to a single chapter are described within the methods section of the appropriate chapter.

2.2 Chondrocyte Model System

2.2.1 Chondrocyte Medium

For preparation of chondrocyte culture medium, 10 mL of 1 M 4-(2-hydroxyethyl)-1-piperazineethanesulfonic acid (HEPES), 5 mL of 200 mM L-glutamine, 5 mL of 10,000 units penicillin + 10 mg/mL streptomycin solution, and 0.075 g of L-Ascorbic acid were added into 100 mL foetal calf serum (FCS, all from Sigma-Aldrich, Dorset, UK). By using 0.2 μm sterile filters, the FCS solution was filtered into 500 mL low glucose Dulbecco's modified Eagle's medium (DMEM, Sigma-Aldrich). Resulting 620 mL DMEM media, supplemented with 16.1% (w/v) FCS, 16 mM HEPES, 1.6 mM L-glutamine, 81 μg/mL penicillin, 80 μg/mL streptomycin and 0.68 mM L-Ascorbic acid, with a pH of 7.4, which is henceforth referred to as DMEM + 16.1% FCS medium. In most cases, the medium was then aliquoted into sterile 150 mL universal containers (Sterilin, Caerphilly, UK) with 100 mL per aliquot. These aliquots were stored in -20^{o}C. Prior to usage, the medium aliquots were thawed in a 37^{o}C water bath.

2.2.2 Collagenase Solution

The collagenase solution for chondrocyte isolation was prepared at an activity of 100 units per mL. The collagenase solution was sterile filtered with a 0.2 μm filter into another container containing the required volume of DMEM + 16.1% FCS. The solution was mixed and aliquoted into 50 mL universal container (Sterilin) with 30 mL for each aliquot. These aliquots were stored at -20^{o}C and thawed to 37^{o}C before usage.

2.2.3 Pronase Solution

The pronase substrate (5.9 units/mg, Sigma-Aldrich), 1 g, was added to 175 mL of DMEM + 16.1% FCS to create a pronase solution with an activity of approximately 34 units/mL.

The pronase solution was filtered with 0.2 μm filter, and aliquoted into 25 mL container (Sterilin) with 10 mL for each aliquot. These aliquots were stored at -20^{o}C and thawed to 37^{o}C before usage.

2.2.4 Chondrocyte Isolation from Bovine Articular Cartilage

Chondrocytes were isolated from the metacarpophalangeal joint of freshly sacrificed 12-24 months old bovine steers. Upon arrival from the abattoir, the bovine foot was scrubbed by using a brush and running water to remove the excess soil, followed by immersion in 70% industrial methylated spirit (IMS) solution for at least 15 minutes. The bovine foot was placed on an appropriate metal dissecting tray and transported into the laminar flow hood to be dissected. By using a no. 20 scalpel blade, a cut was made longitudinally along the front of the joint, followed with another cut above the hoof, perpendicular and continuous with the longitudinal cut. The hide was peeled back by using the same scalpel blade on both sides until the joint capsule was exposed. By using a no. 11 scalpel blade, tendons and ligaments around and inside the joint were severed until the joint could be dislocated and the joint condyles were exposed. The cartilage attached to the proximal metacarpal surface of the joint was removed by using a no. 10 scalpel blade, into a Ø50 mm petri dish (Sterilin) filled with Earle's balanced salt solution (EBSS, Sigma-Aldrich), ensuring that the cartilage slices were fully immersed to prevent dehydration. The EBSS was aspirated and the cartilage tissues were finely diced to ensure better digestion. The fine slices of cartilage tissues were transferred into a 50 mL conical tube (BD, Oxford, UK), with addition of 10 mL pronase solution. The tube was placed onto a roller mixer in a 37^{o}C oven for one hour. The pronase solution was aspirated and replaced with 30 mL collagenase solution. The tube was placed back onto a roller mixer in the 37^{o}C oven and left overnight (14 to 16 hours). On the next day, the digestion solution was filtered through a 70 μm filter into a fresh 50 mL conical tube. The filtered solution was centrifuged at 2000 rpm for 5 minutes (PK131, ALC, Cologno Monzese, Italy). The supernatant was aspirated and the cells were resuspended in 15 mL DMEM + 16.1% FCS medium, followed by another 2000 rpm centrifugation for 5 minutes. The supernatant was aspirated again and the cells were resuspended in 15 mL DMEM + 16.1% FCS. Cell count and viability were determined by trypan blue exclusion assay. Unless mentioned, all procedures associated with cells involve primary chondrocytes isolated in this manner. At least two joints were used for each isolation procedure, depending on the number of cells required.

2.2.5 Trypan Blue Exclusion Assay

This assay involves the stain trypan blue (Sigma-Aldrich) that can only penetrate into cells with compromised membranes, leaving the live cells unstained. The haemocytometer (Improved Neubauer, VWER, Lutterworth, UK) is a glass chamber incorporated with nine distinct grids. Each grid has a known volume of 1×10^{-4} mL. Cell suspension with a volume of 20 µL was mixed with 20 µL trypan blue to create the solution for cell counting. The solution was pipetted into the haemocytometer and the cells were counted under a light microscope. Cells within five of the grids were counted and an average was calculated. The cell number (C) and viability were calculated by:

$$C = A \times D \times 10^4 \times V \qquad (2.1)$$

$$cell\ viability\ (\%) = \frac{number\ of\ unstained\ cells}{total\ number\ of\ cells} \times 100 \qquad (2.2)$$

Where C is the number of cells within the cell suspension, A is the average number of cells counted in a grid, D is the dilution factor between the cell suspension and the trypan blue and V is the volume of cell suspension.

2.2.6 Monolayer Culture

The cells were either cultured in monolayer culture or seeded into agarose constructs. For monolayer culture, the seeding density and volume of medium used to resuspend the cells depend on the culture system, as shown in Table 2.1, unless stated.

Table 2.1 The seeding density and volume of medium used for the different culture systems.

Culture system	Medium volume (mL)	Seeding density (cells/cm^2)
175 cm^2 flask	35	45×10^3
Ø35 mm petri dish	3	50×10^3
24 wells plate (each well)	2	50×10^3

2.2.7 Trypsinising Adherent Cells

For cells cultured in 175 cm^2 culture flask (PAA, Pasching, Austria), the medium was aspirated and replaced with 10 mL Phosphate Buffered Saline solution (PBS, Sigma-Aldrich). The PBS solution was aspirated and replaced with 10 mL trypsin-EDTA solution (0.5 g porcine trypsin and 0.2 g EDTA 4Na per litre of Hanks' Balanced Salt Solution with phenol red, Sigma-Aldrich). The culture flask was placed into a 37^oC incubator for 2 to 5 minutes, allowing the detachment of the cells. Afterward, 20 mL DMEM + 16.1% FCS was added into the flask and was spread around the culture surface to acquire the detached cells. The cell suspension was aspirated and placed into a 50 mL conical tube, and centrifuged at 2000 rpm for 5 minutes. The supernatant was aspirated and the cells were resuspended in 15 mL DMEM + 16.1% FCS.

2.2.8 Agarose Culture

In order to produce 5 mL of 6% (w/v) agarose solution, 0.3 g of agarose type VII (Sigma-Aldrich) was dissolved into 5 mL of EBSS without phenol red (Sigma-Aldrich). The agarose solution was autoclaved and cooled down by placing it into a 60^oC oven for an hour and onto a roller inside a 37^oC oven for half an hour. During the autoclaving and cooling down period, 5 mL of cell suspension with a density of 20×10^6 cells/mL was prepared, and the construct mould was sterilised and assembled.

The cell suspension was added to the agarose solution, creating 10 mL of 3% 10×10^6 cells/mL agarose-cell solution. The solution was gently mixed and placed onto the roller inside the 37^oC over for no more than 5 minutes. By using a sterile Pasteur pipette, the agarose-cell solution was added to the mould and placed into a 4^oC fridge for 20 minutes to set. The agarose-cell constructs were placed into a Ø50 mm Petri dish filled with DMEM + 16.1% FCS, ensuring the full immersion of the constructs. The constructs were cultured over night in a 37^oC incubator prior to further study.

2.2.9 Osmolality Measurement

The measurement of osmolality was carried out using a freezing point depression osmometer (3250, Advanced Instruments, Norwood, US). This osmometer measures the total molar concentration of dissolved solids in the solution. The freezing point of the solution is depressed in direct relation to the amount of solute in solution. Prior to any

measurement, a Clinitrol 290 mOsm/kg reference solution (Advanced Instruments) was measured to calibrate the osmometer. The sample solution with a volume of 250 µL was inserted into the test tube provided. The tube was placed into the osmometer and the measurement started.

2.2.10 Osmolality Alteration

The osmolality of a solution was increased by the addition of D-Mannitol (Sigma-Aldrich), whilst, to decrease the osmolality, the solution was diluted with distilled water. Addition of 1% (w/v) D-Mannitol increases the osmolality of the solution by 57.5 mOsm/kg. Hence, the amount of D-Mannitol or distilled water required to alter the osmolality of a solution was calculated by:

$$M_{D-Mannitol} = \frac{(Osm_r - Osm_b)}{57.5 \times 100} \times V_o \quad (2.3)$$

$$V_f = \frac{Osm_b}{Osm_r} \times V_o \quad (2.4)$$

$$V_{dH_2O} = V_f - V_o \quad (2.5)$$

Where $M_{D-Mannitol}$ is the mass of D-Mannitol required (g), Osm_r is the osmolality required (mOsm/kg), Osm_b is the solution's original osmolality (mOsm/kg), V_o is the solution's original volume, V_f is the diluted solution's volume and V_{dH_2O} is the volume of distilled water required. The osmolality of the solution was confirmed by osmometer measurement.

2.2.11 Sodium Bicarbonate Free Medium

In culture medium, sodium bicarbonate acts as a pH buffer providing the media is maintained in a 5% CO_2 atmosphere. However, if sodium bicarbonate is used in an environment without supplemented CO_2, the pH increases rapidly. During imaging, the cells were exposed to atmospheric conditions. Thus, instead of using the standard DMEM involved in the preparation of DMEM + 16.1% FCS medium, sodium bicarbonate free medium is required.

For preparation of sodium bicarbonate free media, sodium bicarbonate free DMEM (Sigma-Aldrich) was supplemented with 20 mM HEPES, 2 mM L-glutamine, 100 µg/mL penicillin, 100 µg/mL streptomycin and 1 mM L-Ascorbic acid (pH 7.4), followed by

sterilisation by filtering through a 0.2 μm filter. FCS was not added into the solution, as the presence of albumin is suggested to disrupt nuclear staining with DRAQ5 (BioStatus, Shepshed, UK). The sodium bicarbonate free media has an osmolality of 260 mOsm/kg, which is not within the normal physiological range for the chondrocytes. Thus, the osmolality of the media was increased to 300 mOsm/kg by the addition of D-Mannitol as described in section 2.2.10. Unless stated, the staining, imaging and osmotic challenge media were derived from the sodium bicarbonate free media.

2.2.12 Statistical Analysis

Unless stated, for data with a normal distribution, as distinguished by the Lilliefors test, the results are shown as mean ± standard error and the statistical significance was calculated by using one-way ANOVA followed by Bonferroni's correction. In case of non-normally distributed data, the results are shown as median with upper and lower quartile as the error bars, and Mann Whitney U test with the Bonferroni's correction was used to measure the level of significance. For data presentation purposes, *N* indicates the number of replicate experiments, where different replicate experiments involved cells sourced from different isolation procedure. Whilst, *n* indicates the number of replicates represented by the data.

2.3 Confocal Laser Scanning Microscopy

2.3.1 Imaging Hardware

The principle of confocal microscopy was first patented in 1957 by Marvin Minsky, a postdoctoral fellow at Harvard University. The major advantage of confocal microscopy, compared with the conventional epifluorescence microscopy, is the ability to subtract the unfocused background fluorescence signals coming from the excited sample, thereby leaving only the in focus signals. This is achieved by placing a pinhole before the light source to limit the excitation field of illumination and another pinhole before the signal detector to eliminate the out of focus fluorescence emission (Figure 2.1).

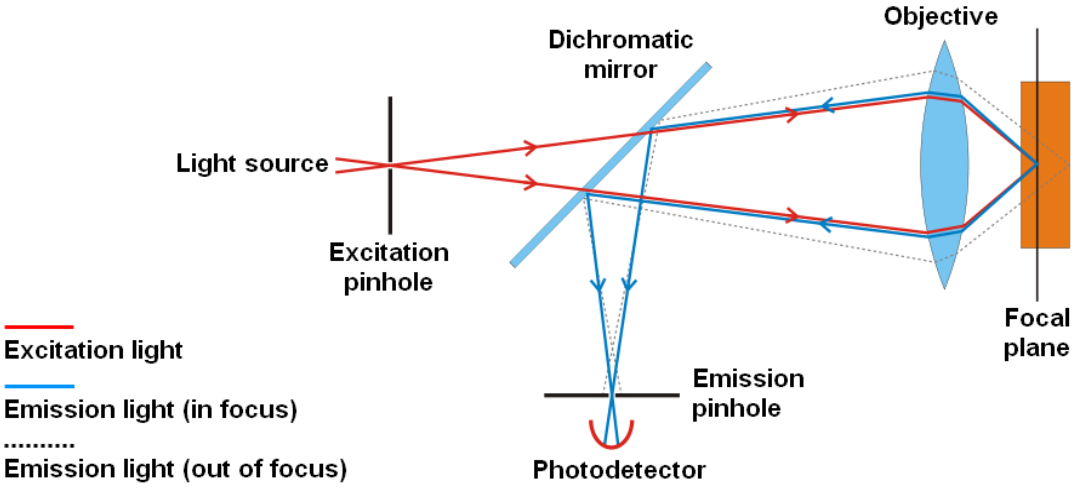

Figure 2.1 The principle of confocal microscopy.

Through the integration with laser illumination and stage scanning microscopy, the confocal laser scanning microscope (CLSM) was developed. The laser provides a light source with a high degree of monochromaticity, polarisation, coherence and intensity. Meanwhile, stage scanning technology allows the positioning of the laser illumination point, thereby making it possible to scan the sample along the focal plane. Firstly, the laser beam passes through excitation pinhole and is focused by an objective lens into a small focal volume within the sample. The fluorescence signals or other light sources emitted by the sample due to the laser beam come back through the objective onto a dichromatic mirror. Due to Stokes shift, the fluorescent light emitted from the sample is at a longer wavelength than the excitation light. The dichromatic mirror has the ability to separate the excitation and emission light by reflecting only the colours above a specified wavelength

limit. The emission signals reflected by the dichromatic mirror then pass through an emission pinhole and the intensity of the signal is detected by a photodetection device, such as a photomultiplier tube (PMT). This intensity is then converted into a digital signal which is recorded by a computer. The intensity recorded from a focal volume represents a pixel or a voxel in the resulting image. Afterwards, the scanner will direct the laser beam onto the next focal volume until the whole specimen is scanned. The intensity information is gathered then used to reconstruct the image of the specimen.

In this study, an inverted CLSM from Leica (TCS SP2, Leica Microsytems GmbH, Wetzlar, Germany) was used. TCS SP2 allows for both non-confocal epifluorescence and confocal imaging. Non-confocal epifluorescence imaging uses a mercury lamp as the light source with three filters, which allows for UV, blue and green light illumination. Confocal imaging involves the 364 nm UV laser, 488 nm Argon laser, 543 nm and 633 nm Helium-Neon laser.

2.3.2 Resolution

The resolution of an image, taken by an optical microscope, is defined as the shortest distance between two points on a specimen that can still be resolved by the observer as separate entities. This is illustrated in the figure below (Figure 2.2 A), where an Airy disc and an Airy pattern represent a point source of light from the specimen. The representation of the intensity of this diffraction pattern is called the point spread function.

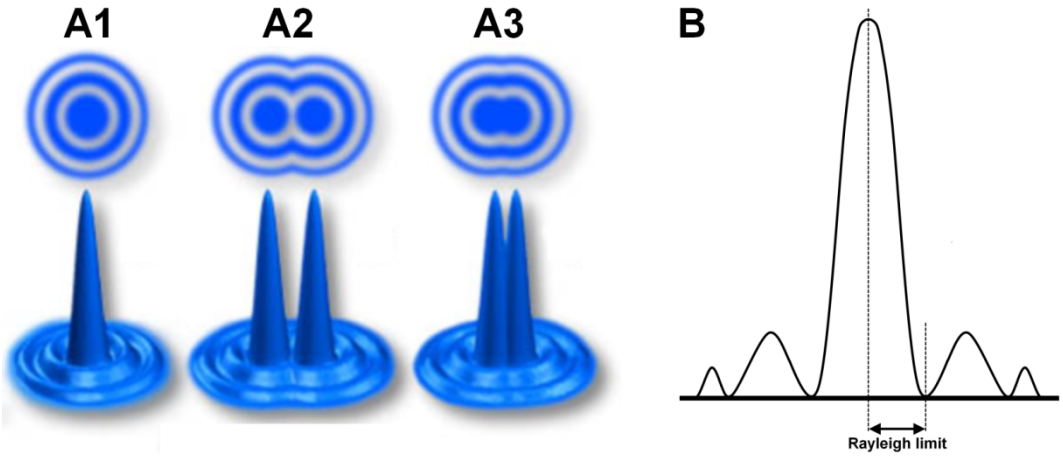

Figure 2.2 A1: Airy disc representing a point light source and its point spread function. A2: Two point light sources individually resolvable. A3: Two point light sources not individually resolvable (Abramowitz and Davidson 2010). B: Point spread function of a diffraction pattern showing the Rayleigh criterion.

Generally, the shortest distance between the two points is defined by the Rayleigh criterion, where a detectable drop in intensity between the diffraction patterns is observable. Thus, it is the distance from the peak to the first dark fringe in the point spread function of the diffraction pattern (Figure 2.2 B). The resolution limit depends on the laser wavelength, the numerical aperture of the objective and the refraction index of the substance at the focal plane. Based on the Rayleigh criterion, the resolution limits can be calculated by (Corle *et al.* 1986; Pawley 1995):

$$R_a = \frac{0.61 \times \lambda}{NA} \qquad (2.6)$$

$$R_l = \frac{1.4 \times \eta \times \lambda}{NA^2} \qquad (2.7)$$

Where R_a is the axial resolution limit, R_l is the lateral resolution limit, η is the refraction index at the focal plane of the sample, λ is the laser wavelength and NA is the objective's numerical aperture.

The resolution of an image, taken by CLSM, also depends on the pixel size of the image. Using the Leica SP2, pixel size in the axial plane (the *X*-*Y* or the imaging plane) can be reduced either by simply increasing the number of pixel per image (image format) or by zooming in to the sample (zoom). By zooming in, a smaller region of interest is scanned with the same number of pixels, thus the field of view is reduced but so too is the actual pixel size, thereby increasing the image resolution. Meanwhile, pixel size in the lateral plane (along the *Z* axis or perpendicular to the imaging plane) solely depends on the distance between the image slices (*Z* series) taken along the sample. This distance is often referred to as the *Z*-step size or ΔZ. Nyquist theorem states that, in order to make a faithful reconstruction of a signal, the minimum sampling frequency should be at least two times the signal frequency. Based on the Nyquist criterion for digital resolution, the smallest resolved structure should be sampled at least by two pixels. However, in order to avoid undersampling, the ideal minimum pixel size should be one fourth of the resolution limit.

In this study, most of the imaging was achieved using a 63× oil immersion objective, with a numerical aperture of 1.4. Assuming that the specimen has a refraction index equal to the refraction index of the oil (1.518), the axial and lateral resolutions can be found in Table 2.2. However as mentioned above, each pixel represents a laser scanning onto the specimen, as a result, for a given field of view, a smaller pixel size gives a higher density of

laser exposure. Therefore, the resolution chosen should depend on the details required for the purpose of imaging. If high resolution is not required, imaging with maximum resolution should be avoided in order to avoid photobleaching and phototoxicity (see section 2.2.3).

Additionally, the resolution in the lateral plane is also affected by the refractive index of the objective immersion media, typically air, water, glycerol or oil. When light travels through two substances with different refractive indices, the change in its phase velocity will cause the light path to deviate, as shown in Figure 2.3 A. Figure 2.3 B illustrates how this phenomena influences the light path when imaging a water based specimen such as cells in culture media, within an oil immersion objective axial displacement of the objective by a distance, *D*, will result in movement of the focal plane, *d*, such that *d* is less than *D*.

Table 2.2 The axial and lateral resolution limits with their corresponding minimum pixel size and *Z*-step size depending on the laser wavelength, numerical aperture of the objective (1.4 NA) and the refraction index at focal plane (η=1.518).

Laser wavelength (nm)	**Axial resolution limit/Minimum pixel size (nm)**	**Lateral resolution limit/Minimum *Z*-step size (nm)**
364 (UV laser)	158.6/39.65	394.7/98.67
488 (Ar laser)	212.6/53.16	529.1/132.3
543 (HeNe laser)	236.6/59.15	588.8/147.2
633 (HeNe laser)	275.8/68.95	686.4/171.6

Three dimensional (3D) imaging involves taking image slices through the specimen such that the *Z* dimension in the resulting reconstruction is solely represented by the objective displacement. However, as shown in Figure 2.3 B, where the focal displacement (*d*) is less than the objective displacement (*D*), the specimen imaged appears longer in the Z axis than its actual size. This aberration can be observed when imaging objects seeded in agarose gel with an oil immersion objective (Figure 2.4 C). The refractive index of the oil (η = 1.518) is higher than that of the agarose, which is 97% water (η = 1.333). This causes elongation of any object imaged within the gel. The distortion is absent when imaging objects seeded in oil using the same objective lens (Figure 2.4 A). Similarly, when compared to the oil, the

refractive index of glycerol is closer to the agarose, and thus a glycerol immersion objective lens produces less distortion when imaging objects mounted in agarose (Figure 2.4 D).

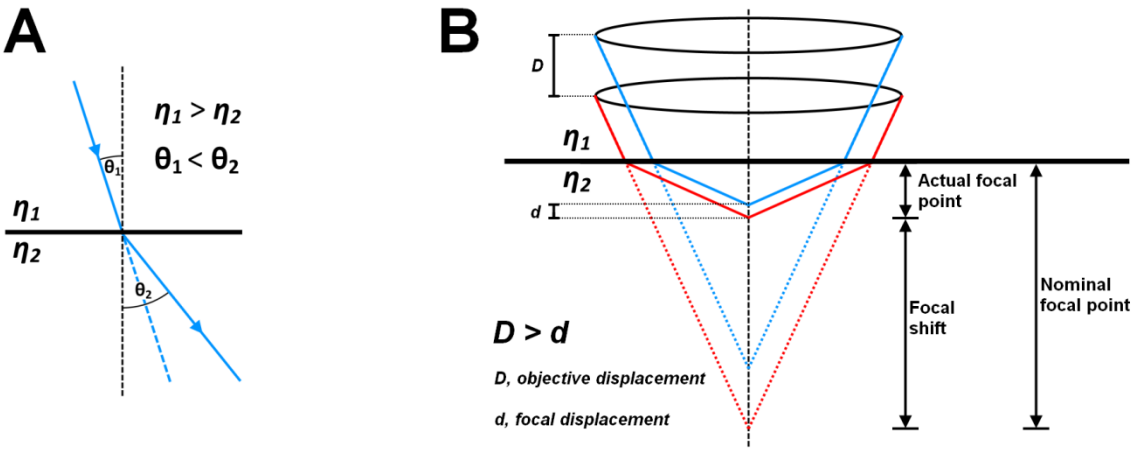

Figure 2.3 A: Alteration of light path angle (θ_1 and θ_2) due to refraction index mis-match (η_1 and η_2). B: Illustration of aberration due to refraction index mis-match, including the focal shift and false focal displacement.

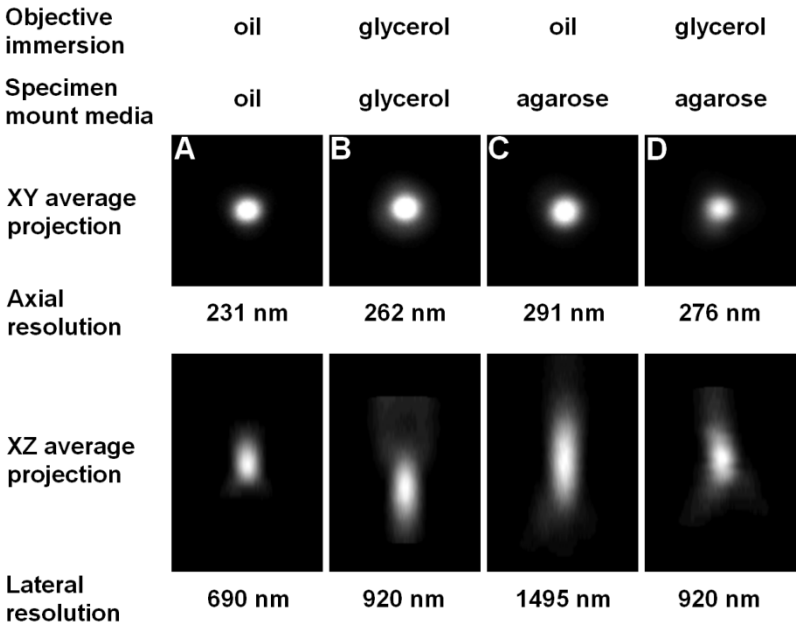

Figure 2.4 *X-Y* and *X-Z* average projections of 0.17 µm bead images. Bead mounted on their corresponding immersion fluid, taken by A: oil immersion objective ×63/1.4NA and B: glycerol immersion objective ×63/1.3NA. Bead embedded in 3% (w/v) agarose construct, taken by C: the oil objective and D: the glycerol objective. The beads were imaged with 488 nm laser, as the diameter of the bead is below the resolution limit (Axial/Lateral = 212.6/529.1 nm), the actual axial and lateral resolutions were assumed to be equal to the bead diameter measured from the images by the full-width half-maximum method.

2.3.3 Photobleaching and Phototoxicity

CLSM imaging involves laser excitation of fluorophores tagged to the sample, causing them to emit fluorescence with a higher wavelength, i.e. weaker than the illuminating laser. With greater laser intensity or prolonged laser exposure, greater fluorescence will be produced, thus increasing the signal to noise ratio and hence the image quality. However, continuous imaging of the sample will cause deterioration of the fluorophores, lowering the fluorescence signals produced from constant illumination intensity. This phenomenon is called photobleaching. Additionally, continuous laser exposure will also induce a degree of damage to living samples, often referred as phototoxicity, associated with the release of oxygen free radicals (Knight *et al.* 2003).

2.3.4 Imaging Time and Averages

Scanning speed, line and frame averaging also play a part in image quality. Increasing the scan speed will lessen the time required for a full scan of the specimen. However, it also brings down the sampling time for each pixel; consequently reducing the number of photons gathered and the signal to noise ratio. On the other hand, reducing the scan speed will improve the image quality, but higher sampling time means longer laser exposure, and hence greater photobleaching. The use of frame averaging allows an entire section image to be repeatedly scanned and the average intensity taken for each pixel, thereby reducing noise. This may also be achieved a line at a time, line averaging, which is more appropriate for obtaining dynamic images. Although averaging improves signal to noise ratios, it also increases laser exposure time and therefore photobleaching.

2.3.5 Pinhole Size

Another way to increase the amount of fluorescence from a sample is by increasing the pinhole size. Ideally, the pinhole size should be adjusted to only allow the signal from the focused volume to pass through. Increasing the pinhole size will give a brighter signal, but it will also allow the detection of out-of-focus signals from around the focal point, thus decreasing the axial and lateral resolution. For ×63/1.4NA oil immersion objective, the ideal pinhole size is 114 μm.

2.3.6 Gain and Offset of PMT

On most CLSM systems, intensity signals derived from the specimen are recorded by a photomultiplier tube (PMT). In the PMT, each of the photons that arrive are transformed into electrons and amplified by a series of electrodes with ascending positive electrical potential, dynode. The multiplied electrons are then transformed into an electrical impulse to be recorded. For Leica TCS SP2, the intensity signals are typically transformed into 8 bit information, which has 256 grey levels; where maximum intensity is represented by 255 (white) and absence of signal is represented by 0 (black).

Gain and Offset setting of the PMT are equivalent to contrast and brightness respectively and allow for adjustment of the input signal such that a maximal number of grey levels are included in the resulting image without saturation. Offset controls the thresholding of the PMT, excluding lower intensity signals in the image, by converting them to zero intensity. Decreasing the Offset will decrease the general background signals (Figure 2.5 B and 2.6 B).

The amplification level of the PMT can be controlled by adjusting its voltage (Gain). Increasing the Gain will enable the detection of weaker signal, but may also cause loss of brighter signals if the image becomes saturated (Figure 2.5 A and 2.6 A). Additionally, the amplification process will introduce noise signals, particularly above 600V (Figure 2.5 C). In order to reduce the Gain while maintaining the level of signals, higher laser intensity is required. However, higher laser intensity will induce greater photobleaching.

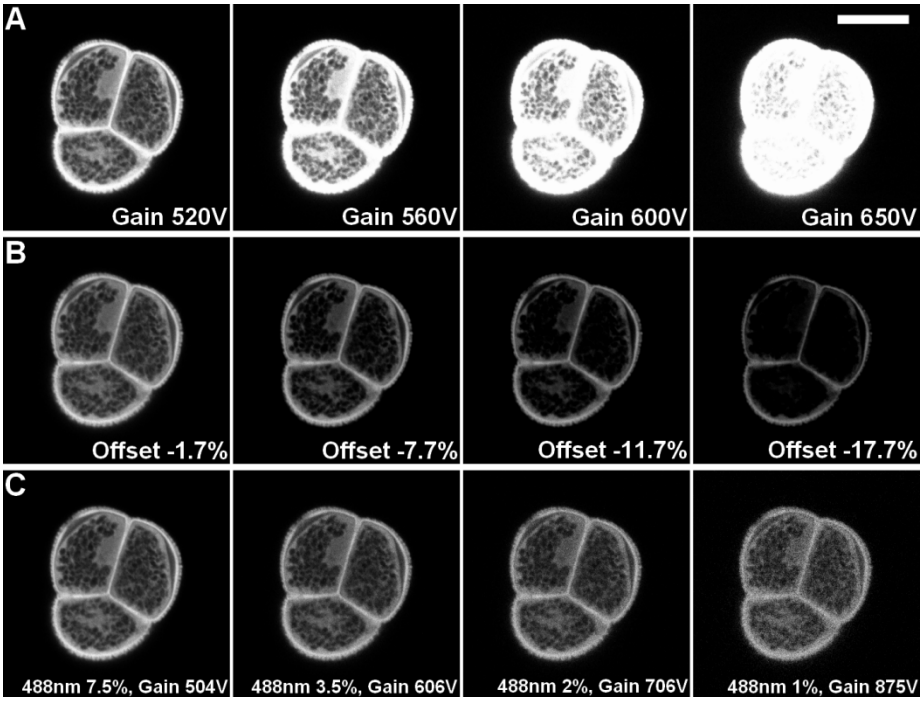

Figure 2.5 The influence of PMT Gain (A) and Offset (B) and laser intensity (C) on image quality of confocal images bisecting the centre of an autofluorescent pollen grain. Unless stated, Gain was 494V, Offset was -1.3% and laser intensity was 8%. In panel C, laser intensity was varied between 7.5% and 1% and PMT Gain and Offset were adjusted to produce the best quality image (Bar: 15 µm).

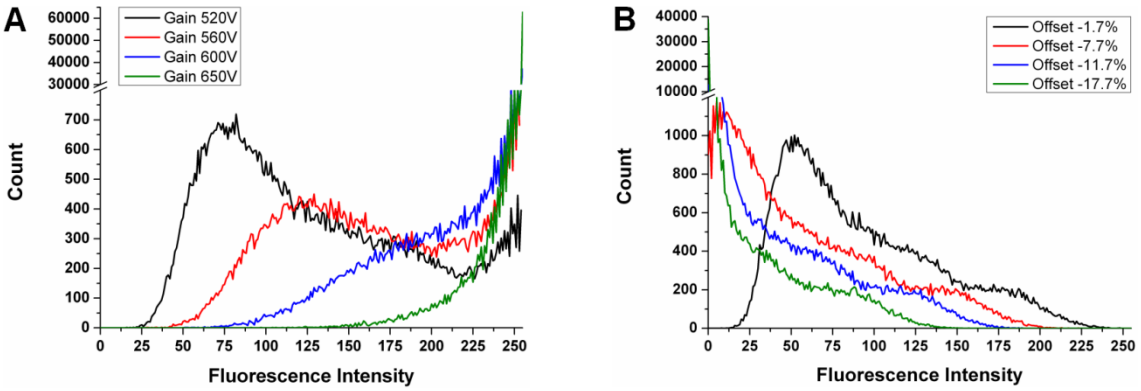

Figure 2.6 Intensity histogram shift of the pollen grain shown in Figure 2.5, A: with different PMT Gain and B: with different PMT Offset.

2.3.7 Selection of Optimal Setting

In each imaging procedure, there is a trade off between image quality and specimen preservation. With greater spatial resolution, image averaging and laser intensity, the

resulting image quality will be higher. However, a greater level of laser exposure will induce a greater damage on the specimen itself (phototoxicity) and on the fluorescent molecules (photobleaching). The optimal imaging setting depends on the characteristic of the specimen and the purpose of the imaging. With this setting, we should be able to acquire the images of the specimen that fulfil the aim of the imaging, while keeping the laser exposure at the minimum.

2.4 Nucleic Acid Dye Selection: Methods

The following section describes the selection process of a suitable fluorescent dye for the imaging of nuclei in living cells. The most essential requirement for live cell imaging is the permeability, since the dye needs to be able to reach the DNA within the nucleus of a living cell. The binding characteristic, advantages and disadvantages and previous applications of the permeant fluorescence dyes are summarised in Table 2.3. In terms of its binding characteristic, a minor groove binding dye would cause significantly less deformity to the DNA compared to intercalative binding (see Appendix A), thus minor groove binding dyes are favoured for live cell imaging.

From this initial selection process, Hoechst 33258, Hoechst 33342, SYTO 16 and DRAQ5 were chosen as the candidates for further investigations of their staining performance. With the exception of DRAQ5, all dyes have been used successfully with chondrocytes. Dihydroethidium was ruled out due to its sensitivity to air (Haugland 2007); LDS 751 was rejected as it also stains the mitochondria (Snyder and Small 2001) and SYBR Green I was ruled out due to its photobleaching properties (Suzuki *et al.* 1997). Acridine orange was rejected as it does not give a clear image of nucleus on living cells based on previous in-house experience. Hoechst dyes bind to the DNA through minor groove binding making them suitable for live cell imaging (Garner 2009). Furthermore, DRAQ5 was also chosen due its promising performance, including minimal photobleaching, as shown in previous studies (Smith *et al.* 2000; Martin *et al.* 2005); even though it is a relatively new dye first described in 1999 (Smith *et al.* 1999).

Table 2.3 The fluorescence nucleic acid dyes considered in the initial selection process, considering permeability, binding characteristic, advantages, disadvantages and previous applications.

Dye	Permeant	Binding Characteristic	Advantages	Disadvantages	Tissue/Cell application
Acridine orange	Yes	Intercalative	• Green fluorescence upon binding with DNA and red fluorescence upon binding with RNA[1]	• Staining on living cells produce blurry image (data not shown) • Problems in imaging heterochromatin[1] • Also used to stain lysosome [5]	• Chondrocytes[13] • Tenocytes[13] • Bone slice[13]
Dihydroethidium	Yes	Intercalative	• Blue fluorescence in the cytoplasm and red fluorescence upon binding with DNA[1]	• Air sensitive[1] • Used widely to detect superoxide generation • Not a DNA specific dye, also stains RNA and mtDNA[1]	• Spermatozoa[15] • Keratinocytes[16] • Myofibroblast[17]
DRAQ5	Yes	Intercalative	• No overlap with GFP/FITC[11] • Does not require rinsing after staining • DNA specific[11] • High permeability[14] • Low photobleaching[10] • Far red emission on binding with DNA[11]	• Relatively new dye, first presented in 1999 • Causes the detachment of histone H1 and H2B[7]	• HeLa cells[10] • Osteosarcoma cells[18] • Fibroblast[19]
Hoechst 33258	Yes	Minor groove binder	• Relatively nontoxic[1] • Virtually no cytoplasmic staining[1] • Slow photobleaching	• Excited with UV laser • A-T specific[1]	• Chondrocytes[20,28] • Breast cancer cells [21] • Keratinocytes[22]

			(1-2 min)[1]		
Hoechst 33342	Yes	Minor groove binder	• Relatively nontoxic[1] • Virtually no cytoplasmic staining[1] • Slightly higher membrane permeability than Hoechst 33258[1,9] • Slow photobleaching (1-2 min)[12]	• Excited with UV laser • Evidence of efflux mechanism by some cell lines[6,8] • Perturb cell cycle[6] • A-T specific[1]	• Chondrocytes[29] • HeLa cells[5] • Fibroblasts[6]
LDS 751	Yes	Intercalative	• Binding to dsDNA results in an ~20 fold fluorescence enhancement[1] • Long wavelength emission maximum[1] • Blue fluorescence upon binding with RNA[1]	• Stains mitochondria by polarizing mitochondrial membrane[2]	• HL-60 cells[23] • Fibroblast[2] • Leukocyte[24]
SYBR Green I	Yes	Intercalative	• Better than acridine orange in staining heterochromatin and mtDNA[3] • Reproduce the pattern shown by UV excited DAPI[3]	• High photobleaching (more than DAPI)[4] • Commonly used for gel electrophoresis • Require UV excitation	• L23 cells[3] • Pancreas sample[4]
SYTO 16	Yes	Intercalative + Minor groove binder	• Twice as fluorescent upon binding with DNA than with RNA[1] • Permeability to virtually all cell membranes[1] • High molar absorptivity[1]	• Not specific to DNA as it will stain cytoplasm, mitochondria and nucleus[1] • 10-20s photobleaching[12]	• Chondrocytes[25] • Lymphocytes[26] • Leukocytes[27]

	• Extremely low intrinsic fluorescence[1] • Quantum yields typically greater than 0.4 when bound to nucleic acid[1]

[1](Haugland 2007), [2](Snyder and Small 2001), [3](Briggs and Jones 2005), [4](Suzuki *et al.* 1997), [5](Canete *et al.* 2001), [6](Durand and Olive 1982), [7](Wojcik and Dobrucki 2008), [8](Teramura *et al.* 2008), [9](Garner 2009), [10](Martin *et al.* 2005), [11](Smith *et al.* 2000), [12](Wlodkowic *et al.* 2008), [13](Jones *et al.* 2005), [14]BioStatus Ltd., [15](Espinoza *et al.* 2009), [16](Olson *et al.* 2008), [17](Lai *et al.* 2006), [18](Njoh *et al.* 2006), [19](Sabbioneda *et al.* 2008), [20](Knight *et al.* 2002), [21](Cheah *et al.* 2009), [22](Cai *et al.* 2008), [23](Frey 1995), [24](Maes *et al.* 2007), [25](Ohashi *et al.* 2006), [26](Sparrow *et al.* 2006), [27](Rosenbaum *et al.* 2002), [28](Hoshiba *et al.* 2008), [29](Kawasaki *et al.* 2004)

2.4.1 Aim

The aim of this procedure is to determine the suitable permeant nucleic acid dye for primary chondrocytes, between Hoechst 333258, Hoechst 33342, SYTO 16 and DRAQ5, based on its photobleaching characteristic, the quality of images produced and its effect on cell proliferation.

2.4.2 Specimen Preparation

For nuclei imaging, primary chondrocytes, isolated as described in section 2.2.4, were seeded at 5×10^3 cells/cm^2 onto glass bottom 24 well plates (MatTek, Ashland, USA), pre-coated with FCS for 1 hour at room temperature.

For the proliferation investigation, cells were seeded onto conventional 24 well plates tissue culture plastic (BD, Oxford, UK) with a seeding density of 5×10^4 cells/cm^2. For all studies, prior to staining, the cells were cultured for 2 days to allow adhesion.

2.4.3 Preparation and Application of Dye

Working stain solutions were prepared in a dark room to prevent bleaching of the fluorescence dyes. SYTO 16 stock solution (1 mM) was prepared in DMSO (Invitrogen, Paisley, UK). Hoechst 33258 and 33342 (Sigma-Aldrich) stock solutions, both at 1 mg/mL, were prepared in distilled water. The dyes were diluted with staining media to produce 3 mL of the initial concentrations, the stain solutions then underwent a series of doubling dilutions to produce the concentrations listed in Table 2.4. The bijou tubes containing the dye were stored at 4^{o}C and protected from light. These staining concentrations were chosen on the basis of previous studies and the concentrations suggested by the manufacturers, as listed in Table 2.5.

On the second day of culture, the dyes were placed in a 37^{o}C water bath for 30 minutes. The cells were rinsed once with 1 mL of PBS and then stained with 1 mL dye solution at 37^{o}C for 30 minutes. Following staining, cells, except for those labelled with DRAQ5, were rinsed with DMEM + 16.1% FCS (3 × 5 minutes).

Table 2.4 The staining concentrations prepared for the staining procedure

Dyes	Concentrations					
	1	**2**	**3**	**4**	**5**	**6**
Hoechst 33258	16 µM	8 µM	4 µM	2 µM	1 µM	0.5 µM
Hoechst 33342	16 µM	8 µM	4 µM	2 µM	1 µM	0.5 µM
SYTO 16	5 µM	2.5 µM	1.25 µM	0.63 µM	0.32 µM	0.18 µM
DRAQ5	20 µM	10 µM	5 µM	2.5 µM	1.25 µM	0.63 µM

For the proliferation investigation, cells in 3 wells were stained with 400 µL 8 µM Hoechst 33342 and another 3 wells were stained with 400 µL 10 µM DRAQ5, both for 15 minutes at 37^{o}C. Afterwards, the stain solutions were replaced by 2 mL DMEM + 16.1% FCS. Unstained control cells were treated in an identical manner.

2.4.4 Fixation and Mounting

Following staining, the cells were washed in PBS and fixed for subsequent microscopy. The cells were fixed in 3.7% formaldehyde (Sigma-Aldrich) in PBS for 15 minutes at room temperature. The samples were then washed in PBS (×3) and distilled water (×2) prior to mounting.

For the mounting procedure, 0.3 g of 1,4-Diazabicyclo[2.2.2]octane (DABCO, Sigma-Aldrich) was diluted in 9 mL of glycerol (Sigma-Aldrich) and 1 mL of PBS, to produce 10 mL of 30 g/L DABCO mountant solution. DABCO solution with a volume of 3 µL was pipetted into each well, and a 10 mm diameter coverslip placed on top. Nail varnish was applied around the coverslip to prevent dehydration and the plate left overnight. The specimens for viability investigation did not undergo the fixation and mounting procedure.

2.4.5 Photobleaching Characteristics

Images were taken using a Leica TCS SP2 confocal microscope with a HCX PL APO 63x/1.4-0.6NA oil immersion objective. In order to investigate the photobleaching characteristics, a series of images were acquired with the same imaging setting. An initial experiment showed that SYTO 16 exhibited rapid photobleaching and was therefore omitted from further evaluation (Appendix B). A total of 25 consecutive images of a nucleus, stained with the highest concentration of each dye, were made at 10× zoom (pixel

size 46.5 × 46.5 nm), a line averaging of 2 and a frame averaging of 3. PMT Gain and Offset and laser intensities were optimised to produce the best quality images over the entire dynamic intensity range (0-255).

Image analysis and processing were performed using LCS SP2 and LCS Lite (Leica Microsystems GmbH). A region of interest (ROI) was created around the nucleus, and the mean fluorescence intensity within the ROI was recorded for each of the consecutive images.

2.4.6 Staining Intensities

Each of the images taken in this stage was a result of 4 line and frame averaging, at 1× zoom (pixel size 465 × 465 nm). In order to compare the fluorescence intensity with different staining concentrations, nuclei were imaged with constant imaging parameters. Firstly, for each dye group, an image from the highest staining concentration was taken with the optimal laser intensity, the PMT Gain and Offset. These settings were then used to image nuclei stained at the lowest staining concentration.

The mean intensity was calculated from the ROIs created around five different nuclei in each image. Measurements were conducted on a total of 15 nuclei from at least 3 separate images.

2.4.7 Image Quality

In order to compare the quality of the images produced by different dyes, at least 12 images (10× zoom, 2 line averages and 3 frame averages) of nuclei were taken using the optimal settings. The images were then analysed visually.

2.4.8 Cell Proliferation

Phase contrast images of the cells stained with each dye were taken using a light microscope (Leica Microsystems GmbH) incorporating a 10× objective lens. Images were taken immediately after staining and after a further 5, 7 and 9 days of culture in DMEM + 16.1% FCS (37˚C and 5% CO_2).

Table 2.5 The staining concentrations suggested and used by previous studies for Hoechst 33258, Hoechst 33342, SYTO 16 and DRAQ5.

Dyes	Ex/Em (nm)	Concentration	Incubation time	Application	Reference
Hoechst 33258	352/461	0.32 to 8 μM	20 to 30 min	Live animal cells	Invitrogen Ltd.
		1.6 μM	5 min	HeLa cells	(Martin *et al.* 2005)
		16 μM	15 min (37°C)	Chondrocytes	(Hoshiba *et al.* 2008)
		5 μM	45 min (37°C)	Chondrocytes	(Knight *et al.* 2002)
Hoechst 33342	350/461	0.32 to 8 μM	20 to 30 min	Live animal cells	Invitrogen Ltd.
		4 μM	15 min	HeLa and 3T3 cells	(Canete *et al.* 2001)
		1.6 μM	10 min	Thymocytes	(Frey 1995)
SYTO 16	488/518	0.01 to 5 μM	10 to 120 min	Eukaryotic cells	Invitrogen Ltd.
		0.25 μM	10 to 15 min	U2OS cells	(Wlodkowic *et al.* 2008)
		1 μM	15 min (37°C)	Chondrocytes	(Ohashi *et al.* 2006)
DRAQ5	647/670	5 to 20 μM	5 to 30 min (20°C) 1 to 3 min (37°C)	Eukaryotic Cells	Biostatus Ltd.
		1 μM	5 min	HeLa cells	(Martin *et al.* 2005)
		20 μM	30 min (20°C)	Human β cells	(Smith *et al.* 1999)

2.5 Nucleic Acid Dye Selection: Results

2.5.1 Photobleaching Characteristics

Figure 2.7 indicates that DRAQ5 has the slowest rate of photobleaching, followed by Hoechst 33342 and Hoechst 33258. The higher photobleaching rate of Hoechst 33258 is due to the use of a higher laser intensity which was required to produce optimal images, possibly due to the reduced permeability of this dye (Haraguchi *et al.* 1999; Singh *et al.* 2004; Garner 2009). Based on these findings, Hoechst 33258 was ruled out of the selection process.

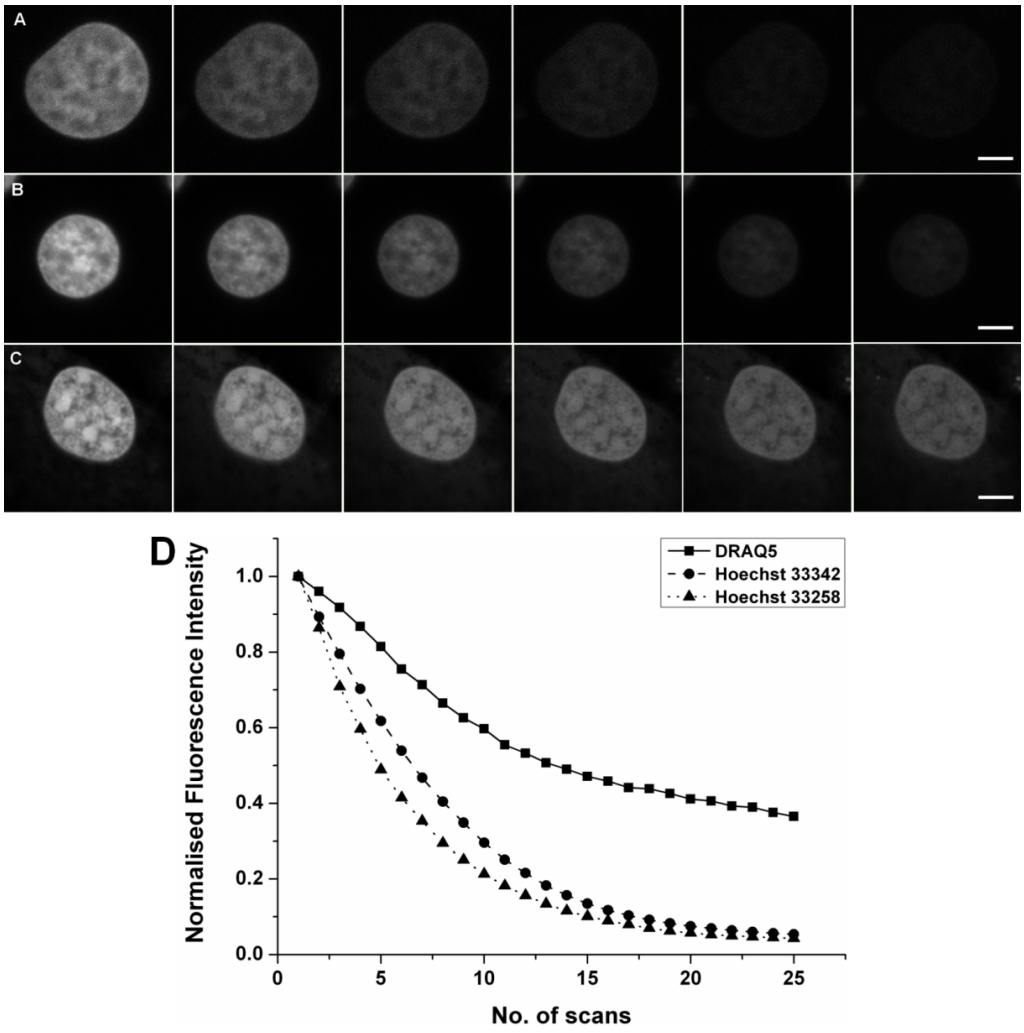

Figure 2.7 Photobleaching characterisation with 10× zoom (pixel size 46.5 × 46.5 nm). Images of nucleus stained with Hoechst 33258 (A), Hoechst 33342 (B) and DRAQ5 (C) from the 1st, 4th, 7th, 10th, 13th and 15th scan (2 line averaging and 3 frame averaging, Bar: 5 μm). D: The graph of fluorescence intensity against number of scans (N = 1, n = 1 nucleus per dye). Images were taken before fixation.

2.5.2 Staining Intensities

Investigation on the correlation between fluorescence signal level and staining concentration for each dye was carried out using images taken after fixation. For both Hoechst 33342 and DRAQ5 stained specimens, at lower concentrations, the images taken become brighter as the staining concentration increases and reach a plateau at higher concentrations (Figure 2.8 and 2.10), as confirmed by the intensity quantified from each staining group (Figure 2.9 and 2.11). From these results, we can conclude that staining with Hoechst 33342 above 8 μM and with DRAQ5 above 10 μM, does not give higher fluorescence signal intensity.

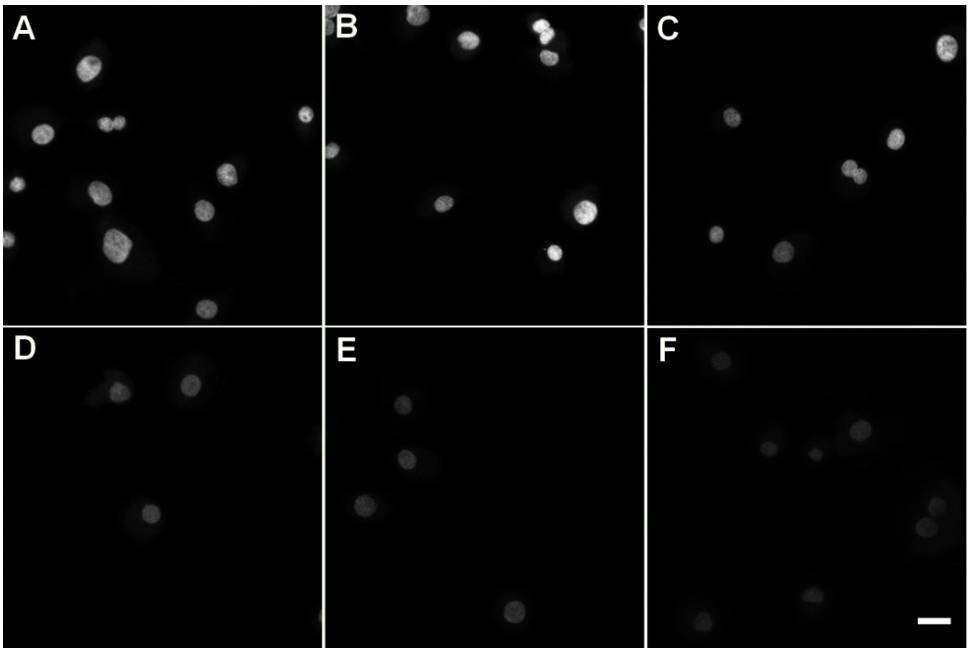

Figure 2.8 Images from Hoechst 33342 stained cells at staining concentration of A: 16 μM, B: 8 μM, C: 4 μM, D: 2 μM, E: 1 μM and F: 0.5 μM after fixation (Bar: 25 μm).

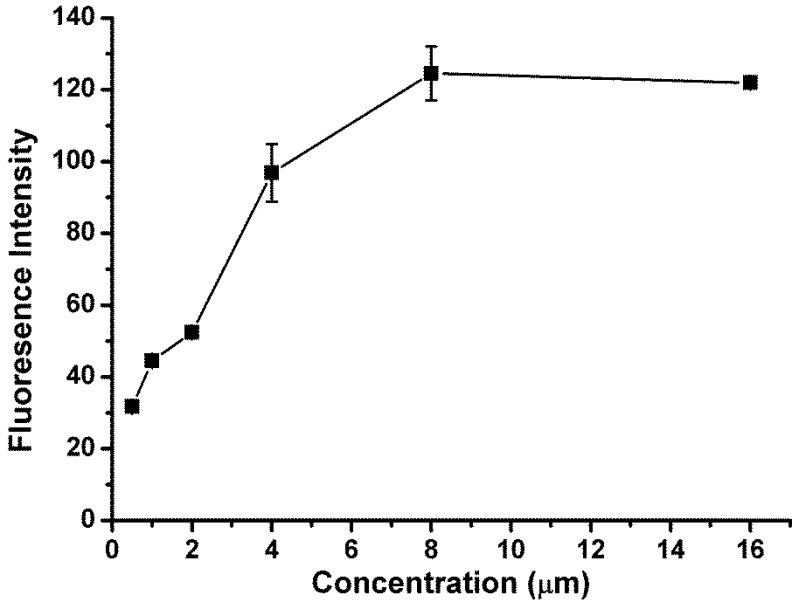

Figure 2.9 Fluorescence intensity against staining concentration for Hoechst 33342 after fixation ($N = 1$, $n = 15$ nuclei per staining concentration). Error bars show standard error.

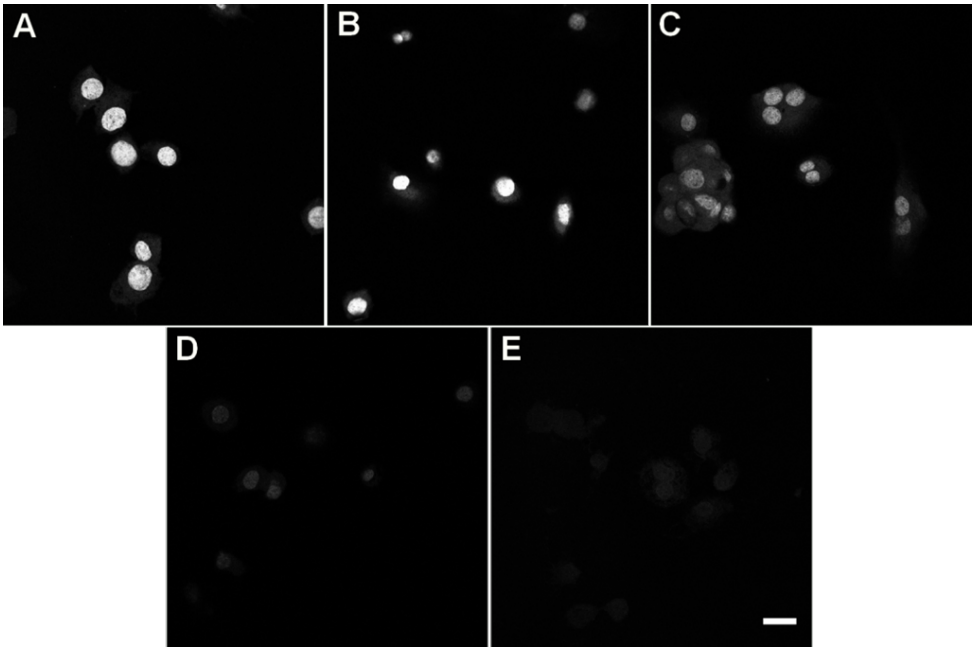

Figure 2.10 Images from DRAQ5 stained cells at staining concentration of A: 20 μM, B: 10 μM, C: 5 μM, D: 2.5 μM and E: 1.25 μM after fixation (Bar: 25 μm).

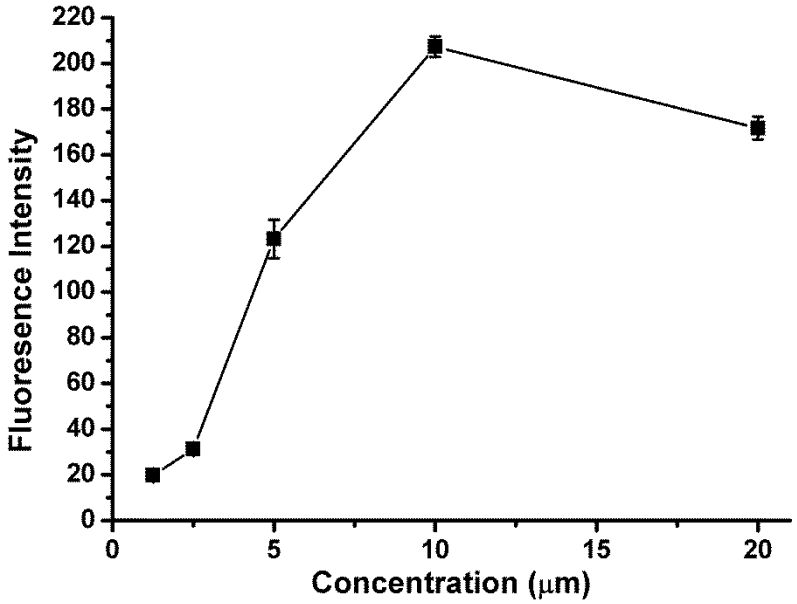

Figure 2.11 Fluorescence intensity against staining concentration for DRAQ5 after fixation (*N* = 1, *n* = 15 nuclei per staining concentration). Error bars show standard error.

2.5.3 Image Quality

Figure 2.12 and 2.13 reveal that decreasing the staining concentration below a critical threshold reduces the clarity of the images. In the case of cells stained with Hoechst 33342, a staining concentration below 2 μM gives poor image quality. For cells stained with DRAQ5, image quality starts to deteriorate below 2.5 μM. However, comparing Figure 2.12 and 2.13, DRAQ5 tends to give a sharper nuclear image and a better detail of nuclear structure.

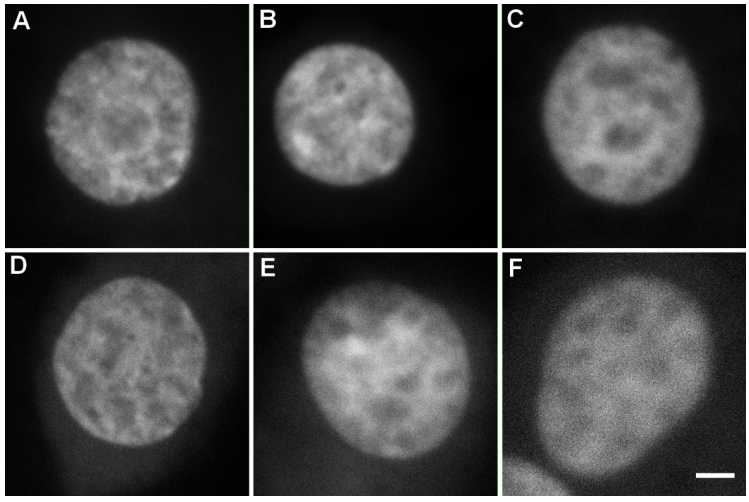

Figure 2.12 Images of nuclei stained with Hoechst 33342 at staining concentration of A: 16 μM, B: 8 μM, C: 4 μM, D: 2 μM, E: 1 μM and F: 0.5 μM, taken with optimal setting for each nucleus, after fixation (Bar: 5 μm).

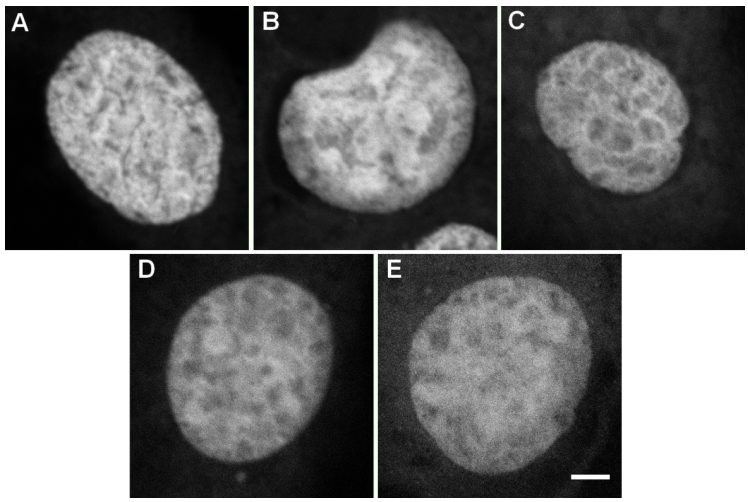

Figure 2.13 Images of nuclei stained with DRAQ5 at staining concentration of A: 20 μM, B: 10 μM, C: 5 μM, D: 2.5 μM and E: 1.25 μM, taken with optimal setting for each nucleus, after fixation (Bar: 5 μm).

2.5.4 Proliferation

Figure 2.14 shows the process of adhesion and proliferation of unstained primary chondrocytes. On the 2nd day of culture, the chondrocytes were attached to the substrate, with a limited degree of cell spreading. On day 5 of culture, they were fully adhered to the culture surface with a more fibroblastic morphology. Additionally, proliferation can be observed by the increase in cell number and the appearance of dividing cells. The chondrocytes reached 100% confluence on day 7 of culture. On the 9th day, cell spreading is reduced due to compaction caused by further proliferation.

The appearance of chondrocytes stained with Hoechst 33342 and DRAQ5 is shown in Figure 2.15 and 2.16 respectively. Hoechst 33342 staining does not severely inhibit the proliferation of chondrocytes compared to the unstained control (Figure 2.15), and shows an increase of cell number through day 5, 7 and 9 of culture. However, on the ninth day of culture, the control had a higher number of cells, suggesting that Hoechst 33342 retards the cell proliferation rate at certain degree even though the cells remain viable, as reported previously (Durand and Olive 1982). DRAQ5 seems to inhibit cell proliferation and the cell number was markedly reduced throughout the culture period, as shown in Figure 2.16. On the 5th day of culture, a degree of cell adhesion onto the culture surface was observed, suggesting that chondrocytes stained with DRAQ5 remain viable for several days, but with severe disruption of cell proliferation.

Hoechst 33342 binds to the DNA by minor groove binding and DRAQ5 intercalates to the DNA structure. This study suggests that intercalating nuclear dyes disrupt the cell proliferation in a greater extent, compared to the minor groove binding stains. From this finding, even though Hoechst 33342 gives a lower quality of images, it is better for live cell imaging. In case of fixed cell imaging, DRAQ5 might be used to give a greater quality of image.

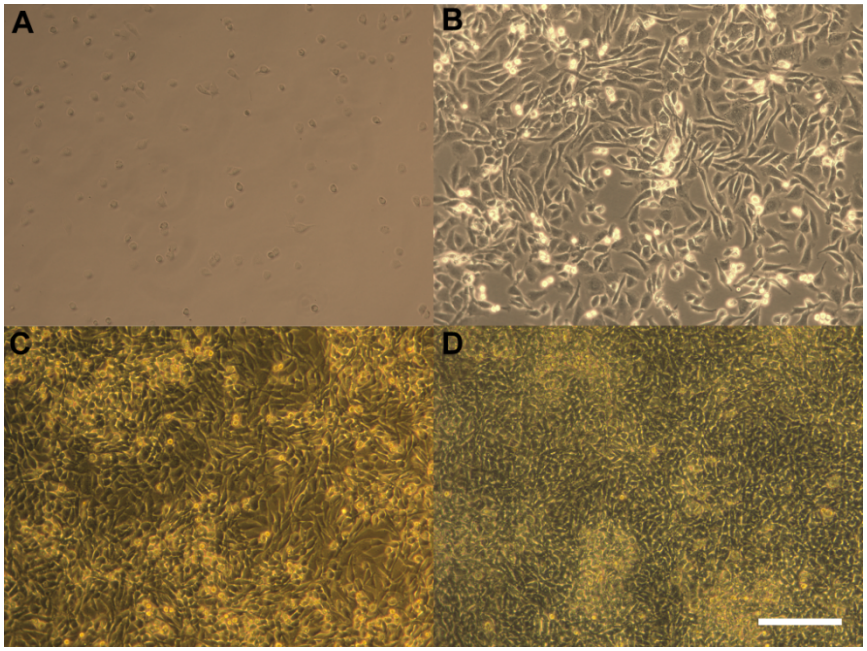

Figure 2.14 The phase contrast images of unstained chondrocytes at A: day 2, B: day 5, C: day 7 and D: day 9 of culture, taken with 10× objective lens (Bar: 200 µm).

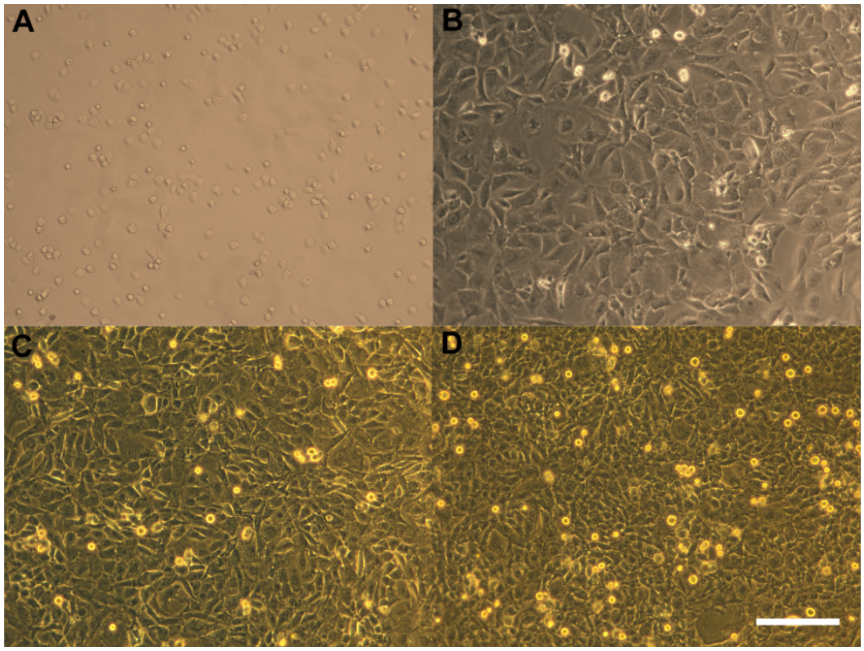

Figure 2.15 The phase contrast images of chondrocytes stained with H33342 at A: day 2, B: day 5, C: day 7 and D: day 9 of culture, taken with 10× objective lens (Bar: 200 μm).

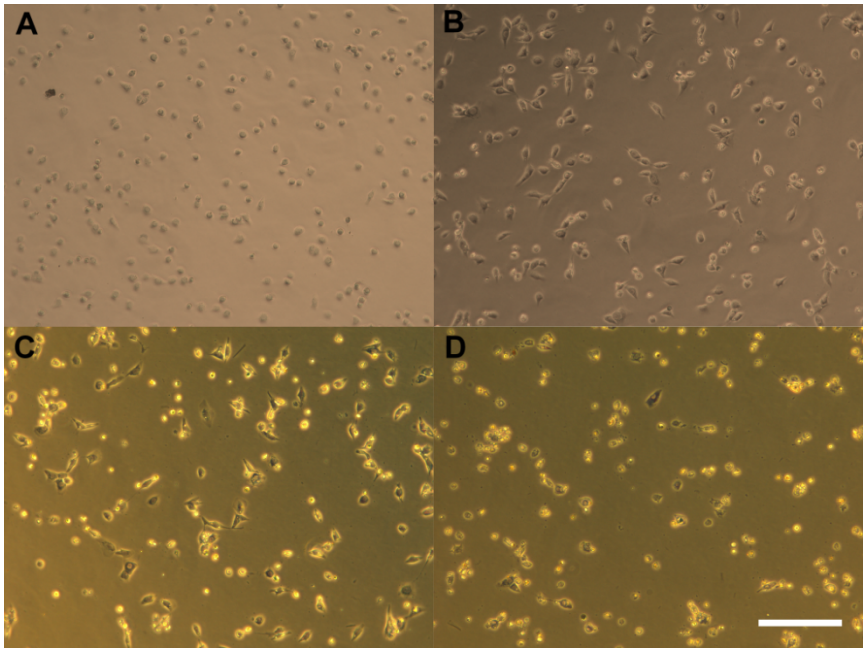

Figure 2.16 The phase contrast images of chondrocytes stained with DRAQ5 at A: day 2, B: day 5, C: day 7 and D: day 9 of culture, taken with 10× objective lens (Bar: 200 μm).

2.5.5 Selected Nucleic Acid Dye

In summary (Figure 2.17), Hoechst 33342 and DRAQ5 were shown to have better photobleaching characteristics compared to SYTO 16 (Appendix B) and Hoechst 33258 (Figure 2.7). For Hoechst 33342 and DRAQ5, staining concentration above 8 μM and 10 μM did not produce a higher level of fluorescence signals (Figure 2.9 and 2.11). Furthermore, DRAQ5 was shown to produce better quality images of the nucleus when compared to Hoechst 33342 stained nuclei (Figure 2.8 and 2.10). However, unlike Hoechst 33342, DRAQ5 was shown to significantly perturb chondrocytes proliferation (Figure 2.15 and 2.16). Based on these findings, Hoechst 33342 was chosen as the nucleic acid dye for subsequent live cell studies, with staining concentration of 8 μM at 37^{o}C for 15 minutes.

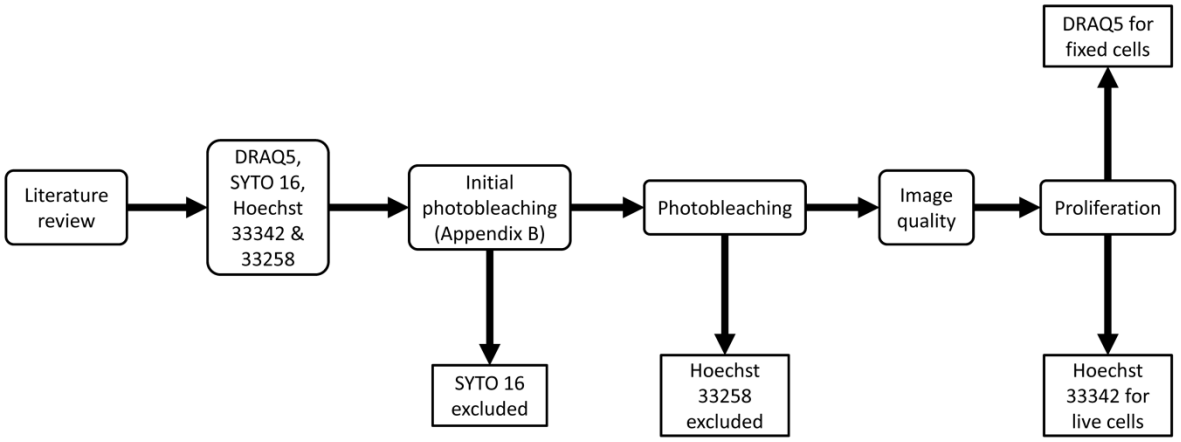

Figure 2.17 Flow chart summarizing the nucleic acid dye selection process.

2.6 Transfection Characterisation

2.6.1 Transfection Mechanism

During transfection process, external genetic material (DNA or RNA), such as plasmid DNA, messenger RNA, short interfering RNA and micro RNA, is introduced into eukaryotic cells. Unfortunately, cellular cytotoxicity and transfection efficiency vary dramatically between different reagent, procedure and cell type. Thus characterisation is required to develop an optimal transfection process.

Methods of transfection can be divided into three main types: physical, chemical and viral based. In viral based delivery system, viral transduction techniques are utilised to deliver the genetic material into cultured eukaryotic cells, using retroviruses, adeno-associated viruses and lentiviruses as carrier. Some examples of physical method include electroporation and microinjection. Electroporation is a highly efficient technique, involving the application of an electrical field to create transient pores (electropores) in the cellular membrane, which allows the insertion of charged molecule, such as DNA and RNA, into the cytoplasm. In the microinjection technique, the genetic materials are delivered directly into the cell via gene guns or manual microinjection. Liposome mediated transfection or lipofection is one example of chemical transfection. Liposomes are synthetic analogues of the cellular membrane phospholipid bilayer. In the presence of DNA or RNA, liposomes have the ability to interact and encapsulate the genetic materials, which are then taken up by the cells through endocytosis and released into the cytoplasm.

In this study, two lipofection transfection reagents were characterised: HiFect (Lonza, Basel, Switzerland) and DharmaFect Duo (Dharmacon, Chicago, USA). Both of these reagents were used to introduce the histone 2B (H2B) specific green fluorescence protein plasmid DNA (GFP-pDNA). Upon the release to the cytoplasm, the GFP-pDNA can only access the nucleus during mitotic cell division.

2.6.2 Material and Methods

Primary chondrocytes were isolated from bovine metacarpophalangeal articular cartilage via enzyme digestion, as previously described (section 2.2.4), and the cells were seeded into 175 cm^2 culture flasks at 4.5×10^4 cells/cm^2, for 5 days. The cells were then

trypsinised and seeded onto 24 well plates at seeding densities of 2, 3 or 6 × 10^4 cells/cm^2. Cells were cultured overnight prior to transfection to allow adhesion.

The detailed transfection procedure in this characterisation study is described in Appendix D. Briefly, this transfection optimisation study examined the influence of cell seeding density (2, 3 and 6 × 10^4 cells/cm^2) and reagent and DNA ratio (8:1, 6:1, 4:1, 3:1, 2:1 and 1:1). Additionally, as a negative control, distilled water was added instead of GFP-pDNA.

After 24 hours of transfection, the media were replaced with fresh DMEM + 16.1% FCS. Fluorescence images of the nuclei and phase contrast images of the cells were acquired using a non-confocal epifluorescence microscope (Leica Microsystems GmbH) with a 20× objective lens. After further 24 hours of culture, the nuclei and cells were imaged again. From each image, the cells and transfected nuclei were counted, and efficiency of the transfection was determined by calculating the ratio between the two counts.

2.6.3 Results

In the HiFect transfection group, the transfection efficiency was highest at the 6 × 10^4 cells/cm^2 seeding density (Figure 2.18 A). The transfection efficiency reached a peak at 6:1 reagent and GFP-pDNA ratio (Figure 2.18 B). The transfection efficiencies were also greater at 48 hours.

The transfection efficiencies in the DharmaFect Duo group were much lower than the HiFect group (Figure 2.19), with cell seeding density not altering the transfection efficiency (Figure 2.19 A). The increase of reagent and GFP-pDNA ratio broadly increases the transfection efficiency (Figure 2.19 B). However, in contrast to the HiFect group, signs of cytotoxicity could be observed at 8:1 and 6:1 ratios (Figure D.2). Additionally, from Figure D.1 C and D.2 C no sign of cytotoxicity could be observed in the absent of GFP-pDNA for either transfection groups.

Due to its higher transfection efficiency and the absent of cytotoxicity, HiFect was chosen as the transfection reagent. As the highest transfection efficiency was achieved at 6 × 10^4 cells/cm^2 with 5:1 ratio, this ratio was chosen. Additionally, 5 × 10^4 cells/cm^2 seeding density was chosen as this is the seeding density used in the other studies in this project (section 3.2.2).

In addition to this characterisation study, the viability of cells transfected by using the chosen parameters was examined. Freshly isolated chondrocytes were cultured for 5 days and seeded onto two Ø35 mm Petri dishes with a seeding density of 5×10^4 cells/cm^2. On the next day, one of the dishes was transfected. Both of the dishes were then trypsinised 24 hours after the transfection procedure. The trypsinised cells underwent the trypan blue exclusion test to measure the viability of the cells. The viability of the transfected sample was 90%, while the one that did not undergo the transfection had a viability of 99%.

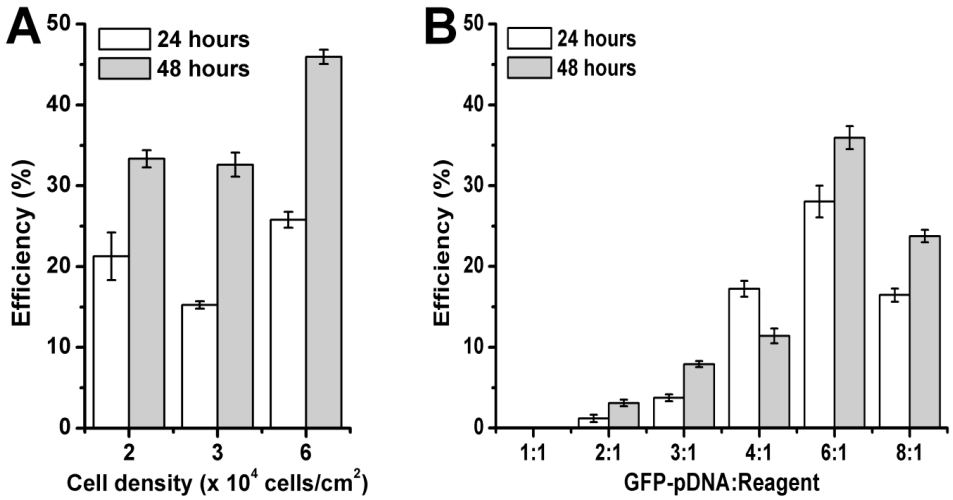

Figure 2.18 The transfection efficiency of HiFect for specimens with different cell density (A) and DNA:Reagent ratio (B), at 24 and 48 hours after transfection (N = 1, n = 3 field of views per condition). Error bars show standard error.

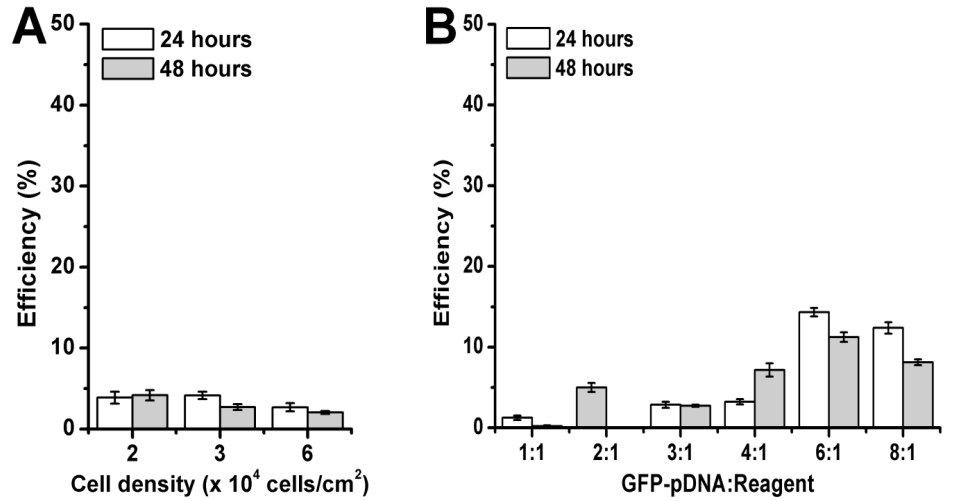

Figure 2.19 The transfection efficiency of DharmaFect Duo for specimens with different cell density (A) and DNA:Reagent ratio (B), at 24 and 48 hours after transfection (N = 1, n = 3 field of views per condition). Error bars show standard error.

2.7 Image Analysis Technique

2.7.1 Sobel Edge Detection – The Chromatin Condensation Parameter

The condensation of chromatin increases the number of distinct spaces within the nucleus. As shown in Figure 2.20 A1, a number of significant dips of fluorescence signal intensity can be observed from the intensity profile across the nucleus with hyper-condensed chromatin. These intensity dips will be recognised by the Sobel edge detection algorithm as strong edges, i.e. high gradient magnitude. Thus, measuring the strong edges within the nucleus normalised to its cross-section area gives the edge density, which represents the level of chromatin condensation. From here onward, this measurement will be referenced as the chromatin condensation parameter.

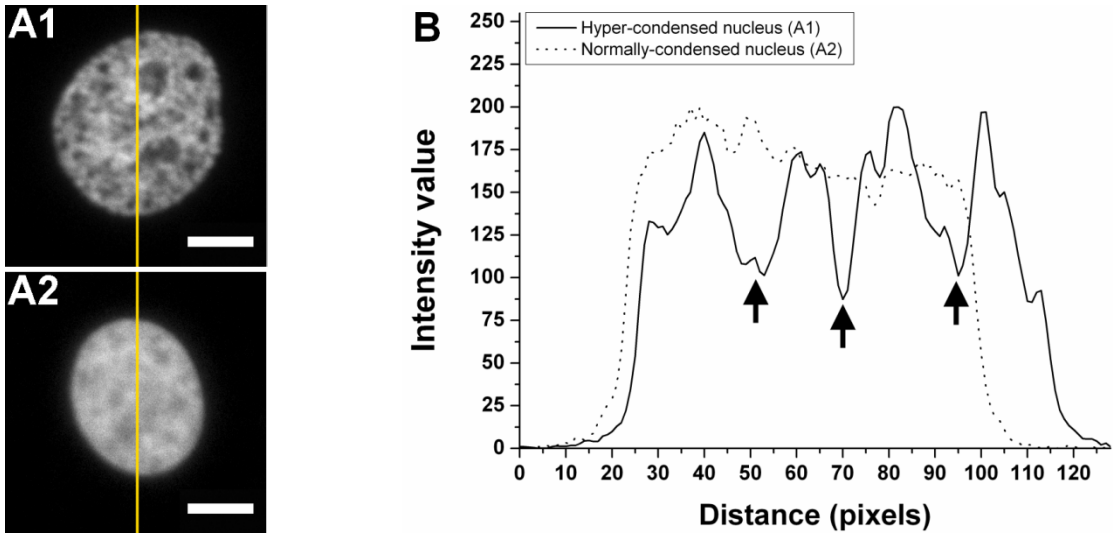

Figure 2.20 Monolayer cultured chondrocyte nuclei A1: with and A2: without hyper-condensed chromatin, both with a region of interest drawn across the nuclei. B: The intensity profile across the hyper-condensed nucleus and normally-condensed chromatin, with arrows showing the dips of signal intensity across the hyper-condensed nucleus (Bar: 5μm).

Edge detection algorithms can be classified into two classes: derivative and gradient based. Sobel edge detection is a gradient based algorithm, where a gradient of consecutive pixels is approximated in *X* and *Y* direction. Sobel edge detection uses two 3×3 kernels and its principle can be described as follow:

$$S_x = \begin{bmatrix} +1 & 0 & -1 \\ +2 & 0 & -2 \\ +1 & 0 & -1 \end{bmatrix} \quad \text{and} \quad S_y = \begin{bmatrix} -1 & -2 & -1 \\ 0 & 0 & 0 \\ +1 & +2 & +1 \end{bmatrix}$$

$$G_x = S_x \times I \tag{2.8}$$

$$G_y = S_y \times I \tag{2.9}$$

$$G = \sqrt{{G_x}^2 + {G_y}^2} \tag{2.10}$$

Where S_x is the Sobel kernel for the approximation of gradient in *X* direction, S_y is the Sobel kernel for the approximation of gradient in *Y* direction, G_x is the approximated gradient in *X* direction, G_y is the approximated gradient in *Y* direction, I is the target image matrix and G is the approximated gradient magnitude.

In a Sobel algorithm, the gradients between a pixel and the 8 surrounding pixels are approximated by using the S_x and S_y kernel matrices. The resulting gradient approximations in *X* and *Y* directions (G_x and G_y) can be combined to give the gradient magnitude (G), which is used to represent the processed pixel of interest in the target image. This process is repeated for each pixel within the target image. The final step of the Sobel algorithm produces a new image showing the level of edges based on the gradient magnitude.

2.7.2 Image Reduction

As the Sobel algorithm only considers the 8 surrounding pixels to approximate the gradient magnitude, it was found to be too sensitive for the images acquired in this study, as seen in Figure 2.22 B1 and D1. Without any modification to the source image, the pixel size is too small such that the slightest gap between the pixels was registered as an edge. Hence Figure 2.22 A1 does not represent the essential edges of its source image (Figure 2.22 A). This can be resolved by image reduction. In image reduction, a set number of pixels are averaged and the mean value is represented as a pixel in the new image. For example, in pixel reduction by a factor of 3, each 3×3 pixel group is averaged and the mean value is represented as a pixel in the new image matrix, as shown in Figure 2.21. Through image reduction, as shown in Figure 2.22, the essential edges become more apparent. However, as the image is reduced, the edge detection algorithm sensitivity in detecting the edges also reduces.

The density of edges of 20 nuclei with condensed and uncondensed chromatin, which were subjected to a series of pixel reduction, was measured (Figure 2.23). Paired Student's *t*-tests were carried out on each image reduction group to represent the significance of the difference between the measurements taken on the nuclei with and without condensed chromatin. Figure 2.23 shows that differences can be clearly observed starting from the image reduction factor of 3. However, the maximum difference occurred at factor 4. Based on this finding, image reduction by a factor of 4 was chosen to be used in the quantification of chromatin condensation.

50	40	75	21	0	63	71	192
52	21	45	36	18	70	19	231
125	120	12	96	1	46	46	63
151	52	92	82	59	25	210	214
45	136	89	64	25	35	26	168
58	45	52	17	73	43	185	147
85	75	45	19	8	62	125	54
65	42	154	26	16	58	142	36

60	39	...
80	47	...
...	...	...

Figure 2.21 The illustration of pixel reduction by factor of 3.

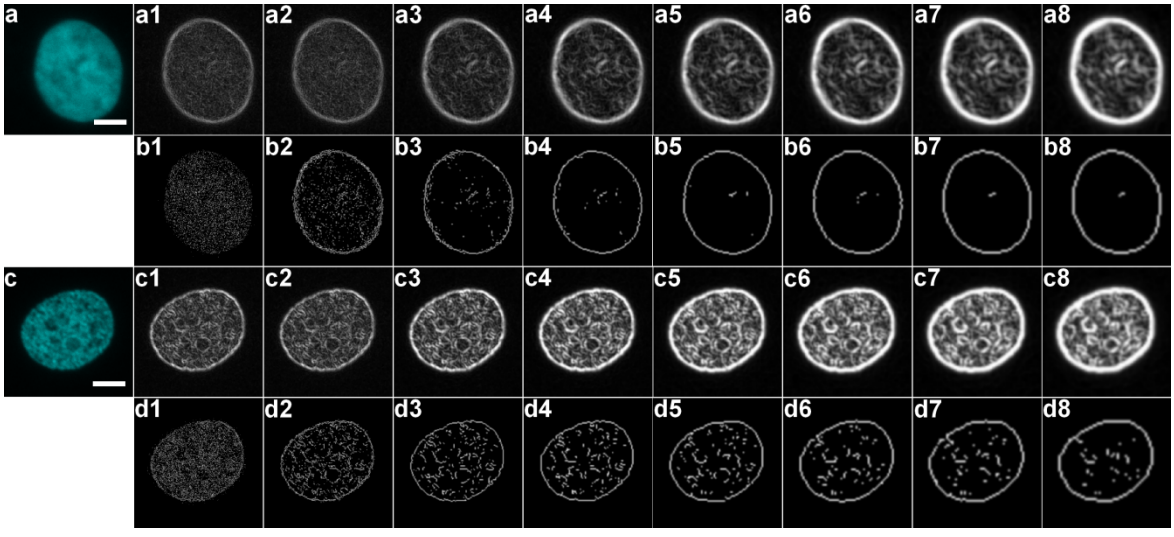

Figure 2.22 Application of Sobel edge detection on normal (A) and hyper-condensed (C) nuclei without any pixel reduction (A1 and C1), with pixel reduction by factor of 2 (A2 and C2), 3 (A3 and C3), 4 (A4 and C4), 5 (A5 and C5), 6 (A6 and C6), 7 (A7 and C7) and 8 (A8 and C8). Thresholded Sobel edge images (B1 to B8 and D1 to D8, Bar: 5 µm).

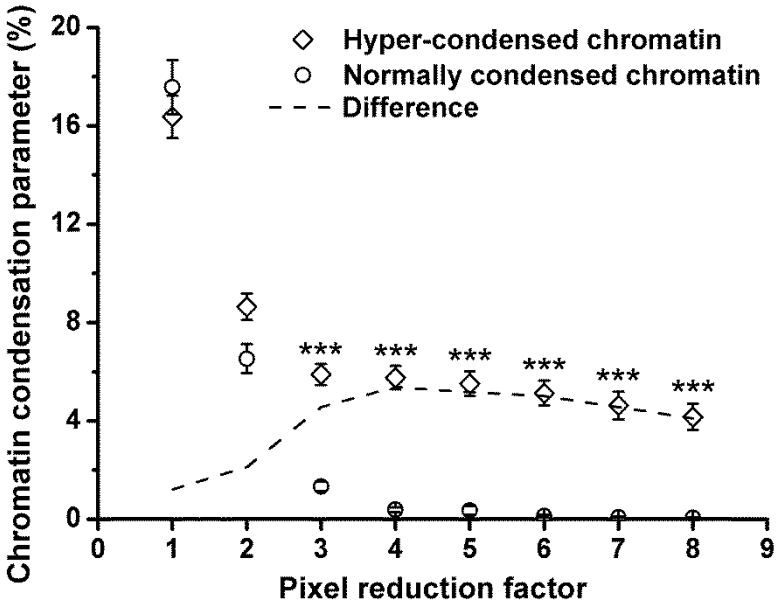

Figure 2.23 The density of edges measured on the nuclei with hyper-condensed chromatin and normally condensed chromatin against the pixel reduction factor (N = 1, n = 20 nuclei per condition, *p<0.05 and ***p<0.001). Error bars show standard error.

2.7.3 Validation Against Visual Assessment

The quantification procedure was applied to the nuclei images acquired from the imaging of osmotically-challenged and fixed chondrocytes (section 3.2). From each osmotic group, 40 nuclei images were acquired, resulting in a total of 640 nuclei images. Visually, an increase in chromatin condensation level can be seen with the application of hyper-osmotic challenge (>400 mOsm/kg), which was confirmed by the significant increase in the chromatin condensation parameter between the 400 and 500 mOsm/kg groups (Figure 3.4). In order to validate these results, visual assessment of the images was carried out.

First, the 640 nuclei were grouped based on their chromatin condensation parameter reading into 8 groups, with the binning range shown in table 2.7. Four images from each group were chosen to represent the group (Figure 2.24). These groups of images were then sorted randomly (not based on the ascending chromatin condensation parameter order) and given to an inspector (20 inspectors in total), who ranked the images based on visual judgement on the level of chromatin condensation. The group with the least chromatin condensation was given rank 1 and the one with the most chromatin condensation was given the rank 8. The visual assessment ranks given were weighted toward the mean of the reading of each group (Table 1). The weighted visual assessment values were averaged for

each group and plotted against the chromatin condensation parameter of the corresponding group.

Table 2.6 The binning range of the chromatin condensation parameter reading for each bin group, including the number of nuclei registered to each group (from 640 nuclei) and the minimum, maximum and mean of the readings.

Group	Bin range of reading	Number of nuclei	Minimum reading (%)	Maximum reading (%)	Mean (%)
1	$n \leq 0.5\%$	171	0	0.499	0.200
2	$0.5\% < n < 2\%$	148	0.503	1.991	1.002
3	$2\% \leq n < 4\%$	61	2.006	3.992	2.977
4	$4\% \leq n < 6\%$	55	4.110	5.960	5.013
5	$6\% \leq n < 8\%$	79	6.010	7.959	7.005
6	$8\% \leq n < 10\%$	56	8.003	9.953	9.007
7	$10\% \leq n < 12\%$	46	10.011	11.988	10.828
8	$12\% \leq n$	24	12.027	17.680	13.545

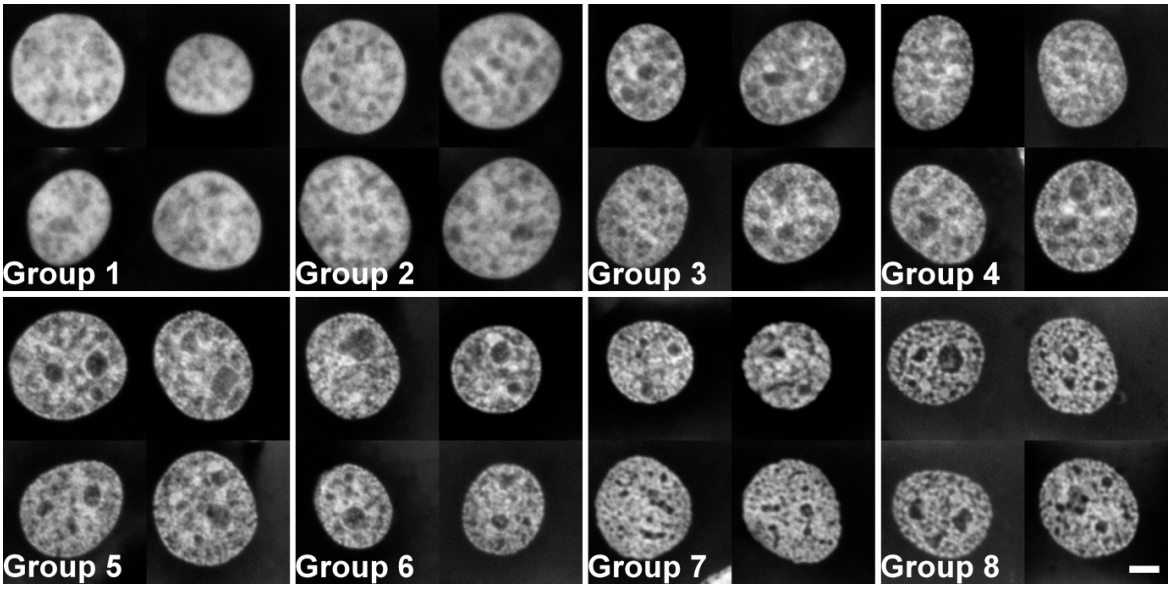

Figure 2.24 Representative images of monolayer chondrocytes nuclei from each bin group (Bar: 5µm).

From Figure 2.25, most of the inspectors ranked group 1, 2 and 8 correctly. Based on the feedbacks from the inspectors, it was more difficult to visually distinguish between group 3 and 4, and also between group 5, 6 and 7. Moreover, overall there was a good agreement between the chromatin condensation parameter quantified and the ranking given by the inspectors.

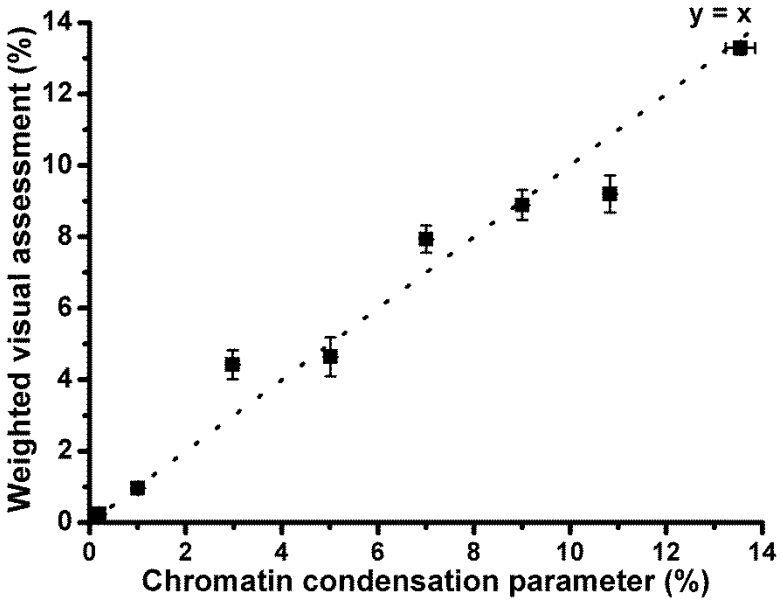

Figure 2.25 The chromatin condensation parameter against the weighted visual assessment values (N = 1, n = 20 inspectors per group) for each bin group, with a dotted line showing a linear relationship y = x. Error bars show standard error.

2.7.4 Automated Measurement of Chromatin Condensation Parameter

MATLAB (MathWorks, Cambridge, UK) incorporating the image processing toolbox was used to apply the Sobel edge detection algorithm to the nuclei images and to determine the edge density of the sample. The image taken by confocal microscopy was loaded into MATLAB, transforming the image into a matrix form where each element represents the intensity of the corresponding pixel. For reference purpose, this image matrix is called the original image matrix.

A threshold value for the original image matrix was calculated by the mode method, which assumes a bimodal histogram. The histogram of the image was iteratively smoothed by applying a 3×3 average filter, until there were only two local maxima. The threshold value is the minimum point between the maxima, such that $y(T) - 1 > y(T) \leq y(T) + 1$. When

an image undergoes a 3×3 average filter, for each target pixel, the intensity for the pixel and its 8 surrounding pixels are averaged, then the intensity value of the pixel is replaced with the average value. In order to get a better outline of the nucleus, the original image matrix was then smoothed six times by applying the 3×3 average filter. The threshold was applied to the original image matrix, producing a binary image showing the pixels that are above the threshold value. A hole filling algorithm was applied to the binary image to exclude the spaces within the nucleus.

At this stage, the pixels showing in the binary image represent the location of the nucleus of interest. By using the pixel location information from the binary image, the nucleus of interest on the original image matrix was extracted and moved into a black background (intensity equal to 0). Afterward, in order to standardise the image, the intensity of the image was redistributed by dividing each pixel intensity by the maximum intensity of the image and multiplied by 255, which is the maximum intensity for 8 bit image. The redistributed image was then reduced as described above. A threshold value for the reduced image was acquired by using the mode method, which was applied to the reduced image, resulting in a binary image showing the pixels that lie above the threshold value. A hole filling algorithm was applied to the binary image to exclude the spaces within the binary image, and the perimeter of the nucleus in the binary image was acquired. In order to reduce the nucleus size by one pixel following the outline of the nucleus, the perimeter image was subtracted from the binary image. The nucleus size was reduced by one pixel again by the same procedure. At this stage, the pixels showing in the binary image represent the location of the inner part of the nucleus. Additionally, summation of the pixels from this binary image gave the area of the nucleus.

The reduced image was standardised by redistributing the intensity as described above. The Sobel edge algorithm was applied to the standardised reduced image. Afterward, the Sobel image produced was thresholded to acquire the strong edges and underwent a thinning morphological algorithm, which transforms an entity within the image into a single pixel thickness entity, as shown in Figure 2.27. The threshold value was kept constant at 0.09 for all the images processed. This value gave the best contrast between the different chromatin condensation levels. By using the pixel location information from the inner part of the nucleus binary image, the processed Sobel image was extracted and moved into a black background. Summation of the pixels from the extracted Sobel image gave the number of

edges within the inner part of the nucleus. Dividing the area of edges by the area of the nucleus, we end up with the edge density, i.e. the chromatin condensation parameter. This MATLAB routine is illustrated as a flow chart, which can be seen at Figure 2.26.

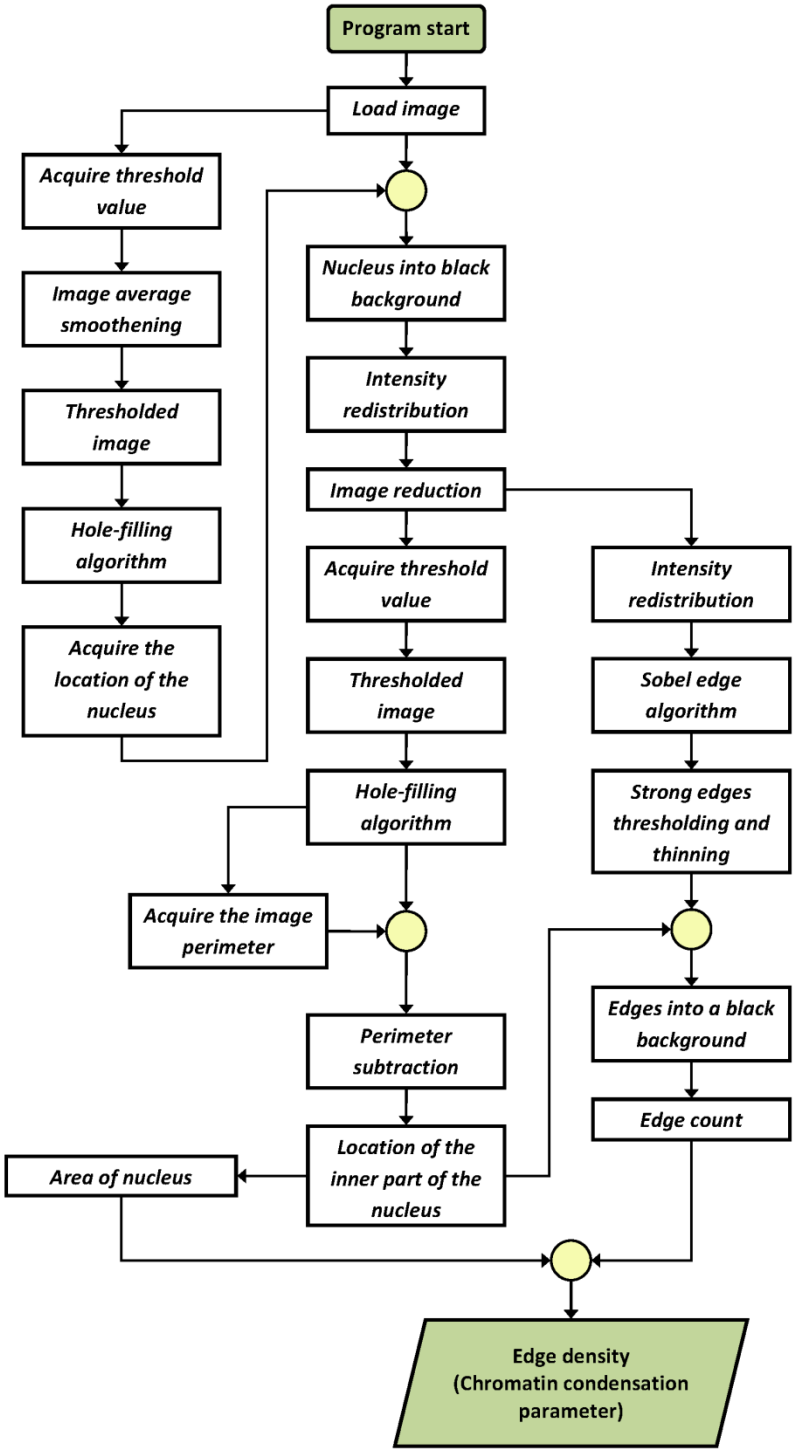

Figure 2.26 The flow chart of MATLAB routine for the quantification of chromatin condensation level.

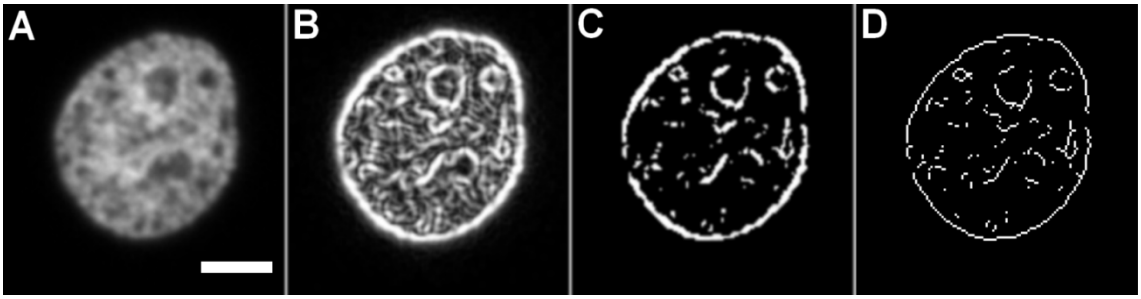

Figure 2.27 The procedure of Sobel image thresholding. A: source image, B: Sobel image, C: after thresholding, D: after thinning morphological operation (Bar: 5 μm).

2.7.5 Automated Measurement of Nucleus Size

The quantification of nucleus size, in both the axial and the lateral plane of imaging, was also achieved with MATLAB. For the measurement of nucleus image taken on the axial plane, the threshold value for the original image matrix was calculated by the mode method. Meanwhile, for the image taken on the lateral plane, the threshold value for the original image was calculated by the iterative self-organising data method. In this thresholding procedure, the image was divided into object and background by choosing a starting threshold. The averages of the intensity of the pixels at or below, and the pixels above the threshold were calculated. The average of these values was then calculated. The threshold was increased and the process was repeated, until the threshold value is larger than the final average. The original image matrix was smoothed six times by running it through a 3×3 average filter, as described before. The threshold value was applied to the smoothed original image, producing a binary image showing the pixels that lie above the threshold value, which is the nucleus, and the hole filling algorithm was applied. At this stage, summation of the binary image gave the cross-section area of the nucleus, and the perimeter of the nucleus and the pixel location of the perimeter were then acquired. The positions of the outermost pixel in horizontal and vertical axis were acquired (Figure 2.28). The difference between the outermost pixels gave the size of the nucleus in horizontal and vertical axis. This MATLAB routine is illustrated as a flow chart in Figure 2.29.

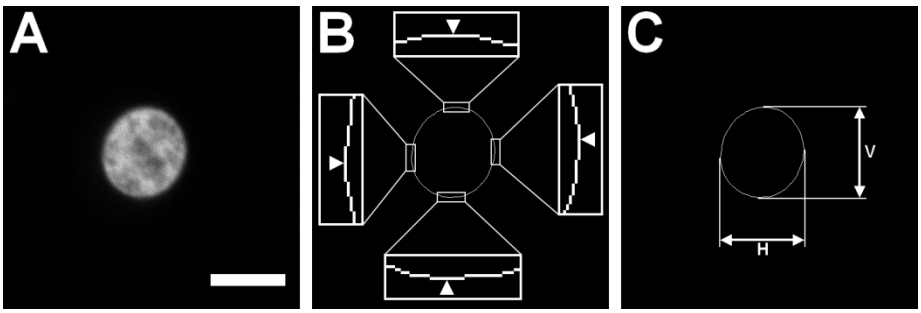

Figure 2.28 Illustration of the horizontal (H) and vertical (V) nucleus size measurement. A: Source image. B: Perimeter image with its outermost pixels (arrow). C: Horizontal and vertical nucleus size (Bar: 5 μm).

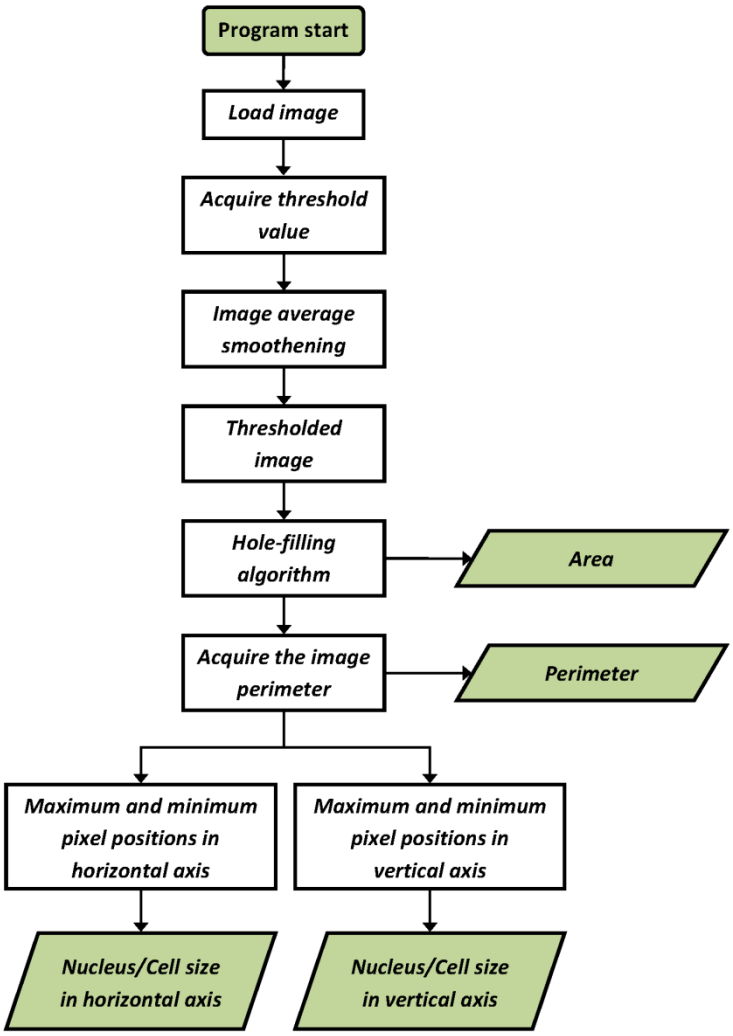

Figure 2.29 The flow chart of MATLAB routine for the quantification of nucleus size.

Chapter 3 The Effects of Osmotic Challenge on Chondrocyte Nuclear Structure

3.1 Introduction

Osmotically-induced alterations of nuclear morphology and chromatin structure may provide a direct biophysical mechanism for controlling cellular metabolism. In this chapter, we test the hypothesis that osmotic challenge influences the morphology and levels of chromatin condensation in the chondrocyte nucleus. Our results show that osmotic challenge significantly alters the morphology and chromatin structure of chondrocyte nuclei. This occurs in a rapid and reversible manner, fitted by a polymer-gel model, suggesting the phenomenon is primarily physicochemical in nature and may be important in cartilage physiology.

3.2 Material and Methods

3.2.1 Monolayer Specimen Preparation

For monolayer specimens, 8×10^6 freshly isolated chondrocytes were seeded into 175 cm^2 culture flasks and cultured for 5 days. For imaging of fixed chondrocytes, the cells were trypsinised and seeded at 5×10^4 cells/cm^2 onto Ø13 mm coverslips (thickness of 0.17 mm, VWR, Lutterworth, UK), housed in 24 well plates. Alternatively, for imaging of live chondrocytes, cells were seeded onto 35 mm glass bottom petri dishes (MatTek) with the same seeding density. In both cases, the chondrocytes were cultured overnight to allow the cells to adhere. Both the coverslips and the glass bottom petri dishes were pre-coated with FCS for 1 hour at room temperature prior to cell seeding.

3.2.2 Preparation of Chondrocyte-Agarose Constructs Incorporated with Porous Glass Endplates

Prior to the agarose-cell solution preparation, a Perspex mould (Figure 3.2) was immersed in 70% ethanol for 1 hour and porous glass ends (5 × 5 × 4 mm) were autoclaved. 10 mL of 3% agarose containing 10×10^6 cells/mL was prepared as described in section 2.2.8. The mould was assembled and the porous glass ends were placed into the mould (Figure 3.1, stages 1-3). The agarose-cell solution was then pipetted into the mould and a Perspex top-plate was carefully slid onto the mould, preventing any bubble formation, and secured by masking tape (Figure 3.1, stages 4-6). The mould was placed into a 4^oC fridge for 20 minutes. The mould was dissembled, releasing identical rectangular constructs (5 × 5 × 5

mm) with a porous glass end plate attached at each end. The agarose-porous glass constructs were placed into a 50 mm Petri dish filled with DMEM + 16.1% FCS; ensuring that the constructs were fully immersed in the medium. The constructs were cultured overnight at 37˚C/5% CO_2.

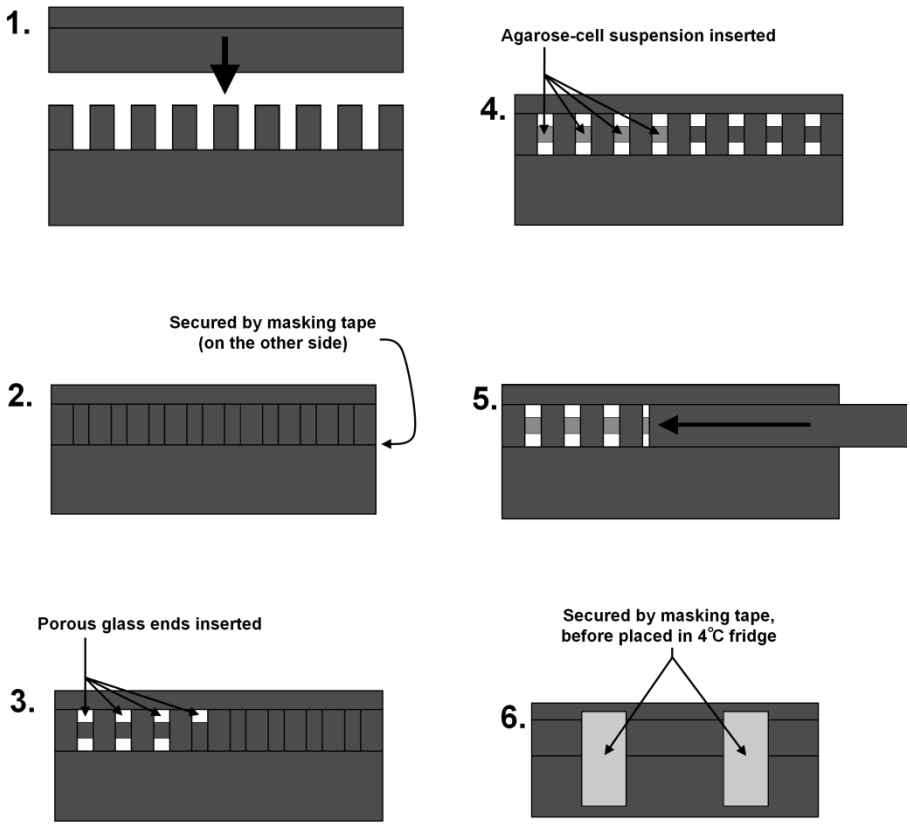

Figure 3.1 Illustration of the preparation of the porous glass-agarose constructs.

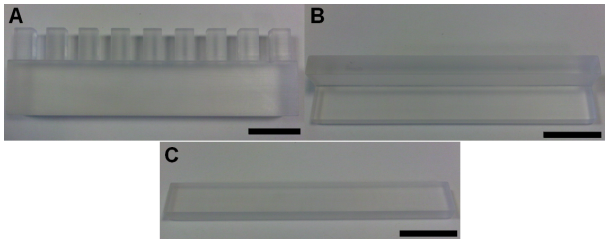

Figure 3.2 The porous glass-agarose constructs mould components, made out of Perspex (Bar: 2 cm).

3.2.3 Osmotic Challenge

Cells in monolayer were subjected to osmotic challenge by incubation in the requisite osmotic challenge medium for 15 min to allow for chromatin reorganisation (Albiez *et al.* 2006). Cells in the 3D agarose specimens were given a longer incubation period of 30 min.

For fixation, chondrocytes were washed with PBS and then fixed by incubation in 1% glutaraldehyde (Agar Scientific, Stansted, UK) buffered with 8 mM sodium cacodylate (Sigma-Aldrich) for 30 min. The fixative solution and PBS initially have osmolalities of approximately 120 mOsm/kg and 300 mOsm/kg, respectively. The osmolality of the fixative solution and PBS were adjusted in the same manner as for the osmotic challenge medium (section 2.2.10), corresponding to the prior osmotic challenge applied to the specimen. The fixed cells were subsequently washed with PBS and stained with 8 μM Hoechst 33342 (Sigma-Aldrich) at 37°C for 15 minutes or 30 minutes for monolayer or 3D agarose specimens respectively. Afterwards, the specimens were washed with sterile distilled water and mounted onto glass slides using Prolong Gold (Invitrogen).

Live chondrocytes were stained with 8 μM Hoechst 33342 as described above. The cells were incubated in iso-osmotic medium (300 mOsm/kg) in a 37°C imaging chamber mounted on the stage of the confocal microscope system. Osmotic challenge was applied by replacing the media.

3.2.4 Confocal Microscopy

High resolution images bisecting the centre of the chondrocyte nuclei were taken by confocal microscopy, using a 63×/1.4NA oil immersion objective, a pixel size of 46.5 × 46.5 nm and an imaging period of 7.68 s/image. The images were taken at a frequency of 400 Hz, meaning that it took 1/400 second to complete a line scan through the image. Thus, it took 7.68 seconds to acquire a single 512 × 512 pixels (8-bit) optical section through the centre of each nucleus, which is constructed from 2 lines and 3 frames averaging. For studies with live cells, each nucleus was imaged at 300 mOsm/kg and following a 15 min or 30 min osmotic challenge for monolayer or 3D agarose specimens respectively. For all live specimens, the imaging period before and after the osmotic challenge was limited to 30 minutes.

To measure the response to osmotic challenge in the *Z* axis, the nuclei were imaged as a Z-series of 32 × 512 pixels images, with a step size of 0.46 μm (0.08 s/image). These images

were acquired at the same resolution and frequency (pixel size 46.5 × 46.5 nm and 400 Hz), however, each *Z*-slice was made from only 1 line and 1 frame scan, thus it took 0.08 second to acquire an image. The *Z*-stacks images were average-intensity projected to the *X*-*Z* plane for the nucleus height measurement.

3.2.5 Image Analysis

The chromatin condensation parameter, cross-section area, perimeter and height in the lateral plane (*Z*-axis) of each nucleus was measured as described in sections 2.7.4 and 2.7.5. The nuclear perimeter was fitted to an ellipse, to acquire the ellipsoid perimeter. To estimate the degree of nuclear deformation with osmotic loading, the perimeter ratio was calculated by dividing the actual nuclear perimeter by the ellipsoid perimeter (Mulchrone and Choudhury 2004). When the perimeter ratio increases, the perimeter of the nucleus increases with respect to that of the modelled ellipse, indicating a more deformed outline.

For the 3D agarose specimen, the diameter of the cell in *X* and *Y* axes were measured from the bright field images using ImageJ (Abramoff *et al.* 2004). These diameters were averaged and divided by 2 to get the approximated cellular radius, whilst the approximated nuclear radius was derived from the nuclear cross-section area. Cell and nuclear volume was then approximated by assuming that the chondrocytes seeded in 3D agarose construct adopted a spherical morphology as previously demonstrated (Lee *et al.* 2000).

The changes in chromatin condensation parameter, area, perimeter ratio, nuclear height in the lateral plane, nuclear and cell volume due to the osmotic challenge were recorded and expressed relative to their original value.

3.2.6 Van der Waals Model of Cell Volume Change

Using a standard van der Waals equation that lacks the attraction term, osmotic pressure (Π) relates to cell volume (V) as:

$$\Pi = \frac{RT}{V - b} \qquad (3.1)$$

Where R is the gas constant, T is absolute temperature and b is the excluded volume.

Based on Equation 3.1, the change in cell volume (ΔV) with osmotic pressure changes ($\Delta\Pi$) was fitted with three fit-parameters (A, B and C) to experiment with:

$$\Delta V = \frac{A}{\Delta \Pi + C} + B \qquad (3.2)$$

3.2.7 Polymer-Gel Model of Chromatin Condensation

The extent of local chromatin heterogeneity was determined using the chromatin condensation parameter, which reflects the edge density (ρ) in the nucleus image. In modelling this, we first consider the osmotic pressure of a polymer solution. In the semi-dilute regime where the volume occupied by the individual chains just covers the total sample volume, the osmotic pressure of a polymer solution (Π) is dependent only on monomer concentration, c_m (Strobl 1996):

$$\frac{\Pi}{k_b T} \propto {c_m}^{9/4} \qquad (3.3)$$

Where k_b is the Boltzmann constant and T is the absolute temperature.

Treating a polymer as a chain of monomer subunits, the polymer concentration (c_p) which we approximate as proportional to the chromatin condensation parameter (ρ), relates to the monomer concentration by the degree of polymerisation, N:

$$N\, c_p = c_m \qquad (3.4)$$

$$\rho \propto c_p \qquad (3.5)$$

Confinement within the nucleus adds a 'basal' osmotic pressure, Π_b:

$$\Pi = \Pi_b + B\, \rho^{9/4} \qquad (3.6)$$

$$B \propto k_b\, T\, N^{9/4} \qquad (3.7)$$

In addition, chromatin entanglements and cross-linking lead to a resistance to dilational stretching (as well as shearing) of the chromatin. Modifying the semi-dilute polymer equation with a term compensating for elastic deformation of the polymer, $\frac{C}{\rho^d}$:

$$\Pi = \Pi_b + B\, \rho^{9/4} - \frac{C}{\rho^d} \qquad (3.8)$$

This last term could be justifiably replaced by a sum of terms with d = 1, 2, 3 as is appropriate for wormlike chain elasticity, but this will generally introduce more fitting factors. We therefore use the parsimonious model above in fitting the data of chromatin

condensation parameter versus osmolality, with four fit-parameters (Π_b, B, C and d) to experiment with.

Curve fitting in Figure 3.5 and 3.11 D were performed with Igor Pro (version 6.22A, WaveMetrics, Portland, OR, USA), using the chromatin condensation parameter data binned in pairs within the osmolality range of reversible nuclear deformation and the cell volume data, respectively. Both van der Waals and polymer-gel models were developed as part of collaboration work with Prof. Dennis Discher and Dr. Joe Swift from the Biophysical Engineering Laboratory, School of Engineering and Applied Science, University of Pennsylvania, Philadelphia, PA, USA.

3.2.8 Transmission Electron Microscopy

For transmission electron microscopy (TEM) imaging, cylindrical 5 mm diameter × 5 mm height chondrocyte-seeded 3% agarose constructs with 10 x 10^6 cells/mL were prepared. Monolayer cultured and 3D agarose-seeded chondrocytes underwent osmotic challenge as described above. The monolayer specimens were fixed as described above while the 3D agarose specimens were fixed overnight at 4°C. The specimens were post-fixed in 1% osmium tetroxide, dehydrated through a graded alcohol series, cleared in propylene oxide and infiltrated with Araldite epoxy resin (all from Sigma-Aldrich). Ultrathin sections (60-90 nm) were cut using a Reichert-Jung Ultracut E Ultramicrotome (Reichert, Buffalo, NY, USA) with a diamond knife. The sections were mounted on copper grids before being stained with saturated aqueous uranyl acetate and Reynolds lead citrate stain (all from Sigma-Aldrich). Sections were examined with a Philips EM201 TEM (Philips, Amsterdam, Netherlands) fitted with a digital camera (AMT, Woburn, MA, USA). The preparation of TEM specimens from the post-fixation stage onward was performed by Mr. Graham D. McPhail from Division of Cellular Pathology, Barts and the London NHS Trust, Royal London Hospital, London, UK.

3.2.9 Real-Time Deoxyribonuclease I PicoGreen Assay

Approximately 10^8 freshly isolated chondrocytes were centrifuged at 600 × g for 5 min and resupended in 5 mL of PBS. The cells were centrifuged again and resuspended in 5 mL of iso-osmotic medium. The cells were treated with 0.2% IGEPAL CA-630 (Sigma-Aldrich) for 5 minutes on ice, to isolate the nuclei. The nuclei were pelleted by centrifugation as

above and resuspended in 14 mL iso-osmotic medium. The nucleus suspension was then separated into 3 equal volumes of 4 mL, for osmotic challenge.

The osmotic challenge procedure in this part of the study was different to that described previously. In order to avoid centrifugation of the specimen before the osmotic challenge, instead of replacing the existing medium, the osmotic challenge medium was added to the iso-osmotic medium to produce the required osmotic condition, while maintaining a constant volume between the osmotic groups. First, for hypo-osmotic challenge, 7 mL dH_2O was added to the sample, producing an osmolality of 100 mOsm/kg. For the iso-osmotic control, 7 mL of iso-osmotic medium was added. For hyper-osmotic challenge, 7 mL of hyper-osmotic challenge medium, with an osmolality of 929 mOsm/kg, was added, creating a solution with an osmolality of 700 mOsm/kg.

Osmotic challenge was applied to the isolated nuclei for 15 minutes. The nuclei were then centrifuged and resuspended in the corresponding osmotically balanced Deoxyribonuclease I (DNase I) buffer (50 mM HEPES, 10 mM NaCl, 10 mM $CaCl_2$, 5 mM MgOAc, 1 mM Dithiothreitol, pH 7.4, all from Sigma-Aldrich). The nuclei were stained by using the Quan-iT PicoGreen reagent (Invitrogen, Paisley, UK), per manufacturer's instructions. Briefly, a 200-fold dilution of the PicoGreen concentrate was prepared in the osmotically balanced DNase I buffer and the nuclei were stained for 5 minutes at room temperature. The nuclei from each osmotic group were placed into a NUNC Maxisorp 96 wells plate (NUNC, Roskilde, Denmark) with 100 μL per well. DNase I was added to yield a concentration of 2 U/million nuclei. The level of fluorescence intensity from the nuclei was monitored over a 180 minutes period at 37^{o}C. The fluorescence readings were corrected for the level of photo-bleaching from the specimens without DNase I and the background reading from the blank control, and were normalised to the first reading at time 0. To control for changes in DNase I activity due to different osmolality, 3.5 μg λ-DNA (Sigma-Aldrich) was digested by 1 U of DNase I, at different osmotic conditions (100, 300, and 700 mOsm/kg).

3.2.10 H2B-GFP Transfection

Monolayer specimens were prepared as described above in Section 3.2.4. Chondrocytes were transfected based on the procedure described in Section 2.6. In detail, 5 μL of 0.6 μg/μL H2B-GFP-pDNA was mixed into 620 μL DMEM to produce 625 μL DNA solution. 125 μL HiFect transfection reagent was added to 500 μL DMEM to produce 625 μL

reagent solution. The DNA solution was then added to the reagent solution, producing 1250 μL transfection solution. The transfection solution was mixed and left at room temperature for 5 minutes. The culture medium was aspirated from the monolayer specimen and replaced with 1250 μL DMEM + 40% FCS and the transfection solution was introduced to the specimen. Transfection was carried out under standard culture conditions for 24 hours whereupon the medium was replaced with 3 mL of fresh DMEM + 16.1% FCS, with incubation for an additional 24 hours to allow cell division.

3.2.11 Microscope Mounted Medium Delivery System

In order to achieve a rapid and controlled delivery time for osmotic challenge medium (approximately 7 seconds at a delivery rate of 1 mL/s for 7 mL medium), a delivery system was developed (Figure 3.3). The medium delivery system consists of two main components: a metal bracket to house the 35 mm petri dish and two syringe pumps to deliver and aspirate the medium. The bracket was manufactured in-house, from stainless steel to allow autoclave sterilisation. One part of the bracket is a round metal plate where the petri dish sits, which also can be mounted onto the confocal microscope stage. The second part is another metal plate, which sits on top of the petri dish that will clamp the dish and the needles in place. The syringe pump system consists of two syringe pumps (PHD 2000, Harvard Apparatus, Kent, UK) each with a sterile 30 mL syringe (BD, Oxford, UK) attached, connected via autoclaveable silicone tubing (ID 1.6 mm, OD 3.175 mm, Cole-Palmer, Vernon Hills, IL, USA) to a sterile 18G blunt needle (BD).

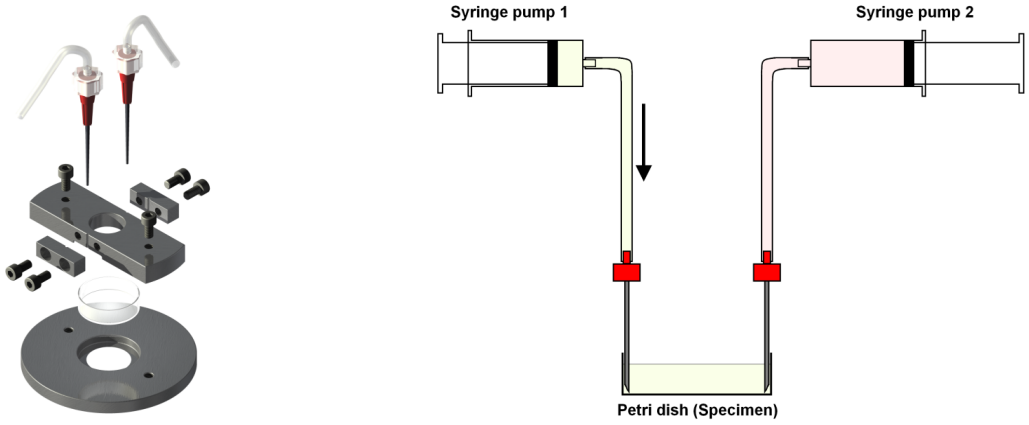

Figure 3.3 Schematic drawing of the medium delivery system: the metal bracket (left) and the syringe pump system (right).

3.2.12 Chromatin Condensation Dynamics in Living Chondrocytes

The culture medium of the H2B-GFP transfected specimen was aspirated and the specimen was mounted into the delivery system, and placed into the 37°C imaging chamber. Iso-osmotic medium was introduced via the delivery system and the cells were incubated for 15 minutes. Using confocal microscopy (63×/1.4NA objective, pixel size 46.5 × 46.5 nm, ΔZ = 0.23 μm, 0.407 s/image), an extended *Z*-stack of images was taken of each nucleus. The imaging frequency was 800 Hz, with bi-directional scanning and without line or frame averaging. Each 512 × 512 pixels *Z*-slice took 0.407 second to complete. The iso-osmotic medium was aspirated and replaced with the requisite osmotic challenge medium, and the same nucleus was imaged continuously via a series of extended *Z*-stacks over a 15 minutes period. Following the osmotic challenge, the medium was aspirated and iso-osmotic medium was reintroduced with further imaging for another 15 minutes period. The chromatin condensation parameter was determined from the *XY* average projection images and the nucleus height was also measured, both using the procedure as described in sections 2.7.4 and 2.7.5.

3.3 Results

3.3.1 Osmotic Changes Alter Chromatin Condensation in Monolayer and 3D Agarose Cultures, Fitting to a Polymer-Gel Model

To assess the effect of different osmolalities on the chondrocyte nucleus, monolayer cultured cells were exposed to media ranging from 100 to 800 mOsm/kg, fixed, stained with Hoechst 33342, and imaged by confocal microscopy (Figure 3.4 A). DNA staining appeared most homogenous in the nuclei exposed to 100 mOsm/kg, reflected by the lowest level of the chromatin condensation parameter (Figure 3.4 B). A dramatic increase in chromatin condensation was apparent between 400 and 500 mOsm/kg, followed by a more gradual increase (Figure 3.4 B).

A polymer-gel model of the relationship between osmolality and chromatin condensation gave an excellent fit to the experimental data ($R^2 > 0.98$, Figure 3.5). Interestingly, the basal osmotic pressure of around 400 mOsm/kg that is applied by the chromatin and the nuclear envelope is close to isotonic. The B and C factors are positive and reasonably small, where the stretching exponent d is understandably nonlinear. The inset shows the first derivative of ρ, with respect to Π, where the steepest chromatin response to osmotic challenge occurred within the range of osmolalities found in articular cartilage *in vivo* (Urban 1994).

The osmotically-induced chromatin condensation observed in fixed cells was confirmed in live-imaged cells (Figure 3.6 and 3.7). Cells in both monolayer and 3D agarose specimens showed reduced level of chromatin condensation with hypoosmotic challenge (300 to 100 mOsm/kg). Meanwhile, the hyperosmotic challenge (300 to 500 or 700 mOsm/kg) increased the level of chromatin condensation. However, the monolayer specimens experienced a higher degree of change when compared with the 3D agarose specimens (Figure 3.8).

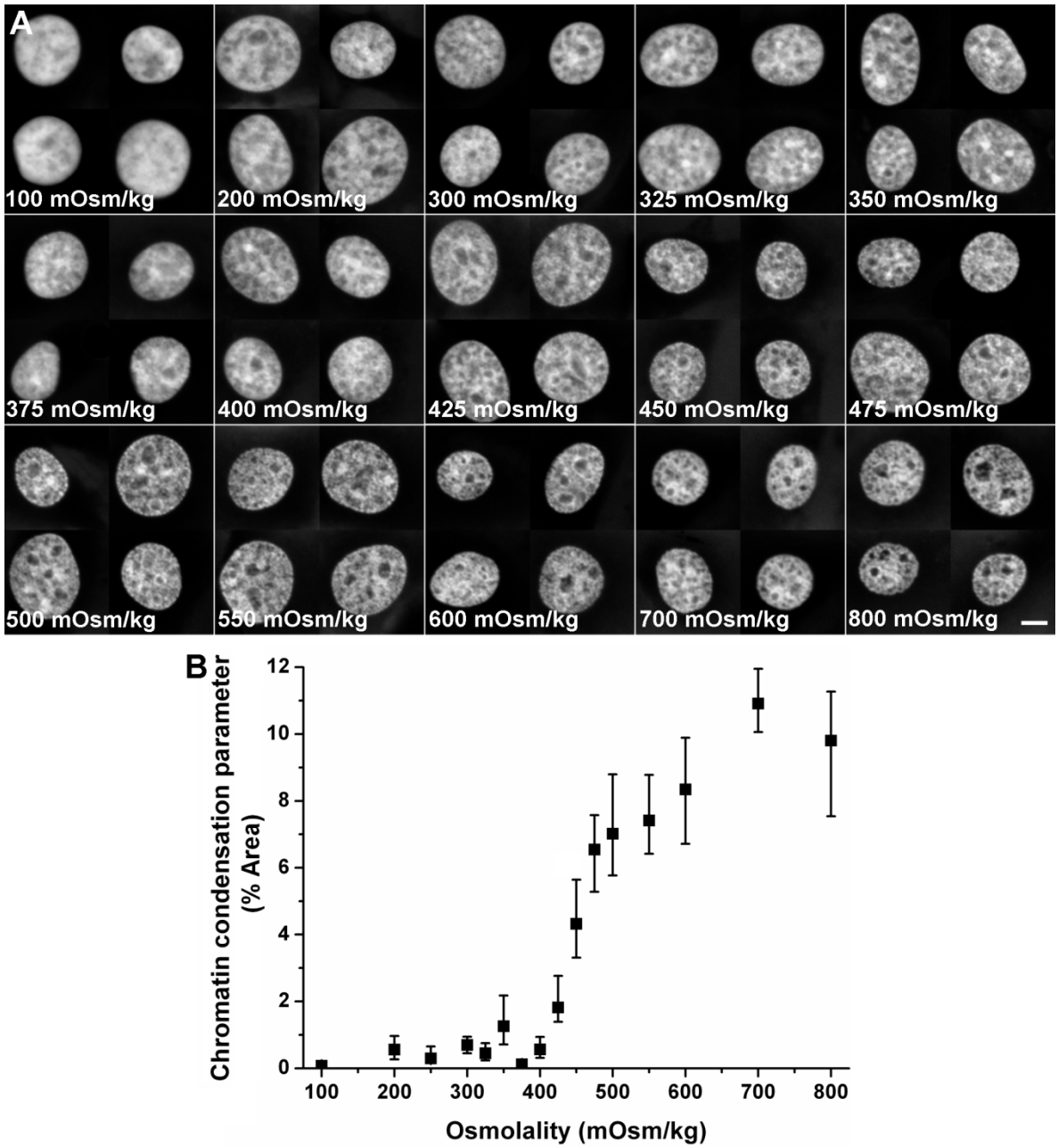

Figure 3.4 A: Images of the nuclei of monolayer chondrocytes fixed following culture in media with osmolalities ranging from 100 mOsm/kg to 800 mOsm/kg for 15 minutes (Bar: 5 μm). B: Chromatin condensation parameter quantified from the nuclei images of each osmotic group ($N = 1$, $n = 40$ nuclei per condition). Error bars show lower and upper quartile.

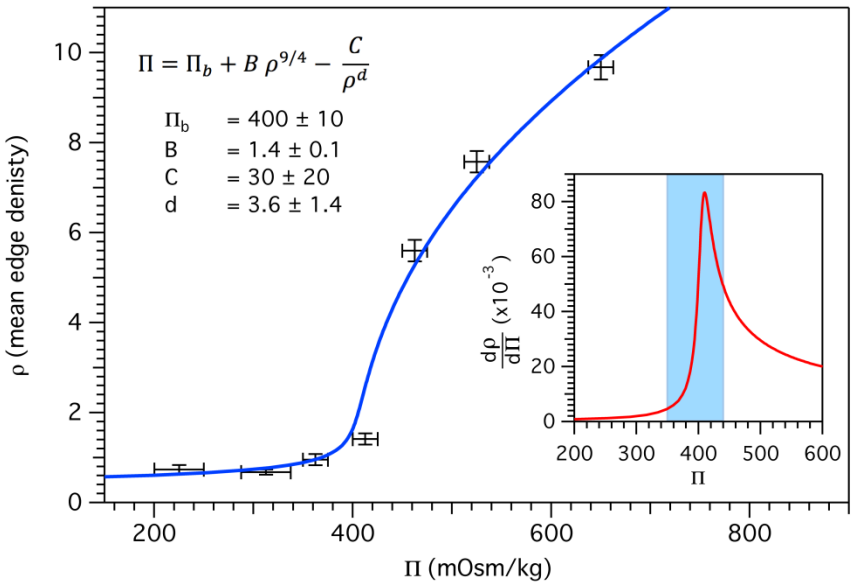

Figure 3.5 Quantified chromatin condensation parameter fit to a semi-dilute polymer-gel model with an additional term compensating for chain elasticity (see section 3.2.6). Data are binned within the osmolality range of reversible density changes. Error bars in ρ show standard error (N = 1, n = 80 nuclei per condition). The inset is calculated from the model and shows the large change in density ($\frac{d\rho}{d\Pi}$) observed within the range of osmolalities associated with *in vivo* articular cartilage (Urban 1994).

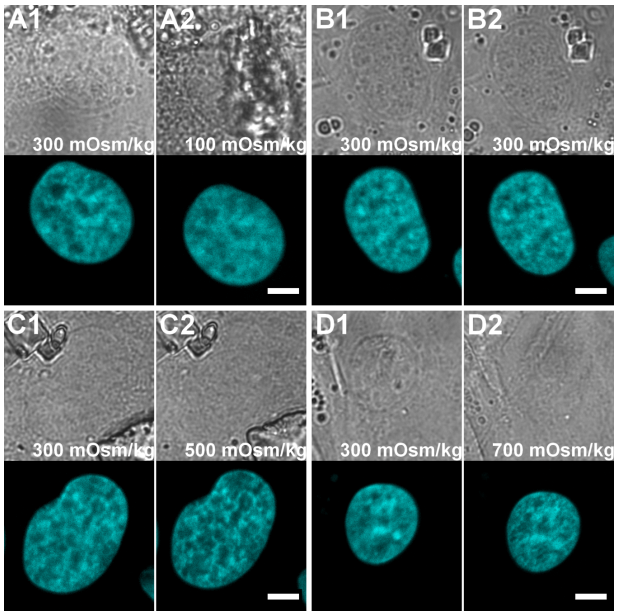

Figure 3.6 Pair bright field images of monolayer cultured chondrocytes and their nucleus confocal image in an iso-osmotic environment of 300 mOsm/kg (A1-D1), followed by 100 (A2), 300 (B2), 500 (C2) and 700 (D2) mOsm/kg osmotic challenge (Bar: 5μm).

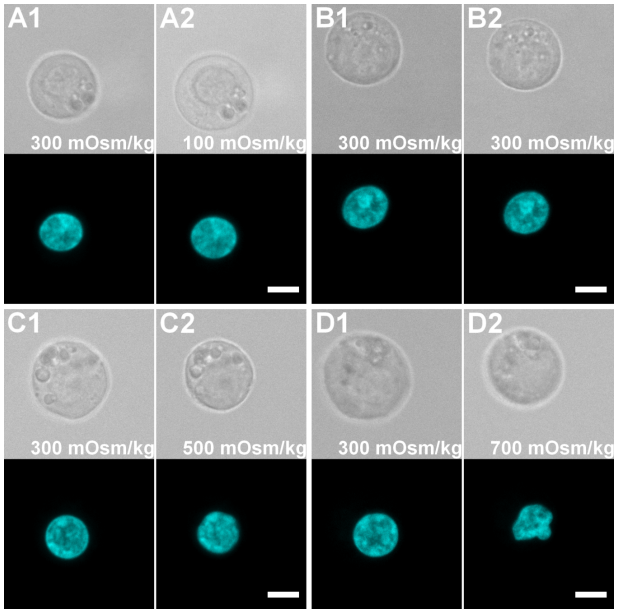

Figure 3.7 Pair bright field images of agarose-seeded chondrocytes and their nucleus confocal image in an iso-osmotic environment of 300 mOsm/kg (A1-D1), followed by 100 (A2), 300 (B2), 500 (C2) and 700 (D2) mOsm/kg osmotic challenge (Bar: 5μm).

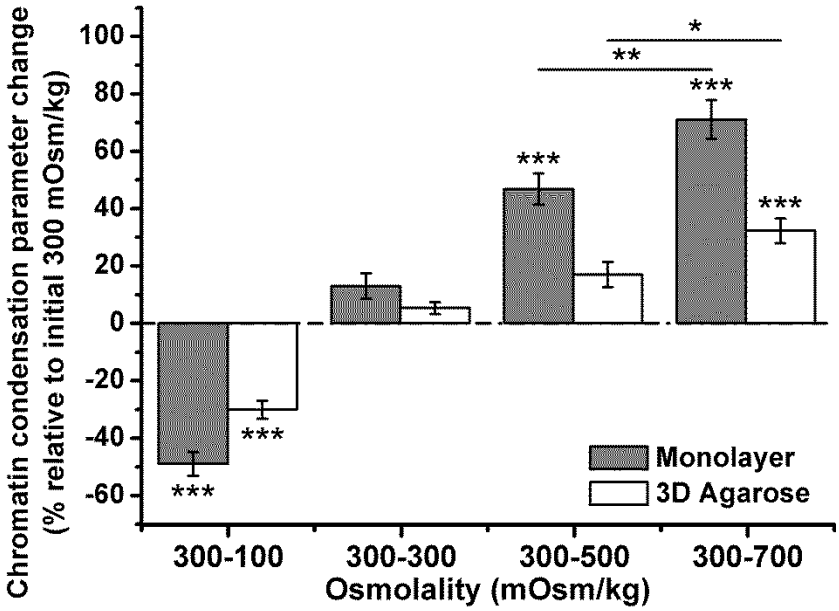

Figure 3.8 The normalised change of chromatin condensation parameter quantified from the live monolayer and agarose-seeded specimen. Statistical significance test was performed to compare the osmotic challenge groups against the control group (300-300 mOsm/kg) and also between the 500 and 700 mOsm/kg group (N = 1, n = 37-40 nuclei per condition) (*p<0.05, **p<0.01 and ***p<0.001). Error bars show standard error.

The effects of osmotic challenge on the chromatin organisation were confirmed by the TEM images of the nuclei (Figure 3.9). Upon the hypo-osmotic challenge, in addition to the loss of peripheral heterochromatin, the chromatin appeared more homogenous with few electron-dense foci, indicating a comparatively decondensed state of chromatin organization. When exposed to hyper-osmotic challenge however, chromatin condensation was observed in electron-dense foci throughout the nuclei in both monolayer and 3D agarose specimens. The TEM images of chondrocytes in agarose also suggest a change in cell volume (Figure 3.10). Upon the hypo-osmotic challenge, agarose with a higher density structure can be observed around the cells, suggesting a compression on the agarose due to the cell swelling. In hyper-osmotic environment, a gap between the cell and the agarose suggests that the cell was shrinking.

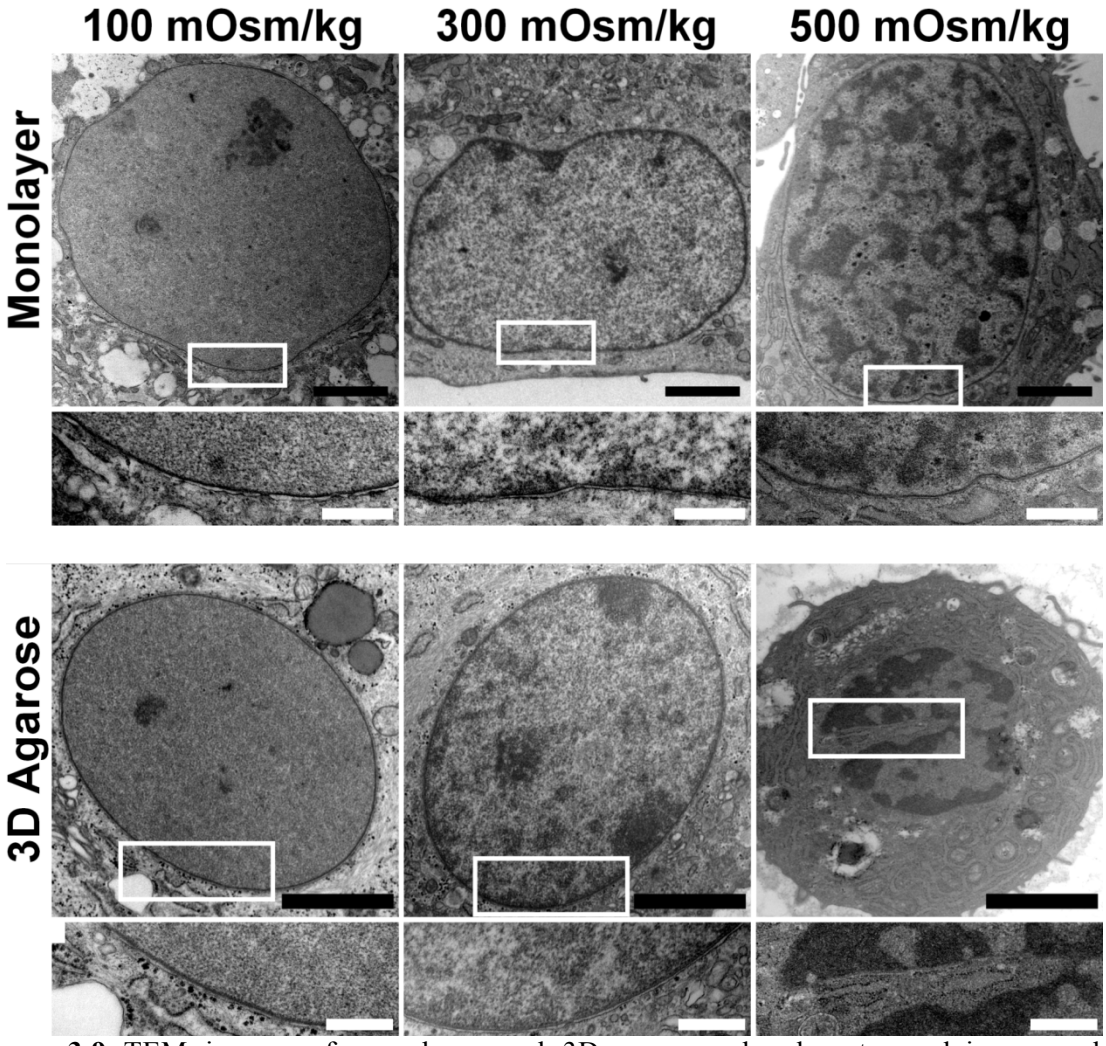

Figure 3.9 TEM images of monolayer and 3D agarose chondrocyte nuclei, exposed to osmolalities of 100, 300, and 500 mOsm/kg (Black bar: 2 μm, white bar: 0.5 μm).

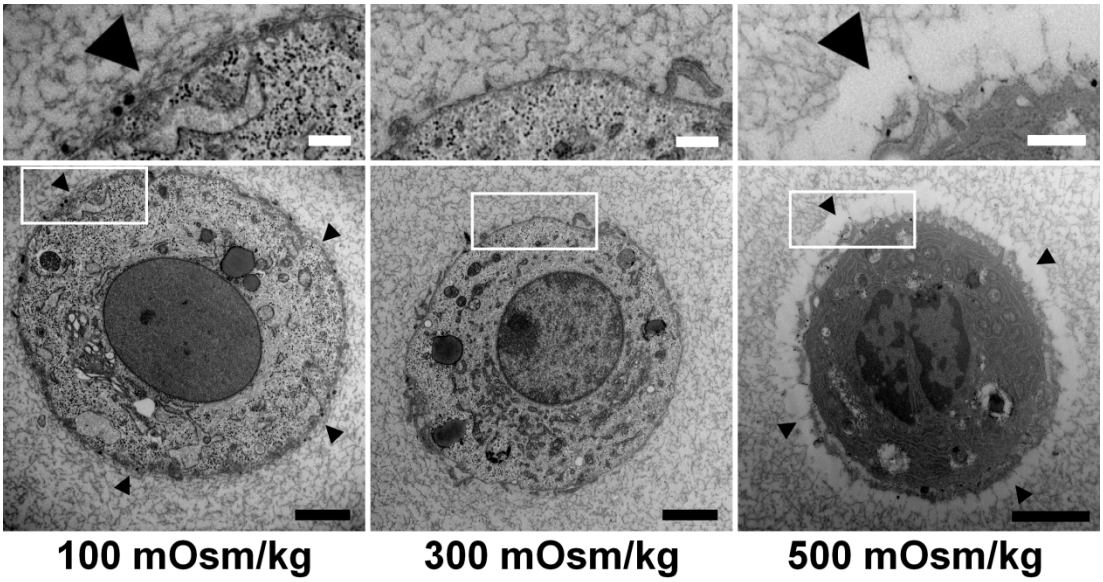

Figure 3.10 TEM images of the 3D agarose chondrocytes, exposed to 100, 300 and 500 mOsm/kg osmotic environment. Arrows showing the compressed agarose structure due to cell swelling in hypo-osmotic environment and the shrinking of cell in hyper-osmotic environment (Black bar: 2 μm, white bar: 0.5 μm).

3.3.2 Cell and Nuclear Morphology Responses to Osmotic Changes Vary with Cell Adhesion

Hyper-osmotic challenge in 3D agarose specimens induced a crumpling of the nuclear envelope, indicated by a statistically significant increase in the perimeter ratio of the nucleus (Figure 3.11 A). This was associated with a decrease in the cross-sectional area of the nucleus (Figure 3.11 B). Both effects were more pronounced at 700 mOsm/kg compared to 500 mOsm/kg, the differences being statistically significant. By contrast, in monolayer, the perimeter ratio and the cross-section area of the nuclei remained relatively stable irrespective of osmotic challenge. However, following hypo-osmotic challenge, there was a significant increase in perimeter ratio and a slight reduction in cross-section area.

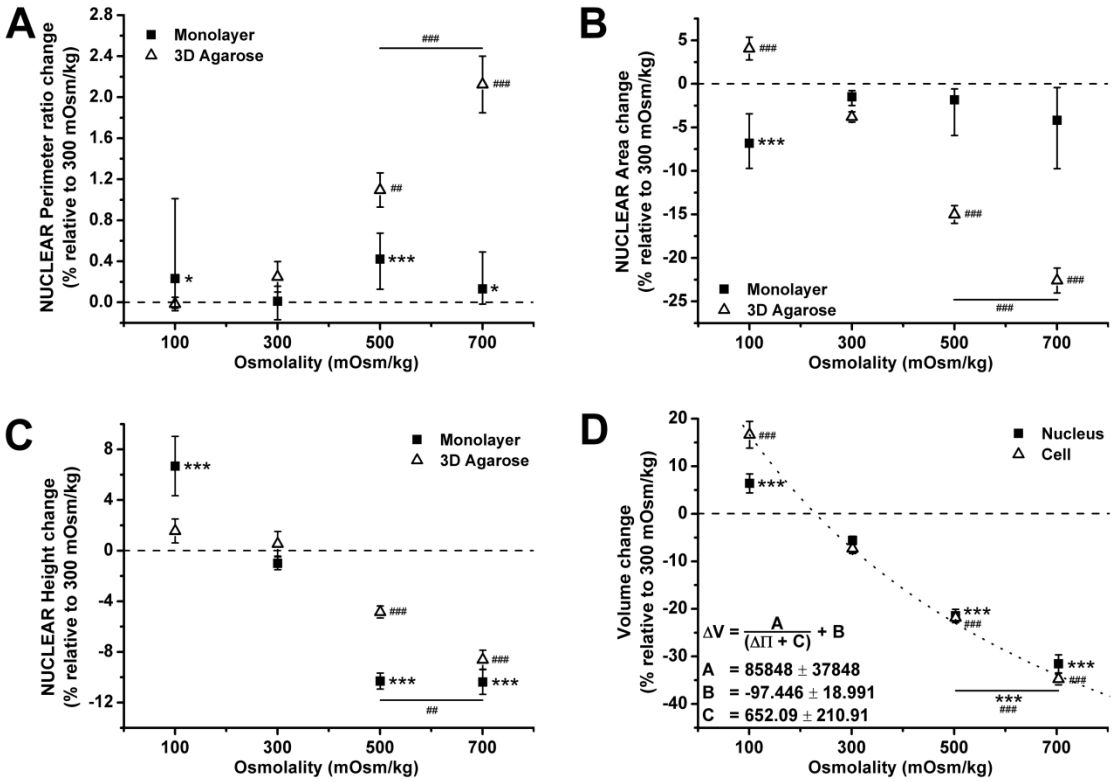

Figure 3.11 The normalised change of (A) perimeter ratio, (B) nuclear cross-section area and (C) height quantified from the live monolayer and 3D agarose specimens. (D) The normalised change of nuclear and cellular volume quantified from the 3D agarose-seeded chondrocytes. The dotted line indicates change in cellular volume fitted to Equation 3.2, the van der Waals equation with no attraction ($R^2 > 0.998$). Statistical significance test was performed to compare the osmotic challenge groups against the control group (300-300 mOsm/kg) and also between the 500 and 700 mOsm/kg group. ($N = 1$, $n = 16$-40 nuclei per condition) (*p<0.05, **,$^{\#\#}p$<0.01 and ***,$^{\#\#\#}p$<0.001, where * for monolayer and $^{\#}$ for 3D agarose). Error bars show standard error, except for perimeter ratio and area data of monolayer specimens, where the error bars show lower and upper quartile.

When chondrocytes in monolayer were exposed to hypo-osmotic challenge (100 mOsm/kg), there was a statistically significant increase in the nuclear height, by approximately 10% (p<0.01, Figure 3.11 C). Upon hyper-osmotic challenge, the height of the nucleus decreased by approximately 10% at both 500 mOsm/kg and 700 mOsm/kg (p<0.001). By contrast, nuclear height in 3D agarose was not affected by hypo-osmotic conditions (p>0.05), but exposure to hyper-osmotic medium induced a reduction in nuclear height of 5% at 500 mOsm/kg and 9% at 700 mOsm/kg, the difference being statistically significant. Additionally, the cell and nuclear volume of the 3D agarose specimen increased upon hypo-osmotic challenge and decreased gradually during hyper-osmotic challenge (Figure 3.11 D). When exposed to iso- and hyper-osmotic challenge, the changes

in cell and nuclear volume were proportional to each other. However, when compared to the change in nuclear volume, a greater change in cell volume occurred upon hypo-osmotic challenge. The 3-parameter van der Waals equation (Equation 3.2) provided an excellent fit for the change in cell volume ($R^2 > 0.998$). With increased osmolality, cell volume decreased until a minimum was reached. Based on the fit, two to three fold higher pressure than the maximum osmotic challenge (700 mOsm/kg) is needed to convincingly see saturation, but such osmolalities are far from physiological. At low osmotic pressure, the cell expanded and contracted over time, potentially due to dynamic volume regulation (Bush and Hall 2001). This might account for the higher variability (shown by the error bar), and so this limit is likely to be underestimated and inaccurate.

3.3.3 Real Time PicoGreen Deoxyribonuclease I Assay

Our results have shown that osmotic challenge alters chromatin condensation level in intact chondrocytes. To confirm that osmotic challenge continues to alter the level of chromatin condensation in the absence of the plasma membrane and cytoplasm, we used a real time DNase I assay (Tolun and Myers 2003) on isolated chondrocyte nuclei. DNase I is an endonuclease that preferentially cleaves the phosphodiester backbone of DNA adjacent to pyrimidine bases. Higher levels of chromatin condensation hinder access of the enzyme to the DNA backbone, thus compacted or condensed regions will be more resistant to DNase I digestion (Martins *et al.* 2007).

Under all osmotic conditions, the fluorescence intensity of the isolated nuclei decreased over time (Figure 3.12 A), showing the digestion of DNA by DNase I. The DNA digestion for the isolated nuclei was markedly less rapid than for the λ-DNA controls (Figure 3.12 B). A single exponential model provided an excellent fit to the results in all cases ($R^2 > 0.98$). Statistically significant differences in DNA digestion were apparent between the osmotic groups ($p<0.05$) from 40 min onward (Figure 3.12 A). The nuclei exposed to 100 mOsm/kg having the highest level of digestion and 700 mOsm/kg the lowest digestion. This is indicative of differences in DNase I access, such that, an increase in osmolality hinders DNase I access to DNA in isolated nuclei. These findings are therefore consistent with microscopy based assessment of chromatin condensation.

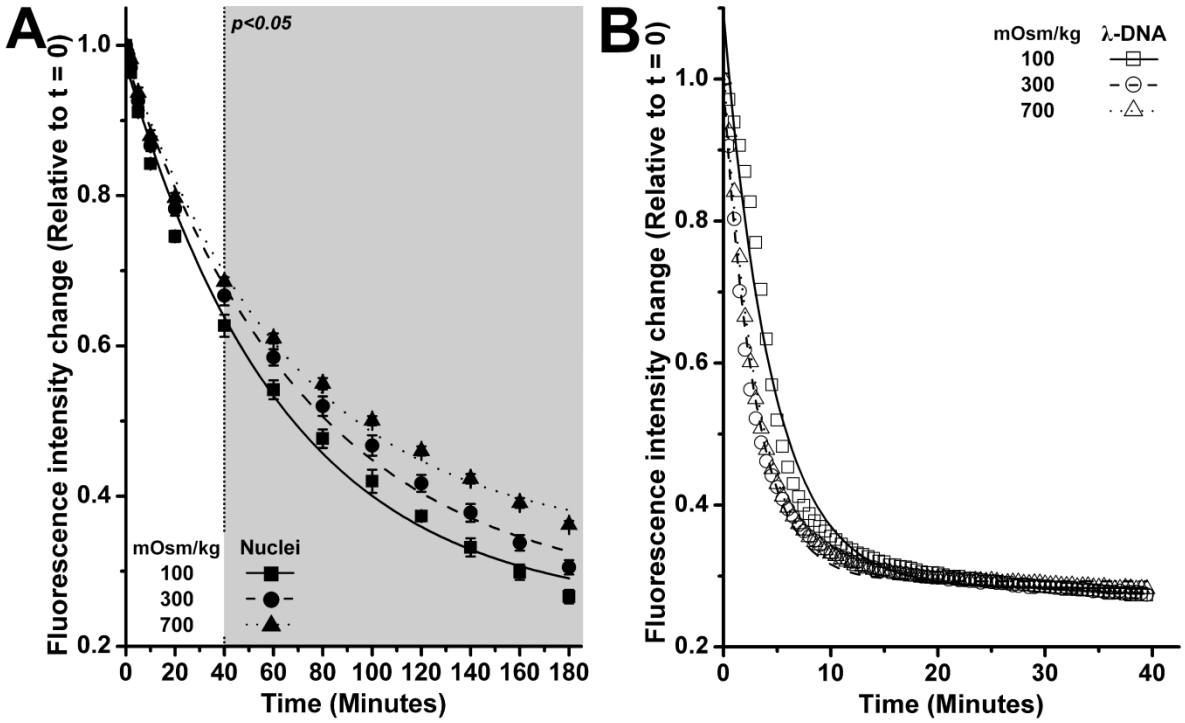

Figure 3.12 The amount of DNA present in the specimen was represented by the PicoGreen fluorescence intensity. Fluorescence intensities were normalized against the initial intensity and fitted to a single exponential function ($R^2 > 0.98$ in all cases). A: Temporal changes in the level of fluorescence intensity from the isolated nuclei exposed to 100, 300 and 700 mOsm/kg, during digestion with DNase I (N = 3, n = 12 well replicates per time point for each condition). The differences between the osmotic groups are statistically significant from t = 40 minutes onwards. Error bars show standard error. B: The DNase I digestion profile for λ-DNA in 100, 300 and 700 mOsm/kg (N = 1, n = 4 well replicates per time point for each condition). Only at the first 5.5 minutes, the fluorescence intensity of λ-DNA exposed to 100 mOsm/kg was statistically higher than the other groups.

3.3.4 Instantaneous and Reversible Effect of Osmotic Challenge

To investigate the response time of chromatin condensation associated with the osmotic challenge, nuclei were monitored in live cells over a 15 minutes period. The effect of osmotic challenge on the nucleus was clearly visible within 20 seconds after the introduction of the osmotic challenge medium (Figure 3.13-3.17) indicated by changes in chromatin condensation levels (Figure 3.18) and nuclear height (Figure 3.19). When chondrocytes were exposed only to the 300 mOsm/kg iso-osmotic medium, the level of chromatin condensation and the nuclear height remained unchanged.

The reintroduction of iso-osmotic medium to cells exposed to 400 and 500 mOsm/kg hyper-osmotic medium resulted in a rapid and complete reversal of the chromatin condensation (Figure 3.15, 3.16 and 3.18). By contrast chromatin condensation levels did

not fall back to the original value following reintroduction of iso-osmotic medium after exposure to 700 mOsm/kg medium (Figure 3.17 and 3.18). Alterations to nuclear height induced by hyper-osmotic challenge at all levels were broadly reversible although there was evidence of a time dependent reduction in nuclear height following reintroduction of iso-osmotic medium (Figure 3.19).

Exposure of the chondrocytes to hypo-osmotic medium (100 mOsm/kg) reduced the level of chromatin condensation and increased nuclear height but with a clear time dependent relaxation over the 15 minutes observation period (Figure 3.13, 3.18 and 3.19). Interestingly, when iso-osmotic medium was reintroduced, chromatin condensation levels increased significantly above the original value before hypo-osmotic challenge and the nucleus height decreased below the original size (Figure 3.13, 3.18 and 3.19).

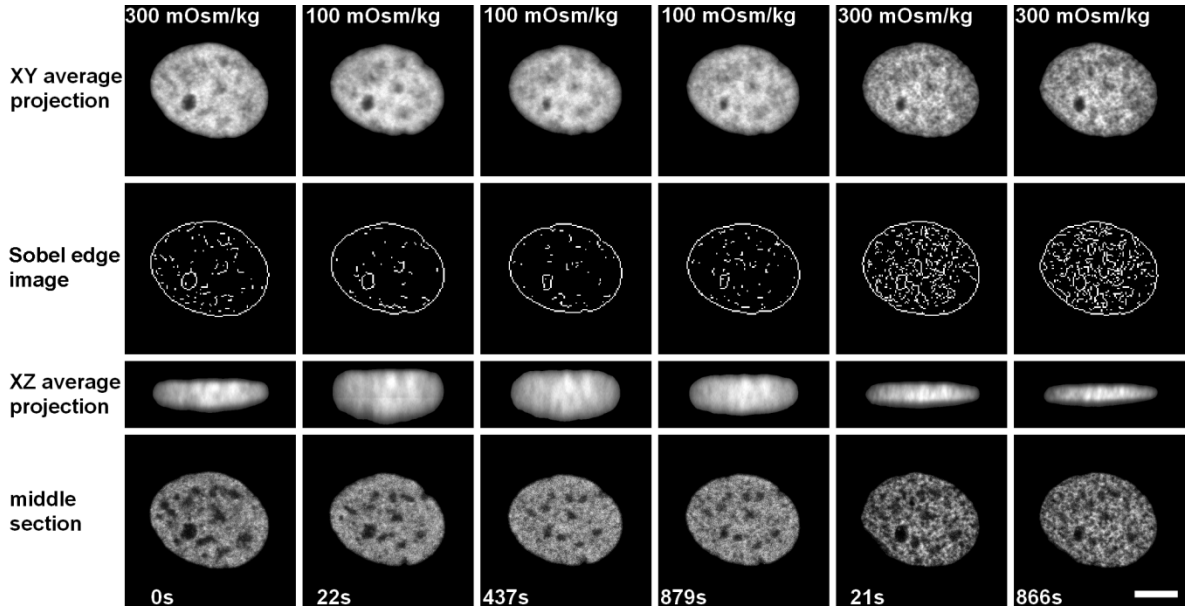

Figure 3.13 Images of a single representative monolayer cultured chondrocyte expressing H2B-GFP fusion-protein in an iso-osmotic environment (300 mOsm/kg), followed by hypo-osmotic challenge (100 mOsm/kg) for 900 seconds, which was then brought back to the iso-osmotic conditions for a further 900 seconds (Bar: 5 μm).

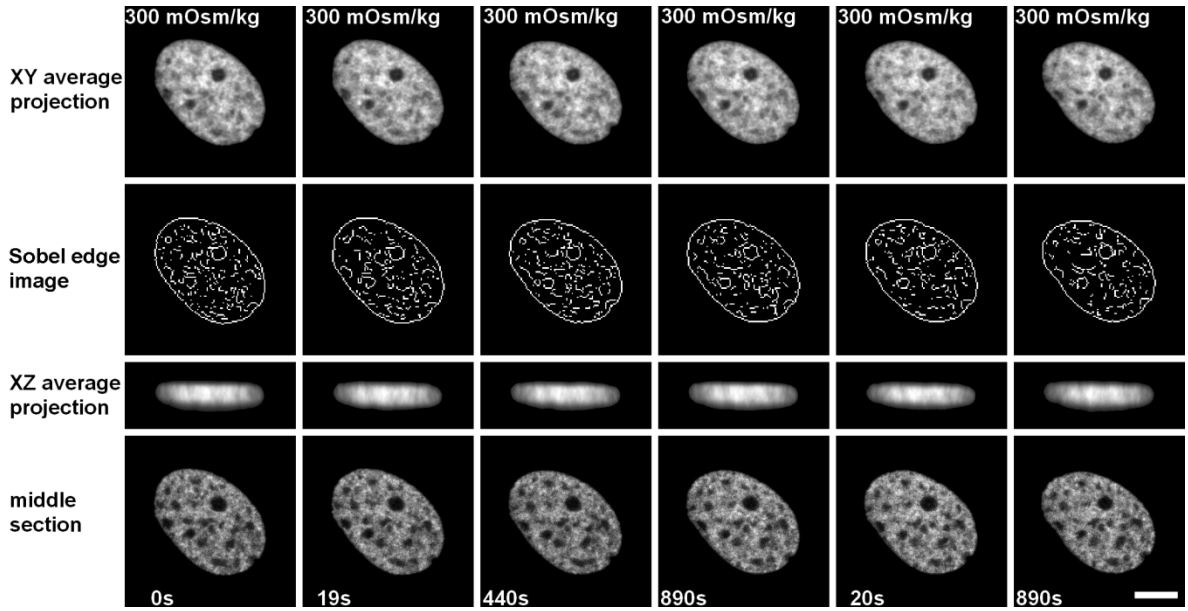

Figure 3.14 Images of a single representative monolayer cultured chondrocyte expressing H2B-GFP fusion-protein maintained in an iso-osmotic environment (300 mOsm/kg) for the full 1800 seconds (Bar: 5 μm).

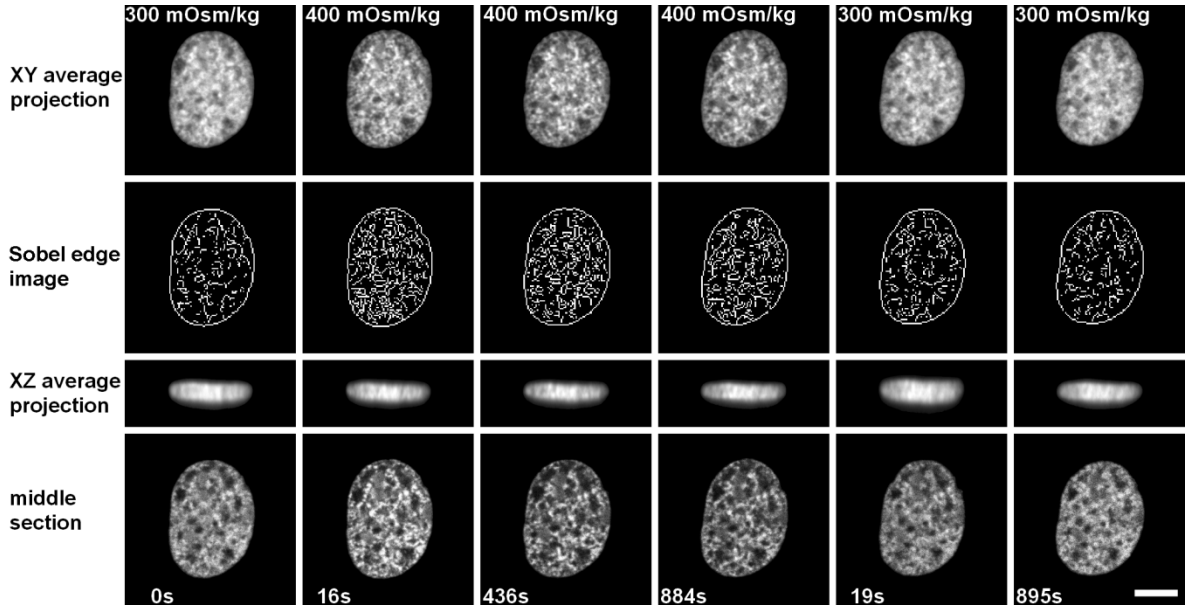

Figure 3.15 Images of a single representative monolayer cultured chondrocyte expressing H2B-GFP fusion-protein in an iso-osmotic environment (300 mOsm/kg), followed by hyper-osmotic challenge (400 mOsm/kg) for 900 seconds, which was then brought back to the iso-osmotic conditions for a further 900 seconds (Bar: 5 μm).

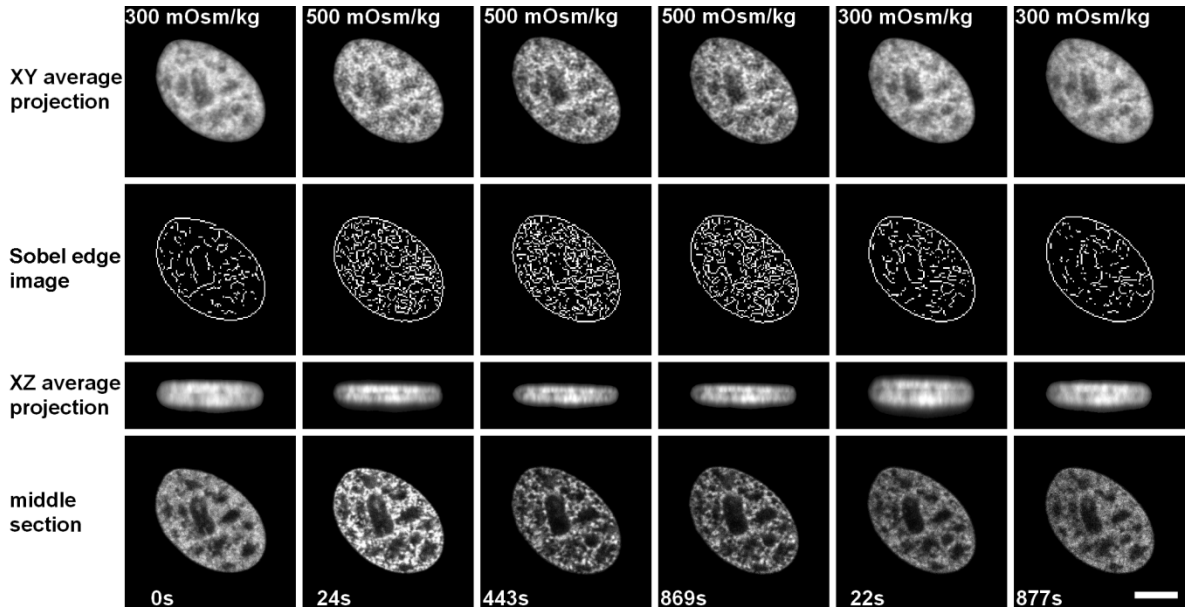

Figure 3.16 Images of a single representative monolayer cultured chondrocyte expressing H2B-GFP fusion-protein in an iso-osmotic environment (300 mOsm/kg), followed by hyper-osmotic challenge (500 mOsm/kg) for 900 seconds, which was then brought back to the iso-osmotic conditions for a further 900 seconds (Bar: 5 μm).

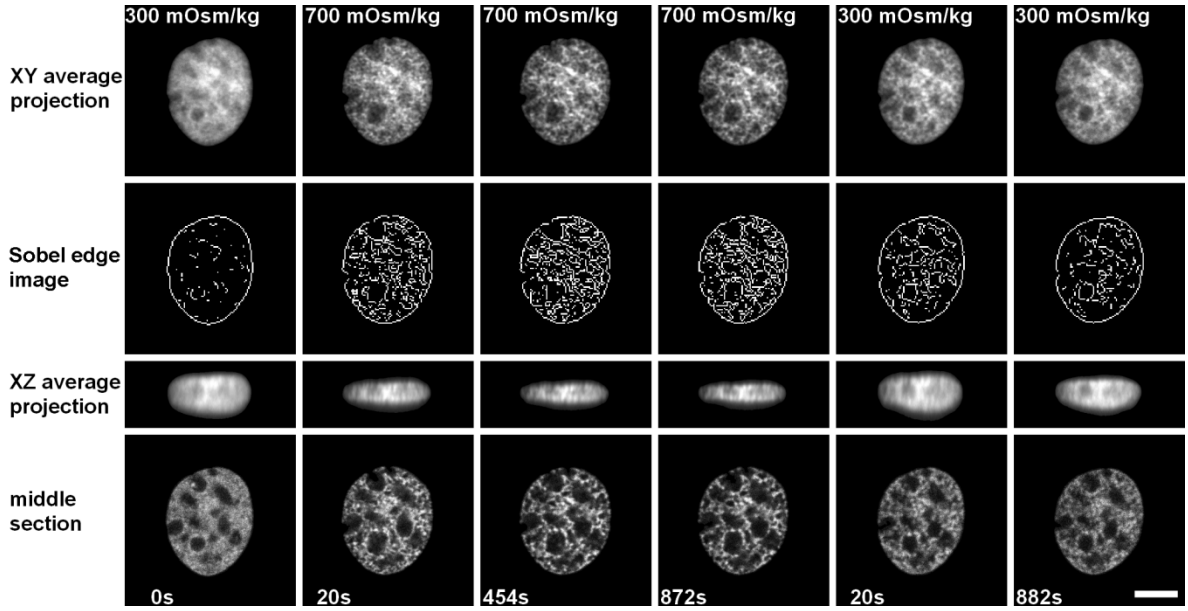

Figure 3.17 Images of a single representative monolayer cultured chondrocyte expressing H2B-GFP fusion-protein in an iso-osmotic environment (300 mOsm/kg), followed by hyper-osmotic challenge (700 mOsm/kg) for 900 seconds, which was then brought back to the iso-osmotic conditions for a further 900 seconds (Bar: 5 μm).

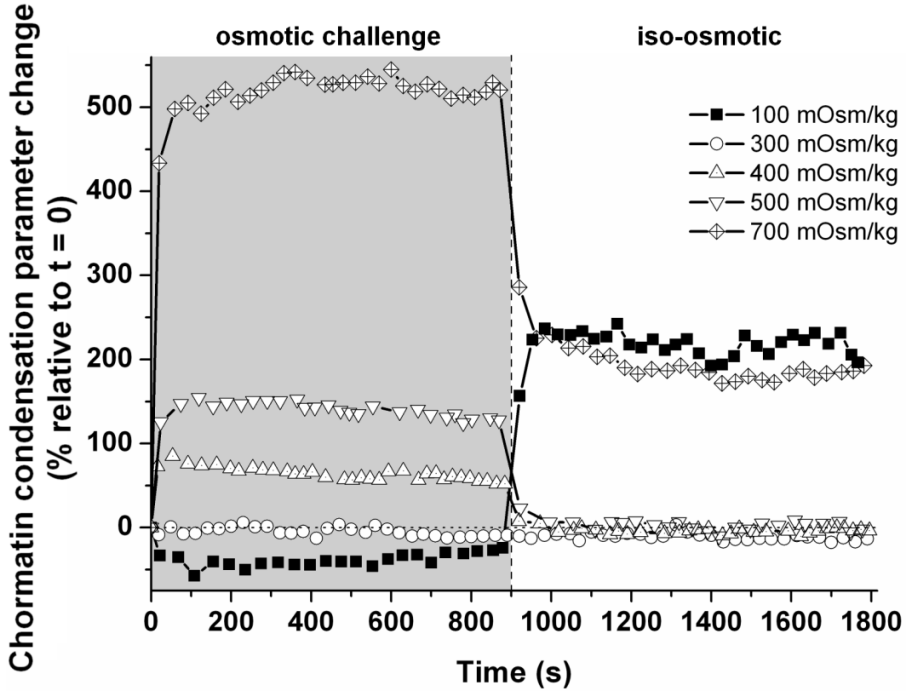

Figure 3.18 Normalised change of the chromatin condensation parameter quantified from live chondrocytes due to osmotic challenge for 15 minutes (900 seconds) followed by a return to iso-osmotic conditions for an additional 15 minutes. The chromatin condensation parameter quantification was acquired from the *XY* average projection images (N = 1, n = 1 nucleus per condition).

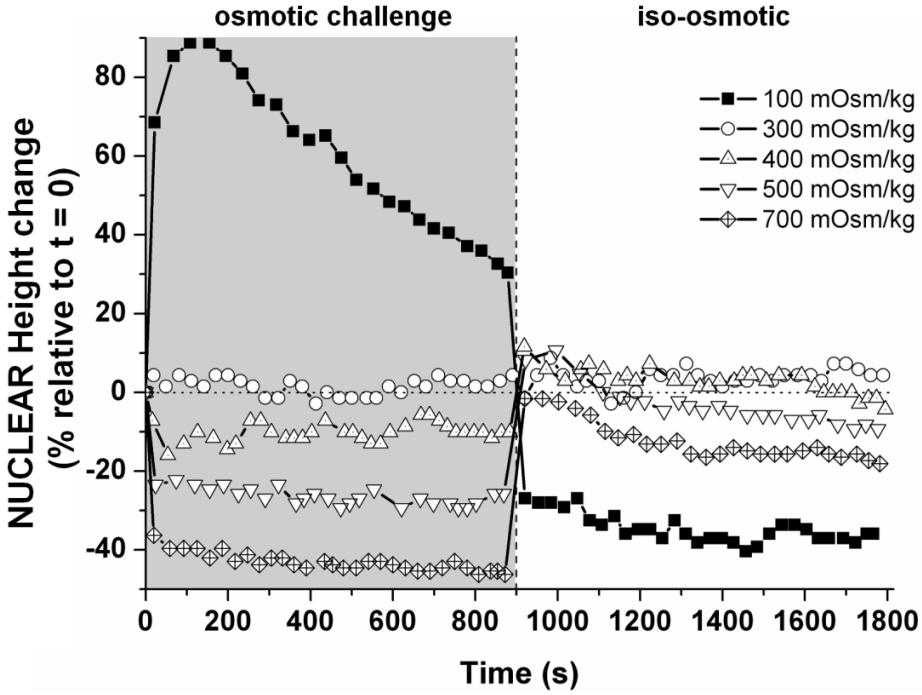

Figure 3.19 Normalised change of the nuclear height quantified from live chondrocytes due to osmotic challenge for 15 minutes (900 seconds) followed by a return to iso-osmotic conditions for an additional 15 minutes. The nuclear height was acquired from the *XZ* average projection images (N = 1, n = 1 nucleus per condition).

3.4 Discussion

In this chapter we have measured the extent of chromatin condensation in fluorescently labelled nuclei using an image analysis method adapted from an approach used previously to quantify actin cytoskeletal order (Knight *et al.* 2001). We show that hyper-osmotic challenge induces the chromatin condensation in chondrocytes (Figure 3.4), in agreement with findings reported in other cell types (Delpire *et al.* 1985; Albiez *et al.* 2006). As in other studies, chromatin condensation occurs in specific localised regions within the nucleus resulting in an increase in both the inter-chromosomal compartment and the spatial heterogeneity of staining (Albiez *et al.* 2006). The most marked condensation occurred between 400 and 500 mOsm/kg, suggesting a set point where chromatin condensation predominantly occurs (Figure 3.4 B). Interestingly, this set point falls within the physiological range of osmolality in unloaded articular cartilage *in vivo* (350 to 450 mOsm/kg) (Urban 1994). Furthermore, Oswald et al. (Oswald *et al.* 2008) showed that the application of extended loading on articular cartilage increases the osmolality of the surface region by around 80 mOsm/kg and the deep region by around 20 mOsm/kg, which increases the *in vivo* osmolality range to around 430 to 470 mOsm/kg. This suggests that the chromatin within the nuclei of articular chondrocytes is likely to be subjected to transition between states of greater and lesser condensation during periods of extended loading and unloading.

As the studies on osmotically-induced chromatin condensation are quite limited at the current time, it is not possible to distinguish whether this chromatin condensation set point due to hyper-osmotic challenge is specific for chondrocytes or not. However, different cells in the body are exposed to a wide range of osmolality, from 1744 mOsm/kg in the renal inner medulla (Marsh and Azen 1975) to 289 mOsm/kg in the serum (Hendry 1961). Furthermore, as reviewed by Burg *et al.* (2007), hyper-osmotic challenge have been shown to induce numerous different changes between different cell types that could depend on the initial differentiated phenotype of the particular cells, whilst some changes are pointing to some general principles that may apply to all cells. This suggests that osmotically-induced response can be divided into two classes: general and phenotype specific response. Hence, further studies on different cell types are required to distinguish whether this chromatin condensation set point is a unique response for chondrocytes or a general response that apply to other cell types as well.

The confined polymer-gel model fits exceptionally well ($R^2 > 0.98$) in the reversible region (300-500 mOsm/kg; Figure 3.5 and 3.18), suggesting that the mechanism underlying the chromatin condensation and decondensation is predominantly physicochemical in nature. Indeed the rapid onset (<20 seconds) of this condensation and reversible recovery revealed by the live cell imaging is also consistent with this view. Moreover, this differentiates osmotically-induced chromatin condensation from other mechanisms that modify chromatin architecture, which are driven, for example by biochemical modification of DNA or histone tails, and which do not manifest so pervasively in this short time scale.

Chromatin condensation upon hyper-osmotic challenge and chromatin decondensation upon hypo-osmotic challenge was observed in both the monolayer and 3D agarose-seeded chondrocytes, however differences in other aspects of nuclear morphology were noted. In the 3D agarose specimens, hyper-osmotic challenge induced significant deformation of the nucleus in both axial and lateral planes (*X*-*Y*-*Z*). By contrast, in monolayer specimens, significant nuclear deformation was only observed in *Z* axis (nuclear height). This suggests that the nuclear envelope is constrained in the axial (*X*-*Y*) plane in monolayer, potentially associated with the major differences in cytoskeletal organization known to exist between chondrocytes in monolayer and agarose (Idowu *et al.* 2000).

Interestingly, upon hyper-osmotic challenge, an irregular deformation of the nuclei in 3D agarose-seeded chondrocytes was observed, in contrast to the uniform shrinking of the cell (Figure 3.7 C and D). Finan and Guilak previously suggested that the nuclear deformation is a direct response of the change in osmolality within the cytoplasm, which increases the osmotic pressure inside the nucleus (Finan and Guilak 2010). According to this model, irregularity suggests that there are regions around or within the nucleus that are more susceptible to deformation. For example this may be due to the crowding of cytoplasmic organelles such as the endoplasmic reticulum, whose membranes are contiguous with the outer nuclear membrane, thereby compressing the nucleus at particular locations. The effect may also be associated with the regional heterogeneity of nucleus mechanics and chromatin condensation in iso-osmotic conditions and/or with hyper-osmotically-induced condensation.

With hyper-osmotic challenge, the differences in volume changes between the cell and the nucleus are statistically insignificant ($p>0.3$, Figure 3.11 D), suggesting the translation of cell shrinking to the reduction in nucleus volume. However, with hypo-osmotic challenge,

the nucleus volume increases to a lesser extent than the cell volume ($p<0.001$), suggesting that the swelling of the nucleus is restricted for example due to structural limitations imposed by the nuclear envelope/lamina and the cytoskeleton. Alternatively, the link between the cell and nucleus might be weakened due to the disorganisation of F-actin associated with hypo-osmotic challenge (Guilak *et al.* 2002). Furthermore, Guilak *et al.* also showed that the application of hypo-osmotic challenge (153 mOsm/kg) on suspended porcine articular chondrocytes increases the cell volume by more than 60% (2002), which is significantly greater than the one reported in this study (16%). This suggests a restriction of the hypo-osmotically induced swelling by the agarose construct encapsulating the cell, which is confirmed by the TEM images (Figure 3.10), showing local compressions of the agarose surrounding the cells.

The functional consequences of osmotically induced chromatin condensation and decondensation were demonstrated in the DNA digestion studies. The reduced and increased rates of DNA digestion for chondrocyte nuclei subjected to hyper-osmotic and hypo-osmotic challenge respectively are consistent with altered access of the DNase I to the DNA backbone with altered levels of chromatin condensation. This effect of chromatin condensation may also alter the access of transcription factors that regulate gene expression. These studies were performed using isolated nuclei and therefore suggest osmotically-induced chromatin condensation can occur in the absence of a functional plasma membrane and cytoplasm. Thus the condensation response is likely to occur due to direct physicochemical alterations rather than a biochemical signalling pathway. This supports the finding from the polymer-gel model discussed above. The nuclear envelope does not exhibit the same selective permeability to low molecular weight species, such as ions, exhibited by the plasma membrane (Mazzanti *et al.* 2001). As such the physicochemical nature of the chromatin condensation may be driven by the physical entrapment of large macromolecular components of the chromatin rather than the restriction of movement across a membrane of small ions that regulates classic whole-cell osmotic effects. Moreover, the presence of fixed charge associated with the chromatin suggests a mechanism potentially more akin to the Gibbs-Donnan effect that is well documented for aggrecan swelling within cartilage (Mazzanti *et al.* 2001).

Upon the reintroduction of iso-osmotic medium to the chondrocytes exposed to 400 and 500 mOsm/kg, the chromatin condensation level and nuclear height recovered rapidly to

their original value, indicating the reversibility of the osmotically induced alteration. These osmolalities cover the physiological osmotic range and the osmotic range where chromatin condensation predominantly occurs as shown earlier in this study. Extended loading of cartilage, such as in human intervertebral discs over the course of a day, is known to lower the fluid content of the tissue (Maroudas 1979), thus increasing the osmolality. When the load is removed during resting, rehydration of the tissue occurs, restoring osmolality to unloaded levels (Torzilli *et al.* 1997). This osmotic cycle, in conjunction with the reversible nature of the chromatin condensation, suggests that reversible chromatin condensation and decondensation events are likely to occur during the cartilage daily loading cycle. When the iso-osmotic medium was reintroduced to the chondrocytes exposed to 100 and 700 mOsm/kg, the chromatin condensation level and the nuclear height was not restored to the original values. Interestingly reintroduction of iso-osmotic medium, for cells incubated in 100 mOsm/kg medium resulting in condensation level greater than iso-osmotic or hypo-osmotic. Thus, incubation in 100 and 700 mOsm/kg medium, osmotic extremes outside the physiological range, may induce alterations to the chromatin and/or to structural elements in the nuclear lamina or cytoskeleton in a manner that is non-recoverable, which may lead to apoptosis (Dmitrieva and Burg 2008).

In summary, hyper-osmotic and hypo-osmotic challenge induce rapid chromatin condensation and decondensation, respectively. These effects predominantly fall within a narrow, physiological range of osmolalities and are rapidly reversible within this range, suggesting these phenomena are relevant to the *in vivo* state. The excellent agreement between experimental data and the polymer-gel model coupled with rapid nature of the chromatin condensation indicate that these effects are predominantly a physicochemical phenomenon. The nucleus provides a major structural component of cells, typically being significantly stiffer than the cytoplasm (Guilak *et al.* 2000). As such the nucleus may contribute to the overall mechanical properties of cells depending upon the level of cell deformation and the nucleus:cytoplasmic volume fraction. Thus alterations in chromatin condensation and overall nuclear architecture may induce changes to cell stiffness and the response of cells to external mechanical loading. Therefore the next chapter of this thesis investigates the effects of compressive loading on chondrocytes subjected to osmotic challenge.

Further, the known relationship between chromatin condensation and gene silencing suggests that osmotically-driven condensation phenomena may regulate transcriptional activity in chondrocytes. Moreover pathologically induced changes in osmolality may induce profound alterations in chromatin condensation within both the loaded and unloaded state, with associated changes in gene expression. Further study is required to elucidate the relationship between osmotically-induced chromatin condensation and transcriptional regulation, which are considered in Chapter 5 of this thesis. For example, to ascertain whether certain gene loci, critical for chondrocyte survival and homeostasis, are shielded from the osmotically induced chromatin condensation. This may involve boundary or insulator elements, regions of non-coding intergenic DNA that bind proteins such as CTCF and other trans-acting factors, that can shield loci from the effects of regulatory regions of neighbouring genes and higher-order chromatin structure (Bell and Felsenfeld 2000; Vogelmann *et al.* 2011). It is tempting to speculate that the physical limitations imposed on the nucleus by both the lamina and the cytoskeleton may be part of this control mechanism; evidenced by the upper swelling limit demonstrated by hypo-osmotic conditions. However, as mentioned in Chapter 1, it is important to note that physiological changes in extracellular osmolality is likely to be a gradual process along the application of load on cartilage tissue, rather than sudden alterations that were utilised in other studies, including this one. To the author's knowledge, the available information on the effect of gradual osmotic challenge is very limited at the current time. Godart *et al.* have shown that sudden hypo-osmotic challenge on erythrocytes induces the recovery of cell volume over time (RVD), whilst, gradual hypo-osmotic challenge (1 mOsm/kg per minute) was shown to cause the cell volume to increase gradually with the application of osmotic challenge, to a level that was reached by the sudden group (Godart *et al.* 1999). This suggests that osmotic response is magnitude dependent instead of rate dependent. However, whether this is the same for chondrocytes is still an open question. Hence, further examination on the effect of gradual osmotic challenge on the changes seen in this study is essential to test their relevance with cartilage physiological conditions during loading. Nevertheless, these osmotically-induced alterations in nuclear morphology and chromatin structure present themselves as a potential step in a mechanism that mediates chondrocyte metabolism upon osmotic challenge.

Chapter 4 Static Compression Load on Osmotically Challenged Chondrocytes

4.1 Introduction

Articular cartilage is subjected to dynamic loading during normal activity and it is well established that these mechanical forces modulate the metabolic activity of chondrocytes. Previous studies have demonstrated that mechanical loading, applied to cartilage explants (Guilak 1995) induces the deformation of chondrocyte and its nucleus, where the application of physiological loading on the explants was shown to induce 0-30% strain on chondrocytes (Broom and Myers 1980; Guilak 1994). The use of three-dimensional culture models, such as agarose, enable cell deformation to be varied independently from other potential mechanotransduction signals, for the purpose of investigating the role of load-induced cell deformation. Application of 20% gross compressive strain on 3% (w/v) agarose constructs was shown to induce ~15% strain on the encapsulated chondrocytes (Lee and Bader 1997), which falls within the physiological range (0-30%). Static compressive load at this level on agarose-seeded chondrocytes was shown to inhibit matrix synthesis, whilst dynamic load (20%, 1 Hz) was shown to promote GAG synthesis and chondrocyte proliferation (Lee and Bader 1997).

The application of prolonged mechanical loading to cartilage and the variation of proteoglycan concentration along the depth of the tissue alter the osmolality of the extracellular environment of chondrocytes, with osmotic challenge known to alter gene expression and the metabolic activity of chondrocytes (Urban *et al.* 1993; Hung *et al.* 2003). In addition, osmotic challenge induces alterations in the morphology of the chondrocyte and its nucleus (Finan *et al.* 2009). Both physical stimuli, mechanical and osmotic challenge, are coupled within the articular cartilage.

In the previous chapter, we have shown that the application of osmotic challenge significantly affects chromatin organisation, and the cellular and nuclear morphology of chondrocytes. These alterations might in turn alter both cellular and nuclear mechanical properties. In this chapter, the effect of osmotic challenge on the deformability of chondrocytes and their nuclei was assessed. Freshly isolated chondrocytes were seeded into agarose constructs with aluminium end plates, cultured overnight and exposed to different osmotic conditions. By using a compression rig, the agarose specimens were subjected to a static 20% compressive strain. Images of the cells and nuclei before and after the compression were acquired by confocal microscopy. The change of cell and nucleus size were measured from the images and analysed.

4.2 Microscope Mounted Compression Rig

In order to apply compressive strain to the agarose seeded chondrocytes, a uni-axial compression rig was developed (Figure 4.1; Pingguan-Murphy *et al.* 2005). The compression rig consists of three main components, a pair of stepper motors located opposite to each other that are connected to a linear actuator to translate the rotation motion of the motor into linear motion, a grip system to hold the specimen (Figure 4.2) and a hydration chamber comprised of a metal bracket with a glass coverslip bottom. On one side, a load cell is placed between the motor and the linear actuator. The stepper motors are controlled by LabView (National Instruments, Austin, US), which requires displacement and velocity as the input.

The set up of the rig starts with assembling the hydration chamber. A coverslip (thickness no. 1.5, VWR, Lutterworth, UK) was placed into the metal bracket and sealed with silicone grease (RS, Northants, UK) to prevent any leakage during the procedure. The chosen hydration medium with a volume of 5 mL was then placed into the hydration chamber. With the grip spacer in place, the agarose construct was placed into the grip and the clamps were tightened until the construct was secured. The construct surface which will be in contact with the coverslip should be at least 1 mm outside the grip, to ensure contact between the agarose construct and the coverslip. The grip was then secured to the compression rig, with the specimen fully immersed in the hydration medium. The grip spacer was removed rendering the specimen ready to undergo compression testing.

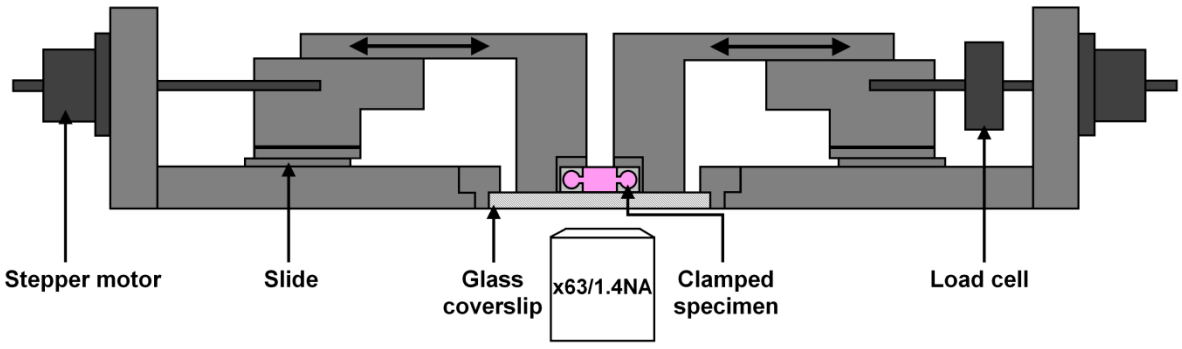

Figure 4.1 Schematic drawing of the compression rig set up.

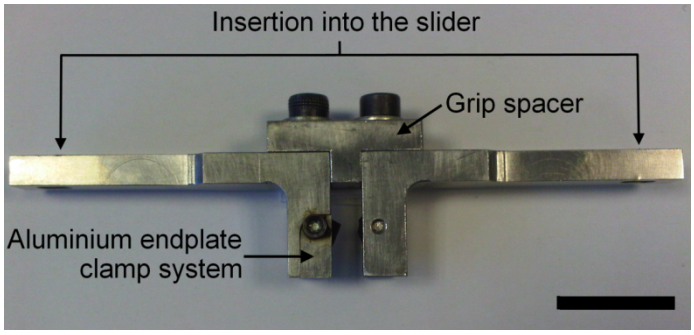

Figure 4.2 Specimen grip for the compression rig (Bar: 2 cm).

4.2.1 Aluminium End Plates

In this compression study, instead of the porous glass end plates that were used in Chapter 3, the agarose constructs were incorporated into aluminium end plates (Figure 4.3). Theoretically, porous glass is an ideal end plate, as it allows the agarose to fuse into its pores, creating a uniform attachment. However, in practice, the agarose is too viscous and gelation occurred before the agarose is completely fused into the porous glass, creating a weak attachment interface. The channel in the aluminium end plate ensures continuity between the agarose and the end plate clamped to the grip. Additionally, porous glass is a brittle material, thus it is very challenging to cut it precisely to the required dimensions. Differences in the size of the porous glass end plates will alter the dimensions of the agarose construct between the end plates and hence the level of applied strain. By contrast, aluminium is relatively easy to machine, providing a higher dimensional accuracy.

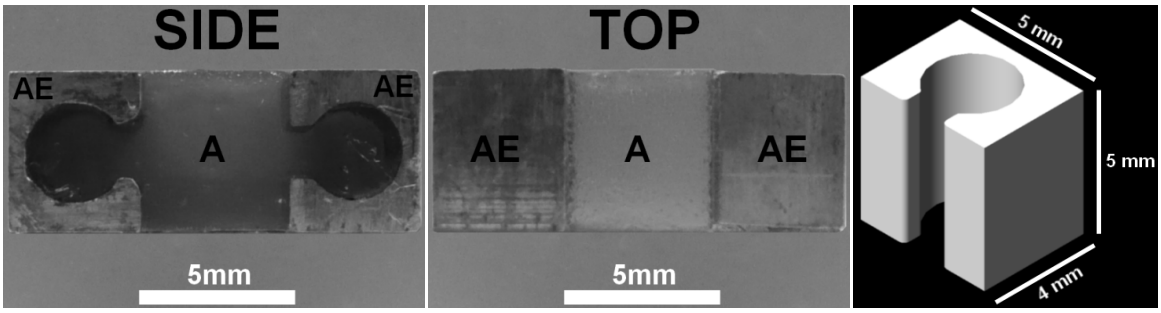

Figure 4.3 Side (left) and top (middle) view of agarose-aluminium end plate construct (Bar: 5 mm). Schematic drawing of the aluminium end plate (right).

4.2.2 Simulation of the Chondrocyte-Agarose-Aluminium and -Porous Glass Constructs Deformation due to Static Compressive Load

Porous glass end plates provide a relatively uniform attachment interface between the agarose and the end plate. By contrast, due to the channel in the aluminium end plates, there is a geometry variation at the aluminium-agarose interface along the *Y* axis (Figure 4.4 B). When constructs are subjected to a compressive load, the stress distribution produced will vary due to the geometric variations, which may alter cellular deformation. However, the most essential part of the construct is the region where the cells are imaged, i.e. the bottom part of the construct that face the glass coverslip. By using Abaqus 6.9-2 (Dassault Systemes, Vélizy-Villacoublay, France), the effect of this geometric variation on the cellular deformation distribution, at the imaging region, upon 20% compressive strain was assessed.

3D solid models of the porous glass (Figure 4.4 A) and aluminium (Figure 4.4 B) end plate and constructs were produced, with dimensions representative of the actual constructs. The materials in these models were assumed to be homogeneous, with a linear isotropic elasticity. The Young's modulus for agarose, porous glass, aluminium and chondrocyte were given the value 100 kPa (Tasci *et al.* 2011; Yusoff *et al.* 2011), 4 GPa (Nanjangud and Green 1995), 70 GPa and 3.5 kPa (Trickey *et al.* 2006; Ofek *et al.* 2009), respectively. The Poisson's ratio for agarose, porous glass, aluminium and chondrocyte were given the value 0.32 (Ross and Scanlon 1999), 0.2 (Nanjangud and Green 1995), 0.35 and 0.4 (Trickey *et al.* 2006; Ofek *et al.* 2009), respectively. In the unstrained state, the cells were assumed to adopt a spherical morphology with a diameter of 10 μm. Additionally, it was also assumed that the cells do not contribute to the mechanical property of the agarose gel due to their low volume fraction (<0.6% at 10×10^6 cells/mL seeding density) (Guilak and Mow 2000; Ahearne *et al.* 2005). For each simulation, 5 chondrocytes, aligned in the *X* and *Y* axis, were seeded into the construct. The cells were positioned 10 μm from the bottom surface of the agarose, facing the glass coverslip. For each line of 5 cells, the first and fifth cells were positioned 10 μm from the end plates, the second and fourth cells were positioned 1250 μm from the end plate at each end and the third cell was positioned 2500 μm from the end plates, i.e. at the middle. The first, second, third and fourth line of cells were positioned 10 μm, 1250 μm, 2500 μm and 3750 μm, respectively, from one side of the construct and the fifth line of cells was positioned 10 μm from the other side of the construct. The cell

arrangement is illustrated in Figure 4.4 C and the boundary conditions are shown in Figure 4.4 D.

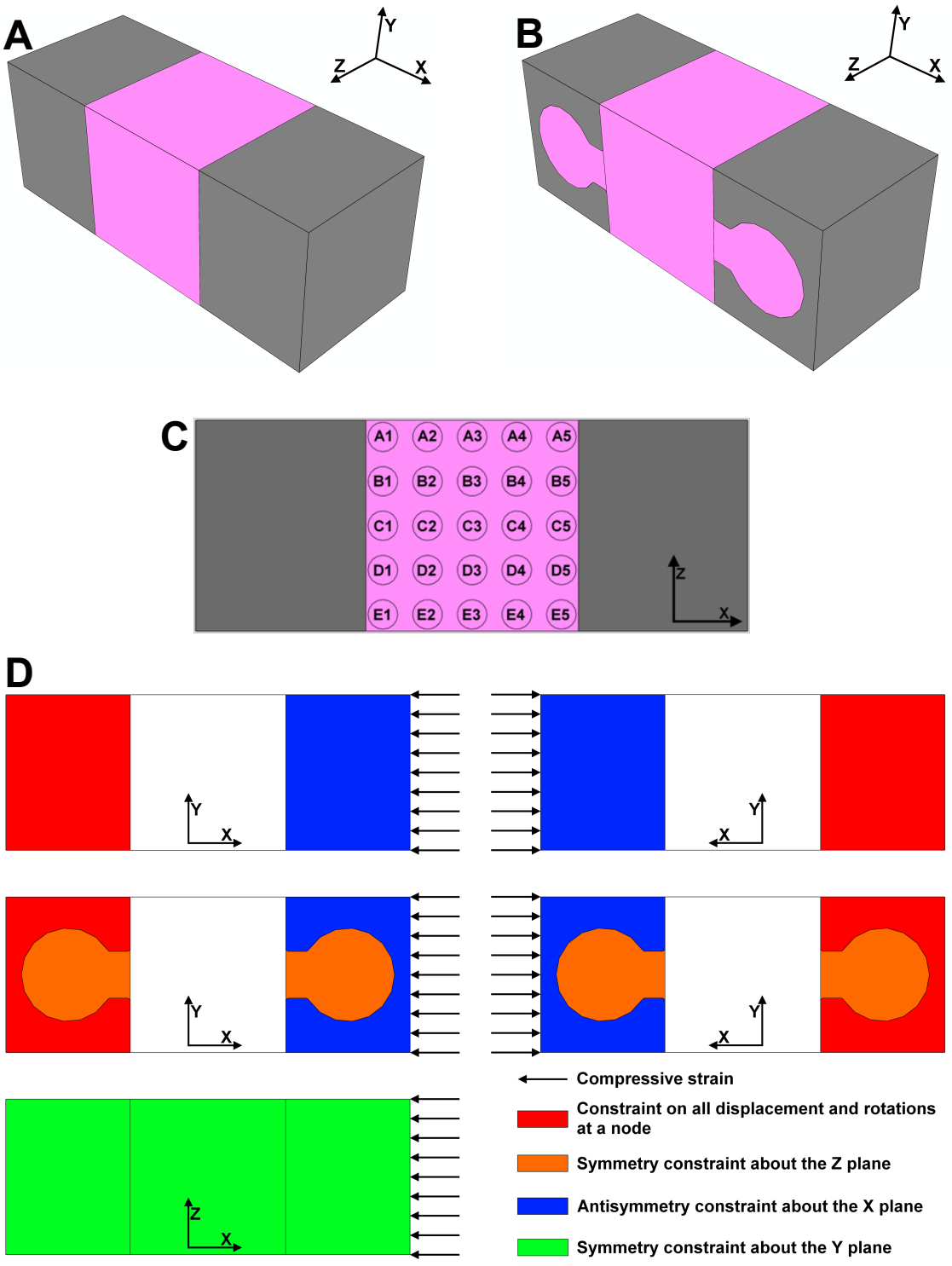

Figure 4.4 A: The chondrocyte-agarose-porous glass end plate construct model. B: The chondrocyte-agarose-aluminium end plate construct model. C: Schematic drawing indicating the location of the chondrocytes. D: 2D schematic drawings of the construct models with colour coded boundary conditions.

C3D4 mesh type was used for the models, which involves a linear tetrahedral element. The constructs were meshed with a global size of 0.3 μm, while 25 seeds were applied to the edge of each cell to provide a finer mesh for the chondrocyte. With this mesh setting, depending on the end plate type and the location of the cells, the constructs contained 30035 to 49519 nodes and 165561 to 283204 elements. Each cell contained 2167 to 2552 nodes and 10404 to 12727 elements. In each simulation, a 20% compressive strain along the *X* axis was applied to the constructs, equivalent to 1 mm of compressive displacement (Figure 4.5 and 4.7).

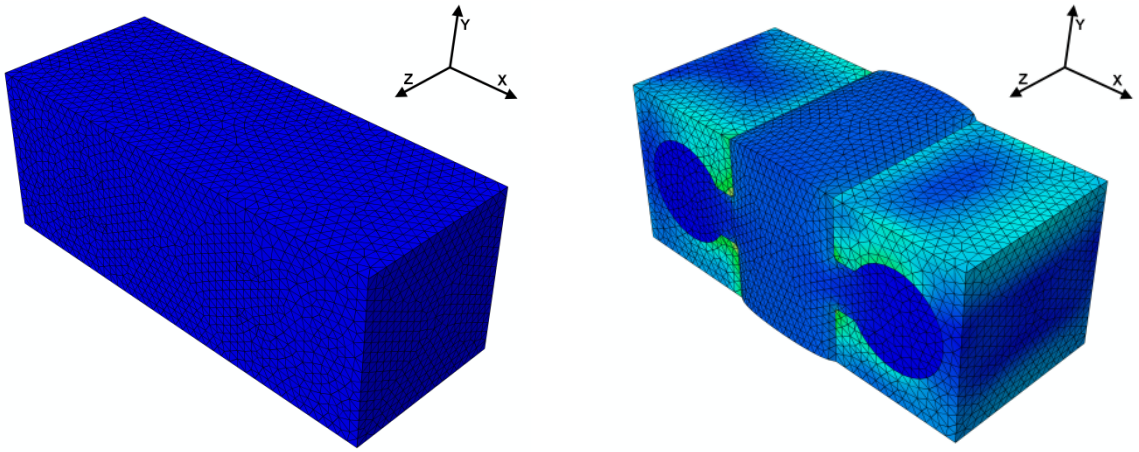

Figure 4.5 Meshed aluminium end plate construct model at 0% compressive strain (left) and meshed construct model at 20% compressive strain (right).

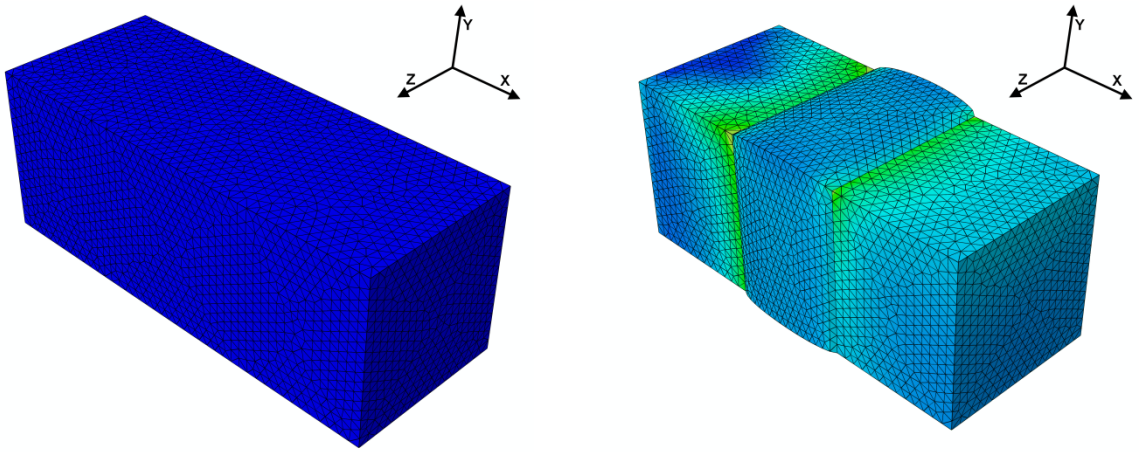

Figure 4.6 Meshed porous glass end plate construct model at 0% compressive strain (left) and meshed construct model at 20% compressive strain (right).

Based on the strain map produced by the simulation (Figure 4.7), differences in the strain distribution can be observed at the middle region of the aluminium and porous glass constructs. The strain distribution of the different constructs at the imaging plane, the region where the cells were positioned, are very similar. Figure 4.8 and 4.10 show the degree of deformation of the chondrocytes at different locations within the aluminium and the porous glass end plates construct models, respectively. For the cell located at the centre (position C3) of the construct with aluminium end plates, the cell size reduced by 26.3% along the *X* axis and increased by 24.6% along the *Z* axis (perpendicular to the compression plane), post application of 20% compressive strain. When compared, similar distribution of the cellular deformation can be seen between the two constructs for centrally-located cells. However, obvious differences can only be seen with the cells positioned at the corners of the construct (A1, A5, E1 and E5), where a greater degree of deformation can be observed in the aluminium end plates construct. Based on these observations, by restricting the imaging region to the centre of the construct cellular deformation resulting from compressive load on porous glass and aluminium end plates constructs are very much alike.

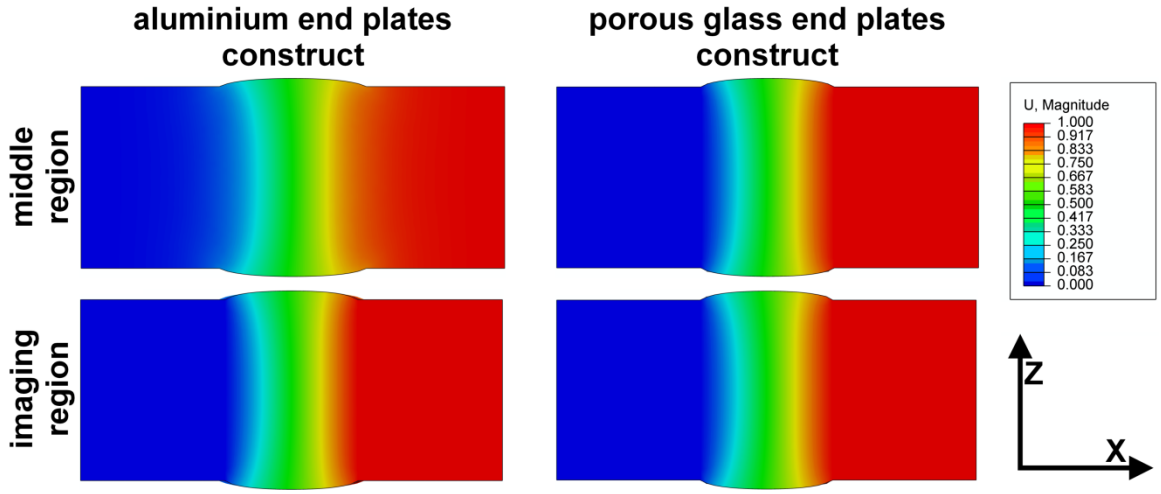

Figure 4.7 Strain map of the aluminium and porous glass end plates constructs post 20% compressive strain, at the middle region of the construct and at the imaging region, where the cells were positioned.

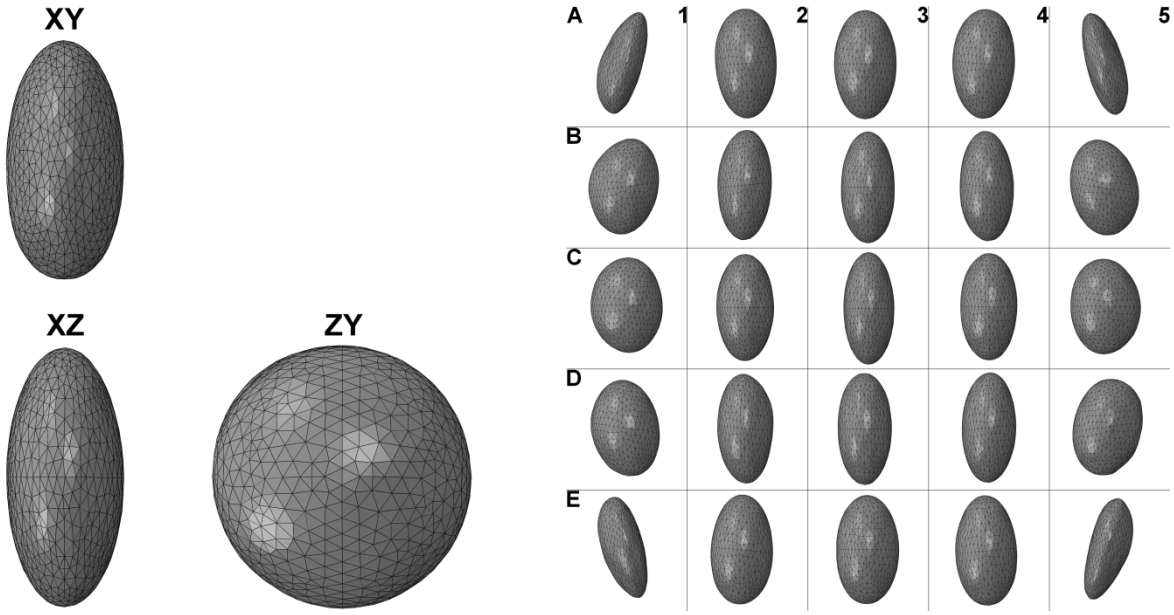

Figure 4.8 *X-Z*, *X-Y* and *Z-Y* views of the chondrocyte located at C3 from the aluminium end plate model (left). The degree of deformation of the chondrocytes in the *X-Z* plane at different locations from the aluminium end plate model (right).

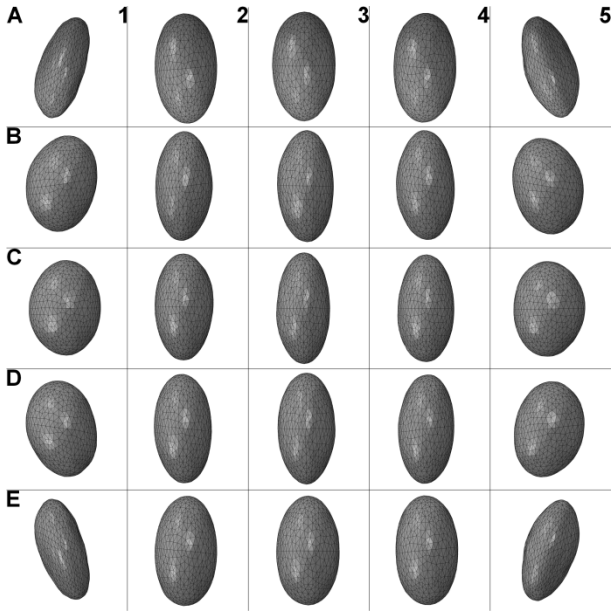

Figure 4.9 The degree of deformation of the chondrocytes in the *X-Z* plane at different locations from the porous glass end plate model.

4.3 Material and Methods

4.3.1 Preparation of Chondrocyte-Agarose Constructs Incorporated with Aluminium End Plates

Freshly isolated chondrocytes were seeded into 3% agarose type VII with aluminium end plates, as described previously in section 3.2.5, with a seeding density of 10×10^6 cells/mL. The constructs were also cultured in DMEM + 16.1% FCS overnight, prior to further investigation.

4.3.2 Osmotic and Compressive Load Application

Prior to the compression procedure, the chondrocyte-agarose construct was stained with 8 μM Hoechst 33342 for 30 minutes at 37°C. Osmotic challenge medium was placed into the hydration chamber. The construct was then mounted into the compression rig as described previously and placed into the 37°C imaging chamber integrated with the confocal microscope system. After a 30 minutes incubation period, high resolution images bisecting the centres of the nucleus and bright field images of the cell were taken by confocal microscopy, using the settings described in section 3.2.3 (63×/1.4NA objective at 46.5 nm/pixel, 7.68 s/image). A 20% uni-axial unconfined static compressive strain was applied at a strain rate of approximately 1%/s. The same cells were imaged following a 30 minute relaxation period.

4.3.3 Image Analysis

The distance between the maximum edge of the cell and nucleus in *X* (parallel to the compression) and *Y* (perpendicular to the compression) axis was measured. Cell size was assessed using ImageJ (Abramoff *et al.* 2004), while the nuclear size and cross-section area were measured in MATLAB as described in section 2.7.5. By assuming that the nuclei were a perfect sphere, the radius calculated from the cross-section area was used to calculate the approximated nucleus volume. In order to approximate the cell volume, the deformation in *Z* axis was assumed to be equal to the deformation in *Y* axis, thus the cell volume was approximated by the following equation: $V = \frac{4}{3}\pi\left[\frac{X}{2} \times \left(\frac{Y}{2}\right)^2\right]$, where *X* is the cell diameter in the *X* axis and *Y* is the cell diameter in the *Y* axis.

4.4 Results

Figure 4.10 shows representative images of chondrocytes and their nuclei in the unstrained state and following the application of 20% compressive strain, under different osmotic conditions. Upon application of compression, cellular deformation was observed in all osmotic groups, but appeared to be more marked with increasing osmolality. Nuclear deformation due to the compressive load can be seen in the hyper-osmotic groups.

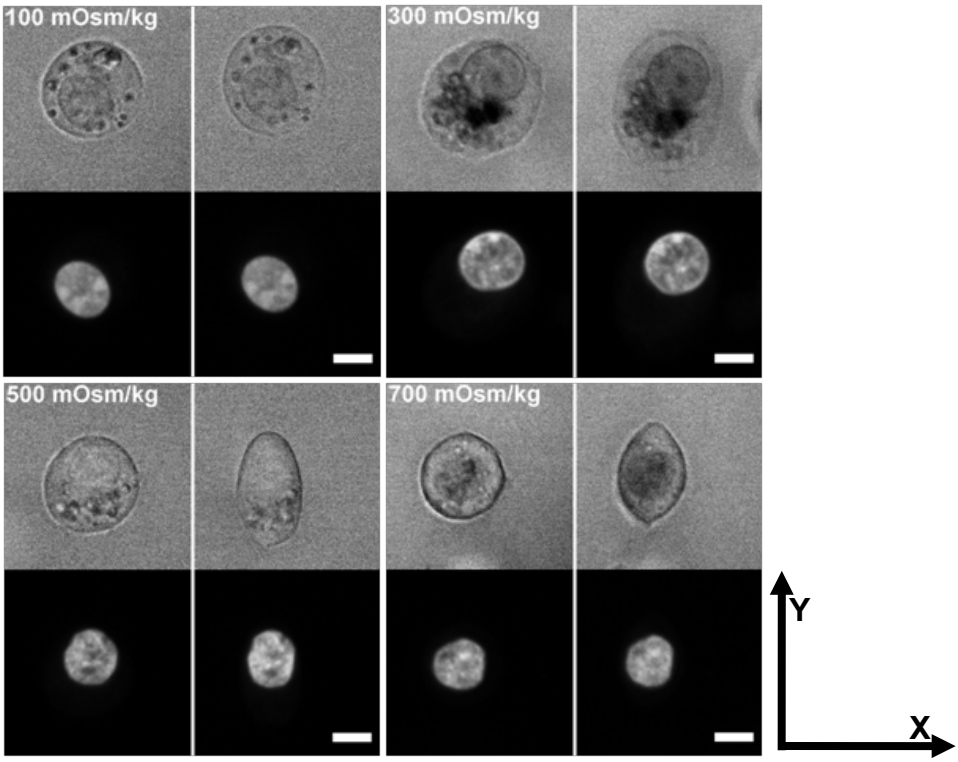

Figure 4.10 Paired bright field images of agarose-seeded chondrocytes and their nucleus confocal image at 0% and at 20% compressive strain (along *X* axis), exposed to different osmotic challenges (100, 300, 500 and 700 mOsm/kg; Bar: 5 μm).

When exposed to the iso-osmotic challenge, the cell size decreased by 11.4% in the *X* axis and increased by 11.5% in the *Y* axis under gross compressive strain (Figure 4.11). Upon compressive strain in hyper-osmotic condition, the deformation in the *X* axis increased significantly to 22.4% in 500 mOsm/kg and 24.1% in 700 mOsm/kg, compared to the iso-osmotic samples. By contrast, the deformations in the *Y* axis remained relatively similar to the iso-osmotic specimens at 9.7% in 500 mOsm/kg and 12.7% in 700 mOsm/kg. Under

hypo-osmotic challenge, an increase in cell size along the *X* axis after the compression was noted, although this effect was not statistically significant compared to the 0% strain data, whilst the deformations in *Y* axis were significantly greater than the other groups, at 17.8%.

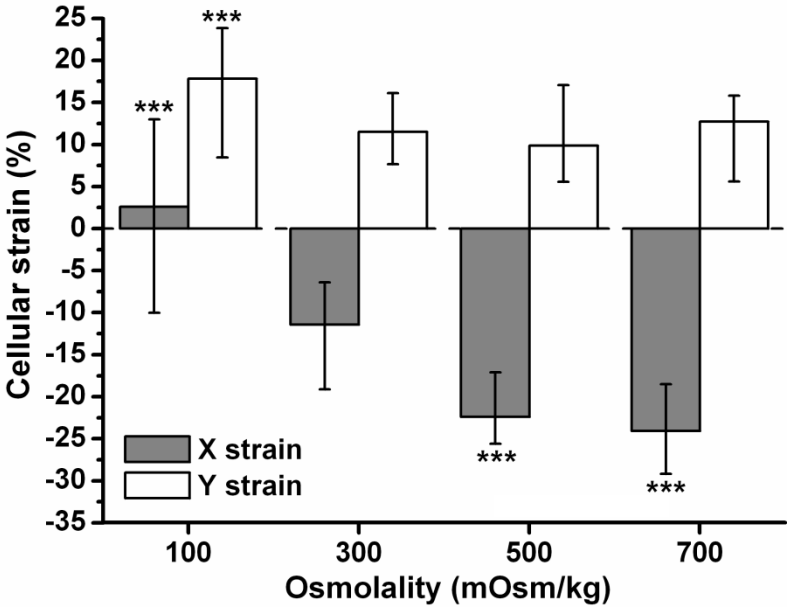

Figure 4.11 Change of cell size in the *X* (parallel to the compressive load) and *Y* (perpendicular to the compressive load) axis post 20% compressive strain. Statistical significance test was performed to compare the osmotic challenge groups against the control group (300-300 mOsm/kg) and also between the 500 and 700 mOsm/kg group ($N = 6$, $n = 80$-124 cells per condition) (*$p<0.05$ and ***$p<0.001$). Error bars show lower and upper quartile.

When exposed to the iso-osmotic challenge, a reduction in nuclear size along the *X* axis (4%) was observed post the 20% compressive strain (Figure 4.12). In hypo-osmotic conditions, the majority of nuclei experienced a lesser degree of reduction of size along the *X* axis compared to iso-osmotic conditions, with some nuclei experiencing an increase (as shown by the error bar). Under hyper-osmotic environment, post the 20% compressive strain, the nuclear size in the *X* axis reduced significantly more (13.8% and 17.7% for the 500 and 700 mOsm/kg group, respectively) when compared to the reduction in the iso-osmotic group. The nuclear size in the *Y* axis remains relatively stable for all osmotic groups, although the deformation along the *Y* axis for the 700 mOsm/kg group was statistically different compared to the iso-osmotic group. Additionally, the deformations along the *Y* axis for all osmotic groups, except the 500 mOsm/kg group, are statistically significant to the 0% strain level (data not shown).

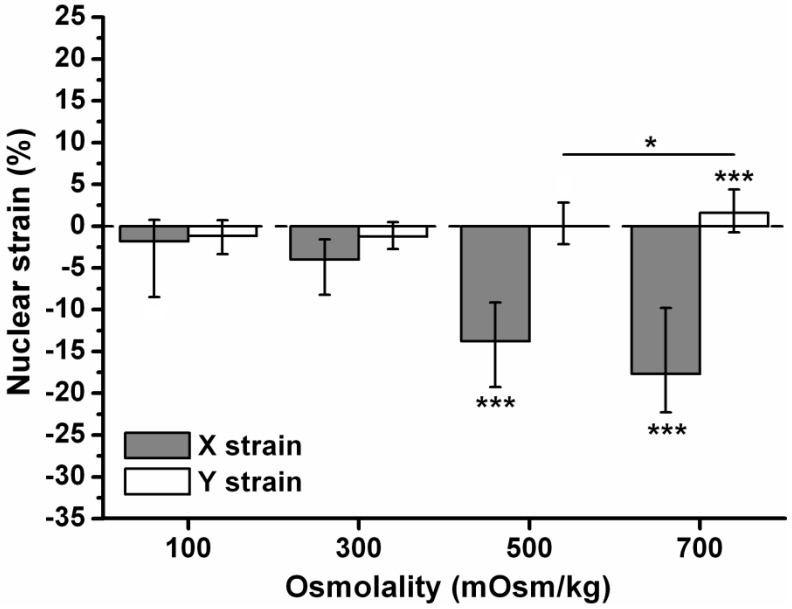

Figure 4.12 Change of nucleus size in the *X* (parallel to the compressive load) and *Y* (perpendicular to the compressive load) axis post 20% compressive strain. Statistical significance test was performed to compare the osmotic challenge groups against the control group (300-300 mOsm/kg) and also between the 500 and 700 mOsm/kg group ($N = 6$, $n = 80$-124 nuclei per condition) (*$p<0.05$, **$p<0.01$ and ***$p<0.001$). Error bars show lower and upper quartile.

The change in volume indicates an unequal translation of deformation between the *X* and *Y* axes. If the deformation in *X* axis is fully translated to the deformation in *Y* axis, there will be no volume change. Under iso-osmotic condition, the cell volume increased by 5.9% and the nuclear volume decreased by 8.4% after the application of compressive strain (Figure 4.13). At 100 mOsm/kg, the cell volume increased by 42.5% which is significantly greater than the iso-osmotic group, whilst the change in nuclear volume was not significantly different to the nuclear volume strain of the iso-osmotic group. Upon hyper-osmotic challenge, in addition to the reduction of cell volume post the 20% compressive strain by 7.1% and 7.5% for the 500 and 700 mOsm/kg groups respectively, the reductions of nuclear volume were also significantly greater than the specimens in iso-osmotic condition (21.3% for the 500 mOsm/kg group and 21.8% for the 700 mOsm/kg group). Figure 4.14 shows the non-linear relationship of nuclear and cellular deformation in the *X* axis post 20% compressive strain.

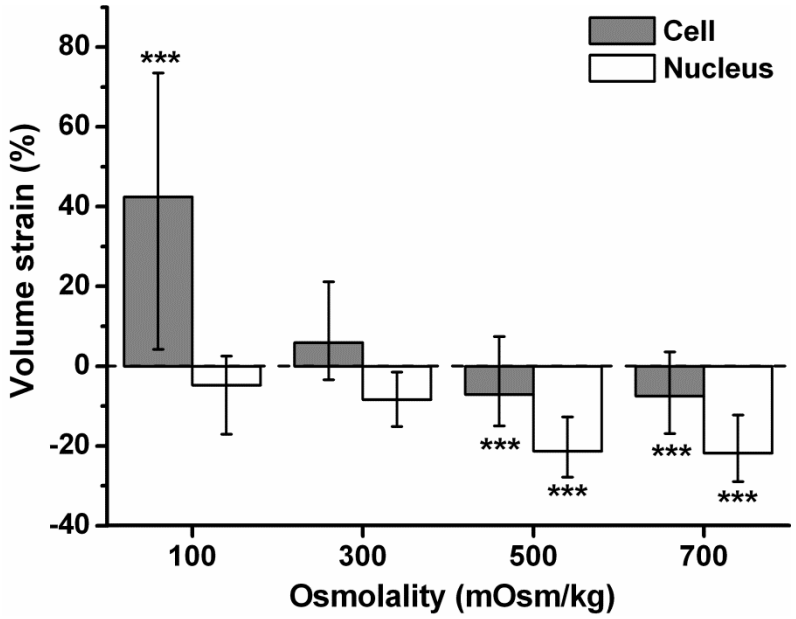

Figure 4.13 Change of cell and nucleus estimated volume post 20% compressive strain. Statistical significance test was performed to compare the osmotic challenge groups against the control group (300-300 mOsm/kg) and also between the 500 and 700 mOsm/kg group (N = 6, n = 80-124 cells per condition) (***p<0.001). Error bars show lower and upper quartile.

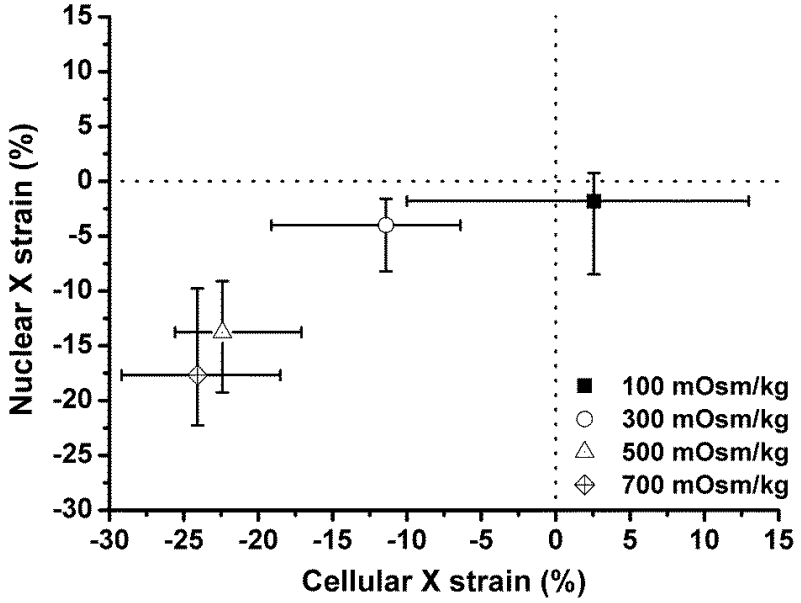

Figure 4.14 Cellular strain against nuclear strain in the X axis post 20% compressive strain (N = 6, n = 80-124 cells per condition). Error bars show lower and upper quartile.

4.5 Discussion

An increase in cell strain along the *X* axis, due to the application of 20% compressive strain, can be seen as the osmolality increases (Figure 4.10 and 4.11). This suggests a change in cell deformability with the alteration of osmotic conditions, despite of the lower cellular *X* strain in the iso-osmotic group when compared to the results of the simulation (Figure 4.8) and to other previous studies (Lee and Knight 2004; Pingguan-Murphy 2006). Cytoskeleton organisation is, in part, responsible in maintaining the mechanical integrity and the resistance to deformation upon application of external physical forces in chondrocytes (Ingber 1994; Trickey *et al.* 2004; Ohashi *et al.* 2006). The exposure of hypo-osmotic challenge to chondrocytes was shown, by a micropipette study, to lower chondrocytes viscosity (Guilak *et al.* 2002), and also to induce Ca^{2+} dependent break down of F-actin (Pritchard and Guilak 2004), dissociation and dispersion of F-actin cortical distribution (Guilak *et al.* 2002; Chao *et al.* 2006). Based on these findings, compared to the iso-osmotic group, one might anticipate a higher cell deformation upon compressive strain under hypo-osmotic condition, however, our results showed otherwise (Figure 4.11). As shown in Chapter 3, the application of hypo-osmotic challenge on agarose seeded chondrocytes induced a limited swelling of the cells due to the containment by the agarose structure. Contained by the agarose, the cells still require fluid intake to balance the osmolality between the environment and the cell, resulting in a swelling pressure which is balanced by the agarose structure. This swelling pressure may increase the cell stiffness, which in turn lower the cellular deformability upon the application of compressive load.

When exposed to hyper-osmotic challenge, cortical arrangement of the F-actin was shown to persist in the chondrocytes (Guilak *et al.* 2002). With addition to the space created between the cell and the agarose as the cell shrink due to hyper-osmotic challenge (as shown by the TEM images in Chapter 3), compared to the iso-osmotic group, one might anticipate an unchanged or a less cell deformation due to the compressive load. Instead, an increase in cellular deformability was observed in the hyper-osmotic group (Figure 4.11), potentially associates with a reduced cell stiffness.

In hypo-osmotic condition, the application of compressive load surprisingly resulted in a significant increase in cell volume (Figure 4.13). An increase in cell stiffness due to the cellular swelling pressure might be responsible for the statistically insignificant deformation in the *X* axis upon the compressive load. Indeed, a portion of the cells

experienced an increase in size along the *X* axis, indicating a distortion of agarose structure due to the swelling pressure post compression. Moreover, the Poisson's ratio of agarose allows lateral expansion of the cell (*Y* strain), which could also contribute to an increase in cell volume. Unfortunately, this unexpected phenomenon cannot be fully explained from the current findings alone. Further investigations are required to understand the effect of osmotic challenge on transfer of mechanical perturbation to chondrocytes upon compression loading, for example, the utilisation of computational simulation of the current set up might be appropriate to elucidate this anomaly.

The nucleus is significantly stiffer and more viscous than the cytoplasm (Guilak *et al.* 2000). Accordingly, reduced levels of nuclear deformation, compared to cell deformation may be expected, as demonstrated by our results (Figure 4.11 and 4.12). Additionally, the lesser deformation may also be due to the time dependent chondrocyte nuclear size recovery after the application of compression load as shown by Knight *et al.*, which was absent for the cell (2002). This recovery might be due to the remodelling of F-actin post compression load (Knight *et al.* 2006), as LINC complex mediates a connection between the cytoskeleton and the nuclear lamina, which plays an essential role in chromatin organisation.

Upon the compressive strain, the nuclear deformations along the *X* axis (the compression axis) are significantly greater than the deformations on the *Y* axis (Figure 4.12), indicating that the deformation is indeed due to the compressive strain instead of the hyper-osmotic challenge, as shown in Chapter 3. Furthermore, in Chapter 3, we have shown that hyper-osmotic challenge induces chromatin condensation, which was shown to stiffen the nucleus (Pajerowski *et al.* 2007). However, culture under hyper-osmotic conditions resulted in a marked increase in nuclear deformation along the *X* axis (Figure 4.12). This increase in deformation is not linearly related to the increase in cellular deformation (Figure 4.14), suggesting that the increase in cellular deformation is not the only factor that induces the increase in nuclear deformation. Potentially the extrusion of water out of the cell may result in alterations in cytoplasmic organisation, allowing the cell deformation to be translated to the nucleus directly. Alternatively, chromatin condensation may induce the formation of inter-chromosomal channels that may be more easily deformed.

In translating the findings of current study, it is essential to note some of the limitations of the current set up. For example, the specimens in current study was exposed to osmotic

challenge for only 30 minutes, whilst time-dependent responses to osmotic challenge have been reported in various studies, including chondrocytes (Borghetti *et al.* 1995; Hopewell and Urban 2003; Dmitrieva *et al.* 2004). Hence, culturing chondrocytes in osmotic challenge media for a longer period of time, such as directly after the seeding procedure, might affects the cell or nucleus deformability differently. Furthermore, as shown in Chapter 3, chondrocytes either shrink or swell upon osmotic challenge, creating a pre-conditioned environment for the agarose that surround the cells. Although osmotic challenge does not alter the swelling property of agarose (Appendix F), this pre-conditioning may alter the compressive strain translation onto the cells.

Significant changes in cellular and nuclear deformability were observed between the 300 and 500 mOsm/kg groups, which falls into the physiological osmolality range of articular cartilage *in vivo* (Urban 1994). This suggests that chondrocytes may deform differently through the depth of articular cartilage due to the variation in osmotic conditions and when the osmolality is altered due to prolonged mechanical load. Moreover, previous studies have suggested that both cell deformation and osmotic challenge affect metabolic processes including gene expression, triggered by a variety of mechanotransduction processes (Ingber 1994; Urban 1994; Guilak *et al.* 1997; Lee and Bader 1997). Thus, it will be interesting to investigate the effects of these changes in deformability on chondrocytes metabolic activity, through studies that permit osmotic challenge and mechanical loading to be coupled or uncoupled. Moreover alteration in gene expression may induce changes to the organisation of cytoplasmic components, such as the cytoskeleton or nuclear organisation that may result in changes to mechanical properties of the cell and nucleus. This may result in a medium/long term adaptation of the cell to osmotic challenge. Chapter 5 investigates these effects through genome wide analysis of expression patterns in chondrocytes following osmotic challenge.

Chapter 5 Genome Wide Analysis on the Effects of Osmotic Challenge

5.1 Introduction

Osmotic challenge has been shown to alter the expression of matrix related genes in chondrocytes (Hung *et al.* 2003; Tew *et al.* 2009) and the exposure of hyper-osmotic condition for 5 hours was shown to induce alterations of genome wide expression profile in osteoarthritic human chondrocytes (Tew *et al.* 2011). However, in Chapter 3, we have shown that the application of hyper-osmotic challenge induced rapid chromatin condensation (<20 seconds) in bovine articular chondrocytes, which is likely to regulate the transcriptional activity at an earlier time point. In this chapter, in order to investigate the effect of hyper-osmotic challenge on chondrocytes transcription regulation, a comprehensive analysis of alterations of gene expression in hyper-osmotically challenged H5 murine chondrocytes was assessed using a cRNA microarray at both 1 and 5 hours. Microarray technology was developed to measure mRNA expression levels of thousands of genes in a number of biological samples simultaneously, so that the discovery of patterns and relationships of their expression become possible (Lockhart and Winzeler 2000). This approach has allowed the investigation to focus on genes that are involved in nuclear organisation and DNA regulation, as well as classic cartilage phenotypic markers that have typically been the focus of previous studies. H5 murine chondrocytes were cultured in monolayer and exposed to 5 osmotic challenge regimens, with variations in osmolality and exposure time. Total RNA of the specimens were extracted and the cRNAs synthesised were measured by microarray. The results were analysed by a series of statistical tests to identify the differentially regulated genes.

5.2 Material and Methods

5.2.1 The Effect Osmotic Challenge on the Chromatin Structure of H5 Murine Chondrocyte Cell Line

In this study, an immortalised mature chondrocyte cell line (H5 strain) derived from the femoral head of male C57BI/6 mice (van Beuningen *et al.* 2002) was used. This decision was taken due to limitations in our in-house facility (the Genome Centre), where bovine microarray was not readily available. The use of cell lines offer several advantages, for example they are relatively easier to culture, cost effective, provide an unlimited supply of relatively pure population of cells and bypass ethical concerns associated with the use of

human and animal tissue. Nonetheless, since cell lines are genetically modified, this may alter their phenotype and their response toward stimuli. However, it was shown that H5 murine chondrocytes synthesise both collagen type II and proteoglycan, that were suppressed upon the addition of IL-1. Additionally, the production of collagen type I and X, the markers for chondrocyte dedifferentiation, were shown to be lower than normal murine cartilage. Prior to the genome wide analysis, the effect of a 15 minute, 1 hour and 5 hours osmotic challenge on H5 chondrocytes chromatin structure was assessed.

Passage 17 cells were seeded onto FCS coated Ø13 mm coverslips (0.17 mm thickness) housed in 24 well plates, with a seeding density of 5×10^4 cells/cm^2. After culturing overnight in DMEM/F12 media supplemented with 15 mM HEPES (Invitrogen) and 10% FCS (pH 7.4), the chondrocytes were osmotically challenged (range 100-800 mOsm/kg) for 15 minutes, 1 hour and 5 hours. The specimens were fixed, stained, imaged and quantified as described previously in section 3.2.3.

5.2.2 Specimen Preparation and Osmotic Challenge

Passage 17 H5 chondrocytes were seeded in 6 wells plates (VWR), with a seeding density of 5×10^4 cells/cm^2 and cultured overnight. Subsequently, the specimens underwent 5 osmotic challenge regimes: 300 mOsm/kg for 1 hour, 300 mOsm/kg for 5 hours, 500 mOsm/kg for 1 hour, 500 mOsm/kg for 5 hours and 500 mOsm/kg for 1 hour followed with 300 mOsm/kg for 4 hours. Each osmotic challenge regime provided 3 replicates, producing a total of 15 specimens for 15 arrays.

5.2.3 RNA Extraction

Total RNA from each specimen was extracted directly after the osmotic challenge regime, using an RNA extraction kit (RNeasy Mini Kit, Qiagen, Crawley, UK). For each well, the osmotic medium was aspirated and replaced with 350 µL Buffer RLT, which is the lysis reagent provided in the kit, supplemented with 1% (v/v) β-mercaptoethanol. The specimen was homogenised by passing the lysate 7 times through a 21-gauge needle (0.8 mm diameter) fitted to a 1 mL RNase-free syringe (both from VWR). 350 µL 70% ethanol (Sigma-Aldrich) was added to the lysate and mixed by pipetting. The specimen was transferred into an RNeasy spin column in a 2 mL collection tube and centrifuged at 8000 × g for 15 seconds. The flow-through was discarded, then 700 µL Buffer RW1 was added

into the RNeasy spin column and centrifuged at 8000 × g for 15 seconds. The flow-through was discarded, then 500 µL Buffer RPE was added into the RNeasy spin column, centrifuged at 8000 × g for 15 seconds and the flow-through was discarded, and this process was repeated with a 2 minutes centrifugation time. The 2 mL collection tube was replaced with a fresh one and the spin column was again centrifuged at 8000 × g for 1 minute, to ensure the removal of Buffer RPE from the specimen. The 2 mL collection tube was replaced with a fresh 1.5 mL collection tube, 30 µL RNase-free water was added into the spin column and it was centrifuged at 8000 × g for 1 minute to elute the RNA. Total RNA of the specimen was quantified by using NanoDrop 1000 (Nanodrop, Labtech International, Ringmer, UK). The integrity of the total RNA was assessed using a capillary gel electrophoresis system (Bioanalyser 2100, Agilent, Wokingham, UK), where the RNA sample should have a low protein and solvent contamination and a good 18s/28s rRNA ratio. All of the RNA specimens used for this microarray study had a RIN score of 10 and a 18s/28s ratio greater than 2.2. The specimens were stored at -80^{o}C prior to further procedures.

5.2.4 cDNA and cRNA Synthesis

The cDNA and cRNA were synthesised from the total RNA by using Illumina TotalPrep RNA Amplification Kit (Ambion, Paisley, UK). For each sample, RNase free water was added to 250 ng of total RNA to produce a final volume of 11 µL and placed on ice. Master mix, consisting of 1 µL T7 Oligo(dT) primer, 2 µL 10 × First Strand Buffer, 4 µL dNTP Mix, 1 µL RNase Inhibitor and 1 µL Array script, was added to the RNA sample, vortex mixed and pulse centrifuged at 1000 × g. The RNA solution was incubated for 2 hours at 42^{o}C, resulting in the production of first strand cDNA.

On ice, 80 µL Second Strand Master mix, consisting of 63 µL DNase and RNase free water, 10 µL 10 × Second Strand Buffer, 4 µL dNTP Mix, 2 µL DNA Polymerase and 1 µL RNase H, was added to the sample, which was vortex mixed and pulse centrifuged at 1000 × g. The sample was incubated for 2 hours at 16^{o}C, resulting in the production of second strand cDNA.

The sample was then transferred into a 1.5 mL tube containing 250 µL cDNA Binding buffer, mixed by pipetting, transferred into a cDNA filter column in a 1.5 mL collection tube and centrifuged at 10000 × g for 1 minute. The flow-through was discarded, 500 µL

Wash buffer was added into the filter column, which was centrifuged at 10000 × g for 1 minute, the flow-through was discarded and the filter column was centrifuged again at 10000 × g for 1 minute. Afterward, 10 μL 50^{o}C DNase and RNase free water was added to the filter column, which was left at room temperature for 2 minutes and centrifuged at 10000 × g for 1 minute to elute the cDNA. In order to elute the remaining cDNA, 9 μL 50^{o}C DNase and RNase free water was added to the filter column and centrifuged at 10000 × g for 2 minutes.

IVT Master mix, consisting of 2.5 μL each of T7 10 × Reaction buffer, T7 Enzyme Mix and Biotin-NTP Mix, was added to the purified cDNA and incubated overnight at 37^{o}C, allowing the transcription of cRNA with biotin incorporation. In order to terminate the reaction, 75 μL DNase and RNase free water was added to the cRNA sample.

In order to obtain a purified cRNA, 350 μL cRNA binding buffer and 250 μL ethanol were added to the sample, mixed by pipetting and transferred into a cRNA filter column in a 1.5 mL collection tube. The sample was centrifuged at 10000 × g for 1 minute and the flow-through was discarded. Afterward, 650 μL Wash buffer was added to the filter column and the sample was centrifuged at 10000 × g for 1 minute. The flow-through was discarded and the sample was centrifuged at 10000 × g for an additional 1 minute to ensure complete removal of the Wash buffer. In order to elute the cRNA, 100 μL 50^{o}C DNase and RNase free water was added to the sample, left for 2 minutes in room temperature and centrifuged at 10000 × g for 1.5 minutes. The cRNA sample was quantified by NanoDrop 1000, and the integrity and fragment sizes were assessed by Agilent Bioanalyser.

5.2.5 Microarray Hybridisation and Scanning

In this study, the cRNA samples were hybridised onto MouseRef-8 v2.0 Expression BeadChips (Illumina), stained with Cy3- streptavidin and the genome wide expression level was measured by Illumina iScan (Illumina, Little Chesterford, UK). The MouseRef-8 v2.0 BeadChip contains 8 arrays, each of which contains 25,697 probes that represent 19,100 genes in total. Each probe consists of a number of beads (up to an average of 30 beads) with specific oligonucleotides attached to them. Each oligonucleotide consists of a 29-mer address sequence and a 50-mer gene-specific sequence.

First, for each sample, at least 750 ng of the cRNA was diluted in RNase free water to give a volume of 5 μL, then 10 μL of HYB was added to the cRNA sample and the sample was

incubated for 5 minutes at 65^{o}C. The hybridisation chamber was assembled and as the cRNA sample cooled down, 15 μL of each cRNA sample was loaded on to each array in the MouseRef-8 v2.0 BeadChip. The BeadChip was then placed into the hybridisation chamber, followed with 20 hours incubation at 58^{o}C to allow the hybridisation process.

The hybridisation chamber was disassembled and the BeadChip was submerged in High-Temperature Wash buffer for 10 minutes at 55^{o}C. Straight after, the BeadChip was placed into a rack containing E1BC Wash buffer, briefly agitated and loaded to an inverted shaker for 5 minutes at room temperature. The BeadChip was then submerged in ethanol for 10 minutes, followed with another 2 minutes wash in E1BC Wash buffer and 10 minutes in Block E1 buffer.

The BeadChip was stained with 0.1% (w/v) Cy3-Streptavidin in Block E1 buffer for 10 minutes at room temperature. The stained BeadChip was submerged in E1BC Wash buffer 5 minutes and dried by centrifugation at 275 × g for 4 minutes at 25^{o}C. Finally, the BeadChip was loaded into the Illumina iScan and the fluorescent signals from each probe within the arrays were measured. Measurement of RNA integrity, cDNA and cRNA synthesis, microarray hybridisation and scanning were done by Dr. Rosamond A. Nuamah from The Genome Centre, William Harvey Research Institute, Barts and The London School of Medicine and Dentistry, Queen Mary, University of London, London, UK.

5.3 Microarray Analysis

5.3.1 Quantile Normalisation

In experiments involving multiple arrays, normalisation is required to eliminate obscuring variation in expression level. The obscuring variation might arise from variations either in the experimental procedure or the production of the material, such as the different number of beads in each probe of the BeadChip which may lead to over or under expressed probes. One of the widely used normalisation methods for microarray analysis is quantile normalisation, as utilised by Bolstad *et al.* (2003).

In quantile normalisation, the aim is to make the distribution of probe intensities in each array for a set of arrays the same. When two distributions are the same, the quantile-quantile plot of these distributions produces a straight diagonal line. Divergence from the diagonal line shows an inequality between the distributions. Two distributions of arrays can then be made the same by projecting the probe intensities to the diagonal line of their quantile-quantile plot. Bolstad *et al.* (2003) showed that this can be done by substituting each intensity reading with its mean quantile.

Quantile normalisation was applied to the genome wide analysis results by using the software GenomeStudio (Illumina, Little Chesterford, UK). In order to quantile normalise two or more arrays:

1. The intensity readings of each array were listed corresponding to the probe, which is referred as the original distribution.
2. The probe intensities of each array were sorted in a descending order, which is referred as the sorted distribution.
3. Ranks were given to the values of the sorted distribution, where the highest value was given the rank (R) = 1, the second highest had R = 2 and so on, until the lowest value had $R = g$, where g is the number of probes in the array.
4. For each rank, the arithmetical mean of the readings from the arrays was calculated and substituted back to the sorted distribution of each array. At this point, the readings for each array are identical in value and order.
5. Each array with the new values was then sorted back to its original distribution.

5.3.2 Hierarchical Clustering

In order to cluster the arrays based on their probe intensities, all of the 15 arrays were clustered by an agglomerative hierarchical clustering with un-weighted pair group method (Jain and Dubes 1988), which was applied by an algorithm written in MATLAB and visualised in form of a dendrogram.

The difference between a pair of arrays was calculated by the Taxicab geometry (Krause 1975), as described by the following equation:

$$d(X_p, X_q) = \sum_{i=1}^{n} |x_{pi} - x_{qi}| \qquad (5.1)$$

Where $d(X_p, X_q)$ is the distance between the arrays *p* and *q*, *n* is the number of probes from each array, x_{pi} and x_{qi} are the intensity readings for the *i* th probe from the array *p* and *q*, respectively.

Agglomerative hierarchical clustering starts with a disjointed clustering, which places each observation (in this case each array) in an individual cluster, i.e. 15 different clusters. With each step of clustering, the distance between each pair of clusters was calculated, and then a pair of clusters with the minimum distance between them was merged as a new cluster. In the first step, 105 different distances were calculated, representing 105 possible pairs from 15 clusters. A new cluster was formed by merging a pair of arrays with the closest distance. At this stage, there were 14 clusters, where one of the clusters comprised of 2 arrays. In the second step, 91 different distances were calculated representing 91 possible pairs from 14 clusters. In order to calculate the distance between a pair of clusters with more than 1 array, un-weighted pair group method was used, as described by the following equation:

$$D(C_r, C_s) = \frac{1}{n_r n_s} \sum_{i=1}^{n_r} \sum_{j=1}^{n_s} d(X_{ri}, X_{sj}) \qquad (5.2)$$

Where $D(C_r, C_s)$ is the distance between the clusters *r* and *s*, n_r and n_s are the number of arrays within the clusters *r* and *s*, respectively, $d(X_{ri}, X_{sj})$ is the distance between the *i* th array in the cluster *r* and the *j* th array in the cluster *s*, which was calculated by Taxicab geometry as described in equation (5.1). Another new cluster was formed by merging a pair of clusters with the closest distance, thus the total number of clusters was reduced to 13 clusters. This clustering step was repeated until all the arrays were fully connected to each

other, forming a single cluster. The resulting cluster was then visualised in the form of a dendrogram, with the arrays on the *X* axis and the distance between them on the *Y* axis.

5.3.3 Empirical Bayesian Method

The next step was to select the genes that are expressed differently between the two conditions that were being compared. Two selection parameters were used to pick these genes: their statistical difference and the amount of change assessed as their fold change in expression. Differentially expressed genes were assessed by calculating the *p*-value between each probe of two osmotic conditions, using the empirical Bayesian method (Smyth 2004) on the quantile normalised results, utilising the algorithm written in MATLAB. The empirical Bayesian method utilises the expression profile from the total genes in the array to assist the inference about each gene individually, which is favourable than more conventional differential statistical test, like the Student's *t*-test.

First, the moderated t-statistics for a chosen probe ($\tilde{t}_p$) was calculated by

$$\tilde{t}_p = \frac{\beta_p}{\tilde{s}_p\sqrt{v_p}} \qquad (5.3)$$

Where β_p is the difference between means of the two groups that being compared and v_p is the inverse of the number of arrays, where in this study $v_p = 1/6$, as there were 6 arrays representing the two groups. The posterior sample variance ($\tilde{s}_p$) was given by

$$\tilde{s}_p{}^2 = \frac{d_0 {s_0}^2 + d_p {s_p}^2}{d_0 + d_p} \qquad (5.4)$$

Where ${s_p}^2$ is the observed sample variance, d_p is the degree of freedom (in this study, $d_p = no.of\ arrays - 2 = 4$), ${s_0}^2$ and d_0 are the prior estimators of sample variance and degree of freedom, which are estimated from the information given by all of the probes tested in the array. The observed sample variance (${s_p}^2$) was calculated by

$${s_p}^2 = \frac{(n_1 - 1){s_1}^2 + (n_2 - 1){s_2}^2}{(n_1 + n_2 - 2)} \qquad (5.5)$$

Where n_1 and n_2 are the number of arrays representing the first and second groups that were being compared, whilst ${s_1}^2$ and ${s_2}^2$ are the variance of the corresponding probe intensity readings in the first and second group. d_0 was determined by solving the following equation:

$$\psi'\left(\frac{d_0}{2}\right) = mean\left\{\frac{\left(e_p - \bar{e}\right)^2 P}{(P-1)} - \psi'\left(\frac{d_p}{2}\right)\right\} \quad (5.6)$$

Where P is the number of probes in the array, $\psi'()$ is the trigamma function, and $\bar{e}$ is the mean of e_p of all the probes in the array, which was calculated by

$$e_p = log\left(s_p{}^2\right) - \psi\left(\frac{d_p}{2}\right) + log\left(\frac{d_p}{2}\right) \quad (5.7)$$

Where $\psi()$ is the digamma function. Once d_0 was estimated, ${s_0}^2$ was then given by

$${s_0}^2 = exp\left\{\bar{e} + \psi\left(\frac{d_0}{2}\right) - log\left(\frac{d_0}{2}\right)\right\} \quad (5.8)$$

The *p*-value was then determined based on the moderated *t*-statistic and used for the next procedure in the analysis of differentially expressed genes.

5.3.4 Type I Error Correction

Microarray analysis involves a large number of simultaneous hypothesis tests, which increase the probability of type I error, where expression levels of a probe that being compared are determined to be statistically significance by chance. Type I error or the false discovery rate can be corrected by adjusting the obtained *p*-value in several methods, such as (in their stringency order) Bonferroni (Feller 1971), Holm (1979) and Benjamini-Hochberg (1995). The Bonferroni method is too stringent for this study, thus *q*-values (the adjusted *p*-values) were calculated from the *p*-values obtained, by the Benjamini-Hochberg method, which was utilised by an algorithm written in MATLAB:

1. *p*-values were sorted in ascending order ($p_1 < p_2 < p_3 < \cdots < p_G$, where G is the number of probes in the array).
2. Ranks were given to each *p*-value, where the smallest *p*-value (p_1) was given the rank (R_1) = 1, p_2 was given $R_2 = 2$ and so on, until p_G was given $R_G = G$.
3. Then the *q*-values was calculated by

$$q_n = p_n \times \frac{G}{R_n} \quad (5.9)$$

where n = 1, 2, 3, ... , G.

5.3.5 Detection *p*-value

Each array within the BeadChip contains a number of negative control probes that are thermodynamically equivalent to the regular probes, without specific targets in the transcriptome. The signals from these negative control probes represent the amount of non-specific cross-hybridisation and other sources of noise. These signals were statistically tested against the intensity readings in the array, producing *Detection p-values*, which is the probability that an intensity reading of a probe is derived from the background fluorescence level. Thus, the higher the signal level, the lower the probability that it could be due to non-specific sources. In this study, a value of 5% was chosen as the threshold for the *p*-value, i.e. when $p \leq 0.05$, the signal is assumed to be statistically significant or *present*, and by contrast, when $p > 0.05$, the signal is assumed to be statistically insignificant or *absent*.

In this study, for every probe in an array that had an *absent* signal, the signal of the corresponding probe in the other 2 replicate arrays of the same osmotic group is either *absent* or has an intensity less than double of the mean noise level, i.e. weakly expressed. A statistical test on the readings of a probe from 2 osmotic groups that weakly expressed can still result in a low *p*-value, i.e. high statistical significant, which can be misleading in the gene selection process. Thus, if *absent* signals are present in both groups, the corresponding probe was filtered out of the selection process.

5.3.6 Fold Change

For each probe, fold change was calculated as the ratio of the mean intensity readings between the osmotic groups that were being compared. For example, in comparing osmotic group 1 vs. osmotic group 2, the fold change of each probe was calculated by dividing the means intensity readings of the probe from group 2 by the mean intensity readings from the corresponding probe from group 1. Fold change greater than 1 shows an up-regulation of the corresponding gene, whilst a value less than 1 shows a down-regulation of the gene.

In some cases, the intensity reading of a probe is less than the mean noise level. Calculating the fold change using these values can be misleading. For example, dividing a weakly expressed probe by a value below the noise level can result in a high fold-change, giving the notion that the gene is highly up-regulated. In order to correct for this misinterpretation of fold change, the intensity readings that lie below the noise level were substituted with the mean noise level, which is 135.

5.3.7 Gene Selection

In summary, for each comparison of a pair of osmotic groups the selection process involves several steps:

1. The *q*-value for each probe was calculated.
2. The probes that have one or more absent signals in both osmotic groups were discarded.
3. For the remaining probes, intensity values below the mean noise level were substituted with the mean noise value.
4. The fold change for the remaining probes was calculated.
5. The probes with *q*-value more than 0.05 or fold change less than 1.5 were discarded, leaving the highly regulated genes that are statistically significant. Number of probes chosen with different threshold level (*q*-value and fold change) can be seen in Appendix H.

5.3.8 Functional Annotation

The selected genes underwent functional annotation analysis by using a web-accessible software package DAVID Bioinformatics Resources 6.7 (Huang *et al.* 2009), which integrates statistical algorithms with the information from more than 40 annotation categories, such as Gene Ontology (GO), Kyoto Encyclopaedia of Genes and Genomes (KEGG) Pathway, Online Mendelian Inheritance in Man (OMIM), Entrez Gene, Ensembl, BioCarta Pathways and many other databases.

In this study, we focused on the annotation from GO and KEGG. The aim of the GO consortium is to standardise the representation of gene and gene product attributes across species and databases. GO terms are grouped into 3 main domains: cellular component, molecular function and biological process. Cellular component describes the genes with products located at the subcellular and macromolecular complexes level. Molecular function describes the activity that the gene product is involved in, such as catalytic or binding activities. Biological process describes the process that the gene is involved in, where a process is a series of events or molecular functions with a defined beginning and end. GO is structured as a hierarchically directed acyclic graph, with the three main domains as the starting points (Level 1). Terms at higher levels describe more specific ontology defined from the more general terms below them, and this relationship is not

limited by the domain, where terms for one domain can be defined by terms from other domains.

KEGG Pathway is a database of manually drawn pathway maps representing the current knowledge on the molecular interaction and reaction networks for: metabolism, genetic information processing, environmental information processing, cellular processes, organismal systems, human diseases and drug development. Principally, KEGG Pathway relates the genes to the signalling pathways and protein interactions that they are involved in.

Each probe in the BeadChip array has a unique Illumina ID (ILMN ID). For each comparison between a pair of osmotic groups, the ILMN IDs of the selected genes and the whole array were submitted to DAVID as the *Gene List* and *Background*, respectively. These ILMN IDs were then assigned with their corresponding DAVID identifiers (DAVID IDs), which enables the mapping of inputted IDs across the entire database. In some cases, an ILMN ID does not have a corresponding DAVID ID, which indicates that the annotation for this particular probe was not available at the time of the analysis, thus it was omitted from the annotation analysis (Table 5.1 and 5.3). At this stage, we have a list of GO and KEGG terms that correspond to the DAVID IDs from the *Gene List*. In order to assess the degree of enrichment for each term, the Fisher's exact test was used to compare the percentage of *Gene List* against the percentage of *Background* corresponding to the term, producing a *p-value* for each term. For comparisons involving a large number of annotations (> 100), the annotation terms were then clustered by Fuzzy clustering, based on the genes assigned to the annotation term, assuming that annotations with similar assigned genes have similar biological meaning. Clustering the GO and KEGG terms reduces the redundancy nature of annotations. The term clusters were ranked by their *Enrichment Score*, which is calculated by

$$E = -\log(P) \qquad (5.10)$$

$$P = \sqrt[n]{p_1 p_2 \dots p_n} \qquad (5.11)$$

Where E is the *Enrichment Score* for a term cluster, P is the combined p-value for the cluster which is the geometric mean of the enrichment p-values of all the terms in the cluster, n is the number of annotation terms in the cluster and p_n is the p-value of the n-th annotation term in the cluster.

5.4 Results

5.4.1 Osmotic Challenge Alters Chromatin Condensation Level in H5 Cells

To assess the effect of different osmolalities and exposure times on the H5 murine chondrocyte nucleus, the cells were cultured in monolayer, fixed, stained with Hoechst dye and imaged by confocal microscopy (Figure 5.1-5.3). As shown in section 3.3.1 with bovine primary chondrocytes, DNA staining appeared most homogeneous in the H5 nuclei exposed to 100 mOsm/kg followed by a marked increase in chromatin condensation between 300 and 500 mOsm/kg and a gradual increase afterwards, as reflected in the chromatin condensation parameter (Figure 5.4). From the 100 to 500 mOsm/kg samples (Figure 5.1-5.3), a number of localised areas of intense DNA staining, i.e. heterochromatin, can be seen within the H5 nuclei, which is less apparent in the bovine chondrocytes nuclei (Figure 3.4). At 1 and 5 hours exposure times, the chromatin condensation also markedly increased between 300 and 500 mOsm/kg (Figure 5.4). However, the level of osmotically-induced chromatin condensation reduces with time (Figure 5.4). Additionally, prolonged culture in 700 mOsm/kg induced a significant distortion of the nuclei, suggesting structural damage to the cell or nucleus.

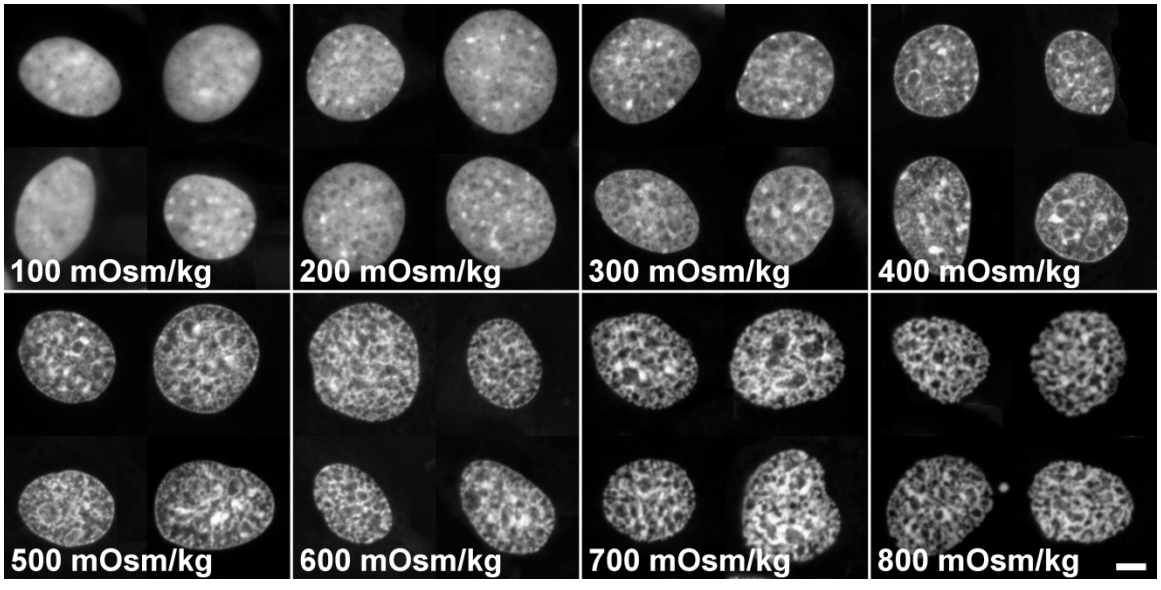

Figure 5.1 Monolayer H5 murine chondrocytes nuclei cultured in media with osmolalities ranging from 100 to 800 mOsm/kg for 15 minutes, followed with fixation (Bar: 5 μm).

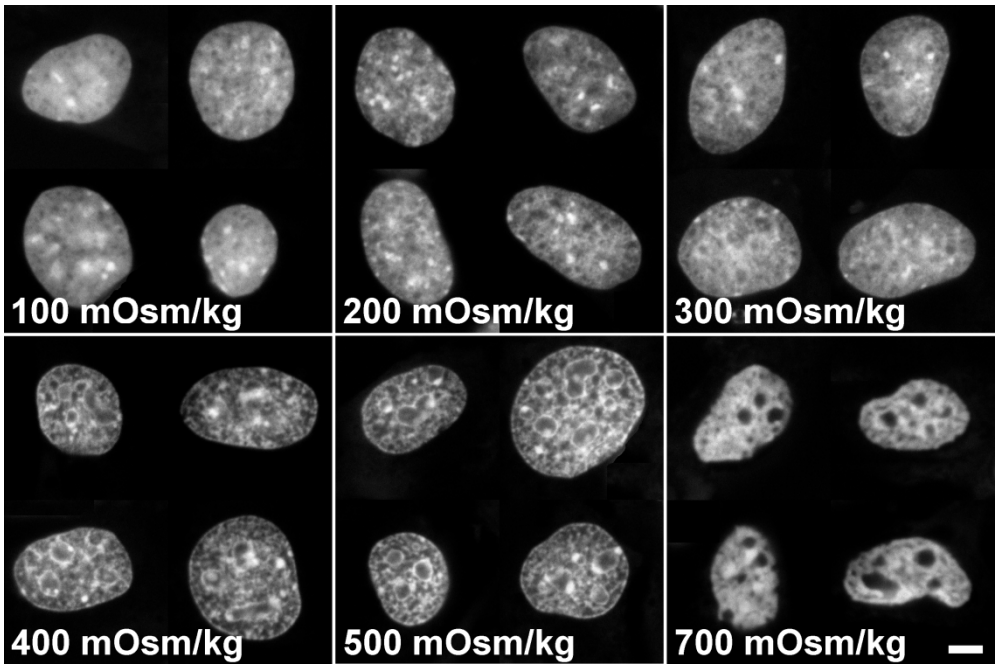

Figure 5.2 Monolayer H5 murine chondrocytes nuclei cultured in media with osmolalities ranging from 100 to 800 mOsm/kg for 1 hour, followed with fixation (Bar: 5 μm).

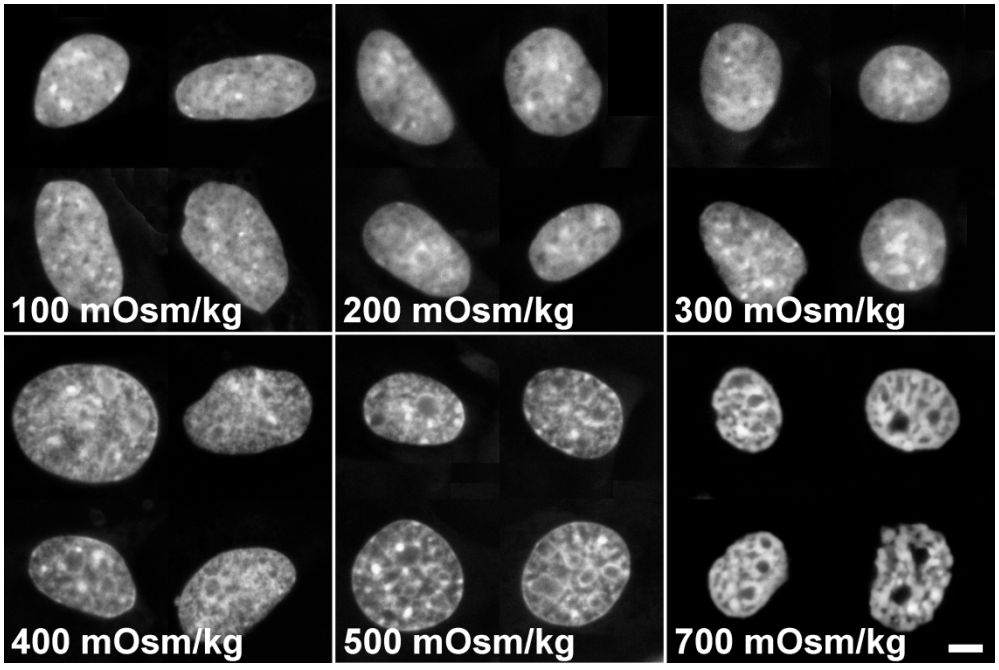

Figure 5.3 Monolayer H5 murine chondrocytes nuclei cultured in media with osmolalities ranging from 100 to 800 mOsm/kg for 5 hours, followed with fixation (Bar: 5 μm).

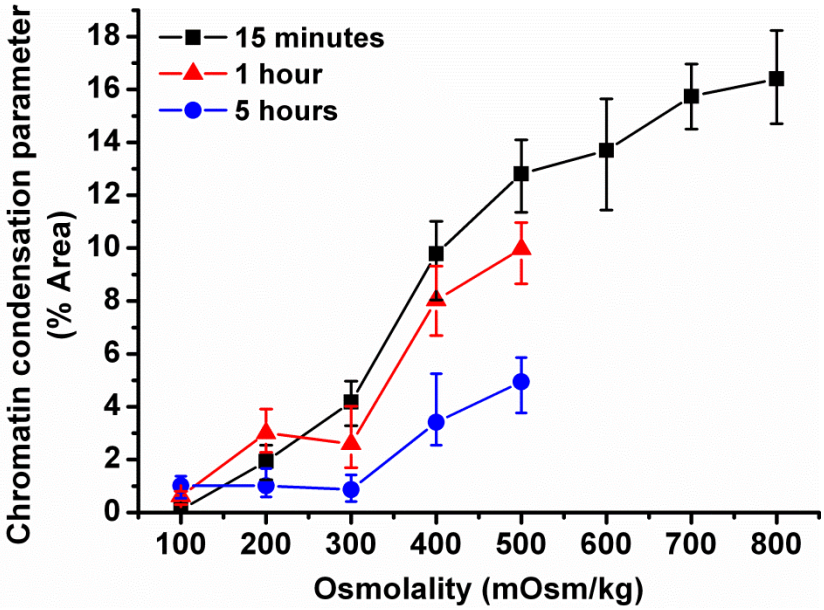

Figure 5.4 Chromatin condensation parameter quantified from images of the nuclear from each osmotic group, exposed to 15 minutes, 1 and 5 hours of osmotic challenge (N = 1, n = 40 nuclei per condition). Error bars show lower and upper quartile.

5.4.2 Hierarchical Clustering

The 15 samples were divided into 5 clusters based on the similarity of the probe intensities (Figure 5.5). Each osmotic group was well defined into each cluster with the exception of the 3rd sample exposed to 500 mOsm/kg for 1 hour (B3). The 500 mOsm/kg 5 hours group (D) has the greatest distance from the other osmotic groups, whilst a degree of similarity can be observed between the 1 hour exposure groups (A, B) and between the 300 mOsm/kg 5 hours and 500 mOsm/kg 1 hour + 300 mOsm/kg 4 hours groups (C, E).

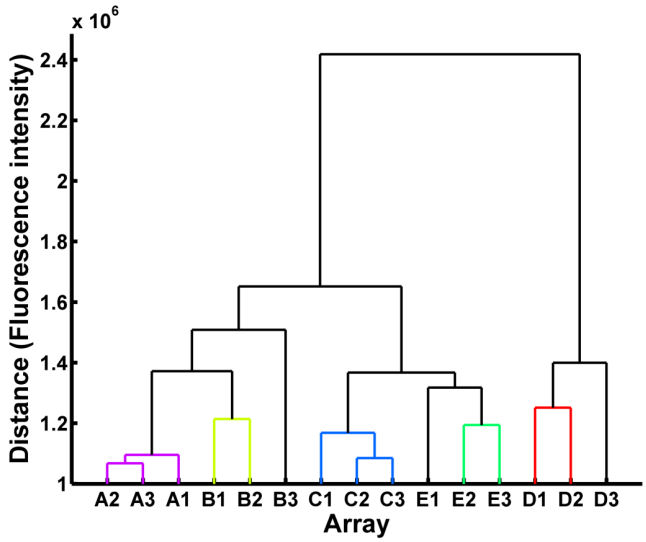

Figure 5.5 Dendrogram showing the hierarchical clustering of the 15 arrays involved in this study. A - 300 mOsm/kg for 1 hour, B - 500 mOsm/kg for 1 hour, C - 300 mOsm/kg for 5 hours, D - 500 mOsm/kg for 5 hours and E - 500 mOsm/kg 1 hour followed with 300 mOsm/kg for 4 hours.

5.4.3 Expression Profiles

The average signal intensity of each probe from the 300 and 500 mOsm/kg specimens at 1 hour and 5 hours exposure times are plotted in Figure 5.6. It is evident that deviation from the equal intensity level (red line) was greater at 5 hours, compared to the 1 hour. However, significant deviations to the right and below the equal intensity level were observed in the 1 hour group, indicating a suppression of a number of genes upon the exposure to 500 mOsm/kg.

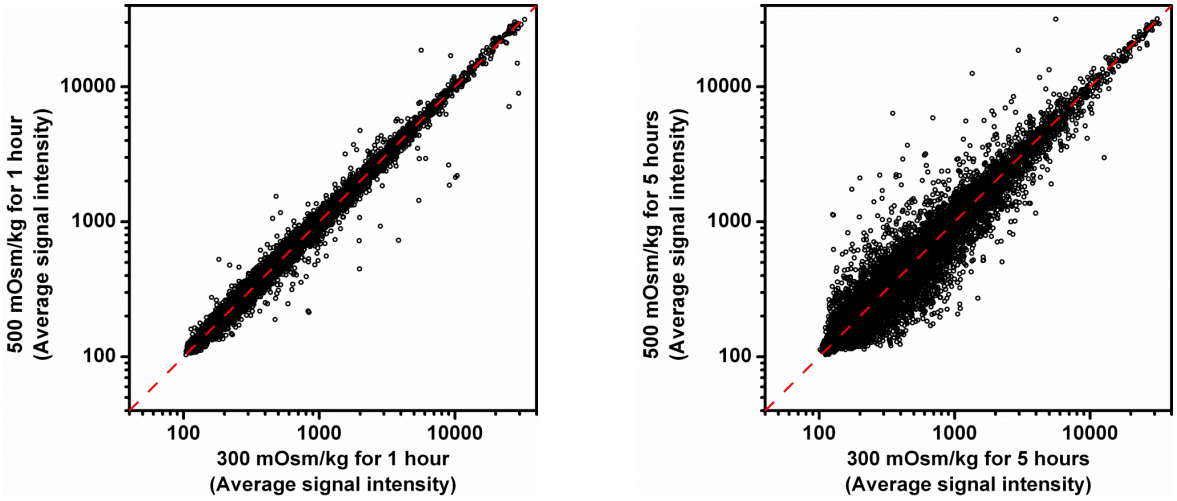

Figure 5.6 Comparisons of average signal intensities between 300 and 500 mOsm/kg specimens at 1 hour (left) and between 300 and 500 mOsm/kg specimens at 5 hours (right). The red line indicates the level of the equal signal intensity between the two groups. Red line represents the equal intensity level.

5.4.4 Differential Expressions: 300 vs. 500 mOsm/kg 1 hour

The first comparison involved the expression profiles from chondrocytes exposed to 300 and 500 mOsm/kg for 1 hour. The signal intensities were compared between the two osmotic groups, resulting in a *q*-value and a fold change value for each probe. The probes with a *q*-value less than 0.05 and a fold change more than 1.5 were selected as the differentially expressed probes, as shown in Figure 5.7 as the shaded area. Out of 25,697 probes in the array, 10,619 probes passed through the *present-absent* filter as described in section 5.3.5. In this comparison, 18 genes were up-regulated, whilst 48 genes were down-regulated. The top 10 regulated genes in this comparison are listed in Table 5.2. The number of annotation terms registered for these genes are listed in Table 5.1 and the detailed annotations can be seen in Appendix I (Table I.1 and I.2). In general, both up- and down-regulated genes are involved in transcription regulation, responses to stress and kinase related processes. Additionally, the down-regulated genes are also involved in chromatin assembly (the histone genes) and regulation of programmed cell death.

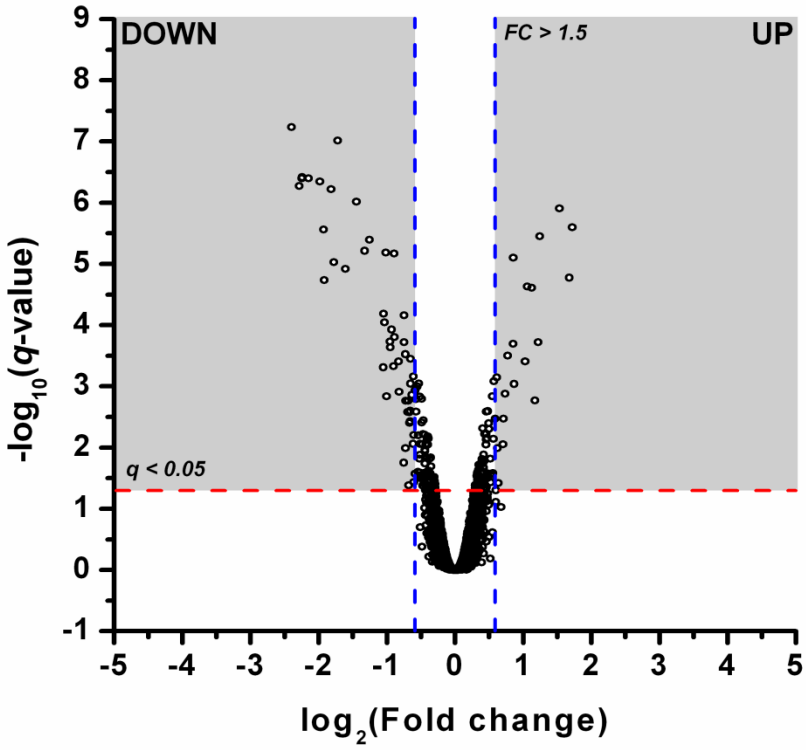

Figure 5.7 Volcano plot for the genes expressed in samples subjected 300 mOsm/kg for 1 hour compared to 500 mOsm/kg for 1 hour, where the *X*-axis is the binary logarithm of fold change and the *Y*-axis is $-\log_{10}$ of *q*-value. The horizontal red line represents the level of $q = 0.05$, whereas the two vertical blue lines represent fold change cut-off threshold at 1.5 fold.

Table 5.1 Number of up- and down-regulated genes chosen from the comparison 300 mOsm/kg 1 hour vs. 500 mOsm/kg 1 hour.

Group	Number of genes (probes)
Total in array	19,100 (25,697)
Without *absent* in both comparison groups	7,387 (10,619)
Up-regulated (q<0.05, $\log_2$(FC) > 0.58)	
Total selected	18 (21)
DAVID IDs	17
Biological process (GO)	13
Cellular component (GO)	9
Molecular function (GO)	10
Pathways (KEGG)	6
Down-regulated (q<0.05, $\log_2$(FC) < -0.58)	
Total selected	48 (49)
DAVID IDs	44
Biological process (GO)	40
Cellular component (GO)	27
Molecular function (GO)	37
Pathways (KEGG)	22

Table 5.2 Top 10 of differentially up- and down-regulated genes (sorted by fold change) from the comparison 300 mOsm/kg 1 hour vs. 500 mOsm/kg 1 hour, with the binary logarithm of fold change and the *q*-value.

Gene	$\log_2$(Fold change)	*q*-value
Up-regulated		
U6 small nuclear RNA	1.722027	2.53E-06
myeloid differentiation primary response gene 116	1.679128	1.68E-05
heat shock protein 1A	1.532801	1.23E-06
heparan sulfate proteoglycan 2	1.244711	3.55E-06
protein phosphatase 1, regulatory subunit 10	1.222973	1.89E-04
protein phosphatase 1, regulatory subunit 10	1.171051	1.70E-03
hexamethylene bis-acetamide inducible 1	1.124966	2.45E-05
similar to spermidine/spermine N1-acetyltransferase	1.060784	2.34E-05
dual specificity phosphatase 1	1.031225	3.93E-04
immediate early response 3	0.869822	9.13E-04
Down-regulated		
inhibitor of DNA binding 1	-2.39691	5.82E-08
histone cluster 1, H2ah	-2.28634	5.32E-07
histone cluster 1, H2ad	-2.2473	4.00E-07
histone cluster 1, H2ak	-2.24099	3.83E-07
histone cluster 1, H2ag	-2.14624	3.99E-07
histone cluster 1, H2ab	-1.98141	4.50E-07
small nucleolar RNA, H/ACA box 65	-1.92845	2.74E-06
histone cluster 1, H2an	-1.91538	1.83E-05
histone cluster 1, H2ac	-1.81684	6.03E-07
histone cluster 1, H2af	-1.77434	9.41E-06

5.4.5 Differential Expressions: 300 vs. 500 mOsm/kg 5 hours

The probe signal intensities from the samples exposed to 300 and 500 mOsm/kg for 5 hours were compared. The probes with a *q*-value less than 0.05 and a fold change more than 1.5 were selected as the differentially expressed probes, as shown in Figure 5.8 as the shaded area. In this comparison, 10,116 probes passed through the *present-absent* filter, whilst 559 genes were up-regulated and 730 genes were down-regulated (Table 5.3). Top 10 regulated genes in this comparison are listed in Table 5.4.

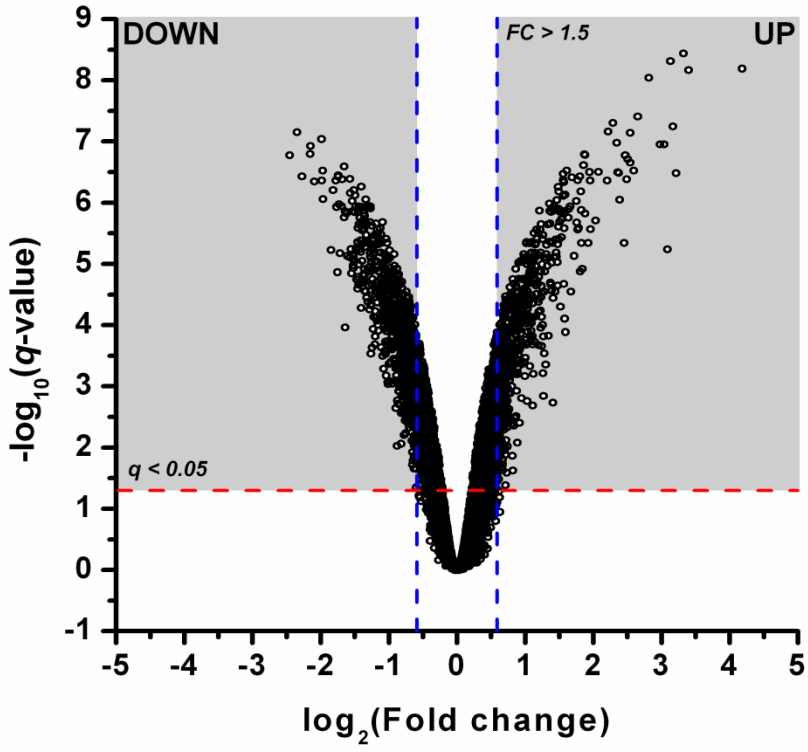

Figure 5.8 Volcano plot for the genes expressed in samples subjected 300 mOsm/kg for 5 hours compared to 500 mOsm/kg for 5 hours, where the *X*-axis is the binary logarithm of fold change and the *Y*-axis is $-\log_{10}$ of *q*-value. The horizontal red line represents the level of $q = 0.05$, whereas the two vertical blue lines represent fold change cut-off threshold at 1.5 fold.

Due to the large number of regulated genes, the annotation terms were clustered based on the genes assigned to each annotation. Only clusters with an *Enrichment Score* greater than 2 (equivalent to $p < 0.01$) were considered in the functional annotation analysis (Table 5.6 and Table 5.7). The detailed annotation clustering can be found in Appendix I (Table I.3 and I.4).

From the annotation clustering for up-regulated genes (Table 5.6), extended hyper-osmotic exposure (500 mOsm/kg 5 hours) promotes transcription regulator and repressor activity, both positive and negative regulation of cellular biosynthetic processes, negative regulation of apoptosis, skeletal system development, chromatin assembly and various kinase related activities. In terms of sub-cellular location, the majority of the up-regulated genes were related to the lytic vacuole, cytoplasmic membrane-bounded vesicle, nucleoplasm and chromatin. These genes were also involved in MAPK signalling, the cell cycle and renal cell carcinoma pathways (Table 5.5).

From the down-regulated genes (Table 5.7), prolonged hyper-osmotic exposure suppresses response to DNA damage stimulus, M phase of mitotic cycle, G1/S transition of mitotic cell cycle, mRNA metabolic process, zinc ion binding, pseudouridine synthesis, protein localisation, ribonucleoprotein complex biogenesis, RNA biosynthetic process, translation, chromosome segregation and chromatin modification. These down-regulated genes were related to the nucleolus, nuceloplasm, spliceosome, centrosome and mitochondrial ribosome. Additionally, these genes were also involved in cell cycle, p53 signalling pathway and RNA degradation pathways (Table 5.5).

Table 5.3 Number of up- and down-regulated probes and genes chosen from the comparison 300 mOsm/kg 5 hours vs. 500 mOsm/kg 5 hours.

Group	Number of genes (probes)
Total	19,100 (25,697)
Without *absent* in both comparison groups	7,074 (10,116)
Up-regulated (q<0.05, $\log_2$(FC) > 0.58)	
Total selected	559 (627)
DAVID IDs	546
Biological process (GO)	410
Cellular component (GO)	325
Molecular function (GO)	391
Pathways (KEGG)	193
Down-regulated (q<0.05, $\log_2$(FC) < -0.58)	
Total selected	730 (834)
DAVID IDs	722
Biological process (GO)	461
Cellular component (GO)	408
Molecular function (GO)	442
Pathways (KEGG)	161

Table 5.4 Top 10 of differentially up- and down-regulated genes (sorted by fold change) from the comparison 300 mOsm/kg 5 hours vs. 500 mOsm/kg 5 hours, with the binary logarithm of fold change and the *q*-value.

Gene	$\log_2$(Fold change)	*q*-value
Up-regulated		
solute carrier organic anion transporter family, member 4a1	4.184998	6.47E-09
heat shock protein 1A	3.397621	6.81E-09
cyclin-dependent kinase inhibitor 1C (P57)	3.321554	3.67E-09
similar to spermidine/spermine N1-acetyltransferase	3.215464	3.29E-07
aldo-keto reductase family 1, member B3 (aldose reductase)	3.089903	5.78E-06
cDNA sequence BC064033	3.066414	5.65E-08
pleckstrin homology-like domain, family A, member 2	3.051937	4.89E-09
crystallin, alpha B	3.039099	1.11E-07
glucose-fructose oxidoreductase domain containing 1	2.979749	1.11E-07
neural precursor cell expressed, developmentally down-regulated gene 9	2.813804	9.11E-09
Down-regulated		
RIKEN cDNA 2810432D09 gene	-2.45193	1.68E-07
gem (nuclear organelle) associated protein 4	-2.34691	7.09E-08
gem (nuclear organelle) associated protein 4	-2.2729	3.74E-07
zinc finger, DHHC domain containing 12	-2.15214	1.59E-07
cell division cycle associated 7	-2.14839	1.18E-07
connective tissue growth factor	-2.09213	4.53E-07
transmembrane protein 41a	-1.98738	9.12E-08
ADP-ribosylation factor GTPase activating protein 1	-1.9834	4.31E-07
ankyrin repeat domain 49	-1.96942	2.98E-07
RIKEN cDNA 1810009O10 gene	-1.96494	8.73E-07

Table 5.5 Top 3 of up- and down-regulated KEGG pathway annotations (sorted by *p*-value) from the comparison 300 mOsm/kg vs. 500 mOsm/kg for 5 hours, with the gene counts and *p*-values.

Pathways	Gene count	*p*-value
Up-regulation		
MAPK signalling pathway	26	1.98E-06
Cell cycle	12	3.53E-03
Renal cell carcinoma	8	8.49E-03
Down-regulation		
Cell cycle	15	1.32E-05
p53 signalling pathway	9	7.04E-04
RNA degradation	8	1.11E-03

Table 5.6 Annotation clusters of the differentially up-regulated genes from the comparison 300 mOsm/kg 5 hours vs. 500 mOsm/kg 5 hours, with the enrichment score, the representative annotation members, the gene count and the *p*-value. The code represents the domain of the annotation.

Cluster	Enrichment score	Annotation	Code*	Gene count	*p*-value
1	6.42	transcription regulator activity	MF	69	9.59E-08
		positive regulation of cellular biosynthetic process	BP	39	1.73E-06
2	4.61	transcription repressor activity	MF	20	1.49E-05
		negative regulation of cellular biosynthetic process	BP	31	1.70E-05
3	4.04	blood vessel morphogenesis	BP	19	3.01E-05
4	3.28	lytic vacuole	CC	15	2.34E-04
5	2.93	negative regulation of apoptosis	BP	18	9.18E-04
6	2.7	embryonic development ending in birth or egg hatching	BP	29	8.89E-05
7	2.55	protein dimerization activity	MF	25	6.78E-05
8	2.42	skeletal system development	BP	21	3.99E-04
9	2.35	response to wounding	BP	25	1.35E-04
10	2.34	protein kinase binding	MF	7	1.77E-02
11	2.28	cytoplasmic membrane-bounded vesicle	CC	22	2.63E-03
12	2.24	transcription factor binding	MF	19	2.18E-03
13	2.16	protein serine/threonine kinase inhibitor activity	MF	6	2.43E-06
		negative regulation of protein kinase activity	BP	9	1.29E-04
14	2.14	nucleoplasm	CC	27	7.04E-03
15	2.12	protein amino acid dephosphorylation	BP	11	2.30E-03
		MAP kinase tyrosine/serine/threonine phosphatase activity	MF	4	4.53E-03
16	2.06	chromatin assembly	BP	9	1.82E-03
		chromatin	CC	12	3.80E-03
17	2.06	late endosome	CC	7	8.89E-04

*BP = Biological process from GO CC = Cellular component from GO MF = Molecular function from GO

Table 5.7 Annotation clusters of the differentially down-regulated genes from the comparison 300 mOsm/kg 5 hours vs. 500 mOsm/kg 5 hours, with the enrichment score, the representative annotation members, the gene count and the *p*-value. The code represents the domain of the annotation.

Cluster	Enrichment score	Annotation	Code*	Gene count	*p*-value
1	21.85	nucleolus	CC	53	8.00E-23
2	20.94	nucleoplasm	CC	51	1.24E-09
3	6.32	response to DNA damage stimulus	BP	32	4.83E-08
4	6.12	M phase of mitotic cell cycle	BP	22	4.06E-06
5	5.93	ncRNA processing	BP	22	9.98E-08
6	5.78	spliceosome	CC	15	5.96E-05
		mRNA metabolic process	BP	26	7.91E-05
7	5.14	zinc ion binding	MF	121	2.99E-11
8	4.89	chromosome, centromeric region	CC	15	1.03E-05
9	4.32	pseudouridine synthase activity	MF	6	8.28E-06
		pseudouridine synthesis	BP	6	1.73E-05
10	4.05	establishment of protein localization	BP	44	4.24E-05
11	3.35	ribonucleoprotein complex biogenesis	BP	20	3.84E-07
		preribosome	CC	4	8.27E-03
12	2.95	centrosome	CC	17	8.87E-05
13	2.72	RNA biosynthetic process	BP	17	1.05E-05
		DNA-directed RNA polymerase II, holoenzyme	CC	8	2.09E-03
14	2.67	mitochondrial ribosome	CC	9	5.43E-05
		translation	BP	22	1.09E-03
		structural constituent of ribosome	MF	12	9.49E-03
15	2.57	condensed chromosome, centromeric region	CC	8	2.63E-03
		chromosome segregation	BP	7	2.67E-02
16	2.35	G1/S transition of mitotic cell cycle	BP	5	1.42E-02
17	2.33	negative regulation of DNA metabolic process	BP	6	6.00E-04
18	2.31	chromatin modification	BP	19	1.26E-03
19	2.24	DNA damage response, signal transduction	BP	10	2.17E-04
20	2.04	mitochondrial genome maintenance	BP	4	5.48E-03

*BP = Biological process from GO CC = Cellular component from GO MF = Molecular function from GO

5.4.6 Time-Dependent Regulation of Gene Expression under Hyper-osmotic Condition

Excluding the genes that are differentially regulated due to the extended culture in iso-osmotic condition (300 mOsm/kg 1 hour vs. 5 hours), less than half of the probes regulated due to 1 hour hyper-osmotic challenge (21 out of 48 probes, Table 5.8) continued to be regulated in the same manner when the specimens were exposed to 5 hours hyper-osmotic challenge. The rest were either regulated in an opposite direction (3 probes) or not regulated at all at 5 hours (24 probes), indicating the transient regulation of these genes.

Table 5.8 Number of genes that are not regulated due to extended culture in iso-osmotic condition, but regulated upon exposure to hyper-osmotic challenge. Categorised on the basis of their nature of regulation over the exposure time.

Gene regulation*			Gene count
300 vs. 500 mOsm/kg		300 mOsm/kg 1 hour vs. 5 hours	
1 hour	5 hours		
↑	↑	–	14
↑	↓	–	0
↑	–	–	6
↓	↓	–	7
↓	↑	–	3
↓	–	–	18
–	↑	–	591
–	↓	–	820

* ↑ = up-regulation, ↓ = down-regulation, – = no regulation

5.4.7 Differential Expressions of DNA Damage Response Genes due to Hyper-osmotic Challenge

Exposing the specimens to hyper-osmotic challenge for 5 hours induced the up- and down-regulation of 12 and 33 genes, respectively, that are involved in the response to DNA damage. Only one of these genes was also regulated after 1 hour of hyper-osmotic exposure, heat shock protein 1A (HSPA1A), which was up-regulated by 2.9 fold at 1 hour and further up-regulated by 10.5 fold at 5 hours. None of the DNA damage response genes were differentially expressed as a result of prolonged culture in iso-osmotic condition (300 mOsm/kg 1 hour vs. 5 hours), except for the expression of serum/glucocorticoid regulated

kinase 1 (SGK1) which was down-regulated due to the extended iso-osmotic culture and maintained in the prolonged hyper-osmotic challenge.

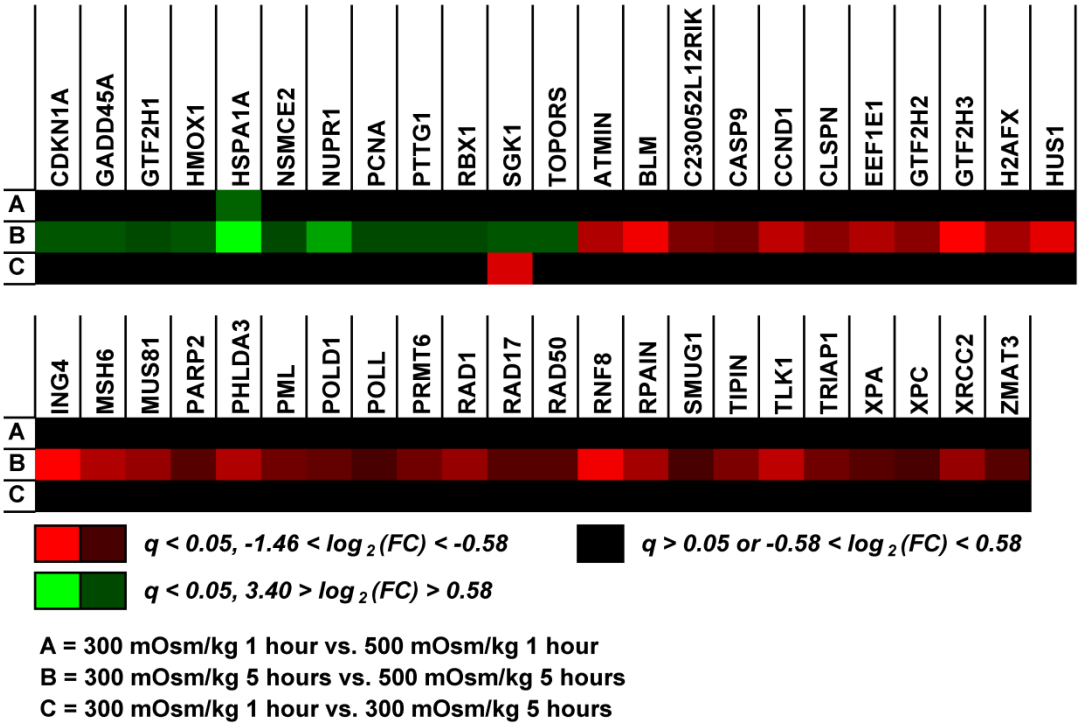

Figure 5.9 The degree of up- and down-regulation of the 45 differentially expressed genes that relate to DNA damage response. Red represents the down-regulation of the gene and green represents the up-regulation of the gene, whilst the brightness represents the degree of the regulation. Black represents the instances without differential regulation.

5.4.8 Differential Expressions of Histone Related Genes due to Hyper-osmotic Challenge

With a shorter hyper-osmotic exposure (1 hour), 8 of the top 10 most down-regulated genes were histone related genes (Table 5.2). Conversely, a distinct set of histone genes, which are members of the chromatin assembly annotation term, were up-regulated at 5 hours (Table 5.6). Out of 73 histone related genes in the array, 23 histone genes were significantly regulated in either the 1 or 5 hours groups (Figure 5.10). None of the histone genes were differentially expressed as a result of prolonged culture in iso-osmotic condition (300 mOsm/kg 1 hour vs. 5 hours). A set of H2a genes were significantly down-regulated by exposure to 500 mOsm/kg for 1 hour, with the expression levels recovering to near control levels by 5 hours. In the 5 hours group, up-regulation of a different set of histone genes (H2a.X, H2b, H3 and H4) was observed. Additionally, at 5 hours, up-regulation of histone binding genes was also observed, for example nuclear autoantigenic sperm protein (NASP),

nucleosome binding protein 1 (NSBP1) and sirtuin 1 (SIRT1). NASP encodes histone H1 binding proteins that are responsible for transporting histones into the nucleus (Richardson *et al.* 2000), and are also known to bind to histones H3 and H4 (Wang *et al.* 2008). NSBP1 and SIRT1 have been shown to modulate the binding of histone H1 to the chromatin (Fatoba and Okorokov 2011; Malicet *et al.* 2011).

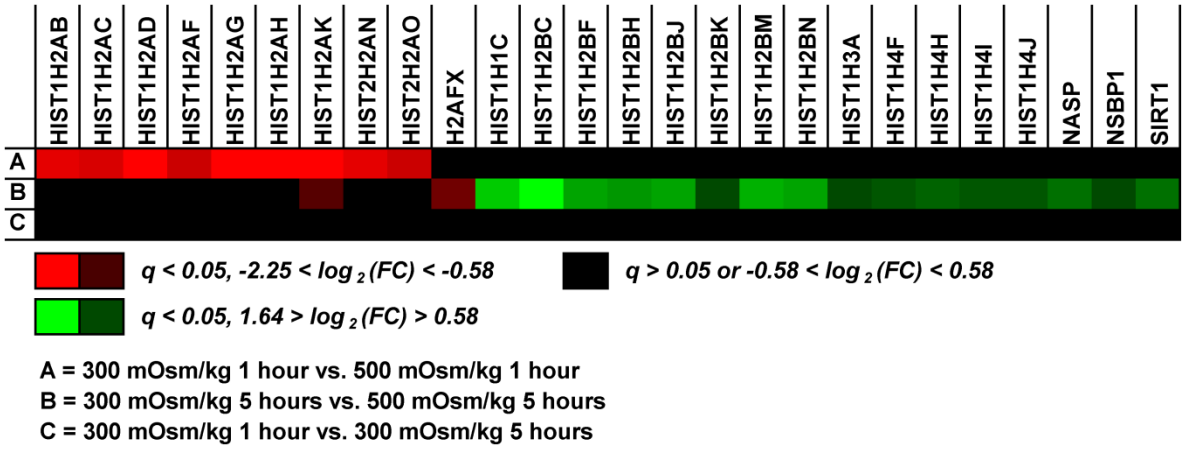

Figure 5.10 The degree of up- and down-regulation of the 23 differentially expressed histone genes out of the 73 histone genes that present in the array. Red represents the down-regulation of the gene and green represents the up-regulation of the gene, whilst the brightness represents the degree of the regulation. Black represents the instances without differential regulation.

5.5 Discussion

In this chapter, expression microarrays were utilised to investigate the effect of hyper-osmotic challenge on the genome-wide expression profile of H5 murine chondrocyte cell line. Exposure to hyper-osmotic challenge for both 1 and 5 hours caused differential regulation of a number of genes. Extended exposure of hyper-osmotic challenge (5 hours) induced the regulation of a significantly higher number of probes when compared to a shorter exposure (1 hour), from 20 to 627 for up-regulation and from 49 to 827 for down-regulation. Whilst extended culture in iso-osmotic condition (300 mOsm/kg 1 hour vs. 5 hours) induced a relatively low amount of gene regulation, where 13 probes were up-regulated and 56 probes were down-regulated. Additionally, our results also showed the transient regulation of some genes over the exposure time of hyper-osmotic challenge (Table 5.8). On the basis of these observations, the response in gene expression seems to develop over the culture period (1 to 5 hours), implying a response towards hyper-osmotic challenge, as suggested by previous studies in various cell types (Burg *et al.* 2007).

It is essential to acknowledge that the databases used in functional annotation analysis, such as GO and KEGG, are incomplete and regularly updated, depending on the findings from the published literature. Thus, the analysis of the same gene list performed in the future may lead to different results. Nevertheless, annotation analysis enables the examination of the functions of co-regulated genes based on the current knowledge. From the functional annotation analysis for both 1 and 5 hours comparisons, hyper-osmotic challenge was shown to regulate a diverse range of genes. The results indicate that hyper-osmotic challenge regulates cell cycle processes such as suppression in M phase and G1/S transition, programmed cell death or apoptosis, DNA damage response, chromatin assembly and kinase related processes, as reported previously in various cell types (de Nadal *et al.* 2002; Burg *et al.* 2007; Mavrogonatou and Kletsas 2012).

In functional annotation analysis, the selection of annotation terms were based on the *p*-value calculated from the Fisher's exact test (section 5.3.8), however, an annotation term with a high *p*-value ($p > 0.05$) is not necessarily irrelevant. The Wnt signalling pathway is currently heavily studied in chondrocytes. In the 5 hour comparisons, hyper-osmotic challenge induced the up-regulation of 10 genes and the down-regulation of 8 genes related to Wnt signalling pathway (KEGG annotation term), which was deemed as insignificant due to the high *p*-value. Nonetheless, functional annotation gives an overview of the most

affected processes, but in order to further characterise the effect of hyper-osmotic challenge in detail, a more rigorous and comprehensive analysis of the function of interest is required. For example, in order to investigate the effect of hyper-osmotic challenge on Wnt signalling pathway, functions of the corresponding genes and how they fit into the pathway should be thoroughly examined.

In Chapter 3, we have shown that hyper-osmotic challenge (500 mOsm/kg) induced a rapid (< 20 seconds) and reversible chromatin condensation in bovine primary chondrocytes. The application of hyper-osmotic challenge also induced an increase of chromatin condensation level in H5 murine chondrocyte nuclei (Figure 5.1). However, this osmotically-induced chromatin condensation appeared to recover over time (Figure 5.4), which agrees with a previous study that showed a recovery of chromatin condensation levels after 24 hours of culture in hyper-osmotic condition (Mavrogonatou and Kletsas 2012). This recovery suggests a process of cellular response to the hyper-osmotic stress that involves the re-modelling of the chromatin structure. Additionally, prolonged exposure to 700 mOsm/kg induced a significant distortion on the H5 nuclei (Figure 5.2 and 5.3), suggesting damage to the chromatin structure, which is consistent with the non-recoverable chromatin condensation observed following 700 mOsm/kg hyper-osmotic challenge (Figure 3.18).

Typically, damage to DNA, induced for example by UV or radiation, leads to the process of DNA repair involving the identification and repair of the damaged DNA. Hyper-osmotic challenge has been shown to induce persistent DNA breaks, a phenomenon which is not yet fully characterised (Dmitrieva and Burg 2008). From the current microarray study, we have shown the up- and down-regulation of various genes that associated with DNA damage response after 5 hours of hyper-osmotic challenge (Figure 5.9), suggesting the modulation of a specific DNA repair mechanism. Of these genes only the expression of HSPA1A was regulated at 1 hour and this gene was further up-regulated at 5 hours, suggesting HSPA1A as the first DNA damage response gene that is robustly activated and therefore may play an essential role in the response to hyper-osmotic challenge.

Within the chromatin of eukaryotic cells, there are five major classes of histone proteins: H2a, H2b, H3 and H4, the four core histones, which assemble to form the nucleosome core particle, and H1, which is bound to the linker DNA between nucleosomes, allowing the formation of higher order structure of chromatin. Each of the histone proteins is represented by a number of functional copies of the histone genes, which are named depending on the

location within the genome (Marzluff *et al.* 2002). The bulk of the histone proteins are encoded by a family of replication-dependent histone genes, termed as the canonical histone proteins and are heavily regulated by the cell cycle (Marzluff *et al.* 2008). These are located in three histone clusters: HIST1, HIST2 and HIST3 (Marzluff *et al.* 2002). The amino acid sequence of the proteins produced by the genes for each histone protein is highly conserved, where some of the genes produced very similar or identical protein and in instances where variability is present, the products differ in only a small number of amino acid residues. For example, HIST1H2AD, -F, -I, -K, -L and –M produce the same 129 amino acid sequence for H2a histone protein , whilst for HIST1H2AB, the 99th amino acid in the HIST1H2AD sequence, which is a Lysine, is replaced by Arginine (Marzluff *et al.* 2002). Unfortunately, the functional distinctions between these canonical histone gene copies are not yet identified, nonetheless, the number of canonical histone gene copies has been shown to be crucial for the development of *Drosophila melanogaster* (Gunesdogan *et al.* 2010).

These canonical histone genes transcribe the only mRNAs in metazoans that are not polyadenylated thus lack a poly(A) tail, which instead is replaced by a 3' stem-loop sequence (Dominski and Marzluff 2007). In this study, Oligo(dT) primers were used in the cDNA synthesis from extracted RNA, which target the poly(A) tails of mRNAs. Without the poly(A) tail, these particular histone mRNAs were not identified by Oligo(dT) and excluded from the microarray analysis. Nonetheless, some of these replication-dependent genes also express polyadenylated mRNAs throughout the cell cycle (Shepard *et al.* 2011), which are shown to be regulated independently to the non-polyadenylated mRNAs, suggesting their physiological significance (Cheng *et al.* 1989). Even though the functional distinction between the mRNAs with and without the poly(A) tail is still unclear, these polyadenylated mRNAs are still translated and are functional (Marzluff and Duronio 2002).

Histone gene expression was markedly affected by hyper-osmotic challenge, with distinct sets of histone genes regulated at 1 hour and at 5 hours (Figure 5.10), confirming the time-dependent and transient regulation of the gene expression. Additionally, at 5 hours, hyper-osmotic challenge also induced the up-regulation of histone binding genes (Figure 5.10), suggesting the delivery of histone proteins into the nucleus and their incorporation to the DNA. As the key component in chromatin structure, this osmotically-induced alteration in histone gene expression may lead to targeted changes in chromatin structure as part of the

cellular response to the effects of hyper-osmotic challenge, including the recovery of chromatin condensation level.

In summary, with addition to a rapid and reversible alteration in chromatin condensation, as shown in the previous chapter, hyper-osmotic challenge also induces profound alterations in gene expression. The number of regulated genes increased significantly with exposure time, suggesting a time-dependent response mechanism toward hyper-osmotic challenge. In addition to the regulation of DNA damage response genes, hyper-osmotic challenge was also shown to alter the expression of histone binding and histone proteins that are responsible for chromatin assembly, which may lead to more permanent alterations in higher order chromatin structure, for example chromatin condensation level recovery.

Chapter 6 General Discussion

6.1 Introduction

Osmotic variation exists in cartilage tissue due to the increase of proteoglycan concentration through the depth of the tissue (Urban 1994), prolonged mechanical loading (Maroudas 1979) and the degradation of ECM in pathological conditions (Bush and Hall 2003). The application of osmotic challenge to cartilage tissue and isolated chondrocytes has been shown to alter matrix production (Urban and Bayliss 1989; Oswald *et al.* 2011) and gene expression (Hung *et al.* 2003; Peffers *et al.* 2010; Tew *et al.* 2011). However, the mechanisms by which chondrocytes perceived the variations in osmolality to drive these changes in metabolism remains unclear. Osmotic challenge has also been shown to alter cellular and nuclear morphology (Guilak *et al.* 2002; Finan and Guilak 2010) and chromatin condensation levels (Albiez *et al.* 2006; Finan *et al.* 2011), whilst, the regulation of gene expression is closely related to the state of chromatin organisation (Brown *et al.* 1997; Croft *et al.* 1999). These osmotically-induced alterations on nuclear morphology and chromatin structure may provide a direct biophysical mechanism for controlling cellular metabolism. This project has principally explored the effect of hypo- and hyper-osmotic challenge on chondrocytes, focusing on cellular and nuclear morphology, chromatin structure, cellular and nuclear deformability and genome wide expression. Accordingly, further insights on the effect of osmolality on chondrocytes have been gained (Figure 6.1). The key outcomes of this study are as follow:

- An image processing algorithm, utilising the Sobel edge detection, was developed in MATLAB to quantify the level of chromatin condensation.
- Hypo-osmotic challenge induces chromatin decondensation and cell swelling, whilst, hyper-osmotic challenge induces chromatin condensation and cell shrinking.
- Reversible and rapid chromatin condensation occurs within the physiological osmolality range of articular cartilage *in vivo*.
- Osmotically-induced chromatin condensation still occurs in the absence of functional membrane and cytoplasm.
- Osmotic challenge induces alterations in cellular and nuclear deformability in chondrocytes.
- Hyper-osmotic challenge induces alterations in gene expression profile and extension of exposure time (1 vs. 5 hours) increases the number of regulated genes.

- Different sets of histone genes are regulated upon hyper-osmotic challenge for 1 hour or 5 hours.

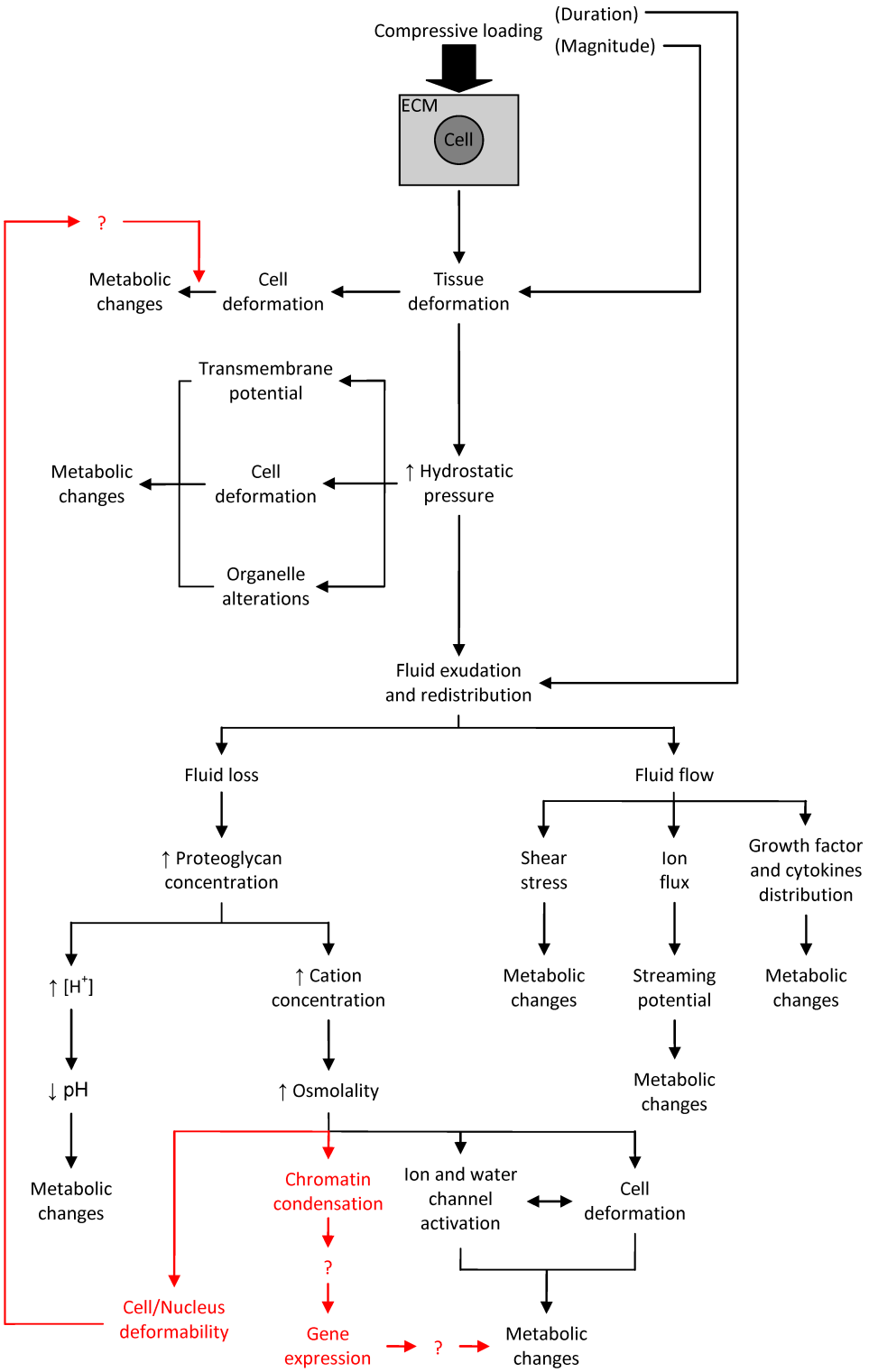

Figure 6.1 Schematic diagram showing the consequential effects of compressive loading on articular cartilage tissue, as possible mechanisms of chondrocyte mechanotransduction. Findings of current study are written in red.

6.2 Evaluation of Methodologies Used in the Present Study

A variety of methods have been used throughout the work presented in this thesis. In many cases these are very well characterised and have been widely used in other studies. However a number of new, or adapted, techniques are presented and in some cases there are limitations to these techniques that need to be recognised to provide appropriate interpretation of data and its significance. For example, in section 3.2.11, we have assessed the dynamics of osmotically-induced chromatin condensation/decondensation in living chondrocytes, by monitoring the H2B-GFP transfected nuclei continuously during the 15 minutes osmotic challenge. The temporal resolution of the imaging is necessarily limited by the microscope's scanning speed, and with the confocal system used (Leica TCS SP2) at least 20 seconds was required to acquire a full *Z*-stack image of the nuclei. In all cases, the osmotically-induced chromatin condensation/decondensation was observed in the nuclei image taken at the first time point, implying that the onset of this alteration occurs within 20 seconds after the osmotic challenge, but may actually be much more rapid. A higher temporal resolution is required to investigate accurately the onset time of chromatin condensation/de-condensation induced by the osmotic challenge. As part of the imaging procedure characterisation, in an attempt to enhance the temporal resolution, the mid-section of the nucleus, instead of the whole nucleus, was imaged over the 15 minutes osmotic challenge. However, it was difficult to maintain the mid-section within the focal plane, due to movement of the nucleus as the osmotic challenge medium was introduced, potentially associated with either change in cell volume or reaction to the flow of osmotic challenge medium. Alternatively, a spinning disc confocal microscopy might be used to improve the temporal resolution. Gaining an improved understanding of the temporal dynamics of the osmotically-induced condensation phenomenon may enhance understanding of the underlying physicochemical mechanism which can, in turn, be subject to theoretical modelling, as described in chapter 3.

Further, in order to quantify the level of chromatin condensation, an image processing algorithm was developed in MATLAB utilising the Sobel edge detection algorithm (section 2.7.4). Osmotically-induced chromatin condensation increases the number or the size of distinct spaces (inter-chromosomal spaces) throughout the nucleus, which increases the number of edges detected by the Sobel edge detection algorithm. The level of chromatin condensation was quantified by the number edges normalised by the nucleus cross section

area. Thus, the use of this image processing algorithm is limited to chromatin condensation with similar nature, such that it cannot be used when the chromatin condensation is concentrated to a distinct number of points, such as chromatin condensation in apoptosis or during cell division.

From section 3.3.1 and 3.3.4, we can see clearly that H2B-GFP transfection of chondrocytes provides nuclei images with greater detail and better photobleaching property when compared to Hoechst 33342. However, the current transfection procedure gives a relatively low efficiency (~40%) for multi cells live imaging. Further characterisation on the procedure or a different transfection approach, such as electroporation, may result in a greater efficiency which is then practical for multi cells live imaging.

6.3 The Effect of Osmotic Challenge on Chondrocytes

When considered in a temporal context, alterations in chromatin condensation level occur rapidly, in less than 20 seconds, and are therefore part of the rapid, acute responses to osmotic challenge, along with change in cell volume (<10 seconds) (Pritchard and Guilak 2004), F-actin content (<60 seconds) (Pedersen *et al.* 1999) and length of the primary cilia (<60 seconds) (Rich and Clark 2012). The rapid nature of these early effects suggest that they are likely to be the initial physicochemical responses to osmotic challenge and the key triggering mechanisms for the other effects that follow, including cell cycle arrest (Burg *et al.* 2007), activation of stress-activated mitogen-activated protein kinases (SAPKs) (de Nadal *et al.* 2002) and, ultimately, alterations in gene expression profile (Tew *et al.* 2011), which has been shown in this study to occur as early as 1 hour after the osmotic challenge (Table 5.1). Indeed, the rapid onset differentiates osmotically-induced chromatin condensation/decondensation from other alterations to chromatin organisations that are enzymatic in nature, such as histone acetylation and methylation, that require a longer time. Moreover, a previous study have shown that alterations in F-actin content, which is also relatively rapid, are dependent on alterations in intracellular Ca^{2+} concentration (Pritchard and Guilak 2004), requiring the upstream activation of the ion channels. However, the onset of Ca^{2+} influx occurs at 25 and 300 seconds after hypo- and hyper-osmotic challenge, respectively, suggesting that changes in cell volume (<10 seconds) and chromatin condensation level (<20 seconds) are independent of Ca^{2+} alterations. In order to characterise the mechanism of osmotically-induced chromatin condensation and its place within the chronology of a cell response to osmotic challenge, it is necessary to investigate its sequence, co-ordination with, and dependency on other osmotically-induced effects. A schematic describing these relationships, including findings from the current study and those from the literature is presented in Figure 6.2.

An array of published data have shown that mechano-responses, such as changes in intracellular Ca^{2+} concentration (Erickson *et al.* 2001) and Indian hedgehog expression (Wu *et al.* 2001), are blocked by targeting a range of signalling pathways, such as IP_3 and cAMP (Valhmu *et al.* 1998; Yellowley *et al.* 1999), which then lead to alterations in chondrocytes proliferation (Wu and Chen 2000) and aggrecan expression (Valhmu *et al.* 1998). Due to its rapid nature, osmotically-induced chromatin condensation is unlikely to be dependent on these signalling cascades; however, the findings from current study are not sufficient to

fully confirm this statement. Hence, further investigations involving various signalling pathway disruptions are required to determine whether osmotically-induced chromatin condensation is a by-product of a signalling pathway or purely a physico-chemical response.

As one of the early responses to osmotic challenge, the increase in cell volume due to hypo-osmotic challenge leads to the activation of various ion channels and other intracellular signalling cascades (Waldegger *et al.* 1998; O'Neill 1999; Lange 2000; Hoffmann *et al.* 2009; Barrett-Jolley *et al.* 2010; Lewis *et al.* 2011), as part of the volume regulation, which then affects the downstream processes, such as cellular metabolism and gene expression (Hardingham and Bading 1999; Hildebrandt and Prowald 2000; Chen *et al.* 2002; Mouw *et al.* 2007; Phan *et al.* 2009; Xu *et al.* 2010). Meanwhile, primary cilia are known to be responsible for sensory mechanisms in a variety of cell types (Satir and Christensen 2008), including chondrocytes (Wann *et al.* 2012), with changes in primary cilia known to alter signal transduction. Conversely, the mechanism by which osmotically-induced chromatin condensation or decondensation affects the downstream processes remains unclear. With reference to the known relationship between chromatin condensation and gene silencing (Brown *et al.* 1997; Croft *et al.* 1999), alteration of chromatin condensation level due to osmotic challenge may potentially affect gene expression directly by inhibiting the access of transcription related enzymes to specific gene loci within the condensed chromatin or by exposing the loci to the interchromosomal space to facilitate transcription. This suggests that, not only is chromatin condensation a rapid physicochemical response to osmotic alterations, but potentially may also control the transcription regulation of the cell in a direct manner.

Changes in osmolality alter many aspects of cell function; however the correlation between these effects remains poorly understood. Previous findings have suggested a time-dependent response mechanism towards the osmotic changes, such as the recovery of matrix production (Hopewell and Urban 2003), cell cycle, ionic strength, transcription (Burg *et al.* 2007) and cell volume via regulatory volume increase or decrease (Bush and Hall 2001; Kerrigan *et al.* 2006). Indeed, our findings also agree with this notion by showing the recovery of chromatin condensation levels (Figure 5.5) and an increase in number of regulated genes (Table 5.1 and 5.3) between the 1 and 5 hours hyper-osmotic challenge regimes. Through confocal imaging, chromatin condensation was shown to

recover near to its initial level after 24 hours of hyper-osmotic challenge (Mavrogonatou and Kletsas 2012). Interestingly, in addition to the rapid chromatin condensation, the application of hyper-osmotic challenge for 1 hour induced alterations in key genes related to nuclear and chromatin structure, including a number of histones (Figure 5.10), the building block of chromatin compaction, which may lead to more permanent alterations in higher order chromatin structure. The regulation of chromatin related genes may, therefore, provide a driving mechanism in the recovery of chromatin organisation. Meanwhile, condensed chromatin is typically considered to be associated with gene silencing. As such, the decondensation of chromatin structure may lead to the activation of distinct sets of genes, i.e. the increase in gene regulation with time, potentially to cause further recovery of chromatin organisation, suggesting the existence of a feed-back mechanism between the increase of gene regulations over time and the recovery of chromatin condensation.

In addition to chromatin condensation, the application of hyper-osmotic challenge has also shown to cause DNA breaks which, in contrast to UV-induced DNA damage, are not repaired when the hyper-osmotic condition is maintained (over 13 to 20 passages) (Dmitrieva *et al.* 2004; Dmitrieva and Burg 2008). However, the nature and mechanistic effects of these DNA breaks remains unclear. Potentially, chromatin condensation may initiate the onset of this structure modification, as the reversibility of osmotically-induced chromatin condensation (Figure 3.18) coincides with the rapid repair of these breaks when the specimens are brought back to an iso-osmotic condition (Dmitrieva *et al.* 2004). While the recovery of chromatin condensation over time implies a time-dependent response in hyper-osmotically challenged cells, these persistent DNA breaks may indicate an alteration within the chromatin structure that is maintained over time, suggesting the ability of a cell to detect the surrounding osmolality and to change its chromatin structure and function accordingly. This provides a mechanism for persistent changes in cell function upon chronic osmotic challenge or the different metabolic activity through the depth of cartilage where variation of osmolality exists. However, further work is necessary to elucidate the relationship between short and longer term alterations in chromatin organisation and genome function with osmotic challenge.

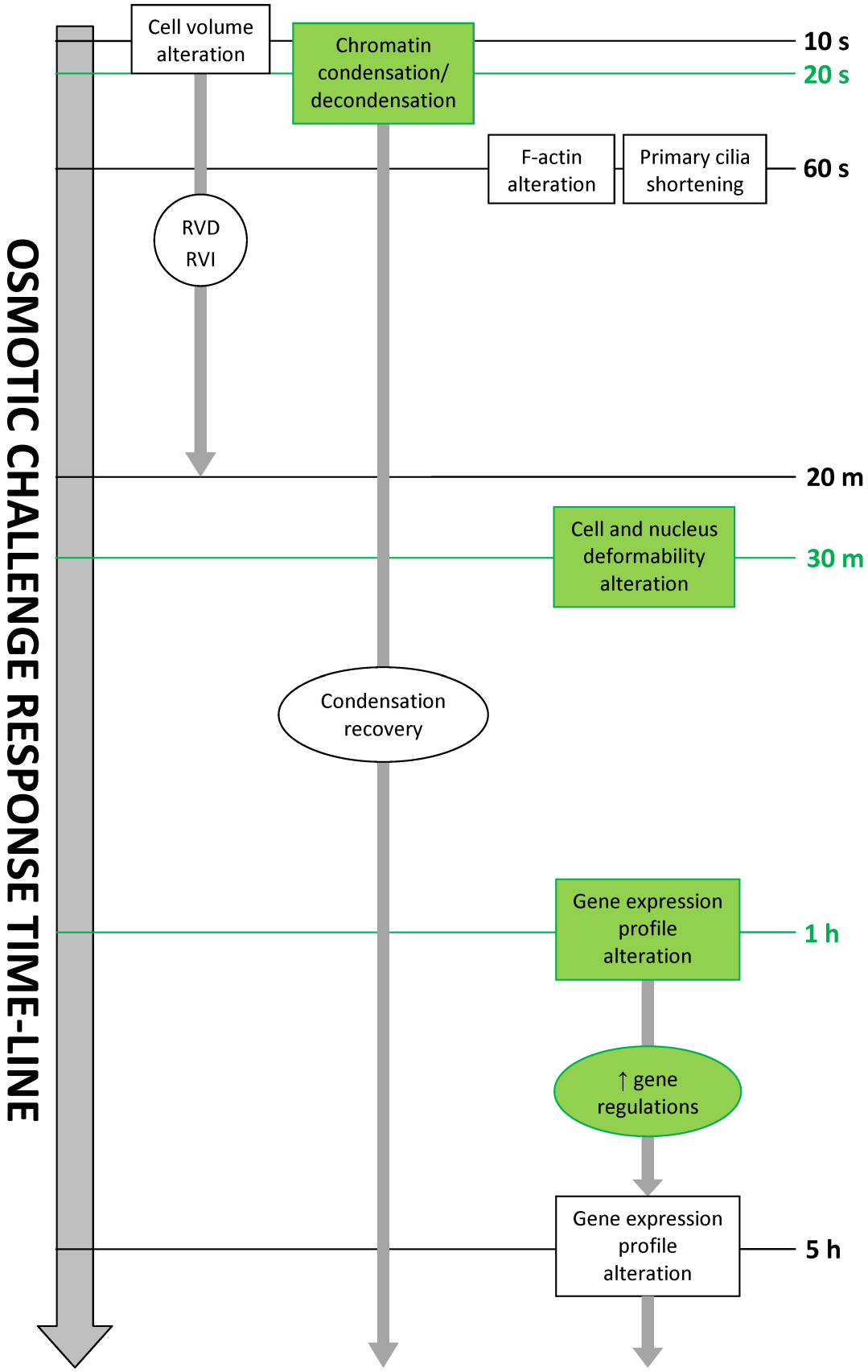

Figure 6.2 Schematic showing the effects of osmotic challenge on cells in a chronological manner..The novel findings of this study are shaded in green.

Many previous studies have suggested that cell deformation upon mechanical loading initiates mechanotransduction processes in chondrocytes (Ingber 1994; Urban 1994; Guilak *et al.* 1997; Lee and Bader 1997). Additionally, we have shown that exposure to hyper- and hypo-osmotic challenge alters cellular and nuclear deformability (Figure 4.11 and 4.12), suggesting that osmolality may regulate the deformation response to mechanical load at both the whole-cell and nuclear levels in chondrocytes. Further studies in other cell types suggest that nuclear distortion results in ordered rearrangement of chromosomal territories that may activate or silence specific gene loci. As yet the genomic consequences of chromatin domains reorganisation due to nuclear deformation have not been explored in chondrocytes. In light of these studies, the increase of nuclear deformability in hyper-osmotic conditions may potentially provide a key mechanism for maintaining chondrocytes homeostasis. As discussed in Chapter 4, the changes in nuclear and cellular deformability upon osmotic challenge might be the consequence of alterations in the level of chromatin condensation leading to changes in nuclear stiffness, plus changes to the cell volume, with associated alterations in cell stiffness and cytoplasm organisation. Both cell volume and chromatin condensation level were shown to recover over time as part of the cellular response towards osmotic challenge, suggesting that both cellular and nuclear deformability might also change over time.

In addition to the other alterations observed in this study, marked and reversible chromatin condensation occurred between 300 and 500 mOsm/kg (Figure 3.4), which falls within the physiological osmotic range of articular cartilage at rest (350-450 mOsm/kg) (Urban 1994) and upon the application of extended loading (430-470 mOsm/kg) (Oswald *et al.* 2008) (Figure 6.2). This suggests that chondrocytes are likely to experience chromatin condensation and decondensation during the articular cartilage diurnal loading cycle, and this process potentially plays an essential role in the control mechanism that maintains chondrocyte function. During pathological condition, the breakdown of collagen network within the extracellular matrix leads to the increase of water content in cartilage tissue and a reduction of extracellular osmolality (Bush and Hall 2003), which may move the osmolality range to a lower level. Moreover, mechanical loading upon the compromised matrix might even results in a lower osmotic shift, thus narrowing the load-induced osmolality range (Figure 6.3). This will cause a reduction in chromatin condensation in the unloaded state and a more limited variation in the condensation with loading compared to

healthy tissue. These alterations could disturb a control mechanism dependent on the level of chromatin condensation. The perturbation of this control mechanism may be one of the triggering factors that disrupt chondrocytes homeostasis during the progression of the disease. Further thorough studies are required to test this assertion, but it has been shown that the exposure of damaged cartilage tissue to hyper-osmotic challenge promotes chondrocytes viability during the recovery process (Amin *et al.* 2011), implying the importance of osmolality in the survival of chondrocytes.

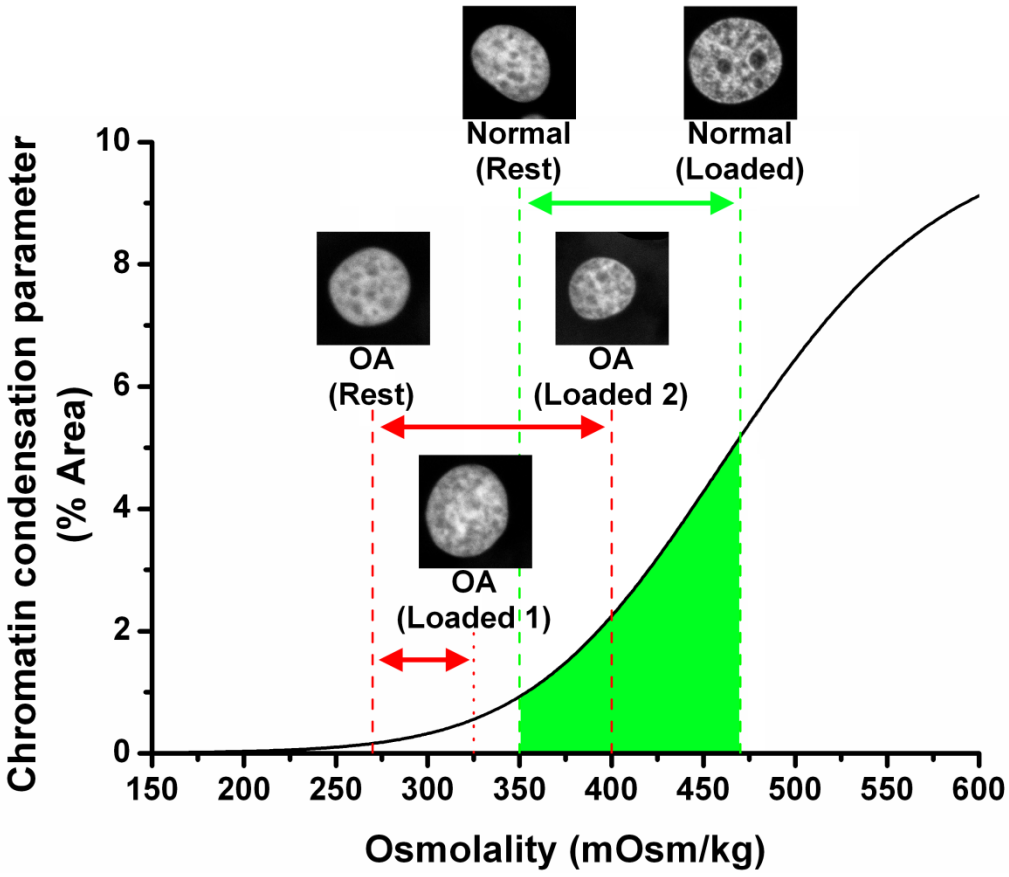

Figure 6.3 Schematic describing the theoretical levels of chromatin condensation in normal and OA cartilage in the unloaded and loaded states. The graph was adapted from Figure 3.4 by fitting the results through a sigmoidal function (R^2>0.96). The extracellular osmolality range of normal cartilage is denoted by the green lines and the green shaded area (350-470 mOsm/kg). The estimated extracellular osmolality ranges of OA cartilage are denoted by the red lines (from 280 mOsm/kg). OA might potentially lower the osmolality range or even narrows the osmolality range as the consequence of mechanical loading on compromised cartilage matrix. The nuclei images represent the level of chromatin condensation at the corresponding osmolality condition.

6.4 Future Work

In the current study, osmotic-induced chromatin condensation and decondensation were shown in chondrocytes *in vitro*, either in monolayer culture, seeded into a 3D agarose system or in isolated nuclei. Further study is required to investigate the existence of these phenomena in chondrocytes *in situ*. This may be achieved via confocal microscopy imaging or through the use of multiphoton approaches that provide improved imaging depth from the tissue surface. Accordingly high resolution image of chromatin condensation may be acquired from live chondrocytes directly within intact articular cartilage, as shown by Han *et al*. (2012). With the addition of TEM from fixed specimens and the estimation of *in situ* extracellular osmolality, as demonstrated by Bush and Hall (2001), we will be able to assess whether chromatin condensation due to osmotic challenge occurs *in situ*. Further, the application of mechanical compression, using techniques that have been used previously in the host laboratory may be used to determine whether load-induced, and depth dependent, variations in chromatin condensation occur within the native tissue.

In previous studies (Delpire *et al.* 1985; Albiez *et al.* 2006; Finan *et al.* 2011; Mavrogonatou and Kletsas 2012), including this current study, alteration in chromatin structure was induced by a sudden osmotic challenge, which was applied in a relatively high rate. Conversely, in physiological condition, the application of mechanical load on cartilage tissue induces the increase of hydrostatic pressure, which then leads to a gradual fluid loss due to the frictional drag forces of the ECM, thus the osmolality rises gradually as the proteoglycan concentration increases. The rate and the degree of fluid loss depend on the magnitude and the temporal aspect of the load, respectively. Although gradual hypo-osmotic challenge was shown to induce an increase in erythrocytes cell volume (Godart *et al.* 1999) and step-wise hyper-osmotic challenge was also shown to induce chromatin condensation in HeLa cells (Albiez *et al.* 2006), further studies involving gradual osmotic challenge is required to model the physiological conditions of articular cartilage. Hence, in order to investigate the physiological relevance of osmotically-induced chromatin condensation, the effect of gradual osmotic challenge on chondrocytes chromatin structure should be observed. Additionally, parallel to this study, the effect of gradual osmotic challenge on cell volume, F-actin organisation and other osmotically-induced responses can be observed as well.

Currently, we have shown that hyper-osmotic challenge induced both chromatin condensation and regulation of gene expression profile in chondrocytes. In an attempt to gain further insight in the correlation between the alterations of chromatin structure with the transcription regulation, we may test the following hypothesis: chromatin condensation due to hyper-osmotic challenge, results in gene silencing as down-regulated genes are predominantly compacted within the condensed chromatin structure, with associated restriction of access of transcription related enzymes. Alternatively up-regulated genes are re-located to the outer part of the condensed chromatin facilitating transcription. To test these hypotheses, the expression level of candidate gene that are heavily down- and up-regulated genes should be confirmed by RT-PCR. Afterwards, the location of these genes in respect to the chromatin condensation can be assessed by specific gene imaging technique, such as fluorescence *in situ* hybridisation (FISH). The use of super resolution imaging, such as STORM, Leica STED and Zeiss PALM, might be preferable to increase the spatial resolution of the image. The next step is adapted from a previous study by Martins *et al*. (2007). Our current results have shown that osmotically-induced chromatin condensation inhibits DNase I digestion by hindering the enzyme's access to the DNA backbone. Accordingly, isolated nuclei will be exposed to a set of osmotic conditions, followed by DNase I digestion. Once the digestion is ceased, the existence of the heavily regulated genes within the remaining DNA can be detected by RT-PCR. The genes that are not digested are likely to be protected by the condensed chromatin.

Previous studies by Dmitrieva *et al.* (2004; 2008) have shown the existence of chromatin structure modification (DNA breaks) that persist over an extended hyper-osmotic challenge and recover rapidly upon exposure of iso-osmotic conditions. This suggests the ability of a cell to sense the level of its surrounding osmolality and may be responsible for maintaining certain alterations in cell function that persist after the cellular adaptation to chronic osmotic challenge. However, these studies involved HeLa and mIMCD3 cells, and in contrast to this study, hyper-osmotic condition was achieved by the addition of NaCl. It is essential to note that cells respond differently to different osmolytes. Nevertheless, Mavrogonatou and Kletsas (2012) showed that the addition of both NaCl and sorbitol induced chromatin condensation that recovered after 24 hours of exposure time. First, the existence of these DNA breaks should be investigated, by the comet assay, in chondrocytes exposed to hyper-osmotic challenge achieved by the addition of either NaCl or D-Mannitol.

Subsequently we can test whether maintaining the DNA breaks upon iso-osmotic challenge, will also maintain cell functions that were altered during an extended hyper-osmotic challenge.

Furthermore, in order to gain further insight on the mechanism of osmotically-induced chromatin condensation, its correlation with the other osmotically-induced effects needs to be assessed. For example, the effects of the blockage of osmolality related SAPKs, the disruption of cytoskeleton organisation or the depletion of intra- and extracellular Ca^{2+} on the osmotically-induced chromatin condensation could be explored.

Appendix A Nucleic Acid Dyes Binding Characteristic

In most cases, nucleic acid dyes become fluorescent upon binding to DNA due to restriction in the internal rotation. These dyes are relatively small molecules and they can therefore bind to several different parts of the DNA molecule such as the backbone or major or minor grooves (Armitage 2005), as shown in Figure A.1. They might bind electrostatically due to the anionic phosphate groups along the DNA backbone, but this binding mode is generally weak under physiological conditions. Alternatively, small molecules may bind to the major groove of the DNA structure although this is rare and more commonly occurs for protein. Thus, intercalation and minor groove binding are the two most common binding modes for nucleic acid fluorescence dyes.

Intercalative binders bind to the DNA by inserting (intercalating) between two adjacent base pairs in the DNA double helix structure (e.g. adenine and thymine or guanine and cytosine), where they tend to lie parallel to and interact with the flat rings of the bases. Meanwhile, in minor groove binding, instead of insertion between the bases, the binder interacts with the minor groove of the DNA. Therefore, the compounds tend to lie parallel to the sugar-phosphate backbone of the double helix, rather than to the bases. However, binding involves interaction with the atoms of the bases such as hydrophobic and/or hydrogen bonding. Intercalation of a compound to DNA causes the separation of the two adjacent base pairs from one another to create a binding site for the compound, thus lengthening the DNA; whilst minor groove binding does not require this kind of perturbation to bind to the DNA. Hence, minor groove binding would cause significantly less deformity of the DNA compared with the intercalative binding.

Compounds that bind by intercalation are usually cationic molecules with a flat ring structure. Minor groove binders usually possess the following four structural features: a positive charge, curvature, flexibility and hydrogen bond donor and acceptor groups to interact with complementary groups on the floor of the groove (i.e. the DNA base pairs). In some cases, a nucleic acid fluorescence probe has the characteristic of both intercalative and minor groove binders, such as some of the cyanine based dyes. In these dyes, both binding modes are commonly observed (Armitage 2005).

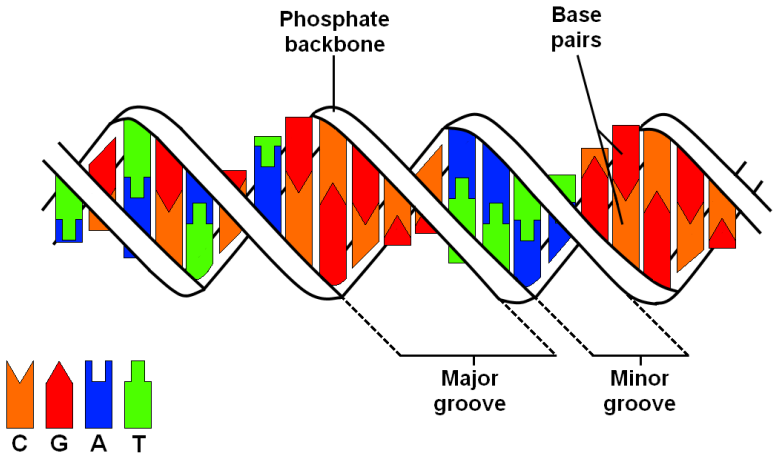

Figure A.1 DNA double helix.

Appendix B Photobleaching Characteristics

From the chondrocytes seeded on glass bottom 24 well plates (as described in section 2.4.3), a total of 15 consecutive images of nuclei, stained with the highest concentration of each dye, were made at 4× zoom (pixel size 116 × 116 nm), a line averaging of 4 and a frame averaging of 3.

The images were taken before fixation and mounting procedure. From Figure B.1, we can see that Hoechst 33258, Hoechst 33342 and DRAQ5 stained nuclei photobleach at a similar rate. By contrast, SYTO 16 stained nuclei photobleach very rapidly, even though it gives a good detail of the nuclear structure. Based on this, SYTO 16 was ruled out of the selection process.

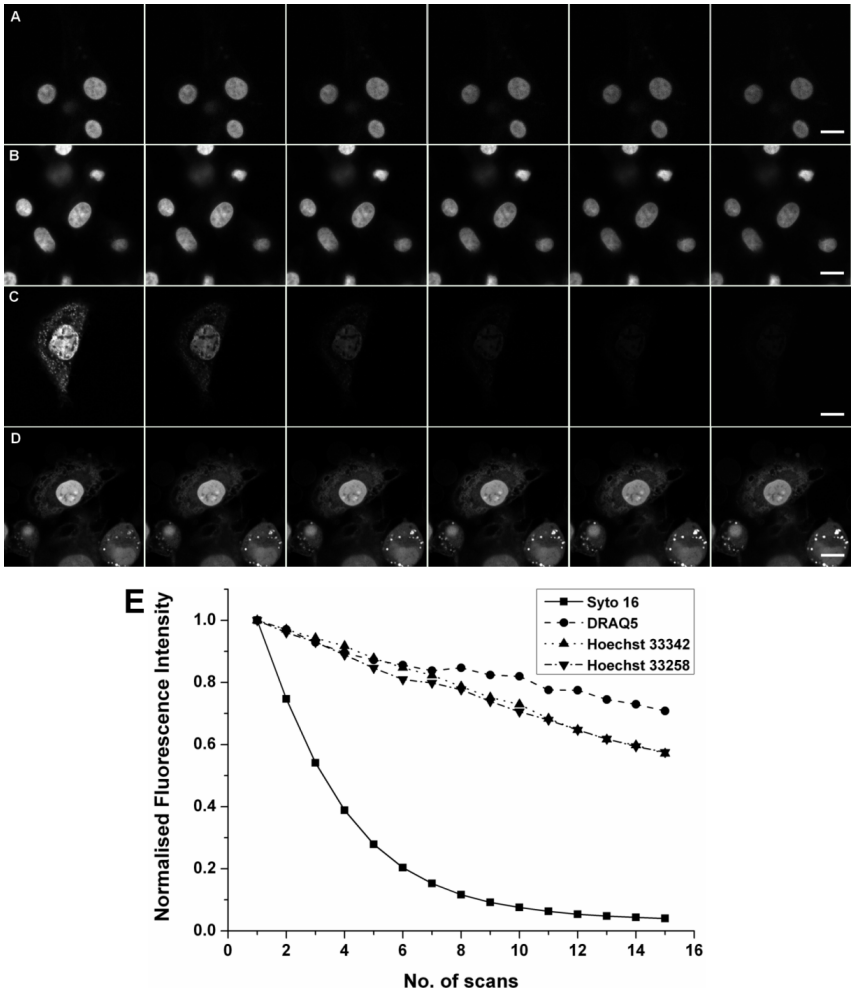

Figure B.1 Photobleaching characterisation with 4× zoom (13.5×10^3 nm^2/pixel). Images of nucleus stained with A: Hoechst 33258, B: Hoechst 33342, C: SYTO 16 and D: DRAQ5 from the 1^{st}, 4^{th}, 7^{th}, 10^{th}, 13^{th} and 15^{th} scan (4 line averaging and 3 frame averaging). E: The graph of fluorescence intensity against number of scans. Images were taken before fixation. (Bar: 10 μm).

Appendix C Preservation of Chromatin Condensation after Fixation

In this control study, 8×10^6 freshly isolated chondrocytes were seeded into 175 cm^2 culture flasks and cultured for 5 days. The cells were trypsinised and seeded at 5×10^4 cells/cm^2 onto 35 mm glass bottom petri dishes, and cultured overnight to allow cell adhesion, as described in section 3.2.1. The cells were stained with 8 μM Hoechst 33342 at 37°C for 15 minutes and subjected to 500 mOsm/kg osmotic challenge for 15 minutes by replacing the staining solution. After the imaging of the nuclei, the cells were then fixed, as described in section 3.2.3. In order to investigate the preservation of chromatin condensation level after fixation procedure, the fixed cells were exposed to 100 mOsm/kg media. High resolution images bisecting the centre of the chondrocyte nuclei were taken by confocal microscopy, as described in section 3.2.4, and the chromatin condensation parameter was measured as described in section 2.7.4.

Hypo-osmotic challenge (100 mOsm/kg) reduced the level of chromatin condensation, as shown in section 3.3.1. From Figure C.1, we can see that the application of hypo-osmotic challenge (100 mOsm/kg) on fixed specimens did not induce chromatin decondensation, which is reflected by the statistically insignificant difference between the normalised change of chromatin condensation parameter before and after the exposure of 100 mOsm/kg media (p=0.2, Figure C.2). These observations suggested that the fixation procedure used in this study is sufficient to preserve the level of chromatin condensation.

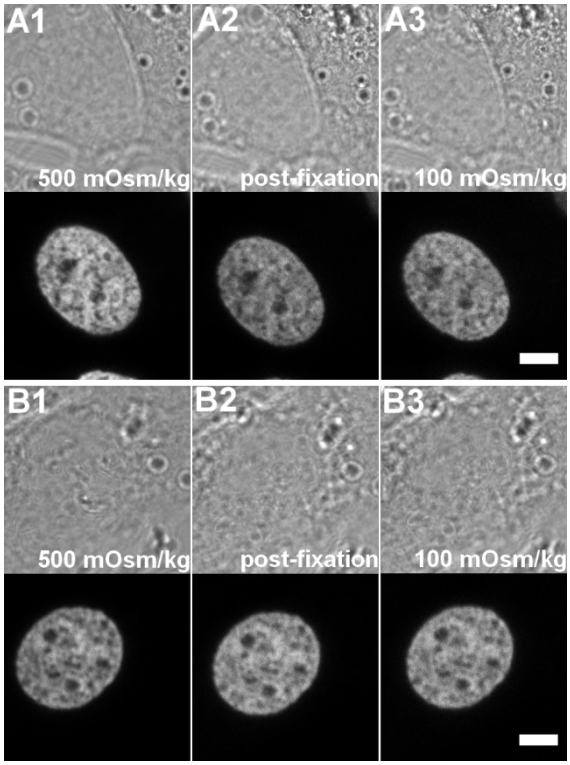

Figure C.1 Pair bright field images of monolayer cultured chondrocytes and their nucleus confocal image in 500 mOsm/kg media (A1 and B1), followed by fixation (A2 and B2) and 100 mOsm/kg (A3 and B3) osmotic challenge (Bar: 5 μm).

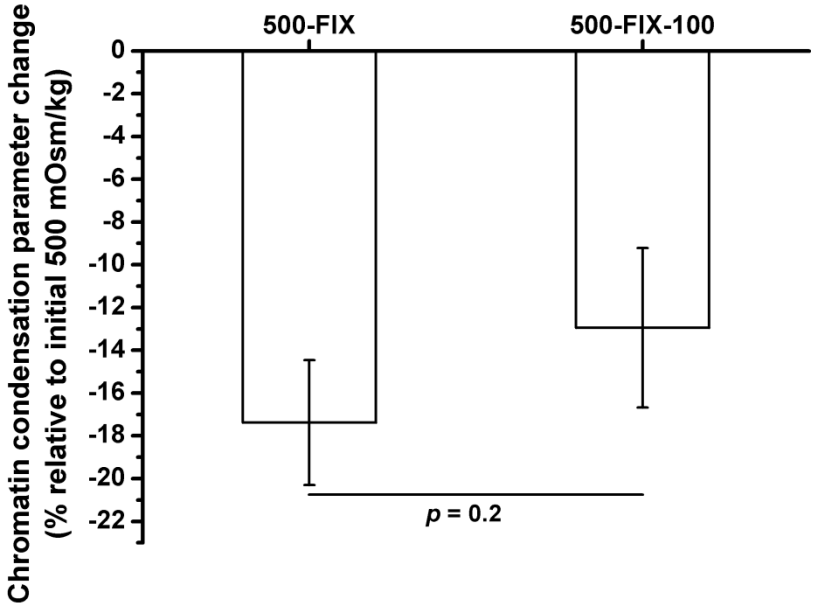

Figure C.2 The normalised change of chromatin condensation parameter quantified from the monolayer specimens post fixation (500-FIX), and after 100 mOsm/kg osmotic challenge (500-FIX-100). Statistical significance was assessed between the two groups by using paired Student's *t*-test (p=0.2) (N = 1, n = 40 nuclei per condition). Error bars show standard error.

Appendix D HiFect vs. DharmaFect Duo

In this characterisation study, the specimen was divided into two groups, the first group for HiFect transfection and the second group for DharmaFect Duo transfection. The group was then divided into three sub-groups, where the first row was for the testing of the effect of cell density, the second and third rows were for the testing of the effect of reagent and DNA ratio, while the fourth row was the control sub-group. In the first sub-group, the amount of GFP-pDNA and reagent were kept constant, while the cell seeding density varies. In the second sub-group, the cell seeding density and the GFP-pDNA were kept constant, while the amount of reagent applied varies, thus we have a range of reagent and DNA ratio. The third sub-group is similar to the second sub-group, but distilled water was applied in place of GFP-pDNA. The amount of reagents, GFP-pDNA and their ratio is listed in Table D.1, which represents the 24 well plate.

Firstly, GFP-pDNA was diluted to a concentration of 0.6 μg/μL. For the HiFect group, 1 μL GFP-pDNA was pipetted into 124 μL DMEM, to produce 125 μL DNA solution. Afterward, the required reagent was pipetted into a volume of DMEM to produce 125 μL reagent solution. The DNA solution was then added to the reagent solution, producing 250 μL transfection solution. The transfection solution was mixed by pipetting and left at room temperature for 5 minutes to allow the formation of lipid-DNA complex. The culture medium was aspirated from the well and replaced with 250 μL DMEM + 40% FCS. Finally, the transfection solution was placed into the well and mixed by pipetting.

For the DharmaFect Duo group, 1 μL GFP-pDNA was pipette into 49 μL DMEM, to produce 50 μL DNA solution. Afterward, the required reagent was pipette into a volume of DMEM to produce 50 μL reagent solution and left at room temperature for 5 minutes. The reagent solution was then added to the DNA solution, producing 100 μL transfection solution. The transfection solution was mixed by pipetting and left at room temperature for 20 minutes to allow the lipid-DNA complex formation. Into the transfection solution, 400 μL DMEM + 16.1% FCS was added to produce 500 μL of the transfection medium. Finally, the culture medium was aspirated and replaced with the transfection medium. After the transfection procedure, the sample was placed into the 37^{o}C incubator.

The cells were imaged at 24 and 48 hours post the transfection (Figure D.1 and D.2), then the transfection efficiency was calculated as the ratio between the numbers of cells and transfected nuclei within the imaging field (Table D.2 and D.3).

Table D.1 The seeding density and the amount of reagent, GFP-pDNA and distilled water (dH_20) for each well.

	HiFect			DharmaFect Duo		
Cell density (cells/cm^2)	2×10^4	3×10^4	6×10^4	2×10^4	3×10^4	6×10^4
Reagent	3µL	3µL	3µL	1.8µL	1.8µL	1.8µL
GFP-pDNA	0.6µg	0.6µg	0.6µg	0.6µg	0.6µg	0.6µg
Ratio	5:1	5:1	5:1	3:1	3:1	3:1
	3×10^4 4.8µL 0.6µg 8:1	3×10^4 3.6µL 0.6µg 6:1	3×10^4 2.4µL 0.6µg 4:1	3×10^4 4.8µL 0.6µg 8:1	3×10^4 3.6µL 0.6µg 6:1	3×10^4 2.4µL 0.6µg 4:1
	3×10^4 1.8µL 0.6µg 3:1	3×10^4 1.2µL 0.6µg 2:1	3×10^4 0.6µL 0.6µg 1:1	3×10^4 1.8µL 0.6µg 3:1	3×10^4 1.2µL 0.6µg 2:1	3×10^4 0.6µL 0.6µg 1:1
Cell density (cells/cm^2)	3×10^4	3×10^4	3×10^4	3×10^4	3×10^4	3×10^4
Reagent	4.8µL	2.4µL	1.2µL	4.8µL	2.4µL	1.2µL
dH_2O	1µL	1µL	1µL	1µL	1µL	1µL
Ratio	8:1	4:1	2:1	8:1	4:1	2:1

Table D.2 The transfection efficiency of specimens transfected by HiFect transfection reagent. The changing variables are highlighted in gray.

HiFect						
Seeding density (cells/cm^2)	GFP-pDNA (µg)	GFP:Reagent	dH_2O (µl)	H_2O:Reagent	Efficiency (%)	
					24 hours	48 hours
2×10^4	0.6	5:1			21.25	33.33
3×10^4	0.6	5:1			15.23	32.6
6×10^4	0.6	5:1			25.77	45.93
3×10^4	0.6	8:1			16.46	23.76
3×10^4	0.6	6:1			28.03	35.93
3×10^4	0.6	4:1			17.22	11.4
3×10^4	0.6	3:1			3.74	7.91
3×10^4	0.6	2:1			1.19	3.09
3×10^4	0.6	1:1			0	0
3×10^4			1	8:1	0	0
3×10^4			1	4:1	0	0
3×10^4			1	2:1	0	0

Table D.3 The transfection efficiency of specimens transfected by DharmaFect Duo transfection reagent. The changing variables are highlighted in gray.

DharmaFect Duo						
Seeding density (cells/cm^2)	**GFP-pDNA (μg)**	**GFP:Reagent**	**dH_2O (μl)**	**H_2O:Reagent**	**Efficiency (%)**	
					24 hours	**48 hours**
2×10^4	0.6	5:1			3.87	4.17
3×10^4	0.6	5:1			4.15	2.70
6×10^4	0.6	5:1			2.68	2.03
3×10^4	0.6	8:1			12.38	8.13
3×10^4	0.6	6:1			14.32	11.24
3×10^4	0.6	4:1			3.21	7.17
3×10^4	0.6	3:1			2.85	2.73
3×10^4	0.6	2:1			5.00	0
3×10^4	0.6	1:1			1.24	0.20
3×10^4			1	8:1	0	0
3×10^4			1	4:1	0	0
3×10^4			1	2:1	0	0

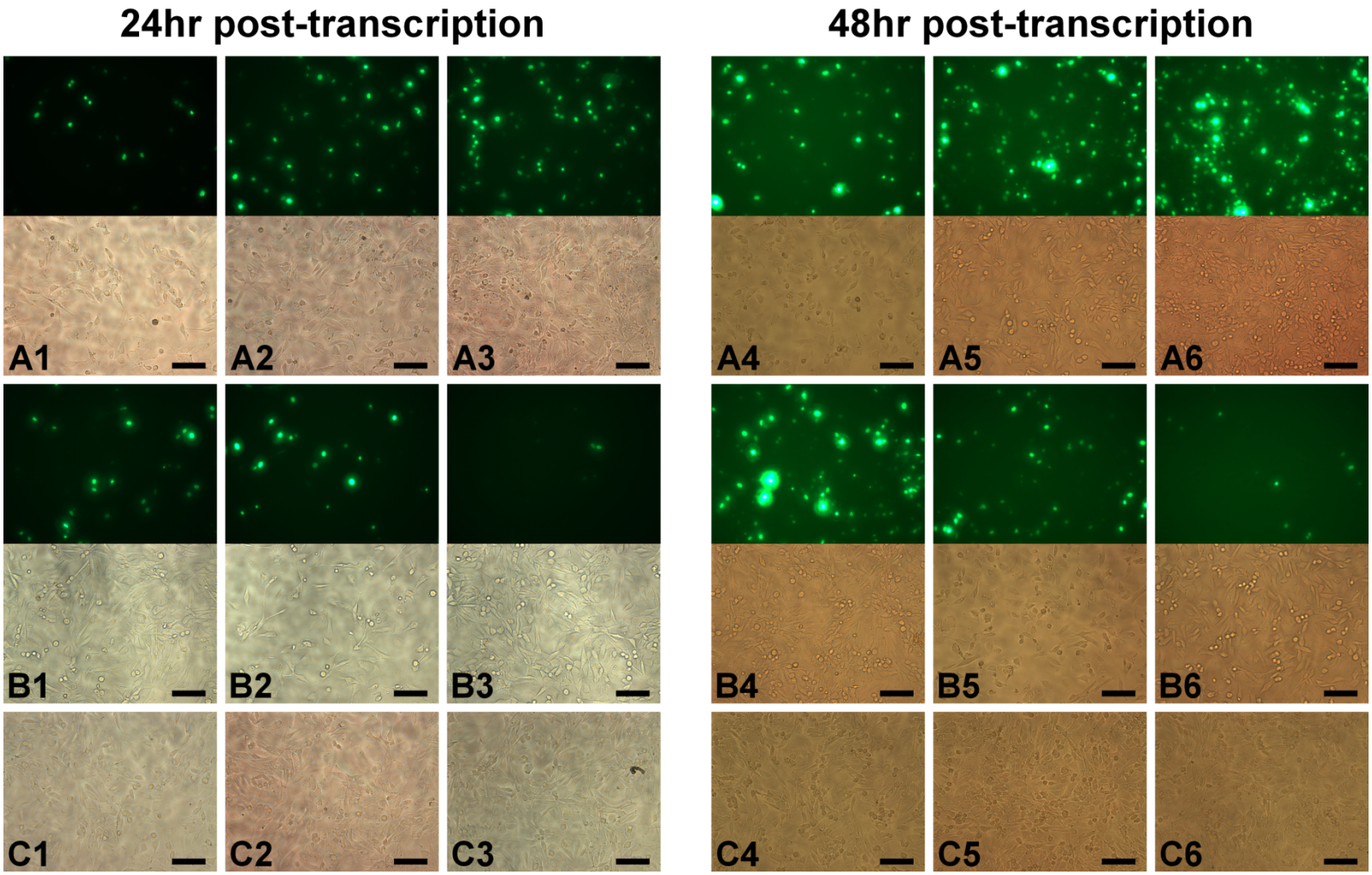

Figure D.1 Images of the chondrocytes and the transfected nuclei from the HiFect transfection group, 24 hours and 48 hours after transfection. Cell density test sub-group: A1 and A4 (2×10^4 cells/cm^2), A2 and A5 (3×10^4 cells/cm^2), A3 and A6 (6×10^4 cells/cm^2). Reagent and DNA ratio test sub-group: B1 and B4 (8:1), B2 and B5 (6:1), B3 and B6 (2:1). Control sub-group: C1 and C4 (8:1), C2 and C5 (4:1), C3 and C6 (2:1) (Bar: 100μm).

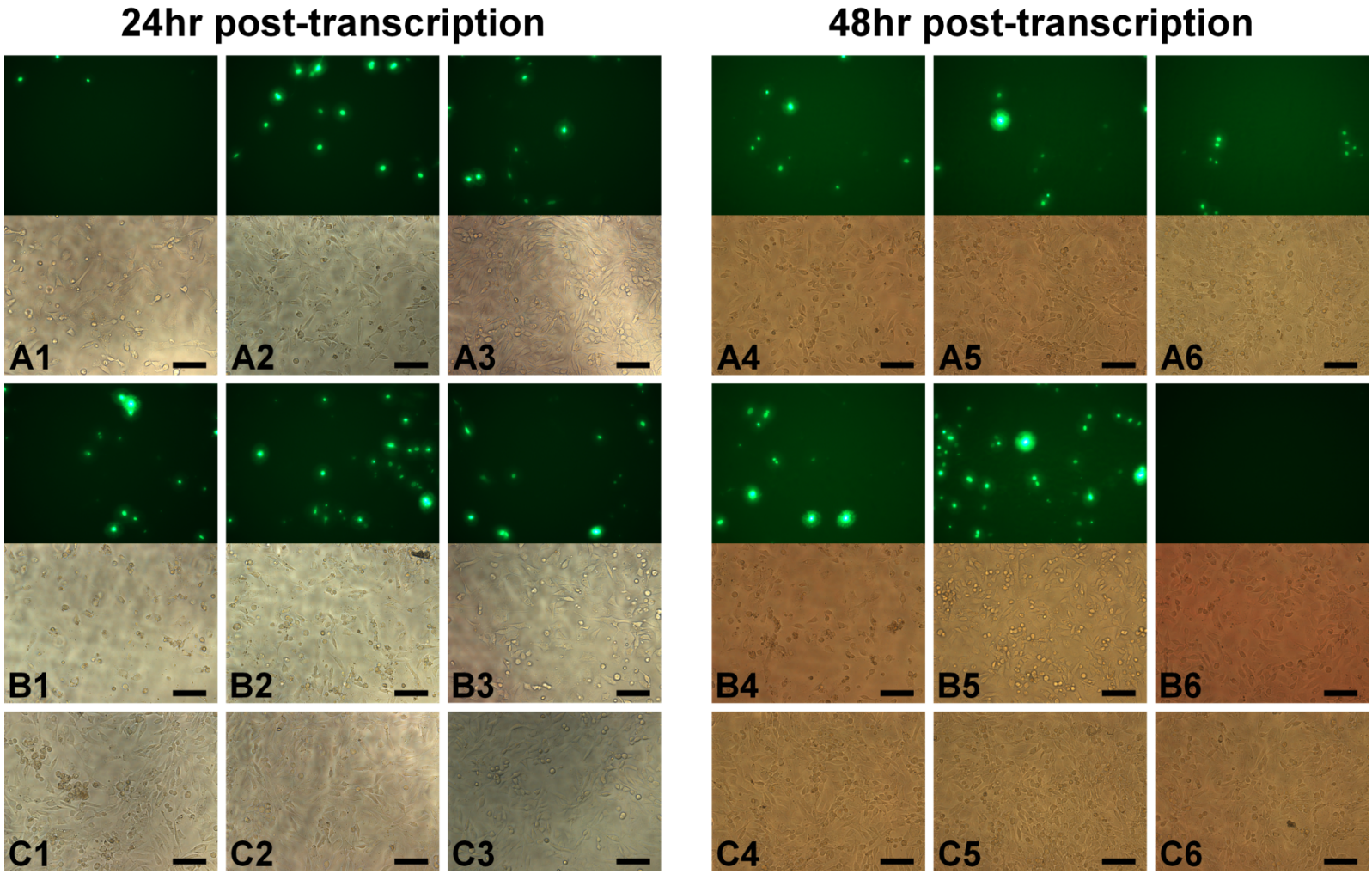

Figure D.2 Images of the chondrocytes and the transfected nuclei from the DharmaFect Duo transfection group, 24 hours and 48 hours after transfection. Cell density test sub-group: A1 and A4 (2×10^4 cells/cm^2), A2 and A5 (3×10^4 cells/cm^2), A3 and A6 (6×10^4 cells/cm^2). Reagent and DNA ratio test sub-group: B1 and B4 (8:1), B2 and B5 (6:1), B3 and B6 (2:1). Control sub-group: C1 and C4 (8:1), C2 and C5 (4:1), C3 and C6 (2:1) (Bar: 100μm).

Appendix E Osmolality and pH Level Over Imaging Procedure

There were two main reasons for the change of osmolality during the confocal imaging procedure: evaporation and mixing. During the imaging procedure, the specimens were placed into a temperature conditioned chamber, to maintain the temperature at 37^{o}C. However, this chamber does not condition for humidity, thus does not prevent evaporation of the specimen medium. Furthermore, during the application of osmotic challenge medium, the previous medium was replaced with the corresponding osmotic medium. However, mixing between the previous medium and the osmotic challenge medium was inevitable as it was impossible to fully extract the previous medium. In section 3.2.3 and 3.2.4, the imaging of Hoechst 33342 stained nuclei, the application of osmotic challenge medium was done manually with Gilson pipette and the time between each osmotic challenge was 45 minutes for monolayer specimens or 1 hour for 3D agarose specimens, which allow evaporation of the osmotic medium. In section 3.2.10 and 3.2.11, the imaging of H2B-GFP transfected nuclei, the application of osmotic challenge was done automatically with the developed delivery system. Due to the design of the glass bottom dish used in this procedure, approximately 0.4 mL of medium was un-replaceable, thus at least 0.4 mL of the previous medium will always mix with the new osmotic challenge medium. As part of the characterisation for the imaging procedure, the osmolality and pH level of the medium at various stages were measured and listed in Table E.1.

Table E.1 The osmolality and pH level of the osmotic challenge medium at various stages of the imaging procedure.

	Osmolality (mOsm/kg)	**pH**
Imaging of Hoechst 33342 stained nuclei		
300 mOsm/kg medium after the 1st osmotic challenge	332	7.4
600 mOsm/kg medium after the 1st washing	590	7.4
600 mOsm/kg medium after the 2nd washing	608	7.4
600 mOsm/kg medium after the 2nd osmotic challenge	641	7.4
Imaging of H2B-GFP transfected nuclei		
100 mOsm/kg medium replacing 300 mOsm/kg medium	118	7.4
300 mOsm/kg medium replacing 100 mOsm/kg medium	278	7.4
500 mOsm/kg medium replacing 300 mOsm/kg medium	476	7.4
300 mOsm/kg medium replacing 500 mOsm/kg medium	314	7.4
700 mOsm/kg medium replacing 300 mOsm/kg medium	660	7.4
300 mOsm/kg medium replacing 700 mOsm/kg medium	325	7.4

Appendix F Agarose Construct in Different Osmolality Environment

As part of the procedure characterisation for Chapter 4, it is essential to assess the effect of osmolality on the swelling property of agarose construct. Cylindrical 5 mm diameter × 5 mm height 3% agarose constructs were prepared as described in section 2.2.8, where instead of cell suspension, DMEM + 16.1% FCS medium was used. The agarose constructs were immersed in DMEM + 16.1% FCS and placed into a 37^{o}C incubator over night. For each agarose construct, the construct was removed from the medium and excess medium was removed, and the mass of the construct was measured. Afterwards, the construct was placed into the corresponding osmotic challenge medium for 2 hours and weighted again. The change in mass for each osmotic group was plotted as shown in Figure F.1. The results showed that osmolality does not change the swelling property of agarose constructs.

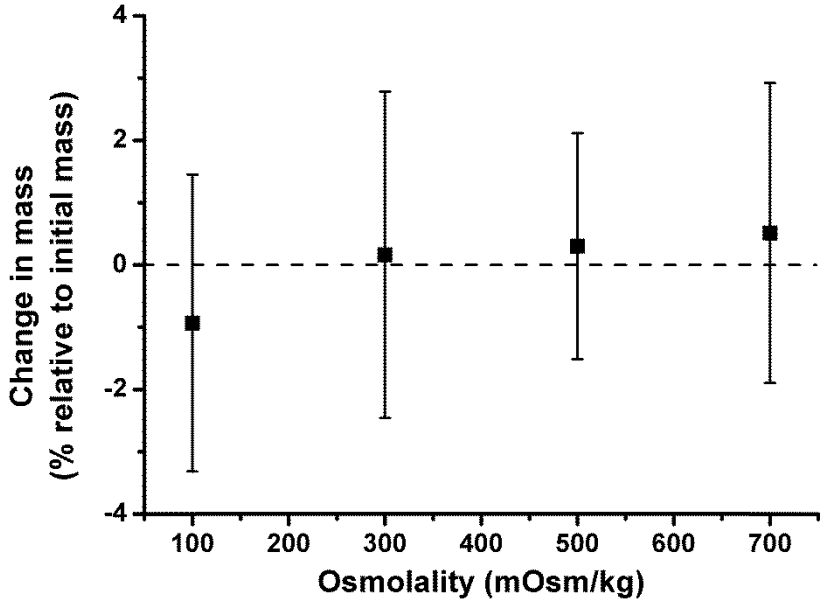

Figure F.1 Percentage change in mass of agarose constructs exposed to 100, 300, 500 and 700 mOsm/kg for 2 hours (N = 20). None of the readings are statistically different to each other.

Appendix G Stepper Motor Characterisation

Prior to the compression study, the displacement of the stepper motor on both sides were characterised to ensure that the specimens are strained accordingly. With the grip spacer in place, a porous glass (5 × 5 × 4 mm) was clamped onto each grip. The hydration chamber was assembled and the grip was secured onto the rig. After removing the spacer, a bright field image of the porous glass attached to the grip without the load cell was acquired by the confocal microscope, using a 63×/1.4NA oil immersion objective. The grip was displaced inward for 1 mm with an increment of 100 μm. For each increment, a bright field image was taken. The same grip was then displaced outward for 1 mm with a decrement of 100 μm and a bright field image was taken for each decrement. This procedure was repeated for the other grip attached to the motor with the load cell. The actual displacement of each porous glass at every increment and decrement step was measured using the software LCS Lite.

The displacement of grip attached to the side without load cell is comparable with the command inputted, as seen in Figure G.1 A. During the increment toward the 1 mm displacement and the decrement back to the original position, there was a degree of disagreement between the input and the actual displacement. This disagreement seems to decrease closer to the 1 mm displacement, where ultimately the grip did reach the displacement of 1 mm. By contrast, for grip attached to the side with load cell, there was a substantial disagreement between the input and the displacement (Figure G.1 B). The substantial disagreement was caused by misalignment of the load cell system. With the misalignment, higher torque is required by the stepper motor to do a certain displacement, altering the actual displacement from the inputted command. The misalignment occurred in the connection between the slider and the load cell. Based on this finding, compressive strain was only applied by the side without load cell.

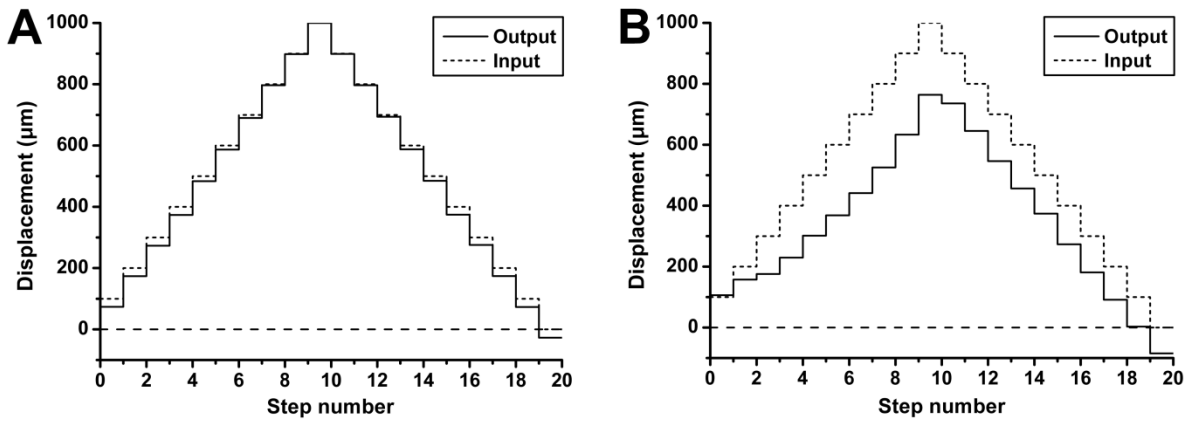

Figure G.1 Displacement of the grip (output) for each 100 µm step (input), A: The grip attached to the side without load cell and B: the grip attached to the side with load cell.

Appendix H Chosen Gene Count with Different Selection Parameter Threshold

In the gene selection process, the number of chosen probes depends on the threshold value for the expression fold change and the *p*- or *q*- value from the empirical Bayesian *t*-test. As part of the characterisation process, a set of threshold values were used to observe the number of probes selected for each osmotic group comparisons. The results were listed in Table H.1 - H.7. From the observation, $q<0.05$ and FC>1.5 seem to give reasonable numbers of probes for the different comparisons and were chosen as the threshold values.

Table H.1 Number of up- and down-regulated probes chosen by different selection parameter thresholds, for the comparison 300 mOsm/kg 1 hour vs. 500 mOsm/kg 1 hour.

***p*- or *q*- value threshold**	**Up-regulated**			**Down-regulated**		
	Fold change			**Fold change**		
	FC>1.5	**FC>2**	**FC>3**	**FC>1.5**	**FC>2**	**FC>3**
***p*<0.05**	23	9	2	49	20	12
***p*<0.01**	23	9	2	49	20	12
***p*<0.001**	22	9	2	49	20	12
***q*<0.05**	21	9	2	49	20	12
***q*<0.01**	18	9	2	44	20	12
***q*<0.001**	13	8	2	32	19	12

Table H.2 Number of up- and down-regulated probes chosen by different selection parameter thresholds, for the comparison 300 mOsm/kg 5 hours vs. 500 mOsm/kg 5 hours.

***p*- or *q*- value threshold**	**Up-regulated**			**Down-regulated**		
	Fold change			**Fold change**		
	FC>1.5	**FC>2**	**FC>3**	**FC>1.5**	**FC>2**	**FC>3**
***p*<0.05**	631	210	55	834	244	27
***p*<0.01**	628	210	55	834	244	27
***p*<0.001**	601	210	55	825	244	27
***q*<0.05**	627	210	55	834	244	27
***q*<0.01**	601	210	55	825	244	27
***q*<0.001**	484	206	55	700	244	27

Table H.3 Number of up- and down-regulated probes chosen by different selection parameter thresholds, for the comparison 300 mOsm/kg 1 hour vs. 300 mOsm/kg 5 hours.

***p*- or *q*- value threshold**	**Up-regulated**			**Down-regulated**		
	Fold change			**Fold change**		
	FC>1.5	**FC>2**	**FC>3**	**FC>1.5**	**FC>2**	**FC>3**
***p*<0.05**	14	1	1	56	21	1
***p*<0.01**	14	1	1	56	21	1
***p*<0.001**	13	1	1	56	21	1
***q*<0.05**	13	1	1	56	21	1
***q*<0.01**	10	1	1	56	21	1
***q*<0.001**	6	1	1	47	21	1

Table H.4 Number of up- and down-regulated probes chosen by different selection parameter thresholds, for the comparison 500 mOsm/kg 1 hour vs. 500 mOsm/kg 5 hours.

***p*- or *q*- value threshold**	**Up-regulated**			**Down-regulated**		
	Fold change			**Fold change**		
	FC>1.5	**FC>2**	**FC>3**	**FC>1.5**	**FC>2**	**FC>3**
***p*<0.05**	636	194	56	888	255	31
***p*<0.01**	630	194	56	888	255	31
***p*<0.001**	585	194	56	868	255	31
***q*<0.05**	629	194	56	887	255	31
***q*<0.01**	582	194	56	867	255	31
***q*<0.001**	441	184	56	685	253	31

Table H.5 Number of up- and down-regulated probes chosen by different selection parameter thresholds, for the comparison 500 mOsm/kg 1 hour vs. 500 mOsm/kg 1 hour followed with 300 mOsm/kg 4 hours.

***p*- or *q*- value threshold**	**Up-regulated**			**Down-regulated**		
	Fold change			**Fold change**		
	FC>1.5	**FC>2**	**FC>3**	**FC>1.5**	**FC>2**	**FC>3**
***p*<0.05**	124	32	20	105	19	2
***p*<0.01**	123	32	20	105	19	2
***p*<0.001**	112	32	20	104	19	2
***q*<0.05**	116	32	20	105	19	2
***q*<0.01**	93	32	20	89	19	2
***q*<0.001**	44	30	20	24	14	2

Table H.6 Number of up- and down-regulated probes chosen by different selection parameter thresholds, for the comparison 300 mOsm/kg 5 hours vs. 500 mOsm/kg 1 hour followed with 300 mOsm/kg 4 hours.

***p*- or *q*- value threshold**	**Up-regulated**			**Down-regulated**		
	Fold change			**Fold change**		
	FC>1.5	**FC>2**	**FC>3**	**FC>1.5**	**FC>2**	**FC>3**
***p*<0.05**	40	11	8	5	1	1
***p*<0.01**	40	11	8	5	1	1
***p*<0.001**	38	11	8	4	1	1
***q*<0.05**	33	11	8	4	1	1
***q*<0.01**	18	10	8	2	1	1
***q*<0.001**	11	10	8	1	1	1

Table H.7 Number of up- and down-regulated probes chosen by different selection parameter thresholds, for the comparison 500 mOsm/kg 5 hours vs. 500 mOsm/kg 1 hour followed with 300 mOsm/kg 4 hours.

***p*- or *q*- value threshold**	**Up-regulated**			**Down-regulated**		
	Fold change			**Fold change**		
	FC>1.5	**FC>2**	**FC>3**	**FC>1.5**	**FC>2**	**FC>3**
***p*<0.05**	950	304	39	650	195	55
***p*<0.01**	950	304	39	646	195	55
***p*<0.001**	918	304	39	606	195	55
***q*<0.05**	949	304	39	644	195	55
***q*<0.01**	917	304	39	602	195	55
***q*<0.001**	707	303	39	431	188	55

Appendix I Functional Annotations

In this appendix, the functional annotations of the chosen genes acquired from DAVID Bioinformatics Resources 6.7 are listed. For 300 mOsm/kg 1 hour vs. 500 mOsm/kg 1 hour, the representative annotations are listed for both up- and down-regulated (Table I.1 and I.2). For 300 mOsm/kg 5 hours vs. 500 mOsm/kg 5 hours, due to the large number of chosen genes, the annotations are clustered based on their gene members as shown in Table I.3 and I.4.

Table I.1 Differentially up-regulated genes from the comparison 300 mOsm/kg 1 hour vs. 500 mOsm/kg 1 hour, with the binary logarithm of fold change, the *q*-value and the annotations.

Gene	$\log_2$(FC)	*q*-value	Biological Process (GO)	Cellular Component (GO)	Molecular Function (GO)	Pathways (KEGG)
RNU6	1.72	2.53E-06	n/a	n/a	n/a	n/a
MYD116	1.68	1.68E-05	response to endoplasmic reticulum stress	endoplasmic reticulum	n/a	n/a
HSPA1A	1.53	1.23E-06	response to DNA damage stimulus	mitochondrial matrix	adenyl ribonucleotide binding	MAPK signaling pathway
HSPG2	1.24	3.55E-06	cartilage development involved in endochondral bone morphogenesis	extracellular matrix part	n/a	n/a
PPP1R10	1.22	1.89E-04	transcription	n/a	zinc ion binding	n/a
PPP1R10	1.17	1.70E-03	transcription	n/a	zinc ion binding	n/a
HEXIM1	1.12	2.45E-05	regulation of cyclin-dependent protein kinase activity	n/a	cyclin-dependent protein kinase inhibitor activity	n/a
LOC100047261	1.06	2.34E-05	cellular amino acid derivative catabolic process	cell fraction	diamine N-acetyltransferase activity	Arginine and proline metabolism
DUSP1	1.03	3.93E-04	protein amino acid dephosphorylation	n/a	MAP kinase tyrosine/serine/threonine phosphatase activity	MAPK signaling pathway
IER3	0.87	9.13E-04	n/a	plasma membrane part	n/a	n/a
BRD2	0.86	7.95E-06	n/a	n/a	n/a	n/a
FOS	0.85	2.01E-04	positive regulation of	nucleoplasm	structure-specific DNA binding	MAPK signaling pathway

			transcription from RNA polymerase II promoter			
LOC100046406	0.77	3.15E-04	n/a	n/a	n/a	n/a
RND3	0.74	1.33E-03	small GTPase mediated signal transduction	Golgi apparatus	guanyl ribonucleotide binding	n/a
DDIT4	0.71	3.37E-03	programmed cell death	n/a	n/a	mTOR signaling pathway
GADD45B	0.70	8.81E-03	activation of MAPKK activity	n/a	n/a	p53 signaling pathway
SLC38A2	0.64	3.78E-02	sodium ion transport	plasma membrane	sodium ion binding	n/a
BRD2	0.62	1.02E-02	n/a	n/a	n/a	n/a
PLEC1	0.61	7.12E-04	n/a	cytoskeleton	actin binding	n/a
BRD2	0.60	4.99E-02	n/a	n/a	n/a	n/a
RASL11B	0.59	3.39E-03	small GTPase mediated signal transduction	n/a	guanyl ribonucleotide binding	n/a

Table I.2 Differentially down-regulated genes from the comparison 300 mOsm/kg 1 hour vs. 500 mOsm/kg 1 hour, with the binary logarithm of fold change, the *q*-value and the annotations.

Gene	$\log_2$(FC)	*q*-value	Biological Process (GO)	Cellular Component (GO)	Molecular Function (GO)	Pathways (KEGG)
ID1	-2.40	5.82E-08	negative regulation of transcription from RNA polymerase II promoter	cell fraction	transcription regulator activity	TGF-beta signaling pathway
HIST1H2AH	-2.29	5.32E-07	chromatin assembly	chromatin	DNA binding	Systemic lupus erythematosus
HIST1H2AD	-2.25	4.00E-07	chromatin assembly	chromatin	DNA binding	Systemic lupus erythematosus
HIST1H2AK	-2.24	3.83E-07	chromatin assembly	chromatin	DNA binding	Systemic lupus erythematosus
HIST1H2AG	-2.15	3.99E-07	chromatin assembly	chromatin	DNA binding	Systemic lupus erythematosus
HIST2H2AB	-1.98	4.50E-07	chromatin assembly	chromatin	DNA binding	Systemic lupus erythematosus
SNORA65	-1.93	2.74E-06	translation	nucleolus	RNA binding	Ribosome
HIST1H2AN	-1.92	1.83E-05	chromatin assembly	chromatin	DNA binding	Systemic lupus erythematosus
HIST2H2AC	-1.82	6.03E-07	chromatin assembly	chromatin	DNA binding	Systemic lupus erythematosus
HIST1H2AF	-1.77	9.41E-06	chromatin assembly	chromatin	DNA binding	Systemic lupus erythematosus

HIST1H2AO	-1.72	9.65E-08	chromatin assembly	chromatin	DNA binding	Systemic lupus erythematosus
JUNB	-1.61	1.21E-05	blood vessel development	n/a	sequence-specific DNA binding	n/a
FOXQ1	-1.44	9.63E-07	regulation of transcription, DNA-dependent	n/a	sequence-specific DNA binding	n/a
CH25H	-1.33	6.11E-06	fatty acid biosynthetic process	endoplasmic reticulum	iron ion binding	Primary bile acid biosynthesis
BC017647	-1.25	4.04E-06	n/a	n/a	n/a	n/a
ERRFI1	-1.05	4.90E-04	cellular response to stress	cytosol	n/a	n/a
HES1	-1.05	6.50E-05	negative regulation of transcription from RNA polymerase II promoter	n/a	DNA binding	Notch signaling pathway
SERTAD1	-1.03	9.03E-05	positive regulation of macromolecule biosynthetic process	n/a	transcription regulator activity	n/a
BHLHB2	-1.02	6.57E-06	negative regulation of RNA metabolic process	n/a	DNA binding	Circadian rhythm
CCL7	-1.00	1.46E-03	inflammatory response	extracellular region part	heparin binding	Cytokine-cytokine receptor interaction
HAS2	-0.95	1.85E-04	n/a	intrinsic to membrane	hyaluronan synthase activity	n/a
CTGF	-0.95	2.31E-04	skeletal system development	proteinaceous extracellular matrix	integrin binding	n/a
SNAI1	-0.93	1.18E-04	hair follicle development	n/a	zinc ion binding	Adherens junction
PHLDA1	-0.90	4.68E-04	programmed cell death	nucleolus	n/a	n/a
ARC	-0.89	6.78E-06	membrane invagination	cytoskeleton	actin binding	n/a
DUSP6	-0.89	1.58E-04	protein amino acid dephosphorylation	n/a	MAP kinase phosphatase activity	MAPK signaling pathway
VEGFA	-0.83	3.94E-04	blood vessel development	extracellular matrix part	heparin binding	Cytokine-cytokine receptor interaction
CCL2	-0.82	1.23E-03	positive regulation of endothelial cell proliferation	extracellular region part	chemokine receptor binding	Cytokine-cytokine receptor interaction
TNFAIP3	-0.75	1.77E-02	programmed cell death	n/a	DNA binding	NOD-like receptor signaling pathway
PLAGL2	-0.75	6.89E-05	positive regulation of programmed cell death	n/a	zinc ion binding	n/a

DUSP8	-0.74	1.91E-04	protein amino acid dephosphorylation	n/a	MAP kinase phosphatase activity	MAPK signaling pathway
ZFP36	-0.73	2.98E-04	nuclear-transcribed mRNA poly(A) tail shortening	cytosol	AU-rich element binding	n/a
HNRPDL	-0.73	1.03E-02	regulation of transcription	n/a	nucleotide binding	n/a
THOC6	-0.72	1.71E-03	n/a	n/a	n/a	n/a
GJB3	-0.69	2.63E-03	placenta development	gap junction	n/a	n/a
ZFP655	-0.69	1.71E-03	regulation of transcription, DNA-dependent	nucleolus	zinc ion binding	n/a
CYR61	-0.68	4.10E-02	angiogenesis	extracellular region	heparin binding	n/a
NGFB	-0.67	2.65E-03	negative regulation of programmed cell death	endoplasmic reticulum lumen	growth factor activity	MAPK signaling pathway
CCDC85B	-0.67	3.94E-03	negative regulation of macromolecule metabolic process	centrosome	n/a	n/a
HBEGF	-0.66	2.51E-03	blood vessel development	plasma membrane	heparin binding	ErbB signaling pathway
CITED2	-0.66	3.71E-03	blood vessel development	nuclear chromatin	DNA binding	n/a
IRX3	-0.65	9.02E-04	regulation of transcription, DNA-dependent	n/a	sequence-specific DNA binding	n/a
ZFP472	-0.65	3.57E-04	regulation of transcription	n/a	zinc ion binding	n/a
P2RY5	-0.63	1.38E-03	cell surface receptor linked signal transduction	intrinsic to membrane	nucleotide receptor activity, G-protein coupled	Neuroactive ligand-receptor interaction
LOC100046898	-0.61	8.70E-03	cellular protein catabolic process	n/a	adenyl ribonucleotide binding	Ubiquitin mediated proteolysis
NGFB	-0.61	6.91E-04	negative regulation of programmed cell death	endoplasmic reticulum lumen	growth factor activity	MAPK signaling pathway
VASN	-0.60	3.67E-02	n/a	intrinsic to membrane	n/a	n/a
ZFP87	-0.60	6.21E-03	regulation of transcription, DNA-dependent	n/a	zinc ion binding	n/a
SPRED1	-0.59	2.68E-02	negative regulation of MAP kinase activity	extrinsic to membrane	stem cell factor receptor binding	Jak-STAT signaling pathway

Table I.3 Annotation clusters of the differentially up-regulated genes from the comparison 300 mOsm/kg 5 hours vs. 500 mOsm/kg 5 hours, with the enrichment score, the annotation members, the gene count and the *p*-value. The code represents the domain of the annotation.

Cluster	Enrichment score	Annotation	Code*	Gene count	*p*-value
1	6.42	regulation of transcription from RNA polymerase II promoter	BP	49	1.29E-09
		DNA binding	MF	92	4.65E-08
		regulation of RNA metabolic process	BP	82	6.78E-08
		transcription regulator activity	MF	69	9.59E-08
		transcription factor activity	MF	51	1.20E-07
		regulation of transcription	BP	109	1.21E-07
		positive regulation of nitrogen compound metabolic process	BP	40	1.92E-07
		positive regulation of gene expression	BP	38	2.29E-07
		positive regulation of nucleobase, nucleoside, nucleotide and nucleic acid metabolic process	BP	39	2.44E-07
		regulation of transcription, DNA-dependent	BP	79	3.19E-07
		positive regulation of transcription	BP	37	3.40E-07
		sequence-specific DNA binding	MF	40	4.06E-07
		positive regulation of RNA metabolic process	BP	34	4.49E-07
		positive regulation of transcription, DNA-dependent	BP	33	1.13E-06
		positive regulation of macromolecule biosynthetic process	BP	38	1.70E-06
		positive regulation of cellular biosynthetic process	BP	39	1.73E-06
		positive regulation of biosynthetic process	BP	39	2.14E-06
		positive regulation of macromolecule metabolic process	BP	42	3.08E-06
		positive regulation of transcription from RNA polymerase II promoter	BP	28	1.12E-05
		transcription	BP	85	1.16E-05
2	4.61	regulation of transcription from RNA polymerase II promoter	BP	49	1.29E-09
		transcription repressor activity	MF	20	1.49E-05
		negative regulation of cellular biosynthetic process	BP	31	1.70E-05
		negative regulation of biosynthetic process	BP	31	2.04E-05
		negative regulation of macromolecule metabolic process	BP	34	2.57E-05
		negative regulation of nitrogen compound metabolic process	BP	29	3.12E-05
		negative regulation of gene expression	BP	29	4.80E-05
		negative regulation of transcription, DNA-dependent	BP	24	5.88E-05
		negative regulation of transcription	BP	27	6.03E-05
		negative regulation of RNA metabolic process	BP	24	6.49E-05
		negative regulation of macromolecule biosynthetic process	BP	29	6.69E-05
		negative regulation of nucleobase, nucleoside, nucleotide and nucleic acid metabolic process	BP	28	6.82E-05

		negative regulation of transcription from RNA polymerase II promoter	BP	16	4.29E-03
3	4.04	blood vessel morphogenesis	BP	19	3.01E-05
		blood vessel development	BP	21	4.93E-05
		vasculature development	BP	21	6.96E-05
		angiogenesis	BP	13	6.78E-04
4	3.28	vacuole	CC	17	8.21E-05
		lysosome	CC	15	2.21E-04
		lytic vacuole	CC	15	2.34E-04
5	2.93	regulation of cell death	BP	32	8.94E-04
		negative regulation of apoptosis	BP	18	9.18E-04
		negative regulation of programmed cell death	BP	18	1.16E-03
		negative regulation of cell death	BP	18	1.21E-03
		anti-apoptosis	BP	10	1.30E-03
		regulation of apoptosis	BP	31	1.34E-03
		regulation of programmed cell death	BP	31	1.64E-03
6	2.7	embryonic development ending in birth or egg hatching	BP	29	8.89E-05
		chordate embryonic development	BP	28	1.85E-04
		in utero embryonic development	BP	18	2.99E-03
		embryonic organ development	BP	15	1.44E-02
		embryonic morphogenesis	BP	18	4.37E-02
7	2.55	protein dimerization activity	MF	25	6.78E-05
		identical protein binding	MF	17	1.20E-02
		protein homodimerization activity	MF	12	2.72E-02
8	2.42	skeletal system development	BP	21	3.99E-04
		bone development	BP	10	9.27E-03
		ossification	BP	9	1.46E-02
9	2.35	response to wounding	BP	25	1.35E-04
		inflammatory response	BP	18	4.63E-04
		defense response	BP	21	5.25E-02
		immune response	BP	20	1.22E-01
10	2.34	enzyme binding	MF	18	4.36E-04
		kinase binding	MF	8	1.23E-02
		protein kinase binding	MF	7	1.77E-02
11	2.28	cytoplasmic membrane-bounded vesicle	CC	22	2.63E-03
		membrane-bounded vesicle	CC	22	3.11E-03
		melanosome	CC	8	6.45E-03
		pigment granule	CC	8	6.45E-03
		cytoplasmic vesicle	CC	24	6.77E-03
		vesicle	CC	24	8.59E-03
12	2.24	transcription factor binding	MF	19	2.18E-03
		transcription corepressor activity	MF	8	5.08E-03
		transcription cofactor activity	MF	12	1.72E-02
13	2.16	protein serine/threonine kinase inhibitor activity	MF	6	2.43E-06

		negative regulation of kinase activity	BP	9	1.29E-04
		negative regulation of protein kinase activity	BP	9	1.29E-04
		negative regulation of transferase activity	BP	9	1.70E-04
		negative regulation of molecular function	BP	14	1.73E-04
		protein kinase inhibitor activity	MF	6	2.29E-04
		kinase regulator activity	MF	10	2.72E-04
		protein kinase regulator activity	MF	9	3.07E-04
		kinase inhibitor activity	MF	6	3.70E-04
		cyclin-dependent protein kinase inhibitor activity	MF	4	4.70E-04
		regulation of protein kinase activity	BP	15	1.51E-03
		regulation of kinase activity	BP	15	2.03E-03
		regulation of transferase activity	BP	15	2.80E-03
		negative regulation of catalytic activity	BP	10	3.38E-03
		regulation of phosphate metabolic process	BP	19	4.42E-03
		regulation of phosphorus metabolic process	BP	19	4.42E-03
		regulation of phosphorylation	BP	18	6.82E-03
		MAPKKK cascade	BP	10	7.46E-03
		cyclin-dependent protein kinase regulator activity	MF	4	8.78E-03
		negative regulation of cyclin-dependent protein kinase activity	BP	3	2.83E-02
		negative regulation of cell cycle	BP	5	3.97E-02
14	2.14	transcription factor complex	CC	18	1.27E-04
		nuclear lumen	CC	37	4.45E-03
		nucleoplasm	CC	27	7.04E-03
		intracellular organelle lumen	CC	42	1.76E-02
		organelle lumen	CC	42	1.84E-02
		nucleoplasm part	CC	22	2.60E-02
		membrane-enclosed lumen	CC	42	2.97E-02
15	2.12	protein amino acid dephosphorylation	BP	11	2.30E-03
		dephosphorylation	BP	12	3.57E-03
		MAP kinase tyrosine/serine/threonine phosphatase activity	MF	4	4.53E-03
		MAP kinase phosphatase activity	MF	4	4.53E-03
		phosphatase activity	MF	16	4.59E-03
		phosphoprotein phosphatase activity	MF	12	5.20E-03
		protein tyrosine phosphatase activity	MF	8	2.90E-02
		protein tyrosine/serine/threonine phosphatase activity	MF	4	9.97E-02
16	2.06	nucleosome	CC	9	1.86E-04
		nucleosome organization	BP	10	4.44E-04
		protein-DNA complex	CC	9	6.95E-04
		nucleosome assembly	BP	9	1.53E-03
		chromatin assembly	BP	9	1.82E-03
		protein-DNA complex assembly	BP	9	1.98E-03
		chromatin	CC	12	3.80E-03
		chromatin assembly or disassembly	BP	10	5.59E-03

		DNA packaging	BP	9	1.11E-02
		macromolecular complex subunit organization	BP	19	2.84E-02
		chromatin organization	BP	17	2.88E-02
		cellular macromolecular complex subunit organization	BP	14	3.41E-02
		chromosome organization	BP	20	3.58E-02
		chromosomal part	CC	15	3.77E-02
17	2.06	late endosome	CC	7	8.89E-04
		phagocytic vesicle	CC	3	2.14E-02
		endocytic vesicle	CC	4	3.50E-02

*BP = Biological process from GO CC = Cellular component from GO MF = Molecular function from GO

Table I.4 Annotation clusters of the differentially down-regulated genes from the comparison 300 mOsm/kg 5 hours vs. 500 mOsm/kg 5 hours, with the enrichment score, the annotation members, the gene count and the *p*-value. The code represents the domain of the annotation.

Cluster	Enrichment score	Annotation	Code*	Gene count	*p*-value
1	21.85	nucleolus	CC	53	8.00E-23
		intracellular non-membrane-bounded organelle	CC	139	1.88E-22
		non-membrane-bounded organelle	CC	139	1.88E-22
2	20.94	membrane-enclosed lumen	CC	116	6.82E-28
		intracellular organelle lumen	CC	113	1.42E-27
		organelle lumen	CC	113	1.83E-27
		nuclear lumen	CC	98	2.24E-27
		nucleolus	CC	53	8.00E-23
		nucleoplasm	CC	51	1.24E-09
		nucleoplasm part	CC	45	6.76E-09
3	6.32	DNA metabolic process	BP	39	3.20E-08
		response to DNA damage stimulus	BP	32	4.83E-08
		cellular response to stress	BP	37	5.47E-07
		DNA repair	BP	22	5.99E-05
4	6.12	cell cycle	BP	53	1.86E-09
		mitotic cell cycle	BP	29	2.68E-08
		cell cycle phase	BP	33	1.03E-07
		organelle fission	BP	24	3.76E-07
		cell cycle process	BP	35	7.42E-07
		M phase of mitotic cell cycle	BP	22	4.06E-06
		cell division	BP	27	5.60E-06
		nuclear division	BP	21	1.11E-05
		mitosis	BP	21	1.11E-05
		M phase	BP	26	1.57E-05
5	5.93	ncRNA processing	BP	22	9.98E-08
		tRNA processing	BP	14	3.21E-07
		ncRNA metabolic process	BP	23	2.10E-06

		tRNA metabolic process	BP	15	2.91E-05
6	5.78	RNA processing	BP	47	1.75E-11
		ribonucleoprotein complex	CC	40	4.35E-08
		spliceosome	CC	15	5.96E-05
		mRNA processing	BP	24	6.35E-05
		mRNA metabolic process	BP	26	7.91E-05
		RNA splicing	BP	20	9.41E-05
7	5.14	zinc ion binding	MF	121	2.99E-11
		transition metal ion binding	MF	135	3.79E-09
		metal ion binding	MF	153	3.74E-03
		cation binding	MF	153	5.31E-03
		ion binding	MF	153	9.20E-03
8	4.89	chromosome	CC	31	5.93E-06
		chromosome, centromeric region	CC	15	1.03E-05
		chromosomal part	CC	26	3.47E-05
9	4.32	pseudouridine synthase activity	MF	6	8.28E-06
		pseudouridine synthesis	BP	6	1.73E-05
		RNA modification	BP	9	4.12E-05
		intramolecular transferase activity	MF	6	9.18E-04
10	4.05	protein transport	BP	44	3.40E-05
		establishment of protein localization	BP	44	4.24E-05
		protein localization	BP	45	4.75E-04
11	3.35	ribonucleoprotein complex biogenesis	BP	20	3.84E-07
		ribosome biogenesis	BP	17	1.97E-06
		preribosome	CC	4	8.27E-03
12	2.95	microtubule organizing center	CC	19	5.94E-05
		centrosome	CC	17	8.87E-05
		microtubule cytoskeleton	CC	27	2.11E-03
		cytoskeletal part	CC	39	2.38E-03
13	2.72	RNA biosynthetic process	BP	17	1.05E-05
		transcription, DNA-dependent	BP	16	2.85E-05
		DNA-directed RNA polymerase II, holoenzyme	CC	8	2.09E-03
		transcription from RNA polymerase II promoter	BP	8	1.86E-02
		transcription initiation	BP	5	3.61E-02
14	2.67	organellar ribosome	CC	9	5.43E-05
		mitochondrial ribosome	CC	9	5.43E-05
		ribosome	CC	17	4.18E-04
		ribosomal subunit	CC	9	8.90E-04
		translation	BP	22	1.09E-03
		mitochondrial matrix	CC	14	3.68E-03
		mitochondrial lumen	CC	14	3.68E-03
		large ribosomal subunit	CC	6	5.61E-03
		organellar large ribosomal subunit	CC	5	6.36E-03
		mitochondrial large ribosomal subunit	CC	5	6.36E-03

		structural constituent of ribosome	MF	12	9.49E-03
15	2.57	chromosome, centromeric region	CC	15	1.03E-05
		condensed chromosome, centromeric region	CC	8	2.63E-03
		kinetochore	CC	8	3.64E-03
		condensed chromosome kinetochore	CC	7	6.16E-03
		condensed chromosome	CC	9	2.37E-02
		chromosome segregation	BP	7	2.67E-02
16	2.35	interphase	BP	8	1.29E-03
		interphase of mitotic cell cycle	BP	7	4.97E-03
		G1/S transition of mitotic cell cycle	BP	5	1.42E-02
17	2.33	negative regulation of DNA metabolic process	BP	6	6.00E-04
		cell cycle checkpoint	BP	8	2.77E-03
		regulation of DNA metabolic process	BP	8	4.78E-03
		DNA integrity checkpoint	BP	6	6.91E-03
		negative regulation of DNA replication	BP	4	7.32E-03
		regulation of DNA replication	BP	4	2.54E-02
18	2.31	chromatin modification	BP	19	1.26E-03
		chromatin organization	BP	21	4.95E-03
		chromosome organization	BP	23	1.84E-02
19	2.24	regulation of cell cycle	BP	21	7.26E-05
		DNA damage response, signal transduction	BP	10	2.17E-04
		cell cycle checkpoint	BP	8	2.77E-03
		DNA integrity checkpoint	BP	6	6.91E-03
		DNA damage checkpoint	BP	5	2.36E-02
20	2.04	DNA-dependent DNA replication	BP	7	1.65E-03
		mitochondrial genome maintenance	BP	4	5.48E-03
		mitochondrial DNA metabolic process	BP	3	2.71E-02
		mitochondrial DNA replication	BP	3	2.71E-02

*BP = Biological process from GO CC = Cellular component from GO MF = Molecular function from GO

BIBLIOGRAPHY

Abramoff, M. D., P. J. Magalhaes and S. J. Ram (2004). "Image Processing with ImageJ." Biophotonics International **11**(7): 36-42.

Abramowitz, M. and M. W. Davidson. (2010, 2010). "Numerical Aperture and Resolution." Microscopy Resource Center Retrieved November 2, 2011, from http://www.olympusmicro.com/primer/anatomy/numaperture.html.

Aebi, U., J. Cohn, L. Buhle and L. Gerace (1986). "The nuclear lamina is a meshwork of intermediate-type filaments." Nature **323**(6088): 560-564.

Ahearne, M., Y. Yang, A. J. El Haj, K. Y. Then and K. K. Liu (2005). "Characterizing the viscoelastic properties of thin hydrogel-based constructs for tissue engineering applications." Journal of the Royal Society Interface **2**(5): 455-463.

Akizuki, S., V. C. Mow, F. Muller, J. C. Pita, D. S. Howell and D. H. Manicourt (1986). "Tensile properties of human knee joint cartilage: I. Influence of ionic conditions, weight bearing, and fibrillation on the tensile modulus." J Orthop Res **4**(4): 379-392.

Alberts, B. (2008). Molecular biology of the cell. New York, Garland Science ; [London : Taylor & Francis, distributor].

Albiez, H., M. Cremer, C. Tiberi, L. Vecchio, L. Schermelleh, S. Dittrich, K. Kupper, B. Joffe, T. Thormeyer, J. von Hase, S. Yang, K. Rohr, H. Leonhardt, I. Solovei, C. Cremer, S. Fakan and T. Cremer (2006). "Chromatin domains and the interchromatin compartment form structurally defined and functionally interacting nuclear networks." Chromosome Res **14**(7): 707-733.

Allen, J. L., M. E. Cooke and T. Alliston (2012). "ECM stiffness primes the TGFbeta pathway to promote chondrocyte differentiation." Mol Biol Cell **23**(18): 3731-3742.

Amin, A. K., J. S. Huntley, J. T. Patton, I. J. Brenkel, A. H. Simpson and A. C. Hall (2011). "Hyperosmolarity protects chondrocytes from mechanical injury in human articular cartilage: an experimental report." J Bone Joint Surg Br **93**(2): 277-284.

Angele, P., J. U. Yoo, C. Smith, J. Mansour, K. J. Jepsen, M. Nerlich and B. Johnstone (2003). "Cyclic hydrostatic pressure enhances the chondrogenic phenotype of

human mesenchymal progenitor cells differentiated in vitro." Journal of orthopaedic research : official publication of the Orthopaedic Research Society **21**(3): 451-457.

Armitage, B. A. (2005). "Cyanine Dye–DNA Interactions: Intercalation, Groove Binding, and Aggregation " Topics in Current Chemistry **253**: 55-76.

Armstrong, C. G. and V. C. Mow (1982). "Variations in the intrinsic mechanical properties of human articular cartilage with age, degeneration, and water content." J Bone Joint Surg Am **64**(1): 88-94.

Arokoski, J., I. Kiviranta, J. Jurvelin, M. Tammi and H. J. Helminen (1993). "Long-distance running causes site-dependent decrease of cartilage glycosaminoglycan content in the knee joints of beagle dogs." Arthritis Rheum **36**(10): 1451-1459.

Athanasiou, K. A., A. Agarwal, A. Muffoletto, F. J. Dzida, G. Constantinides and M. Clem (1995). "Biomechanical properties of hip cartilage in experimental animal models." Clin Orthop Relat Res(316): 254-266.

Bachrach, N. M., V. C. Mow and F. Guilak (1998). "Incompressibility of the solid matrix of articular cartilage under high hydrostatic pressures." Journal of biomechanics **31**(5): 445-451.

Bader, D. L. and D. A. Lee (2000). Structure-Properties of Soft Tissues Articular Cartilage. in: Structural biological materials : design and structure-property relationships

M. Elices. Amsterdam ; Oxford, Pergamon**:** xv,361 p.

Barrett-Jolley, R., R. Lewis, R. Fallman and A. Mobasheri (2010). "The emerging chondrocyte channelome." Front Physiol **1**: 135.

Baumgarten, M., R. D. Bloebaum, S. D. Ross, P. Campbell and A. Sarmiento (1985). "Normal human synovial fluid: osmolality and exercise-induced changes." J Bone Joint Surg Am **67**(9): 1336-1339.

Bayliss, M. T., D. Osborne, S. Woodhouse and C. Davidson (1999). "Sulfation of chondroitin sulfate in human articular cartilage. The effect of age, topographical position, and zone of cartilage on tissue composition." J Biol Chem **274**(22): 15892-15900.

Bayliss, M. T., J. P. Urban, B. Johnstone and S. Holm (1986). "In vitro method for measuring synthesis rates in the intervertebral disc." J Orthop Res **4**(1): 10-17.

Behrens, F., E. L. Kraft and T. R. Oegema (1989). "Biochemical-Changes in Articular-Cartilage after Joint Immobilization by Casting or External Fixation." Journal of Orthopaedic Research **7**(3): 335-343.

Bell, A. C. and G. Felsenfeld (2000). "Methylation of a CTCF-dependent boundary controls imprinted expression of the Igf2 gene." Nature **405**(6785): 482-485.

Benaud, C., R. B. Dickson and E. W. Thompson (1998). "Roles of the matrix metalloproteinases in mammary gland development and cancer." Breast Cancer Res Treat **50**(2): 97-116.

Benjamin, M., C. W. Archer and J. R. Ralphs (1994). "Cytoskeleton of cartilage cells." Microsc Res Tech **28**(5): 372-377.

Benjamini, Y. and Y. Hochberg (1995). "Controlling the False Discovery Rate - a Practical and Powerful Approach to Multiple Testing." Journal of the Royal Statistical Society Series B-Methodological **57**(1): 289-300.

Benya, P. D. and J. D. Shaffer (1982). "Dedifferentiated chondrocytes reexpress the differentiated collagen phenotype when cultured in agarose gels." Cell **30**(1): 215-224.

Berezney, R. and D. S. Coffey (1974). "Identification of a Nuclear Protein Matrix." Biochemical and Biophysical Research Communications **60**(4): 1410-1417.

Bjelle, A. (1975). "Content and composition of glycosaminoglycans in human knee joint cartilage. Variation with site and age in adults." Connect Tissue Res **3**(2): 141-147.

Blaschke, U. K., E. F. Eikenberry, D. J. Hulmes, H. J. Galla and P. Bruckner (2000). "Collagen XI nucleates self-assembly and limits lateral growth of cartilage fibrils." J Biol Chem **275**(14): 10370-10378.

Bolstad, B. M., R. A. Irizarry, M. Astrand and T. P. Speed (2003). "A comparison of normalization methods for high density oligonucleotide array data based on variance and bias." Bioinformatics **19**(2): 185-193.

Bolzer, A., G. Kreth, I. Solovei, D. Koehler, K. Saracoglu, C. Fauth, S. Muller, R. Eils, C. Cremer, M. R. Speicher and T. Cremer (2005). "Three-dimensional maps of all chromosomes in human male fibroblast nuclei and prometaphase rosettes." PLoS Biol **3**(5): e157.

Borden, K. L. (2002). "Pondering the promyelocytic leukemia protein (PML) puzzle: possible functions for PML nuclear bodies." Mol Cell Biol **22**(15): 5259-5269.

Borghetti, P., L. Della Salda, E. De Angelis, M. C. Maltarello, P. G. Petronini, E. Cabassi, P. S. Marcato, N. M. Maraldi and A. F. Borghetti (1995). "Adaptive cellular response to osmotic stress in pig articular chondrocytes." Tissue Cell **27**(2): 173-183.

Brandt, K. D., S. L. Myers, D. Burr and M. Albrecht (1991). "Osteoarthritic changes in canine articular cartilage, subchondral bone, and synovium fifty-four months after transection of the anterior cruciate ligament." Arthritis Rheum **34**(12): 1560-1570.

Briggs, C. and M. Jones (2005). "SYBR Green I-induced fluorescence in cultured immune cells: a comparison with Acridine Orange." Acta Histochem **107**(4): 301-312.

Brittberg, M. (2003). Update on the Swedish experience of cartilage surface repair. in: Current developments in autologous chondrocyte transplantation. G. Bentley. London, Royal Society of Medicine Press. **Round Table Series Vol. 77**.

Broom, N. D. and D. B. Myers (1980). "A study of the structural response of wet hyaline cartilage to various loading situations." Connective tissue research **7**(4): 227-237.

Brown, K. E., S. S. Guest, S. T. Smale, K. Hahm, M. Merkenschlager and A. G. Fisher (1997). "Association of transcriptionally silent genes with Ikaros complexes at centromeric heterochromatin." Cell **91**(6): 845-854.

Brown, P. D. and P. D. Benya (1988). "Alterations in chondrocyte cytoskeletal architecture during phenotypic modulation by retinoic acid and dihydrocytochalasin B-induced reexpression." J Cell Biol **106**(1): 171-179.

Browning, J. A., R. E. Walker, A. C. Hall and R. J. Wilkins (1999). "Modulation of Na+ x H+ exchange by hydrostatic pressure in isolated bovine articular chondrocytes." Acta Physiologica Scandinavica **166**(1): 39-45.

Burg, M. B., J. D. Ferraris and N. I. Dmitrieva (2007). "Cellular response to hyperosmotic stresses." Physiological Reviews **87**(4): 1441-1474.

Buschmann, M. D., Y. A. Gluzband, A. J. Grodzinsky and E. B. Hunziker (1995). "Mechanical compression modulates matrix biosynthesis in chondrocyte/agarose culture." Journal of cell science **108 (Pt 4)**: 1497-1508.

Buschmann, M. D., Y. A. Gluzband, A. J. Grodzinsky, J. H. Kimura and E. B. Hunziker (1992). "Chondrocytes in agarose culture synthesize a mechanically functional extracellular matrix." Journal of orthopaedic research : official publication of the Orthopaedic Research Society **10**(6): 745-758.

Bush, P. G. and A. C. Hall (2001). "The osmotic sensitivity of isolated and in situ bovine articular chondrocytes." J Orthop Res **19**(5): 768-778.

Bush, P. G. and A. C. Hall (2001). "Regulatory volume decrease (RVD) by isolated and in situ bovine articular chondrocytes." Journal of Cellular Physiology **187**(3): 304-314.

Bush, P. G. and A. C. Hall (2003). "The volume and morphology of chondrocytes within non-degenerate and degenerate human articular cartilage." Osteoarthritis and Cartilage **11**(4): 242-251.

Cai, B. X., D. Luo, X. F. Lin and J. Gao (2008). "Compound K suppresses ultraviolet radiation-induced apoptosis by inducing DNA repair in human keratinocytes." Arch Pharm Res **31**(11): 1483-1488.

Canete, M., A. Juarranz, P. Lopez-Nieva, C. Alonso-Torcal, A. Villanueva and J. C. Stockert (2001). "Fixation and permanent mounting of fluorescent probes after vital labelling of cultured cells." Acta Histochem **103**(2): 117-126.

Capco, D. G., K. M. Wan and S. Penman (1982). "The Nuclear Matrix - 3-Dimensional Architecture and Protein-Composition." Cell **29**(3): 847-858.

Caterson, B., C. R. Flannery, C. E. Hughes and C. B. Little (2000). "Mechanisms involved in cartilage proteoglycan catabolism." Matrix Biol **19**(4): 333-344.

Caterson, B. and D. A. Lowther (1978). "Changes in the metabolism of the proteoglycans from sheep articular cartilage in response to mechanical stress." Biochimica et Biophysica Acta (BBA) - General Subjects **540**(3): 412-422.

Chao, P. G., Z. Tang, E. Angelini, A. C. West, K. D. Costa and C. T. Hung (2005). "Dynamic osmotic loading of chondrocytes using a novel microfluidic device." J Biomech **38**(6): 1273-1281.

Chao, P. H., A. C. West and C. T. Hung (2006). "Chondrocyte intracellular calcium, cytoskeletal organization, and gene expression responses to dynamic osmotic loading." Am J Physiol Cell Physiol **291**(4): C718-725.

Cheah, Y. H., F. Juliana Nordin, R. Sarip, T. T. Tee, A. Hawariah Lope Pihie, M. S. H, B. Amini Abd Rashid, N. R. Abdullah and Z. Ismail (2009). "Combined xanthorrhizol-curcumin exhibits synergistic growth inhibitory activity via apoptosis induction in human breast cancer cells MDA-MB-231." Cancer Cell Int **9**(1): 1.

Chen, J., A. E. Baer, P. Y. Paik, W. Yan and L. A. Setton (2002). "Matrix protein gene expression in intervertebral disc cells subjected to altered osmolarity." Biochem Biophys Res Commun **293**(3): 932-938.

Cheng, G. H., A. Nandi, S. Clerk and A. I. Skoultchi (1989). "Different 3'-end processing produces two independently regulated mRNAs from a single H1 histone gene." Proc Natl Acad Sci U S A **86**(18): 7002-7006.

Chowdhury, T. T., D. M. Salter, D. L. Bader and D. A. Lee (2008). "Signal transduction pathways involving p38 MAPK, JNK, NFkappaB and AP-1 influences the response of chondrocytes cultured in agarose constructs to IL-1beta and dynamic compression." Inflammation research : official journal of the European Histamine Research Society ... [et al.] **57**(7): 306-313.

Chrisman, O. D. (1969). "Biochemical aspects of degenerative joint disease." Clin Orthop Relat Res **64**: 77-86.

Clark, T. G. and R. W. Merriam (1977). "Diffusible and Bound Actin in Nuclei of Xenopus-Laevis Oocytes." Cell **12**(4): 883-891.

Corle, T. R., C. H. Chou and G. S. Kino (1986). "Depth response of confocal optical microscopes." Opt Lett **11**(12): 770-772.

Crisp, M., Q. Liu, K. Roux, J. B. Rattner, C. Shanahan, B. Burke, P. D. Stahl and D. Hodzic (2006). "Coupling of the nucleus and cytoplasm: role of the LINC complex." Journal of Cell Biology **172**(1): 41-53.

Croft, J. A., J. M. Bridger, S. Boyle, P. Perry, P. Teague and W. A. Bickmore (1999). "Differences in the localization and morphology of chromosomes in the human nucleus." Journal of Cell Biology **145**(6): 1119-1131.

de Nadal, E., P. M. Alepuz and F. Posas (2002). "Dealing with osmostress through MAP kinase activation." Embo Reports **3**(8): 735-740.

Dechat, T., K. Pfleghaar, K. Sengupta, T. Shimi, D. K. Shumaker, L. Solimando and R. D. Goldman (2008). "Nuclear lamins: major factors in the structural organization and function of the nucleus and chromatin." Genes Dev **22**(7): 832-853.

Delpire, E., C. Duchene, G. Goessens and R. Gilles (1985). "Effects of Osmotic Shocks on the Ultrastructure of Different Tissues and Cell-Types." Experimental Cell Research **160**(1): 106-116.

Diamant, B., J. Karlsson and A. Nachemson (1968). "Correlation between lactate levels and pH in discs of patients with lumbar rhizopathies." Experientia **24**(12): 1195-1196.

Dijkgraaf, L. C., L. G. de Bont, G. Boering and R. S. Liem (1995). "The structure, biochemistry, and metabolism of osteoarthritic cartilage: a review of the literature." J Oral Maxillofac Surg **53**(10): 1182-1192.

Dmitrieva, N. I. and M. B. Burg (2008). "Analysis of DNA breaks, DNA damage response, and apoptosis produced by high NaCl." Am J Physiol Renal Physiol **295**(6): F1678-1688.

Dmitrieva, N. I., Q. Cai and M. B. Burg (2004). "Cells adapted to high NaCl have many DNA breaks and impaired DNA repair both in cell culture and in vivo." Proceedings of the National Academy of Sciences of the United States of America **101**(8): 2317-2322.

Dominski, Z. and W. F. Marzluff (2007). "Formation of the 3 ' end of histone mRNA: Getting closer to the end." Gene **396**(2): 373-390.

Donohue, J. M., D. Buss, T. R. Oegema, Jr. and R. C. Thompson, Jr. (1983). "The effects of indirect blunt trauma on adult canine articular cartilage." J Bone Joint Surg Am **65**(7): 948-957.

Durand, R. E. and P. L. Olive (1982). "Cytotoxicity, Mutagenicity and DNA damage by Hoechst 33342." J Histochem Cytochem **30**(2): 111-116.

Eggli, P. S., E. B. Hunziker and R. K. Schenk (1988). "Quantitation of structural features characterizing weight- and less-weight-bearing regions in articular cartilage: a stereological analysis of medial femoral condyles in young adult rabbits." Anat Rec **222**(3): 217-227.

Elder, B. D. and K. A. Athanasiou (2008). "Synergistic and additive effects of hydrostatic pressure and growth factors on tissue formation." PLoS One **3**(6): e2341.

Erickson, G. R., L. G. Alexopoulos and F. Guilak (2001). "Hyper-osmotic stress induces volume change and calcium transients in chondrocytes by transmembrane, phospholipid, and G-protein pathways." J Biomech **34**(12): 1527-1535.

Erickson, G. R., D. L. Northrup and F. Guilak (2003). "Hypo-osmotic stress induces calcium-dependent actin reorganization in articular chondrocytes." Osteoarthritis Cartilage **11**(3): 187-197.

Espinoza, J. A., M. A. Schulz, R. Sanchez and J. V. Villegas (2009). "Integrity of mitochondrial membrane potential reflects human sperm quality." Andrologia **41**(1): 51-54.

Eyre, D. (2002). "Collagen of articular cartilage." Arthritis Res **4**(1): 30-35.

Fatoba, S. T. and A. L. Okorokov (2011). "Human SIRT1 associates with mitotic chromatin and contributes to chromosomal condensation." Cell Cycle **10**(14): 2317-2322.

Feller, W. (1971). An introduction to probability theory and its applications. Vol. 1. New York ; London, Wiley.

Fey, E. G., K. M. Wan and S. Penman (1984). "Epithelial Cytoskeletal Framework and Nuclear Matrix Intermediate Filament Scaffold - 3-Dimensional Organization and Protein-Composition." Journal of Cell Biology **98**(6): 1973-1984.

Finan, J. D., K. J. Chalut, A. Wax and F. Guilak (2009). "Nonlinear osmotic properties of the cell nucleus." Ann Biomed Eng **37**(3): 477-491.

Finan, J. D. and F. Guilak (2010). "The effects of osmotic stress on the structure and function of the cell nucleus." J Cell Biochem **109**(3): 460-467.

Finan, J. D., H. A. Leddy and F. Guilak (2011). "Osmotic stress alters chromatin condensation and nucleocytoplasmic transport." Biochemical and Biophysical Research Communications **408**(2): 230-235.

Finan, J. D., H. A. Leddy and F. Guilak (2011). "Osmotic stress alters chromatin condensation and nucleocytoplasmic transport." Biochem Biophys Res Commun **408**(2): 230-235.

Fioravanti, A., D. Benetti, G. Coppola and G. Collodel (2005). "Effect of continuous high hydrostatic pressure on the morphology and cytoskeleton of normal and osteoarthritic human chondrocytes cultivated in alginate gels." Clin Exp Rheumatol **23**(6): 847-853.

Fioravanti, A., F. Nerucci, M. Annefeld, G. Collodel and R. Marcolongo (2003). "Morphological and cytoskeletal aspects of cultivated normal and osteoarthritic human articular chondrocytes after cyclical pressure: a pilot study." Clin Exp Rheumatol **21**(6): 739-746.

Fitzgerald, J. B., M. Jin, D. H. Chai, P. Siparsky, P. Fanning and A. J. Grodzinsky (2008). "Shear- and compression-induced chondrocyte transcription requires MAPK activation in cartilage explants." J Biol Chem **283**(11): 6735-6743.

Floman, Y., D. R. Eyre and M. J. Glimcher (1980). "Induction of osteoarthrosis in the rabbit knee joint: biochemical studies on the articular cartilage." Clin Orthop Relat Res(147): 278-286.

Foster, H. A. and J. M. Bridger (2005). "The genome and the nucleus: a marriage made by evolution. Genome organisation and nuclear architecture." Chromosoma **114**(4): 212-229.

Freeman, W. D. S. C. and A. Maroudas (1975). "Charged group behaviour in cartilage proteoglycans in relation to pH." Ann Rheum Dis **34**(Suppl. 2): 44.

Frey, T. (1995). "Nucleic acid dyes for detection of apoptosis in live cells." Cytometry **21**(3): 265-274.

Garner, D. L. (2009). "Hoechst 33342: The dye that enabled differentiation of living X-and Y-chromosome bearing mammalian sperm." Theriogenology **71**(1): 11-21.

Gersh, I. and H. R. Catchpole (1960). "The nature of ground substance of connective tissue." Perspect Biol Med **3**: 282-319.

Gieni, R. S. and M. J. Hendzel (2008). "Mechanotransduction from the ECM to the genome: are the pieces now in place?" J Cell Biochem **104**(6): 1964-1987.

Godart, H., J. C. Ellory and R. Motais (1999). "Regulatory volume response of erythrocytes exposed to a gradual and slow decrease in medium osmolality." Pflugers Archiv : European journal of physiology **437**(5): 776-779.

Gouttenoire, J., C. Bougault, E. Aubert-Foucher, E. Perrier, M. C. Ronziere, L. Sandell, E. Lundgren-Akerlund and F. Mallein-Gerin (2010). "BMP-2 and TGF-beta1 differentially control expression of type II procollagen and alpha 10 and alpha 11 integrins in mouse chondrocytes." Eur J Cell Biol **89**(4): 307-314.

Grazi, E., P. Cuneo and A. Cataldi (1992). "The control of cellular shape and motility. Mg2+ and tropomyosin regulate the formation and the dissociation of microfilament bundles." Biochem J **288 (Pt 3)**: 727-732.

Greenwald, A. S. and J. J. O'Connor (1971). "The transmission of load through the human hip joint." J Biomech **4**(6): 507-528.

Gruenbaum, Y., A. Margalit, R. D. Goldman, D. K. Shumaker and K. L. Wilson (2005). "The nuclear lamina comes of age." Nat Rev Mol Cell Biol **6**(1): 21-31.

Gu, W. Y., W. M. Lai and V. C. Mow (1993). "Transport of fluid and ions through a porous-permeable charged-hydrated tissue, and streaming potential data on normal bovine articular cartilage." J Biomech **26**(6): 709-723.

Gu, W. Y., W. M. Lai and V. C. Mow (1998). "A mixture theory for charged-hydrated soft tissues containing multi-electrolytes: Passive transport and swelling behaviors." Journal of Biomechanical Engineering-Transactions of the Asme **120**(2): 169-180.

Guilak, F. (1994). "Volume and Surface-Area Measurement of Viable Chondrocytes in-Situ Using Geometric Modeling of Serial Confocal Sections." Journal of Microscopy-Oxford **173**: 245-256.

Guilak, F. (1995). "Compression-induced changes in the shape and volume of the chondrocyte nucleus." J Biomech **28**(12): 1529-1541.

Guilak, F., G. R. Erickson and H. P. Ting-Beall (2002). "The effects of osmotic stress on the viscoelastic and physical properties of articular chondrocytes." Biophys J **82**(2): 720-727.

Guilak, F. and C. T. Hung (2005). Physical regulation of cartilage metabolism. in: Basic orthopaedic biomechanics and mechano-biology. V. C. Mow and R. Huiskes. Philadelphia, PA, Lippincott Williams & Wilkins**:** 179-207.

Guilak, F. and V. C. Mow (2000). "The mechanical environment of the chondrocyte: a biphasic finite element model of cell-matrix interactions in articular cartilage." Journal of Biomechanics **33**(12): 1663-1673.

Guilak, F., A. Ratcliffe and V. C. Mow (1995). "Chondrocyte deformation and local tissue strain in articular cartilage: a confocal microscopy study." Journal of orthopaedic research : official publication of the Orthopaedic Research Society **13**(3): 410-421.

Guilak, F., R. L. Sah and S. L. A. (1997). Physical regulation of cartilage metabolism. in: Basic orthopaedic biomechanics. V. C. Mow and W. C. Hayes. Philadelphia, Lippincott-Raven**:** 179-207.

Guilak, F., J. R. Tedrow and R. Burgkart (2000). "Viscoelastic properties of the cell nucleus." Biochem Biophys Res Commun **269**(3): 781-786.

Gunesdogan, U., H. Jackle and A. Herzig (2010). "A genetic system to assess in vivo the functions of histones and histone modifications in higher eukaryotes." Embo Reports **11**(10): 772-776.

Haapala, J., J. Arokoski, J. Pirttimaki, T. Lyyra, J. Jurvelin, M. Tammi, H. J. Helminen and I. Kiviranta (2000). "Incomplete restoration of immobilization induced softening of young beagle knee articular cartilage after 50-week remobilization." Int J Sports Med **21**(1): 76-81.

Hall, A. C. (1999). "Differential effects of hydrostatic pressure on cation transport pathways of isolated articular chondrocytes." Journal of Cellular Physiology **178**(2): 197-204.

Hall, A. C., J. P. Urban and K. A. Gehl (1991). "The effects of hydrostatic pressure on matrix synthesis in articular cartilage." J Orthop Res **9**(1): 1-10.

Han, S. K., W. Wouters, A. Clark and W. Herzog (2012). "Mechanically induced calcium signaling in chondrocytes in situ." J Orthop Res **30**(3): 475-481.

Haraguchi, T., D. Q. Ding, A. Yamamoto, T. Kaneda, T. Koujin and Y. Hiraoka (1999). "Multiple-color fluorescence imaging of chromosomes and microtubules in living cells." Cell Struct Funct **24**(5): 291-298.

Hardingham, G. E. and H. Bading (1999). "Calcium as a versatile second messenger in the control of gene expression." Microsc Res Tech **46**(6): 348-355.

Hardingham, T. E. (1979). "The role of link-protein in the structure of cartilage proteoglycan aggregates." Biochem J **177**(1): 237-247.

Hardingham, T. E. and A. J. Fosang (1992). "Proteoglycans: many forms and many functions." FASEB J **6**(3): 861-870.

Haugland, R. P. (2007). Handbook of fluorescent probes and research chemicals. Eugene, Oregon, Molecular Probes.

Heinegard, D. and A. Oldberg (1989). "Structure and biology of cartilage and bone matrix noncollagenous macromolecules." FASEB J **3**(9): 2042-2051.

Helminen, H., J. Jurvelin, I. Kiviranta, K. Paukkonen, A.-M. Saamanen and M. Tammi (1987). Joint loading effects on articular cartilage: a historical review. in: Joint loading : biology and health of articular structures. H. J. Helminen, I. Kiviranta, M. Tammiet al. Bristol, Wright**:** 1-46.

Helminen, H. J., M. M. Hyttinen, M. J. Lammi, J. P. Arokoski, T. Lapvetelainen, J. Jurvelin, I. Kiviranta and M. I. Tammi (2000). "Regular joint loading in youth assists in the establishment and strengthening of the collagen network of articular cartilage and contributes to the prevention of osteoarthrosis later in life: a hypothesis." J Bone Miner Metab **18**(5): 245-257.

Hendry, E. B. (1961). "Osmolarity of human serum and of chemical solutions of biologic importance." Clinical chemistry **7**: 154-164.

Hildebrandt, J. P. and A. Prowald (2000). "Ca(2+) and p38 MAP kinase regulate mAChR-mediated c-Fos expression in avian exocrine cells." Am J Physiol Cell Physiol **278**(5): C879-884.

Hinterwimmer, S., M. Krammer, M. Krotz, C. Glaser, R. Baumgart, M. Reiser and F. Eckstein (2004). "Cartilage atrophy in the knees of patients after seven weeks of partial load bearing." Arthritis Rheum **50**(8): 2516-2520.

Hoch, D. H., A. J. Grodzinsky, T. J. Koob, M. L. Albert and D. R. Eyre (1983). "Early changes in material properties of rabbit articular cartilage after meniscectomy." J Orthop Res **1**(1): 4-12.

Hodge, W. A., R. S. Fijan, K. L. Carlson, R. G. Burgess, W. H. Harris and R. W. Mann (1986). "Contact pressures in the human hip joint measured in vivo." Proc Natl Acad Sci U S A **83**(9): 2879-2883.

Hoffmann, E. K., I. H. Lambert and S. F. Pedersen (2009). "Physiology of cell volume regulation in vertebrates." Physiol Rev **89**(1): 193-277.

Holm, S. (1979). "A Simple Sequentially Rejective Multiple Test Procedure." Scandinavian Journal of Statistics **6**(2): 65-70.

Holm, S., A. Maroudas, J. P. Urban, G. Selstam and A. Nachemson (1981). "Nutrition of the intervertebral disc: solute transport and metabolism." Connect Tissue Res **8**(2): 101-119.

Holmes, M. H., W. M. Lai and V. C. Mow (1985). "Singular perturbation analysis of the nonlinear, flow-dependent compressive stress relaxation behavior of articular cartilage." J Biomech Eng **107**(3): 206-218.

Hopewell, B. and J. P. Urban (2003). "Adaptation of articular chondrocytes to changes in osmolality." Biorheology **40**(1-3): 73-77.

Hoshiba, T., T. Yamada, H. Lu, N. Kawazoe, T. Tateishi and G. Chen (2008). "Nuclear deformation and expression change of cartilaginous genes during in vitro expansion of chondrocytes." Biochem Biophys Res Commun **374**(4): 688-692.

Howell, D. S., B. V. Treadwell and S. B. Trippel (1992). Etiopathogenesis of osteoarthritis. in: Osteoarthritis, diagnosis and medical/surgical management. R. W. Moskowitz, Saunders**:** xxii, 761p.

Huang, D. W., B. T. Sherman and R. A. Lempicki (2009). "Systematic and integrative analysis of large gene lists using DAVID bioinformatics resources." Nature Protocols **4**(1): 44-57.

Hulmes, D. J., J. C. Jesior, A. Miller, C. Berthet-Colominas and C. Wolff (1981). "Electron microscopy shows periodic structure in collagen fibril cross sections." Proc Natl Acad Sci U S A **78**(6): 3567-3571.

Hulmes, D. J. S. (2008). Collagen Diversity, Synthesis and Assembly. in: Collagen : structure and mechanics. P. Fratzl. New York, Springer**:** 15-48.

Hung, C. T., M. A. LeRoux, G. D. Palmer, P. H. Chao, S. Lo and W. B. Valhmu (2003). "Disparate aggrecan gene expression in chondrocytes subjected to hypotonic and hypertonic loading in 2D and 3D culture." Biorheology **40**(1-3): 61-72.

Hunter, C. J., S. M. Imler, P. Malaviya, R. M. Nerem and M. E. Levenston (2002). "Mechanical compression alters gene expression and extracellular matrix synthesis by chondrocytes cultured in collagen I gels." Biomaterials **23**(4): 1249-1259.

Hynes, R. O. (2002). "Integrins: bidirectional, allosteric signaling machines." Cell **110**(6): 673-687.

Idowu, B. D., M. M. Knight, D. L. Bader and D. A. Lee (2000). "Confocal analysis of cytoskeletal organisation within isolated chondrocyte sub-populations cultured in agarose." Histochem J **32**(3): 165-174.

Ingber, D. E. (1994). Cellular Tensegrity and Mechanochemical Transduction. in: Cell Mechanics and Cellular Engineering. V. C. Mow, R. Hochmuth, F. Guilak and R. Tran-Soy-Tay. New York, Springer-Verlag**:** 329-342.

Insall, R. and L. Machesky (2001). Cytoskeleton. Enyclopedia of Life Sciences, John Wiley & Sons, Ltd.

Jain, A. K. and R. C. Dubes (1988). Algorithms for clustering data, Prentice-Hall.

Jones, C. W., D. Smolinski, A. Keogh, T. B. Kirk and M. H. Zheng (2005). "Confocal laser scanning microscopy in orthopaedic research." Progress in Histochemistry and Cytochemistry **40**(1): 1-71.

Jones, I. L., A. Klamfeldt and T. Sandstrom (1982). "The effect of continuous mechanical pressure upon the turnover of articular cartilage proteoglycans in vitro." Clin Orthop Relat Res(165): 283-289.

Jurvelin, J., I. Kiviranta, M. Tammi and J. H. Helminen (1986). "Softening of canine articular cartilage after immobilization of the knee joint." Clin Orthop Relat Res(207): 246-252.

Kaab, M. J., K. Ito, J. M. Clark and H. P. Notzli (2000). "The acute structural changes of loaded articular cartilage following meniscectomy or ACL-transection." Osteoarthritis and cartilage / OARS, Osteoarthritis Research Society **8**(6): 464-473.

Kawasaki, K., S. Sugihara, K. Nishida, T. Ozaki, A. Yoshida, A. Ohtsuka and H. Inoue (2004). "Hoechst 33342 is a useful cell tracer for a long-term investigation of articular cartilage repair." Arch Histol Cytol **67**(1): 13-19.

Kempson, G. E., H. Muir, C. Pollard and M. Tuke (1973). "The tensile properties of the cartilage of human femoral condyles related to the content of collagen and glycosaminoglycans." Biochim Biophys Acta **297**(2): 456-472.

Kerrigan, M. J., C. S. Hook, A. Qusous and A. C. Hall (2006). "Regulatory volume increase (RVI) by in situ and isolated bovine articular chondrocytes." J Cell Physiol **209**(2): 481-492.

Kiviranta, I., M. Tammi, J. Jurvelin, J. Arokoski, A. M. Saamanen and H. J. Helminen (1992). "Articular cartilage thickness and glycosaminoglycan distribution in the canine knee joint after strenuous running exercise." Clin Orthop Relat Res(283): 302-308.

Knight, M. M., J. Bravenboer, D. A. Lee, G. van Osch, H. Weinans and D. L. Bader (2002). "Cell and nucleus deformation in compressed chondrocyte-alginate constructs: temporal changes and calculation of cell modulus." Biochimica Et Biophysica Acta-General Subjects **1570**(1): 1-8.

Knight, M. M., S. A. Ghori, D. A. Lee and D. L. Bader (1998). "Measurement of the deformation of isolated chondrocytes in agarose subjected to cyclic compression." Medical Engineering & Physics **20**(9): 684-688.

Knight, M. M., B. D. Idowu, D. A. Lee and D. L. Bader (2001). "Temporal changes in cytoskeletal organisation within isolated chondrocytes quantified using a novel image analysis technique." Medical & Biological Engineering & Computing **39**(3): 397-404.

Knight, M. M., S. R. Roberts, D. A. Lee and D. L. Bader (2003). "Live cell imaging using confocal microscopy induces intracellular calcium transients and cell death." Am J Physiol Cell Physiol **284**(4): C1083-1089.

Knight, M. M., T. Toyoda, D. A. Lee and D. L. Bader (2006). "Mechanical compression and hydrostatic pressure induce reversible changes in actin cytoskeletal organisation in chondrocytes in agarose." J Biomech **39**(8): 1547-1551.

Knight, M. M., J. van de Breevaart Bravenboer, D. A. Lee, G. J. van Osch, H. Weinans and D. L. Bader (2002). "Cell and nucleus deformation in compressed chondrocyte-alginate constructs: temporal changes and calculation of cell modulus." Biochim Biophys Acta **1570**(1): 1-8.

Knudson, C. B. and W. Knudson (1993). "Hyaluronan-binding proteins in development, tissue homeostasis, and disease." FASEB J **7**(13): 1233-1241.

Knudson, W., D. J. Aguiar, Q. Hua and C. B. Knudson (1996). "CD44-anchored hyaluronan-rich pericellular matrices: an ultrastructural and biochemical analysis." Exp Cell Res **228**(2): 216-228.

Kosak, S. T., J. A. Skok, K. L. Medina, R. Riblet, M. M. Le Beau, A. G. Fisher and H. Singh (2002). "Subnuclear compartmentalization of immunoglobulin loci during lymphocyte development." Science **296**(5565): 158-162.

Krause, E. F. (1975). Taxicab geometry. Menlo Park, Calif. ; London, Addison-Wesley.

Kurosawa, H., T. Fukubayashi and H. Nakajima (1980). "Load-Bearing Mode of the Knee-Joint - Physical Behavior of the Knee-Joint with or without Menisci." Clinical Orthopaedics and Related Research(149): 283-290.

Kurz, B., M. Jin, P. Patwari, D. M. Cheng, M. W. Lark and A. J. Grodzinsky (2001). "Biosynthetic response and mechanical properties of articular cartilage after injurious compression." J Orthop Res **19**(6): 1140-1146.

Lai, C. F., V. Seshadri, K. Huang, J. S. Shao, J. Cai, R. Vattikuti, A. Schumacher, A. P. Loewy, D. T. Denhardt, S. R. Rittling and D. A. Towler (2006). "An osteopontin-NADPH oxidase signaling cascade promotes pro-matrix metalloproteinase 9 activation in aortic mesenchymal cells." Circ Res **98**(12): 1479-1489.

Lai, W. M., J. S. Hou and V. C. Mow (1991). "A Triphasic Theory for the Swelling and Deformation Behaviors of Articular-Cartilage." Journal of Biomechanical Engineering-Transactions of the Asme **113**(3): 245-258.

Lai, W. M., J. S. Hou and V. C. Mow (1991). "A triphasic theory for the swelling and deformation behaviors of articular cartilage." J Biomech Eng **113**(3): 245-258.

Lammi, M. J., R. Inkinen, J. J. Parkkinen, T. Hakkinen, M. Jortikka, L. O. Nelimarkka, H. T. Jarvelainen and M. I. Tammi (1994). "Expression of reduced amounts of structurally altered aggrecan in articular cartilage chondrocytes exposed to high hydrostatic pressure." Biochem J **304 (Pt 3)**: 723-730.

Lamond, A. I. and W. C. Earnshaw (1998). "Structure and function in the nucleus." Science **280**(5363): 547-553.

Lanctot, C., T. Cheutin, M. Cremer, G. Cavalli and T. Cremer (2007). "Dynamic genome architecture in the nuclear space: regulation of gene expression in three dimensions." Nat Rev Genet **8**(2): 104-115.

Lange, K. (2000). "Regulation of cell volume via microvillar ion channels." J Cell Physiol **185**(1): 21-35.

Langelier, E., R. Suetterlin, C. D. Hoemann, U. Aebi and M. D. Buschmann (2000). "The chondrocyte cytoskeleton in mature articular cartilage: structure and distribution of actin, tubulin, and vimentin filaments." J Histochem Cytochem **48**(10): 1307-1320.

Lee, D. A. and D. L. Bader (1997). "Compressive strains at physiological frequencies influence the metabolism of chondrocytes seeded in agarose." Journal of Orthopaedic Research **15**(2): 181-188.

Lee, D. A. and M. M. Knight (2004). "Mechanical loading of chondrocytes embedded in 3D constructs: in vitro methods for assessment of morphological and metabolic response to compressive strain." Methods Mol Med **100**: 307-324.

Lee, D. A., M. M. Knight, J. F. Bolton, B. D. Idowu, M. V. Kayser and D. L. Bader (2000). "Chondrocyte deformation within compressed agarose constructs at the cellular and sub-cellular levels." Journal of Biomechanics **33**(1): 81-95.

Lee, R. C., J. B. Rich, K. M. Kelley, D. S. Weiman and M. B. Mathews (1982). "A comparison of in vitro cellular responses to mechanical and electrical stimulation." The American surgeon **48**(11): 567-574.

Lewis, R., K. E. Asplin, G. Bruce, C. Dart, A. Mobasheri and R. Barrett-Jolley (2011). "The role of the membrane potential in chondrocyte volume regulation." J Cell Physiol **226**(11): 2979-2986.

Lockhart, D. J. and E. A. Winzeler (2000). "Genomics, gene expression and DNA arrays." Nature **405**(6788): 827-836.

Loening, A. M., I. E. James, M. E. Levenston, A. M. Badger, E. H. Frank, B. Kurz, M. E. Nuttall, H. H. Hung, S. M. Blake, A. J. Grodzinsky and M. W. Lark (2000). "Injurious mechanical compression of bovine articular cartilage induces chondrocyte apoptosis." Archives of Biochemistry and Biophysics **381**(2): 205-212.

Loeser, R. F. (2000). "Chondrocyte integrin expression and function." Biorheology **37**(1-2): 109-116.

Macginitie, L. A., Y. A. Gluzband and A. J. Grodzinsky (1994). "Electric-Field Stimulation Can Increase Protein-Synthesis in Articular-Cartilage Explants." Journal of Orthopaedic Research **12**(2): 151-160.

Maes, M. L., L. B. Davidson, P. F. McDonagh and L. S. Ritter (2007). "Comparison of sample fixation and the use of LDS-751 or anti-CD45 for leukocyte identification in mouse whole blood for flow cytometry." J Immunol Methods **319**(1-2): 79-86.

Malicet, C., M. Rochman, Y. Postnikov and M. Bustin (2011). "Distinct properties of human HMGN5 reveal a rapidly evolving but functionally conserved nucleosome binding protein." Mol Cell Biol **31**(13): 2742-2755.

Maniotis, A. J., C. S. Chen and D. E. Ingber (1997). "Demonstration of mechanical connections between integrins cytoskeletal filaments, and nucleoplasm that stabilize nuclear structure." Proceedings of the National Academy of Sciences of the United States of America **94**(3): 849-854.

Mankin, H. J., V. C. Mow and J. A. Buckwalter (2000). Articular cartilage structure, composition and function. in: Orthopaedic basic science : biology and biomechanics

of the musculoskeletal system. J. A. Buckwalter, T. A. Einhorn and S. R. Simon. Rosemont, Ill., American Academy of Orthopaedic Surgeons**:** xix,873p.

Mansour, J. M. and V. C. Mow (1976). "The permeability of articular cartilage under compressive strain and at high pressures." J Bone Joint Surg Am **58**(4): 509-516.

Marcus, R. E. (1973). "The effect of low oxygen concentration on growth, glycolysis, and sulfate incorporation by articular chondrocytes in monolayer culture." Arthritis Rheum **16**(5): 646-656.

Maroudas, A. (1968). "Physicochemical properties of cartilage in the light of ion exchange theory." Biophys J **8**(5): 575-595.

Maroudas, A. (1979). Physico-chemical properties of articular cartilage. in: Adult Articular Cartilage. M. A. R. Freeman. London, Pitman Medical**:** 215-290.

Maroudas, A., M. T. Bayliss and M. F. Venn (1980). "Further studies on the composition of human femoral head cartilage." Ann Rheum Dis **39**(5): 514-523.

Maroudas, A. and R. Schneiderman (1987). ""Free" and "exchangeable" or "trapped" and "non-exchangeable" water in cartilage." J Orthop Res **5**(1): 133-138.

Maroudas, A., E. Wachtel, G. Grushko, E. P. Katz and P. Weinberg (1991). "The effect of osmotic and mechanical pressures on water partitioning in articular cartilage." Biochim Biophys Acta **1073**(2): 285-294.

Maroudas, A. I. (1976). "Balance between swelling pressure and collagen tension in normal and degenerate cartilage." Nature **260**(5554): 808-809.

Marsh, D. J. and S. P. Azen (1975). "Mechanism of NaCl reabsorption by hamster thin ascending limbs of Henle's loop." The American journal of physiology **228**(1): 71-79.

Martin, R. M., H. Leonhardt and M. C. Cardoso (2005). "DNA labeling in living cells." Cytometry A **67**(1): 45-52.

Martins, R. P., A. E. Platts and S. A. Krawetz (2007). "Tracking chromatin states using controlled DNase I treatment and real-time PCR." Cellular & Molecular Biology Letters **12**(4): 545-555.

Marzluff, W. F. and R. J. Duronio (2002). "Histone mRNA expression: multiple levels of cell cycle regulation and important developmental consequences." Current Opinion in Cell Biology **14**(6): 692-699.

Marzluff, W. F., P. Gongidi, K. R. Woods, J. P. Jin and L. J. Maltais (2002). "The human and mouse replication-dependent histone genes." Genomics **80**(5): 487-498.

Marzluff, W. F., E. J. Wagner and R. J. Duronio (2008). "Metabolism and regulation of canonical histone mRNAs: life without a poly(A) tail." Nature Reviews Genetics **9**(11): 843-854.

Mauck, R. L., M. A. Soltz, C. C. Wang, D. D. Wong, P. H. Chao, W. B. Valhmu, C. T. Hung and G. A. Ateshian (2000). "Functional tissue engineering of articular cartilage through dynamic loading of chondrocyte-seeded agarose gels." Journal of biomechanical engineering **122**(3): 252-260.

Mavrogonatou, E. and D. Kletsas (2012). "Differential response of nucleus pulposus intervertebral disc cells to high salt, sorbitol, and urea." Journal of Cellular Physiology **227**(3): 1179-1187.

Mazzanti, M., J. O. Bustamante and H. Oberleithner (2001). "Electrical dimension of the nuclear envelope." Physiol Rev **81**(1): 1-19.

McDonald, D., G. Carrero, C. Andrin, G. de Vries and M. J. Hendzel (2006). "Nucleoplasmic beta-actin exists in a dynamic equilibrium between low-mobility polymeric species and rapidly diffusing populations." Journal of Cell Biology **172**(4): 541-552.

McInnes, I. B. and G. Schett (2007). "Cytokines in the pathogenesis of rheumatoid arthritis." Nat Rev Immunol **7**(6): 429-442.

Mendler, M., S. G. Eich-Bender, L. Vaughan, K. H. Winterhalter and P. Bruckner (1989). "Cartilage contains mixed fibrils of collagen types II, IX, and XI." J Cell Biol **108**(1): 191-197.

Misteli, T., J. F. Caceres and D. L. Spector (1997). "The dynamics of a pre-mRNA splicing factor in living cells." Nature **387**(6632): 523-527.

Mizuno, S. (2005). "A novel method for assessing effects of hydrostatic fluid pressure on intracellular calcium: a study with bovine articular chondrocytes." American Journal of Physiology-Cell Physiology **288**(2): C329-C337.

Mouw, J. K., S. M. Imler and M. E. Levenston (2007). "Ion-channel regulation of chondrocyte matrix synthesis in 3D culture under static and dynamic compression." Biomech Model Mechanobiol **6**(1-2): 33-41.

Mow, V. C., M. C. Gibbs, W. M. Lai, W. B. Zhu and K. A. Athanasiou (1989). "Biphasic indentation of articular cartilage--II. A numerical algorithm and an experimental study." J Biomech **22**(8-9): 853-861.

Mow, V. C., W. Y. Gu and F. H. Chen (2005). Structure and Function of Articular Cartilage and Meniscus. in: Basic orthopaedic biomechanics & mechano-biology. V. C. Mow and R. Huiskes. Philadelphia, Pa. ; London, Lippincott Williams & Wilkins**:** xvi, 720 p.

Mow, V. C., A. Ratcliffe and A. R. Poole (1992). "Cartilage and diarthrodial joints as paradigms for hierarchical materials and structures." Biomaterials **13**(2): 67-97.

Muir, H. (1983). "Proteoglycans as organizers of the intercellular matrix." Biochem Soc Trans **11**(6): 613-622.

Muir, H., P. Bullough and A. Maroudas (1970). "The distribution of collagen in human articular cartilage with some of its physiological implications." J Bone Joint Surg Br **52**(3): 554-563.

Mulchrone, K. F. and K. R. Choudhury (2004). "Fitting an ellipse to an arbitrary shape: implications for strain analysis." Journal of Structural Geology **26**(1): 143-153.

Muller, F. J., L. A. Setton, D. H. Manicourt, V. C. Mow, D. S. Howell and J. C. Pita (1994). "Centrifugal and biochemical comparison of proteoglycan aggregates from articular cartilage in experimental joint disuse and joint instability." J Orthop Res **12**(4): 498-508.

Murmann, A. E., J. Gao, M. Encinosa, M. Gautier, M. E. Peter, R. Eils, P. Lichter and J. D. Rowley (2005). "Local gene density predicts the spatial position of genetic loci in the interphase nucleus." Exp Cell Res **311**(1): 14-26.

Nanjangud, S. C. and D. J. Green (1995). "Mechanical-Behavior of Porous Glasses Produced by Sintering of Spherical-Particles." Journal of the European Ceramic Society **15**(7): 655-660.

Neuhaus, J. M., M. Wanger, T. Keiser and A. Wegner (1983). "Treadmilling of actin." J Muscle Res Cell Motil **4**(5): 507-527.

Newport, J. W. and D. J. Forbes (1987). "The nucleus: structure, function, and dynamics." Annu Rev Biochem **56**: 535-565.

Njoh, K. L., L. H. Patterson, M. Zloh, M. Wiltshire, J. Fisher, S. Chappell, S. Ameer-Beg, Y. Bai, D. Matthews, R. J. Errington and P. J. Smith (2006). "Spectral analysis of the DNA targeting bisalkylaminoanthraquinone DRAQ5 in intact living cells." Cytometry A **69**(8): 805-814.

O'Hara, B. P., J. P. Urban and A. Maroudas (1990). "Influence of cyclic loading on the nutrition of articular cartilage." Ann Rheum Dis **49**(7): 536-539.

O'Neill, W. C. (1999). "Physiological significance of volume-regulatory transporters." Am J Physiol **276**(5 Pt 1): C995-C1011.

Oegema, T. R., Jr., J. L. Lewis and R. C. Thompson, Jr. (1993). "Role of acute trauma in development of osteoarthritis." Agents Actions **40**(3-4): 220-223.

Ofek, G., R. M. Natoli and K. A. Athanasiou (2009). "In situ mechanical properties of the chondrocyte cytoplasm and nucleus." Journal of Biomechanics **42**(7): 873-877.

Ogg, S. C. and A. I. Lamond (2002). "Cajal bodies and coilin--moving towards function." J Cell Biol **159**(1): 17-21.

Ohashi, T., M. Hagiwara, D. L. Bader and M. M. Knight (2006). "Intracellular mechanics and mechanotransduction associated with chondrocyte deformation during pipette aspiration." Biorheology **43**(3-4): 201-214.

Ohshima, H., J. P. Urban and D. H. Bergel (1995). "Effect of static load on matrix synthesis rates in the intervertebral disc measured in vitro by a new perfusion technique." J Orthop Res **13**(1): 22-29.

Olson, E. R., T. Melton, Z. Dong and G. T. Bowden (2008). "Stabilization of quercetin paradoxically reduces its proapoptotic effect on UVB-irradiated human keratinocytes." Cancer Prev Res (Phila Pa) **1**(5): 362-368.

Oswald, E. S., H. S. Ahmed, S. P. Kramer, J. C. Bulinski, G. A. Ateshian and C. T. Hung (2011). "Effects of hypertonic (NaCl) two-dimensional and three-dimensional culture conditions on the properties of cartilage tissue engineered from an expanded mature bovine chondrocyte source." Tissue Eng Part C Methods **17**(11): 1041-1049.

Oswald, E. S., P. H. Chao, J. C. Bulinski, G. A. Ateshian and C. T. Hung (2006). "Chondrocyte nuclear response to osmotic loading." Conf Proc IEEE Eng Med Biol Soc **1**: 3659-3661.

Oswald, E. S., P. H. Chao, J. C. Bulinski, G. A. Ateshian and C. T. Hung (2008). "Dependence of zonal chondrocyte water transport properties on osmotic environment." Cell Mol Bioeng **1**(4): 339-348.

Otterness, I. G., J. D. Eskra, M. L. Bliven, A. K. Shay, J. P. Pelletier and A. J. Milici (1998). "Exercise protects against articular cartilage degeneration in the hamster." Arthritis Rheum **41**(11): 2068-2076.

Pajerowski, J. D., K. N. Dahl, F. L. Zhong, P. J. Sammak and D. E. Discher (2007). "Physical plasticity of the nucleus in stem cell differentiation." Proc Natl Acad Sci U S A **104**(40): 15619-15624.

Palmoski, M., E. Perricone and K. D. Brandt (1979). "Development and reversal of a proteoglycan aggregation defect in normal canine knee cartilage after immobilization." Arthritis Rheum **22**(5): 508-517.

Parkkinen, J. J., J. Ikonen, M. J. Lammi, J. Laakkonen, M. Tammi and H. J. Helminen (1993). "Effects of cyclic hydrostatic pressure on proteoglycan synthesis in cultured chondrocytes and articular cartilage explants." Archives of Biochemistry and Biophysics **300**(1): 458-465.

Parkkinen, J. J., J. Ikonen, M. J. Lammi, J. Laakkonen, M. Tammi and H. J. Helminen (1993). "Effects of cyclic hydrostatic pressure on proteoglycan synthesis in cultured chondrocytes and articular cartilage explants." Arch Biochem Biophys **300**(1): 458-465.

Parkkinen, J. J., M. J. Lammi, H. J. Helminen and M. Tammi (1992). "Local stimulation of proteoglycan synthesis in articular cartilage explants by dynamic compression in vitro." J Orthop Res **10**(5): 610-620.

Parkkinen, J. J., M. J. Lammi, R. Inkinen, M. Jortikka, M. Tammi, I. Virtanen and H. J. Helminen (1995). "Influence of short-term hydrostatic pressure on organization of stress fibers in cultured chondrocytes." J Orthop Res **13**(4): 495-502.

Parkkinen, J. J., M. J. Lammi, A. Pelttari, H. J. Helminen, M. Tammi and I. Virtanen (1993). "Altered Golgi apparatus in hydrostatically loaded articular cartilage chondrocytes." Ann Rheum Dis **52**(3): 192-198.

Pawley, J. B. (1995). Handbook of biological confocal microscopy. New York ; London, Plenum Press.

Pedersen, S., S. F. Pedersen, B. Nilius, I. H. Lambert and E. K. Hoffmann (1999). "Mechanical stress induces release of ATP from Ehrlich ascites tumor cells." Biochimica Et Biophysica Acta-Biomembranes **1416**(1-2): 271-284.

Peffers, M. J., P. I. Milner, S. R. Tew and P. D. Clegg (2010). "Regulation of SOX9 in normal and osteoarthritic equine articular chondrocytes by hyperosmotic loading." Osteoarthritis Cartilage **18**(11): 1502-1508.

Phan, M. N., H. A. Leddy, B. J. Votta, S. Kumar, D. S. Levy, D. B. Lipshutz, S. H. Lee, W. Liedtke and F. Guilak (2009). "Functional characterization of TRPV4 as an osmotically sensitive ion channel in porcine articular chondrocytes." Arthritis Rheum **60**(10): 3028-3037.

Pingguan-Murphy, B. (2006). Calcium Mediated Signalling Pathways for Chondrocytes in 3D Constructs Subjected to Cyclic Loading. Engineering Department. London, Queen Mary, University of London. **PhD**.

Pingguan-Murphy, B., M. El-Azzeh, D. L. Bader and M. M. Knight (2006). "Cyclic compression of chondrocytes modulates a purinergic calcium signalling pathway in a strain rate- and frequency-dependent manner." Journal of cellular physiology **209**(2): 389-397.

Pingguan-Murphy, B., D. A. Lee, D. L. Bader and M. M. Knight (2005). "Activation of chondrocytes calcium signalling by dynamic compression is independent of number of cycles." Archives of Biochemistry and Biophysics **444**(1): 45-51.

Poole, A. R., T. Kojima, T. Yasuda, F. Mwale, M. Kobayashi and S. Laverty (2001). "Composition and structure of articular cartilage: a template for tissue repair." Clin Orthop Relat Res(391 Suppl): S26-33.

Poole, C. A. (1997). "Articular cartilage chondrons: form, function and failure." J Anat **191 (Pt 1)**: 1-13.

Poole, C. A., M. H. Flint and B. W. Beaumont (1987). "Chondrons in cartilage: ultrastructural analysis of the pericellular microenvironment in adult human articular cartilages." J Orthop Res **5**(4): 509-522.

Prasanth, K. V. and D. L. Spector (2005). The Cell Nucleus. Enyclopedia of Life Sciences, John Wiley & Sons, Ltd.

Prehm, P. (1983). "Synthesis of hyaluronate in differentiated teratocarcinoma cells. Mechanism of chain growth." Biochem J **211**(1): 191-198.

Pritchard, S. and F. Guilak (2004). "The role of F-actin in hypo-osmotically induced cell volume change and calcium signaling in anulus fibrosus cells." Annals of Biomedical Engineering **32**(1): 103-111.

Prockop, D. J. and K. I. Kivirikko (1995). "Collagens: molecular biology, diseases, and potentials for therapy." Annu Rev Biochem **64**: 403-434.

Radin, E. L., H. G. Parker, J. W. Pugh, Steinber.Rs, I. L. Paul and R. M. Rose (1973). "Response of Joints to Impact Loading .3. Relationship between Trabecular Microfractures and Cartilage Degeneration." Journal of Biomechanics **6**(1): 51-&.

Ragan, P. M., V. I. Chin, H. H. Hung, K. Masuda, E. J. Thonar, E. C. Arner, A. J. Grodzinsky and J. D. Sandy (2000). "Chondrocyte extracellular matrix synthesis and turnover are influenced by static compression in a new alginate disk culture system." Archives of Biochemistry and Biophysics **383**(2): 256-264.

Ratcliffe, A., M. E. Billingham, F. Saed-Nejad, H. Muir and T. E. Hardingham (1992). "Increased release of matrix components from articular cartilage in experimental canine osteoarthritis." J Orthop Res **10**(3): 350-358.

Ratcliffe, A., C. Hughes, P. R. Fryer, F. Saed-Nejad and T. Hardingham (1987). "Immunochemical studies on the synthesis and secretion of link protein and aggregating proteoglycan by chondrocytes." Coll Relat Res **7**(6): 409-421.

Reboul, P., J. P. Pelletier, G. Tardif, J. M. Cloutier and J. Martel-Pelletier (1996). "The new collagenase, collagenase-3, is expressed and synthesized by human chondrocytes but not by synoviocytes. A role in osteoarthritis." J Clin Invest **97**(9): 2011-2019.

Reddy, K. L., J. M. Zullo, E. Bertolino and H. Singh (2008). "Transcriptional repression mediated by repositioning of genes to the nuclear lamina." Nature **452**(7184): 243-247.

Redler, I., V. C. Mow, M. L. Zimny and J. Mansell (1975). "The ultrastructure and biomechanical significance of the tidemark of articular cartilage." Clin Orthop Relat Res(112): 357-362.

Redman, S. N., S. F. Oldfield and C. W. Archer (2005). "Current strategies for articular cartilage repair." Eur Cell Mater **9**: 23-32; discussion 23-32.

Repo, R. U. and N. Mitchell (1971). "Collagen synthesis in mature articular cartilage of the rabbit." J Bone Joint Surg Br **53**(3): 541-548.

Rich, D. R. and A. L. Clark (2012). "Chondrocyte primary cilia shorten in response to osmotic challenge and are sites for endocytosis." Osteoarthritis Cartilage **20**(8): 923-930.

Richardson, R. T., I. N. Batova, E. E. Widgren, L. X. Zheng, M. Whitfield, W. F. Marzluff and M. G. O'Rand (2000). "Characterization of the histone H1-binding protein, NASP, as a cell cycle-regulated somatic protein." J Biol Chem **275**(39): 30378-30386.

Roberts, S., B. Weightman, J. Urban and D. Chappell (1986). "Mechanical and biochemical properties of human articular cartilage in osteoarthritic femoral heads and in autopsy specimens." J Bone Joint Surg Br **68**(2): 278-288.

Roberts, S. R., M. M. Knight, D. A. Lee and D. L. Bader (2001). "Mechanical compression influences intracellular Ca2+ signaling in chondrocytes seeded in agarose constructs." Journal of applied physiology **90**(4): 1385-1391.

Rosenbaum, J. T., M. Brischetto, S. Crespo, M. Bierwirth, K. Oveson, S. R. Planck and M. D. Becker (2002). "Simultaneous in vivo imaging of leukocyte migration: heterogeneity among iris, limbus, and choroid vessels." Curr Eye Res **24**(3): 214-218.

Ross, K. A. and M. G. Scanlon (1999). "Analysis of the elastic modulus of agar gel by indentation." Journal of Texture Studies **30**(1): 17-27.

Rothwell, A. G. and G. Bentley (1973). "Chondrocyte multiplication in osteoarthritic articular cartilage." J Bone Joint Surg Br **55**(3): 588-594.

Ryan, M. C. and L. J. Sandell (1990). "Differential expression of a cysteine-rich domain in the amino-terminal propeptide of type II (cartilage) procollagen by alternative splicing of mRNA." J Biol Chem **265**(18): 10334-10339.

Saamanen, A. M., M. Tammi, J. Jurvelin, I. Kiviranta and H. J. Helminen (1990). "Proteoglycan alterations following immobilization and remobilization in the articular cartilage of young canine knee (stifle) joint." J Orthop Res **8**(6): 863-873.

Saamanen, A. M., M. Tammi, I. Kiviranta, J. Jurvelin and H. J. Helminen (1987). "Maturation of proteoglycan matrix in articular cartilage under increased and decreased joint loading. A study in young rabbits." Connect Tissue Res **16**(2): 163-175.

Sabbioneda, S., A. M. Gourdin, C. M. Green, A. Zotter, G. Giglia-Mari, A. Houtsmuller, W. Vermeulen and A. R. Lehmann (2008). "Effect of proliferating cell nuclear antigen ubiquitination and chromatin structure on the dynamic properties of the Y-family DNA polymerases." Mol Biol Cell **19**(12): 5193-5202.

Sandell, L. J., N. Morris, J. R. Robbins and M. B. Goldring (1991). "Alternatively spliced type II procollagen mRNAs define distinct populations of cells during vertebral development: differential expression of the amino-propeptide." J Cell Biol **114**(6): 1307-1319.

Satir, P. and S. T. Christensen (2008). "Structure and function of mammalian cilia." Histochem Cell Biol **129**(6): 687-693.

Scheer, U. and R. Hock (1999). "Structure and function of the nucleolus." Curr Opin Cell Biol **11**(3): 385-390.

Schmidt, M. B., V. C. Mow, L. E. Chun and D. R. Eyre (1990). "Effects of proteoglycan extraction on the tensile behavior of articular cartilage." J Orthop Res **8**(3): 353-363.

Schneiderman, R., D. Keret and A. Maroudas (1986). "Effects of mechanical and osmotic pressure on the rate of glycosaminoglycan synthesis in the human adult femoral head cartilage: an in vitro study." J Orthop Res **4**(4): 393-408.

Scott, J. E. (1996). "Proteodermatan and proteokeratan sulfate (decorin, lumican/fibromodulin) proteins are horseshoe shaped. Implications for their interactions with collagen." Biochemistry **35**(27): 8795-8799.

Setton, L. A., V. C. Mow and D. S. Howell (1995). "Mechanical-Behavior of Articular-Cartilage in Shear Is Altered by Transection of the Anterior Cruciate Ligament." Journal of Orthopaedic Research **13**(4): 473-482.

Shapiro, F. and M. J. Glimcher (1980). "Induction of Osteoarthrosis in the Rabbit Knee-Joint - Histologic-Changes Following Meniscectomy and Meniscal Lesions." Clinical Orthopaedics and Related Research(147): 287-295.

Shaw, P. J. (2005). Nucleolus. Enyclopedia of Life Sciences, John Wiley & Sons, Ltd.

Shepard, P. J., E. A. Choi, J. T. Lu, L. A. Flanagan, K. J. Hertel and Y. S. Shi (2011). "Complex and dynamic landscape of RNA polyadenylation revealed by PAS-Seq." Rna-a Publication of the Rna Society **17**(4): 761-772.

Shieh, A. C. and K. A. Athanasiou (2002). "Biomechanics of single chondrocytes and osteoarthritis." Crit Rev Biomed Eng **30**(4-6): 307-343.

Shlopov, B. V., W. R. Lie, C. L. Mainardi, A. A. Cole, S. Chubinskaya and K. A. Hasty (1997). "Osteoarthritic lesions: involvement of three different collagenases." Arthritis Rheum **40**(11): 2065-2074.

Singh, S., B. S. Dwarakanath and T. L. Mathew (2004). "DNA ligand Hoechst-33342 enhances UV induced cytotoxicity in human glioma cell lines." J Photochem Photobiol B **77**(1-3): 45-54.

Slowman, S. D. and K. D. Brandt (1986). "Composition and glycosaminoglycan metabolism of articular cartilage from habitually loaded and habitually unloaded sites." Arthritis Rheum **29**(1): 88-94.

Smith, P. J., N. Blunt, M. Wiltshire, T. Hoy, P. Teesdale-Spittle, M. R. Craven, J. V. Watson, W. B. Amos, R. J. Errington and L. H. Patterson (2000). "Characteristics of a novel deep red/infrared fluorescent cell-permeant DNA probe, DRAQ5, in intact human cells analyzed by flow cytometry, confocal and multiphoton microscopy." Cytometry **40**(4): 280-291.

Smith, P. J., M. Wiltshire, S. Davies, L. H. Patterson and T. Hoy (1999). "A novel cell permeant and far red-fluorescing DNA probe, DRAQ5, for blood cell discrimination by flow cytometry." Journal of Immunological Methods **229**(1-2): 131-139.

Smyth, G. K. (2004). "Linear models and empirical bayes methods for assessing differential expression in microarray experiments." Stat Appl Genet Mol Biol **3**: Article3.

Snyder, D. S. and P. L. Small (2001). "Staining of cellular mitochondria with LDS-751." J Immunol Methods **257**(1-2): 35-40.

Sparrow, R. L., H. Komodromou, E. Tippett, T. Georgakopoulos and W. Xu (2006). "Apoptotic lymphocytes and CD34+ cells in cryopreserved cord blood detected by the fluorescent vital dye SYTO 16 and correlation with loss of L-selectin (CD62L) expression." Bone Marrow Transplant **38**(1): 61-67.

Steinmeyer, J., S. Knue, R. X. Raiss and I. Pelzer (1999). "Effects of intermittently applied cyclic loading on proteoglycan metabolism and swelling behaviour of articular cartilage explants." Osteoarthritis Cartilage **7**(2): 155-164.

Stockwell, R. A. (1967). "The cell density of human articular and costal cartilage." J Anat **101**(Pt 4): 753-763.

Stockwell, R. A. (1971). "The interrelationship of cell density and cartilage thickness in mammalian articular cartilage." J Anat **109**(Pt 3): 411-421.

Strobl, G. R. (1996). The physics of polymers : concepts for understanding their structures and behavior. Berlin ; London, Springer Verlag.

Suzuki, T., K. Fujikura, T. Higashiyama and K. Takata (1997). "DNA staining for fluorescence and laser confocal microscopy." J Histochem Cytochem **45**(1): 49-53.

Takahashi, K., T. Kubo, Y. Arai, I. Kitajima, M. Takigawa, J. Imanishi and Y. Hirasawa (1998). "Hydrostatic pressure induces expression of interleukin 6 and tumour

necrosis factor alpha mRNAs in a chondrocyte-like cell line." Ann Rheum Dis **57**(4): 231-236.

Tammi, M., A. M. Saamanen, A. Jauhiainen, O. Malminen, I. Kiviranta and H. Helminen (1983). "Proteoglycan alterations in rabbit knee articular cartilage following physical exercise and immobilization." Connect Tissue Res **11**(1): 45-55.

Tasci, A., S. J. Ferguson and P. Buchler (2011). "Numerical assessment on the effective mechanical stimuli for matrix-associated metabolism in chondrocyte-seeded constructs." J Tissue Eng Regen Med **5**(3): 210-219.

Teramura, T., K. Fukuda, S. Kurashimo, Y. Hosoi, Y. Miki, S. Asada and C. Hamanishi (2008). "Isolation and characterization of side population stem cells in articular synovial tissue." BMC Musculoskelet Disord **9**: 86.

Tew, S., S. Redman, A. Kwan, E. Walker, I. Khan, G. Dowthwaite, B. Thomson and C. W. Archer (2001). "Differences in repair responses between immature and mature cartilage." Clinical Orthopaedics and Related Research(391): S142-S152.

Tew, S. R., M. J. Peffers, T. R. McKay, E. T. Lowe, W. S. Khan, T. E. Hardingham and P. D. Clegg (2009). "Hyperosmolarity regulates SOX9 mRNA posttranscriptionally in human articular chondrocytes." Am J Physiol Cell Physiol **297**(4): C898-906.

Tew, S. R., O. Vasieva, M. J. Peffers and P. D. Clegg (2011). "Post-transcriptional gene regulation following exposure of osteoarthritic human articular chondrocytes to hyperosmotic conditions." Osteoarthritis Cartilage **19**(8): 1036-1046.

Thomas, R. S., A. R. Clarke, V. C. Duance and E. J. Blain (2011). "Effects of Wnt3A and mechanical load on cartilage chondrocyte homeostasis." Arthritis Res Ther **13**(6): R203.

Thompson, R. C., T. R. Oegema, J. L. Lewis and L. Wallace (1991). "Osteoarthrotic Changes after Acute Transarticular Load - an Animal-Model." Journal of Bone and Joint Surgery-American Volume **73A**(7): 990-1001.

Tolun, G. and R. S. Myers (2003). "A real-time DNase assay (ReDA) based on PicoGreen (R) fluorescence." Nucleic Acids Research **31**(18): e111.

Torzilli, P. A., E. Askari and J. T. Jenkins (1990). Water content and solute diffusion properties in articular cartilage. in: Biomechanics of diarthrodial joints. V. C. Mow and S. L. Y. Woo. New York, N.Y., Springer-Verlag**:** 363-390.

Torzilli, P. A., M. Bhargava, S. Park and C. T. Chen (2010). "Mechanical load inhibits IL-1 induced matrix degradation in articular cartilage." Osteoarthritis Cartilage **18**(1): 97-105.

Torzilli, P. A., R. Grigiene, C. Huang, S. M. Friedman, S. B. Doty, A. L. Boskey and G. Lust (1997). "Characterization of cartilage metabolic response to static and dynamic stress using a mechanical explant test system." Journal of Biomechanics **30**(1): 1-9.

Trickey, W. R., F. P. T. Baaijens, T. A. Laursen, L. G. Alexopoulos and F. Guilak (2006). "Determination of the Poisson's ratio of the cell: Recovery properties of chondrocytes after release from complete micropipette aspiration (Trickey et al., Journal of Biomechanics, 39 (2006) 78-87 - Response to Dr. Schachar." Journal of Biomechanics **39**(12): 2344-2345.

Trickey, W. R., T. P. Vail and F. Guilak (2004). "The role of the cytoskeleton in the viscoelastic properties of human articular chondrocytes." Journal of Orthopaedic Research **22**(1): 131-139.

Trippel, S. B. (1995). "Growth factor actions on articular cartilage." J Rheumatol Suppl **43**: 129-132.

Turnay, J., E. Pfannmuller, M. A. Lizarbe, W. M. Bertling and K. von der Mark (1995). "Collagen binding activity of recombinant and N-terminally modified annexin V (anchorin CII)." J Cell Biochem **58**(2): 208-220.

Ueki, M., N. Tanaka, K. Tanimoto, C. Nishio, K. Honda, Y. Y. Lin, Y. Tanne, S. Ohkuma, T. Kamiya, E. Tanaka and K. Tanne (2008). "The effect of mechanical loading on the metabolism of growth plate chondrocytes." Ann Biomed Eng **36**(5): 793-800.

Urban, J. P. (1994). "The chondrocyte: a cell under pressure." Br J Rheumatol **33**(10): 901-908.

Urban, J. P. and M. T. Bayliss (1989). "Regulation of proteoglycan synthesis rate in cartilage in vitro: influence of extracellular ionic composition." Biochim Biophys Acta **992**(1): 59-65.

Urban, J. P., A. C. Hall and K. A. Gehl (1993). "Regulation of matrix synthesis rates by the ionic and osmotic environment of articular chondrocytes." J Cell Physiol **154**(2): 262-270.

Valhmu, W. B., E. J. Stazzone, N. M. Bachrach, F. Saed-Nejad, S. G. Fischer, V. C. Mow and A. Ratcliffe (1998). "Load-controlled compression of articular cartilage induces a transient stimulation of aggrecan gene expression." Archives of Biochemistry and Biophysics **353**(1): 29-36.

van Beuningen, H. M., R. Stoop, P. Buma, N. Takahashi, P. M. van der Kraan and W. B. van den Berg (2002). "Phenotypic differences in murine chondrocyte cell lines derived from mature articular cartilage." Osteoarthritis Cartilage **10**(12): 977-986.

Vanwanseele, B., F. Eckstein, H. Knecht, A. Spaepen and E. Stussi (2003). "Longitudinal analysis of cartilage atrophy in the knees of patients with spinal cord injury." Arthritis Rheum **48**(12): 3377-3381.

Vanwanseele, B., F. Eckstein, H. Knecht, E. Stussi and A. Spaepen (2002). "Knee cartilage of spinal cord-injured patients displays progressive thinning in the absence of normal joint loading and movement." Arthritis Rheum **46**(8): 2073-2078.

Vener, M. J., R. C. Thompson, Jr., J. L. Lewis and T. R. Oegema, Jr. (1992). "Subchondral damage after acute transarticular loading: an in vitro model of joint injury." J Orthop Res **10**(6): 759-765.

Videman, T., J. E. Michelsson, R. Rauhamaki and A. Langenskiold (1976). "Changes in 35S-sulphate uptake in different tissues in the knee and hip regions of rabbits during immobilization, remobilization the development of osteoarthritis." Acta Orthop Scand **47**(3): 290-298.

Vogelmann, J., A. Valeri, E. Guillou, O. Cuvier and M. Nollmann (2011). "Roles of chromatin insulator proteins in higher-order chromatin organization and transcription regulation." Nucleus **2**(5): 358-369.

Wachtel, E., A. Maroudas and R. Schneiderman (1995). "Age-related changes in collagen packing of human articular cartilage." Biochim Biophys Acta **1243**(2): 239-243.

Waldegger, S., S. Steuer, T. Risler, A. Heidland, G. Capasso, S. Massry and F. Lang (1998). "Mechanisms and clinical significance of cell volume regulation." Nephrol Dial Transplant **13**(4): 867-874.

Walter, J., L. Schermelleh, M. Cremer, S. Tashiro and T. Cremer (2003). "Chromosome order in HeLa cells changes during mitosis and early G1, but is stably maintained during subsequent interphase stages." J Cell Biol **160**(5): 685-697.

Wang, H., S. T. Walsh and M. R. Parthun (2008). "Expanded binding specificity of the human histone chaperone NASP." Nucleic Acids Research **36**(18): 5763-5772.

Wang, P., L. Yang and A. H. Hsieh (2011). "Nucleus pulposus cell response to confined and unconfined compression implicates mechanoregulation by fluid shear stress." Ann Biomed Eng **39**(3): 1101-1111.

Wann, A. K. T., N. Zuo, C. J. Haycraft, C. G. Jensen, C. A. Poole, S. R. McGlashan and M. M. Knight (2012). "Primary cilia mediate mechanotransduction through control of ATP-induced Ca2+ signaling in compressed chondrocytes." Faseb Journal **26**(4): 1663-1671.

Watanabe, H., Y. Yamada and K. Kimata (1998). "Roles of aggrecan, a large chondroitin sulfate proteoglycan, in cartilage structure and function." J Biochem **124**(4): 687-693.

Weightman, B. and G. Kempson (1979). Load carriage. in: Adult articular cartilage. M. A. R. Freeman. London, Pitman Medical**:** 293-341.

Wlodkowic, D., J. Skommer and Z. Darzynkiewicz (2008). "SYTO probes in the cytometry of tumor cell death." Cytometry A **73**(6): 496-507.

Wojcik, K. and J. W. Dobrucki (2008). "Interaction of a DNA intercalator DRAQ5, and a minor groove binder SYTO17, with chromatin in live cells--influence on chromatin organization and histone-DNA interactions." Cytometry A **73**(6): 555-562.

Wright, M. O., R. A. Stockwell and G. Nuki (1992). "Response of plasma membrane to applied hydrostatic pressure in chondrocytes and fibroblasts." Connective tissue research **28**(1-2): 49-70.

Wu, J. J., P. E. Woods and D. R. Eyre (1992). "Identification of cross-linking sites in bovine cartilage type IX collagen reveals an antiparallel type II-type IX molecular relationship and type IX to type IX bonding." J Biol Chem **267**(32): 23007-23014.

Wu, M. H., J. P. G. Urban, Z. F. Cui, Z. Cui and X. Xu (2007). "Effect of extracellular pH on matrix synthesis by chondrocytes in 3D agarose gel." Biotechnology Progress **23**(2): 430-434.

Wu, Q. Q. and Q. Chen (2000). "Mechanoregulation of chondrocyte proliferation, maturation, and hypertrophy: Ion-channel dependent transduction of matrix deformation signals." Experimental Cell Research **256**(2): 383-391.

Wu, Q. Q., Y. Zhang and Q. Chen (2001). "Indian hedgehog is an essential component of mechanotransduction complex to stimulate chondrocyte proliferation." Journal of Biological Chemistry **276**(38): 35290-35296.

Xu, T., P. Bianco, L. W. Fisher, G. Longenecker, E. Smith, S. Goldstein, J. Bonadio, A. Boskey, A. M. Heegaard, B. Sommer, K. Satomura, P. Dominguez, C. Zhao, A. B. Kulkarni, P. G. Robey and M. F. Young (1998). "Targeted disruption of the biglycan gene leads to an osteoporosis-like phenotype in mice." Nat Genet **20**(1): 78-82.

Xu, X., J. P. Urban, U. K. Tirlapur and Z. Cui (2010). "Osmolarity effects on bovine articular chondrocytes during three-dimensional culture in alginate beads." Osteoarthritis Cartilage **18**(3): 433-439.

Yellowley, C. E., C. R. Jacobs and H. J. Donahue (1999). "Mechanisms contributing to fluid-flow-induced Ca2+ mobilization in articular chondrocytes." Journal of Cellular Physiology **180**(3): 402-408.

Yielding, K. L., D. Platt and H. L. Holley (1954). "Synovial fluid. I. Comparison of sodium and potassium concentrations in normal and diseased joint fluid." Proc Soc Exp Biol Med **85**(4): 665-667.

Yusoff, N., N. A. Abu Osman and B. Pingguan-Murphy (2011). "Design and validation of a bi-axial loading bioreactor for mechanical stimulation of engineered cartilage." Medical Engineering & Physics **33**(6): 782-788.

PUBLICATIONS AND CONFERENCE PROCEEDINGS

Publications:

Chen, J., **J. Irianto**, S. Inamdar, P. Pravincumar, D.A. Lee, D.L. Bader and M.M. Knight (2012). "Cell mechanics, structure and function are regulated by the stiffness of the 3D microenvironment." Biophysical Journal **103**(6):1188-1197.

Irianto, J., J. Swift, R.P. Martins, G.D. McPhail, M.M. Knight, D.E. Discher and D.A. Lee (2013). "Physiological Osmotic Challenge Drives Rapid and Reversible Chromatin Condensation in Chondrocytes." Biophysical Journal **104**(4):759-769

Conference proceedings:

J. Irianto, R.P. Martins, R.A. Nuamah, C.A. Mein, D.A. Lee. "The Effect of Osmotic Challenge on Levels of Chromatin Condensation and Histone Expressions in Chondrocyte". *2013 ORS Annual Meeting 26th-29th January 2013, San Antonio, TX, USA* (Poster presentation).

J. Irianto, M.M. Knight, R.P. Martins, D.A. Lee. "Osmolality Challenge Affects the Cell and Nuclear Deformation of Chondrocytes Seeded in Agarose and Subjected to Static Compression Loading". *2012 ORS Annual Meeting 4th-7th February 2012, San Francisco, CA, USA* (Poster presentation).

J. Irianto, M.M. Knight, D.A. Lee. "The Effect of Osmotic Challenge on the Chromatin Condensation Level of Chondrocyte Nucleus". *Bioengineering11 12th-13th September 2011, London, UK* (Poster presentation).

J. Irianto, M.M. Knight, R.P. Martins, D.A. Lee. "Osmotic Challenge Influences the Morphology and Levels of Chromatin Condensation in the Chondrocyte Nucleus". *2011 ORS Annual Meeting 13th-16th January 2011, Long Beach, CA, USA* (Poster presentation).